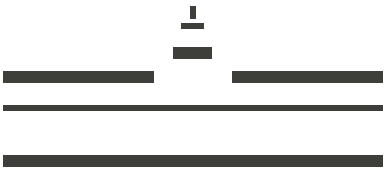

Westfälische
Wilhelms-Universität
Münster

Fach: Mathematik

Optimizing tCS and TMS multi-sensor setups using realistic head models

Inaugural Dissertation

zur Erlangung des Doktorgrades der Naturwissenschaften

– Dr. rer. nat. –

im Fachbereich Mathematik und Informatik

der Mathematisch-Naturwissenschaftlichen Fakultät

der Westfälischen Wilhelms-Universität Münster

eingereicht von

Sven Wagner

aus Herten

– 2015 –

Dekan:	Prof. Dr. Martin Stein
Erster Gutachter:	Priv.-Doz. Dr. Carsten H. Wolters (Institut für Biomagnetismus und Biosignalanalyse)
Zweiter Gutachter:	Prof. Dr. Martin Burger (Universität Münster)
Tag der mündlichen Prüfung:	26.08.2015
Tag der Promotion:	

Abstract

The scope of this thesis was to introduce and analyze a novel simulation pipeline for transcranial current stimulation (tCS), transcranial magnetic stimulation (TMS) or combined tCS and TMS (tCMS) which can be used to predict inter-individually optimized stimulation protocols for patients and their specific disease. Major findings of this thesis include:

(1) A guideline for efficient yet accurate volume conductor modeling in tCS, TMS and tCMS was developed and presented. This head model generation pipeline allows to build highly realistic, individually shaped, geometry-adapted hexahedral head models in less than one day of working time.

(2) By providing analytical forward expressions for the adjoint approach (Vallaghe and colleagues [135]) and the partial integration approach (Schimpf and colleagues [120]), EEG forward computations and tCS simulations were linked in a clear mathematical way. Using this relation, the accuracy and efficiency of commonly-used tetrahedral and hexahedral finite element approaches for brain stimulation techniques were investigated. It was shown that while the accuracy of the most easy to realize approach based on regular hexahedral elements is already quite high, it can substantially be improved if a geometry-adaptation of the elements is employed in conjunction with an isoparametric FEM approach. While the latter approach does not involve any additional difficulties for the user, it reaches the high accuracies of surface-segmentation based tetrahedral FEM, which is considerably more difficult to implement and topologically less flexible in practice.

(3) In order to find an optimal solver method for brain stimulation, the accuracy and efficiency of three preconditioner methods were investigated: Incomplete cholesky without fill in (IC(0)), Jacobi and algebraic multigrid (AMG) for the conjugate gradient (CG) method. It was shown that a solver accuracy level of 10^{-7} is sufficient to attain realistic numerical solutions with the three preconditioner methods. However, the investigation of the solver clock time revealed that the AMG-CG solver significantly outperforms the Jacobi-CG and IC(0)-CG solvers with regard to computational efficiency.

(4) With quantification of the optimized current flow fields in simplified, spherical models and realistically shaped FE head models, a proof of concept that the novel optimization method for tCS, TMS and tCMS is working properly was presented. The optimized current flow fields were visually inspected. A quantification revealed that the optimized current flow fields show substantially higher focality and directional agreement with the target vectors in comparison to standard current density vector fields. Finally, an in-depth mathematical analysis of the optimization method was provided. While the numerical and modeling errors are thus clearly under control, the influence of inter-individually varying conductivity profiles on optimal electrode configurations was investigated for an auditory cortex stimulation. The probability density functions of the optimized stimulation protocols at the main electrodes were shown to be most sensitive to the uncertainty in the skull conductivity.

In conclusion, a proof of concept that the simulation pipeline for tCS/TMS and tCMS is working properly was presented and that the calculation of individually optimized stimulation is not only feasible for single patients but also for a larger number of patients in clinical trial studies.

Zusammenfassung

Das Hauptziel dieser Arbeit war die Entwicklung und die Untersuchung eines Simulationsleitfadens für die elektrische und magnetische Hirnstimulation, welcher es erlaubt, individuelle Stimulationsprotokolle für Patienten und deren Krankheiten zu bestimmen. Hauptresultate dieser Arbeit sind:

(1) Für die transkranielle Stromstimulation (tCS) und die transkranielle Magnetstimulation (TMS) wurden Richtlinien zur effizienten Volumenleitermodellierung entwickelt, vorgestellt und untersucht. Aufgrund der Effizienzsteigerung können nun patientenspezifische, praxistaugliche und sehr realistische Kopfmodelle innerhalb von weniger als zwei Arbeitstagen erzeugt werden.

(2) In einer weiteren Studie wurden analytische Formeln für zwei EEG Vorwärts-Verfahren entwickelt und miteinander verglichen. Als Ergebnis konnte gezeigt werden, dass die EEG Quellenanalyse und die Simulationen der durch tCS induzierten Ströme direkt miteinander gekoppelt sind, und dass quasi-analytische EEG Vorwärts-Formeln in Kugelmodellen dazu benutzt werden können, um die numerischen Genauigkeiten von verschiedenen Modellierungsansätzen für tCS zu untersuchen. Während die Genauigkeit des kubischen Ansatz schon relativ hoch war, lieferte der geometrie-adaptierte kubische Ansatz noch deutlich bessere numerische Ergebnisse. Die Genauigkeiten des geometrie-adaptierten Ansatzes lagen auf dem Niveau des Tetraederansatzes, welcher, im Gegensatz zu den kubischen Ansätzen, deutlich schwerer zu implementieren ist, und auf teilweise unrealistischen praktischen Annahmen basiert.

(3) Um einen optimalen iterativen Löser für tCS und TMS zu bestimmen, wurden numerische Genauigkeiten und die benötigte Löserzeit der Jacobi, IC(0) und AMG Vorkonditionierermethoden für die konjugierte Gradientenmethode (CG) untersucht. Durch die Berechnung der numerischen Fehler RDM und MAG konnte gezeigt werden, dass alle drei Löser identische numerische Resultate liefern. Durch eine Untersuchung der benötigten Löserzeit wurde zusätzlich verdeutlicht, dass der AMG-CG Löser schneller und effektiver ist, als die Löser IC(0)-CG und Jacobi-CG.

(4) Eine neue und hoch-innovative Optimierungsmethode, welche sowohl für die tCS und TMS, wie auch für eine kombinierte Stimulation mit beiden Methoden anwendbar ist, wurde entwickelt und in verschiedenen Kopfmodellen getestet. Im Gegensatz zu einer standartmäßigen Stimulation mit zwei großen Elektroden, wiesen die optimierten Ströme eine deutlich höhere Fokalität und einen leicht verbesserten Stromfluss parallel zum Zielvektor auf. Um die Ergebnisse auf ein solides mathematisches Fundament zu bringen, wurde die Optimierungsmethode mathematisch analysiert. Die Existenz (und in manchen Fällen Eindeutigkeit) eines Minimums für das Optimierungsproblem mit Nebenbedindungen wurde bewiesen. Während die numerischen Ungenauigkeiten und die Modellierungsfehler daher klar kontrolliert werden können, sind die Auswirkungen von individuellen Leitfähigkeiten auf die Berechnung der optimierten Stimulationsprotokolle bisher weitestgehend unbekannt. In einer weiteren Studie konnte gezeigt werden, dass die Stimulation an den Hauptelektroden sehr stark durch die Unsicherheit in der Leitfähigkeit des Schädel beeinflusst wird.

Zusammenfassend kann gesagt werden, dass die in dieser Arbeit entwickelten Simulations- und Optimierungsmethoden für die transkranielle Stromstimulation und die transkranielle Magnetstimulation anwendbar sind und zu realitätsnahen Stromverteilungen im Gehirn führen. Da zusätzlich die Effizienz der Modellgenerierung deutlich gesteigert wurde, ist die Berechnung von individualisierten Stimulationsprotokollen nicht nur für einzelne Patienten, sondern auch für eine breite Masse an Patienten in klinischen Studien möglich.

Acknowledgements

I want to thank everyone who made this thesis possible, especially:

- My thesis supervisor PD. Dr. rer. nat. Carsten Wolters for the opportunity to work in his group, his valuable scientific advice and his professional guidance during the last years.
- My co-supervisor Prof. Dr. Martin Burger for his scientific input and always being willing to provide rapid and helpful feedback.
- Prof. Dr. Xiaoyi Jiang for accepting to be a reviewer of this work.
- Prof. Dr. Christo Pantev for giving me the opportunity to work at the Institute for Biomagnetism and Biosignalanalysis.
- Felix Lucka, Johannes Vorwerk and Benjamin Lanfer for proofreading this thesis and for scientific information exchange.
- Simon Homölle and Britte Agsten for a great cooperation.
- All colleagues at the IBB for the great working atmosphere.
- The SCIRun team for providing a powerful, flexible and freely-available tool for modeling, simulation, and visualization.
- My project cooperation partners from Oldenburg (Prof. Christoph Herrmann, Dr. Toralf Neuling), Nijmegen (Prof. Dick Stegeman, Prof. Thom Oostendorp, Dr. Sumientra Rampersad, Arno Janssen), Rostock (Prof. Ursula van Rienen, Dr. Christian Schmidt) and Tampere (Prof. Sampsa Pursiainen) for a very productive collaboration and valuable scientific information exchange.
- My family for their support at all times.
- Finally, I would like to thank my wife Nadine for her continuous understanding, support and love during the past years.

Furthermore, I am grateful to the German Research Foundation (DFG) and PD. Dr. rer. nat. Carsten Wolters for funding this work through the project WO1425/3-1 and the Priority

Program 1665 of the DFG (WO1425/5-1).

Keywords: Transcranial electric and magnetic stimulation, head volume conductor modeling, finite element method, alternating direction method of multipliers, preconditioned conjugate gradient method, current density optimization

Contents

List of Figures

1 Introduction

1.1. General introduction

EEG and MEG source analysis

Electroencephalography (EEG) and *magnetoencephalography* (MEG)-based source reconstruction of electrical activity in the brain is a general tool for neuroscientific research and clinical diagnosis. In order to reconstruct the active brain regions from the measured external electric potentials or magnetic fields (i.e., *inverse problem of EEG/MEG source analysis*), the so called *forward problem* has to be solved as accurately as possible. The forward problem consists of simulating the electric or magnetic fields at the measurement sensors for known primary brain current sources. The primary sources are generated by ionic currents within the dendrites of the large pyramidal cells of the activated neurons in the cortex sheet of the human brain [151]. In order to model the primary sources, a point current dipole is widely-used in EEG and MEG source analysis. De Munck and colleagues [31] were able to demonstrate that an equivalent point dipole is a good approximation to the electric brain activity with respect to position, orientation and strength. For this reason, the equivalent current dipole is often used to represent brain activity in a small subregion inside the brain.

Hermann von Helmholtz was able to demonstrate that the bioelectric and biomagnetic inverse problems do not have a unique solution [56], i.e., several source configurations lead to an identical potential distribution at the measurement sites. For this reason, a variety of inverse approaches has been invented [56]. While the main drawback of EEG/MEG source analysis is the low spatial resolution due to the non-uniqueness of the inverse problem, the high temporal resolution is its main advantage [52].

tDCS/tACS and TMS

Transcranial direct current stimulation (tDCS) is a non-invasive, easy-to-perform and inexpensive brain stimulation technique which modifies neural excitability by providing constant weak direct currents through scalp electrodes [84]. Changes in neural membrane potentials are induced in a polarity-dependent manner. For example, anodal stimulation enhances cortical excitability in the motor cortex region, while cathodal stimulation inhibits it [84]. In order to assess the efficiency of stimulation, experimental and clinical studies have been performed [37, 38, 84]. Positive effects of stimulation have been reported for neurological and neuropsychiatric disorders such as Alzheimer's disease [37], Parkinson's disease [12], epilepsy [38] and tinnitus [66]. Moreover, cognitive functions were substantially enhanced [61] and motor rehabilitation after stroke was improved [59] after weak direct current stimulation. As a tool for clinical studies and neuroscientific research, the interest in tDCS has been growing substantially over the past decade.

In experimental studies, the conventional strategy is to apply the current via two large electrodes with the active electrode (anode) being placed above the presumed target region and the reference electrode (cathode) far away from the target region [38, 84]. Accurate and detailed *finite element* (FE) head models have been created to investigate the induced current density distribution [33, 115, 142, 144]. A similar stimulation method is *transcranial alternating current stimulation* (tACS), in which the applied current is alternating at a certain frequency. This stimulation method is well suited to modulate brain oscillations in a frequency-specific manner [54].

Another important brain stimulation technique that is frequently-used in brain research and clinical neurophysiology is *transcranial magnetic stimulation* (TMS), which uses an externally generated magnetic field to induce electric currents in the underlying brain tissue. While tDCS is only able to modulate and modify neural excitability, the electric fields induced by TMS are strong enough to non-invasively induce action potentials in a focal region underneath the stimulating coil [117]. Recently, TMS has been approved for the treatment of depression and migraine by the U.S. Food and Drug Administration (FDA) [82]. Significant effects of stimulation in comparison to sham stimulation (look and sound of active coil is replicated but no magnetic field is generated) have been reported for the treatment of neuropsychiatric disorders such as schizophrenia [99], epilepsy [131], depression [21] and Parkinson's disease [125]. Moreover, positive effects of stimulation have been reported for neuroanatomical disorders such as a stroke [67].

An extended transcranial magnetic stimulation form is called *repetitive transcranial magnetic stimulation* (rTMS), which delivers multiple magnetic pulses at rates of up to 50 Hz. It has been demonstrated that the application of rTMS above the motor cortex induces long-lasting changes of motor-evoked potentials [85, 106]. This offers new possibilities for the application of rTMS such as investigating the influence of certain brain regions in neural processing or studying the pathophysiology of diseases. Furthermore, rTMS can be used to validate the effects of transcranial direct current stimulation. Antal and colleagues [3] measured

the phosphine threshold (PT) using short trains of 5 Hz TMS pulses before, immediately after, 10 min and 20 min after the end of the tDCS stimulation. They found a reduced PT immediately and 10 min after the end of anodal stimulation, whereas cathodal stimulation enhanced the PT.

1.2. Current status in tDCS, TMS and volume conductor modeling

Transcranial direct current stimulation modeling

With regard to current flow estimation in tDCS, spherical shell models with three or more nested compartments [77, 103] and realistically shaped MRI-derived FE head models [82, 95, 114, 142] have been used recently. Volume conductor models taking into account separate skull layers [57, 82, 103], the highly-conductive *cerebrospinal fluid* (CSF) compartment [26, 95, 116, 144], a white matter compartment [95, 114, 116, 144] and white matter anisotropy [57, 90, 114, 130] have been employed. The location of the stimulating electrodes [26, 36, 82, 116], the size and shape of the electrodes [36, 144] and idiosyncratic details in brain anatomy [33, 82] have been shown to strongly influence the cortical current flow. While significant effects of stimulation as compared to sham were reported [38, 84], computer simulation studies have revealed that the cortical current flow field is rather widespread with the largest intensities located in non-target brain regions [82, 142]. It is therefore a matter of debate whether the effects of stimulation are driven by a stimulation of the target region or elicited by the stimulation of non-target cortical lobes.

In order to overcome the limitations of conventional bipolar electrode montages, sensor optimization approaches have been recently introduced [33, 60, 96, 115]. Im and colleagues [60] used an evolution strategy algorithm to search for two electrode locations which generate maximal current flow towards a certain target direction. They used structural MRI data of a standard brain atlas and tessellated it into 118.433 tetrahedral elements and 19.981 nodes. Im and colleagues reported that they could calculate optimal bipolar scalp electrode montages which can stimulate target brain regions with minimal injection currents. Recently, Park and colleagues [96] calculated optimal injection currents/potentials at 12 electrodes by solving a constrained optimization problem. They evaluated the current density distribution in a realistic head model using the finite element method (FEM). Park and colleagues [96] reported that the average current density values in the target area were increased (between 35 % and 78 %) after the optimization. In addition, they were able to show that the average current density in non-target regions is reduced by a maximal factor of 14.2 % by controlling the input values of the electrodes. Dmochowski and colleagues [33] used a multi-electrode-array consisting of 64 fixed electrode locations to calculate optimized stimulation protocols for presumed target regions. They applied *least square*, *weighted least squares with individual* L_1 *constraint*, *linearly constrained minimum variance* and *optimization for intensity* optimization approaches for this purpose. In order to analyze their optimization methods, Dmochowski and colleagues [33] employed radial and tangential targets and reported that compared to

conventional bipolar electrode montages their optimization approach achieved electric fields which exhibit greater focality and target intensity at cortical targets simultaneously using the same total current applied.
Sadleir and colleagues [115] derived a method of steering current towards a selected target area by reference to a 19-electrode montage applied to a high-resolution FE head model. They used a non-linear optimization procedure to maximize mean current densities inside the left inferior frontal gyrus while simultaneously restricting overall current and median current densities within the accumbens [115].

Transcranial magnetic stimulation modeling

While tDCS simulation studies revealed that the current flow field is rather broad with the largest intensities possibly located in sensor-remote cortical regions [82, 142], the current flow induced by TMS is comparably focal with highest cortical current densities directly under the rim of the stimulating coil [92, 143, 145]. The effects of the individual cortical folding [62, 92], brain tissue anisotropy [74, 93] and brain anomalities [143] have been recently investigated. Volume conductor models including the highly-conductive CSF compartment [62, 92, 93, 145], a white matter compartment [62, 92, 93, 145] and white matter anisotropy [29, 62, 92, 93] have been utilized.

Recently, a simulation study for TMS investigating the mechanisms which lead to neural activation in the motor cortex has been presented by Salvador and colleagues [117]. They simulated the neurons at different directions, namely at the fiber bends of the pyramidal tract neurons, at the axonal terminates for cortical interneurons and axon collaterals, and at a combination of both for pyramidal associated fibers [117]. While posterior-anterior oriented electrical fields have been shown to efficiently stimulate the neurons, the association fibers are less effected by them [117]. Salvador and colleagues [117] concluded that the outcome of stimulation strongly depends on the pulse waveform and the current density direction relative to the neurons.

With regard to TMS multi-coil optimization, several methods have been proposed [44, 69, 111]. Recently, Gomez and colleagues [44] introduced a genetic algorithmic-based technique for multi-array TMS montages. This technique is used to minimize the volume of excited brain tissue required to generate a predefined penetration depth of the electric field [44]. For validation, they used a target depth of $d_{stim} = 24\,\text{mm}$ and were able to demonstrate that the excited volume could be decreased by factors of 3 and 2.6 when using a multi-array and single-array TMS device as compared to a figure-of-eight coil. Furthermore, when exciting only 0.3 % of the volume, the optimized field arrays were shown to reach a depth of 27 mm into the head while the field of the figure-of-eight coil only reached a depth of 15 mm [44].
Ruohonen and Ilmoniemi [111] adapted the minimum norm estimate for the inverse problem in MEG to TMS multi-array optimization for presumed target vectors. They used a planar coil set consisting of 36 small circular coil elements in a square lattice and calculated the optimized driving currents in an unbounded volume conductor model. They reported that the induced electric field was substantially more focused when 36 independent coil elements were

used as compared to single coil stimulation. Moreover, the target brain region can be changed without moving the coils.

Volume conductor modeling

Several studies have been conducted to investigate the importance of modeling different head tissue compartments with regard to computer simulation studies. In EEG source analysis, the importance of using realistically shaped isotropic three-compartment head models (in contrast to spherical approximations) has been demonstrated [56, 91, 108]. However, such head models ignore the layered structure of the skull in top and bottom compacta and spongosia [2, 113], whose important influence was shown by Dannhauer and colleagues [25]. Furthermore, modeling skull holes and inhomogeneities [25, 68, 98], the highly conducting CSF compartment [8, 102, 110] as well as white matter conductivity anisotropy [43, 50] have been shown to be important to accurately model the head volume conductor. Ignoring the above phenomena can result in substantial deviations between simulation and reliability for EEG/MEG source analysis and tDCS/TMS simulation studies.

The determination of tissue conductivity parameters does not have the support of a capable technology such as *magnetic resonance imaging* (MRI) or *computer tomography* (CT). The electric conductivities of scalp, skull and brain tissues have been shown to vary across and within individuals due to variations in age, disease state and environmental factors [9, 89]. However, with respect to tissue anisotropy, Basser and colleagues [7] introduced the assumption that the white matter conductivity tensors share the eigenvectors with the water diffusion tensors, which can be measured non-invasively by means of diffusion tensor MRI (DT-MRI). This assumption was used to derive an effective medium approach that describes a linear relationship between the effective electrical conductivity tensor and the effective water diffusion tensor in brain tissues [134]. This model was validated experimentally in phantom models by Tuch and colleagues [134] and Oh and colleagues [88]. The conductivity of human CSF at body temperature has been measured by Baumann and colleagues [8] to be $1.79\,\mathrm{Sm}^{-1}$ (average over 7 subjects, ranging in age from 4.5 months to 70 years, with a standard deviation of less than 2.4 % between subjects and for frequencies between 10 and 10.000 Hz). Akhtari and colleagues [2] performed physical measurements with excised human skull fragments and found that the spongy bone is, on average, about 3.6 times more conductive than the compact tissue (with a maximal factor of 8.2). An accurate modeling of brain tissue conductivity anisotropy is still a challenging task. As discussed above, brain conductivity tensors can be computed from measured DT-MRI. However, DT-MRI data suffers from geometrical distortions and intensity modulations due to susceptibility artifacts. In this thesis, a relatively new nonlinear registration method that uses a reversed gradient approach based on images acquired in positive and negative phase-encoding direction is used [112]. By using this technique, smooth and diffeomorphic transformations are computed to correct for susceptibility artifacts, which allows for an adequate fusion with the T1w and T2w images during the head model setup procedure.

The FE resolution in terms of the "number of FE nodes" is an important parameter for

both numerical and head modeling accuracy. The latter is the possibility of including tissue inhomogeneity and anisotropy into the volume conductor model. In the late 90's, evaluation studies often only used sub-optimal (a few thousand) numbers of nodes. Modern parallel algebraic multigrid FE solver methods [71, 152] together with improved computer technology now enable resolutions (and thus numerical as well as modeling accuracies) of up to millions of FE nodes [5, 139, 142].

1.3. Scope and organization of this thesis

The overall scope of this thesis is to provide and evaluate a simulation pipeline for tDCS or tACS or TMS which can be used to predict inter-individually optimized stimulation protocols for patients and their specific disease. The novel simulation pipeline, which can be roughly divided into four parts, is exemplarily applied for an auditory cortex stimulation:

- Fast and robust generation of detailed and accurate volume conductor models for single patients
- Implementation of an accurate and fast numerical finite element approach for high-resolution volume conductor models with white matter anisotropy
- Implementation and validation of accurate and efficient solver methods
- Estimation of inter-individually optimized stimulation protocols for a focused stimulation of the auditory cortices while minimizing current density in non-auditory cortex regions

Based on this division of the simulation pipeline, the thesis is organized as follows:

In Chapter 2, basic notations and background of EEG/MEG source analysis and volume conductor modeling are presented. First, the partial differential equation (PDE) for the EEG forward problem is presented and, second, the EEG/MEG lead field theory is derived. Subsequently, Helmholtz' principle of reciprocity [53] is introduced and the relationship between the reciprocal electrode lead vector field and the lead field is derived. Next, three EEG forward approaches are introduced, namely the full subtraction approach [34], the partial integration approach [120] and the adjoint approach [135]. In order to investigate numerical accuracy of the EEG forward approaches, quasi-analytical EEG forward solutions in sphere models are presented [30]. Finally, the novel modeling pipeline for high-resolution, geometry-adapted hexahedral finite element models with white matter anisotropy is introduced.

In Section 3.2, numerical errors of the commonly-used FE approaches for transcranial direct current stimulation are investigated. Direct validation of the numerical performance of FE approaches for tDCS is a very challenging task, as there is currently no analytical expression available for tDCS current flow estimation. Since in EEG source analysis numerical validation of EEG forward approaches is feasible in sphere models [30], the theoretic relation between EEG source analysis and tDCS simulations is derived. In combination with quasi-analytical EEG forward expressions in sphere models [30], this concept allows to directly investigate

and compare numerical errors of the commonly-used hexahedral and tetrahedral modeling approaches for tDCS. This step is important with regard to the validation of tDCS current simulations and provides evidence for the reliability of computer simulation studies.

In Section 3.3, the *Jacobi conjugate gradient* (Jacobi-CG), *Incomplete cholesky without fill-in conjugate gradient* (IC(0)-CG) and *Algebraic multigrid conjugate gradient* (AMG-CG) methods for solving the large sparse discretized FE equation system resulting from the modeling of tDCS/TMS are derived and their performance with regard to computational complexity and numerical accuracy is investigated. The variation of one stimulation parameter (inter-individual conductivity profile; location and/or size of the electrodes/coils; individual subject; multi-array tDCS or TMS array) leads to different FE equation systems which have to be solved to estimate the current flow fields. For algorithmic-based fixed-sensor optimization approaches, the number of forward calculations is given by $S - 1$, where S is the number of surface electrodes [33]. Hence, for an extended 10-10 EEG electrode configuration with 74 electrodes, 73 large (but sparse) equation systems have to be solved. As the final goal in modeling brain stimulation techniques is to calculate optimized stimulation protocols for individual patients and their specific disease, the equation systems should be solved in a computationally efficient but accurate way.

In Section 3.4, a *complete electrode model (CEM)*-based modeling approach for tDCS is introduced and current flow field orientation and magnitude changes as compared to the *point-electrode model (PEM)*-based, geometry-adapted modeling pipeline for tDCS are investigated. In the PEM-based modeling pipeline for tDCS, the contact impedance of the electrodes and the contact impedance between electrode and skin tissue are neglected. As the shunting currents through the electrodes affect the current density distribution, a complete electrode model [100] can be useful for tDCS, since it might increase the accuracy of the simulation, especially in the skin compartment. This is especially important for a combined EEG-tDCS (or EEG-tACS) measurement/stimulation, where the tDCS/tACS stimulation artefact has to be filtered from the raw EEG signal before evaluation.

In Section 4.1, the sensitivity of the current density distribution in the brain towards the most important head tissue compartments to be modeled in tDCS computer simulation studies is investigated. For this reason, a low-parametric, three compartment finite element head model (skin, skull, brain) which constitutes a simplification of the brain anatomy is generated. Next, this head model is extended step by step to a more realistic six-compartment FE head model (skin, skull compacta, skull spongiosa, CSF, gray and white matter) with white matter anisotropy. In each consecutive step, the effects of the increased accuracy of the volume conductor model on the tDCS current density distribution is investigated by quantifying the current orientation and magnitude changes. In this way, the influence of each individual tissue compartment is investigated, providing a deeper insight into volume conduction effects in transcranial direct current stimulation. It is thus investigated which tissue compartments are important to be modeled in tDCS computer simulation studies. Keeping this in mind, a guideline for efficient yet accurate volume conductor modeling in tDCS is presented.

As the induced current flow field is rather widespread with the largest intensities located in non-target regions, the applicability of commonly-used bipolar electrode montages for targeting the frontal lobe, the occipital lobe and the auditory cortices is investigated in Sections 4.2 and 4.3.

In Section 5, a novel optimization algorithm for safe and well-targeted multi-array transcranial direct current stimulation is proposed. Existence of at least one minimizer is proven and residual and objective convergence results for the proposed optimization methods are shown. Optimization results in spherical shell models and a highly-realistic FE head model are calculated and the focality of the optimized current flow is investigated. Moreover, the maximal current density in non-target regions is evaluated and the interplay between the averaged current density in non-target regions and the target current density is depicted for different target depths. In a next step, the novel optimization method is used to calculate optimized stimulation protocols for a bi-hemispheric auditory cortex stimulation and the focality and directional agreement with the auditory target vectors is investigated.

As inter-individually varying conductivity profiles and idiosyncratic differences in brain anatomy strongly influence the current flow, large differences in the optimal stimulation pattern can be expected. For this reason, in Section 5.4 the influence of inter-individually varying conductivity profiles on optimal stimulation pattern for a multi-array right-hemispheric auditory cortex stimulation is analyzed. A multi-variate generalized polynomial chaos technique is applied to quantify the uncertainty of the optimal electrode configurations. Furthermore, the stochastic measures, probability density functions and sensitivity of the quantities of interest are investigated.

In Section 6.1, volume conduction effects in transcranial magnetic stimulation are studied. In order to investigate which tissue compartments are essential to be modeled in TMS simulation studies, the effects of using separate skull layers as compared to an isotropic skull compartment is evaluated. Furthermore, the difference in the potential field distribution between a low-parametric three compartment (skin, skull, brain) head model and a more realistic six-compartment (skin, skull compacta, skull spongiosa, CSF, gray matter and white matter) head model are investigated. Using the results of this study, a guideline for efficient yet accurate volume conductor modeling in transcranial magnetic stimulation is presented.

In Section 6.2, a novel optimization method for safe and well-targeted multi-array TMS is introduced. Optimization results in a spherical shell model and a highly-realistic five compartment head model are presented. Moreover, the existence of at least one minimizer to the discretized optimization problem for TMS is shown.

Finally, a combined tCS and TMS (tCMS) optimization is performed and the existence of at least one minimizing element to the optimization problem for tCMS optimization is shown. For validation of the optimization method, the current flow resulting from the optimized stimulation pattern are calculated in sphere models and the interplay between the averaged current density in non-target regions and the target current density is investigated.

2 Basics

The aim of this chapter is to provide basic notions and background of EEG/MEG source analysis and volume conductor modeling. First, the PDE for the EEG forward problem is presented and, second, the EEG/MEG lead field theory is derived. Subsequently, Helmholtz' principle of reciprocity [53] is introduced and the relationship between the reciprocal electrode lead vector field and the lead field is derived. Next, three EEG forward approaches are introduced, namely the full subtraction approach [34], the partial integration approach [120] and the adjoint approach [135]. In order to investigate numerical accuracy of the EEG forward approaches, quasi-analytical EEG forward expressions in sphere models are presented [30]. Finally, the novel modeling pipeline for high-resolution, geometry-adapted hexahedral finite element models with white matter anisotropy is introduced.

2.1. EEG forward problem

Maxwell's equations for electromagnetism are a set of four coupled partial differential equations which are fundamental for EEG and MEG source analysis.

Definition 2.1 (Maxwell's equations of electromagnetism [78])**.** Let $\boldsymbol{E}$ and $\boldsymbol{B}$ be an electric and a magnetic field, respectively. Furthermore, let ϵ_0 be the electrical permittivity, μ_0 the magnetic permeability, ρ the charge density and $\boldsymbol{J}$ the current density distribution. Maxwell's equations are defined as

$$\nabla \cdot \boldsymbol{E} = \frac{\rho}{\epsilon_0} \tag{2.1}$$

$$\nabla \times \boldsymbol{E} = -\frac{\partial \boldsymbol{B}}{\partial t} \tag{2.2}$$

$$\nabla \cdot \boldsymbol{B} = 0 \tag{2.3}$$

$$\nabla \times \boldsymbol{B} \quad = \quad \mu_0(\boldsymbol{J} + \epsilon_0 \frac{\partial \boldsymbol{E}}{\partial t}) \tag{2.4}$$

In the low frequency regime of EEG and MEG source analysis (below 1000 Hz), the quasi-static approximation to Maxwell's equations can be used [56, 97]. In the quasi-static approximation, the time derivatives in Maxwell's equations are neglected [56]. This implies that the right-hand side in Equation 2.2 is identically zero, i.e., $\nabla \times \boldsymbol{E} = 0$. Therefore, the electric potential $\boldsymbol{E}$ is a gradient field and can thus be expressed by a scalar potential Φ

$$\boldsymbol{E} = -\nabla\Phi \tag{2.5}$$

Next, the current density $\boldsymbol{J}$ is divided into the sum of a primary current $\boldsymbol{J}^p$ (representing neural activity) and the return currents $\sigma\boldsymbol{E}$

$$\boldsymbol{J} = \boldsymbol{J}^p + \sigma\boldsymbol{E} \overset{(2.5)}{=} \boldsymbol{J}^p - \sigma\nabla\Phi \tag{2.6}$$

with σ being the conductivity distribution of the volume.
Taking the gradient of Equation 2.4 under quasi-static assumption, using the fact that the gradient of a curl is zero and applying Equation 2.6, one obtains

$$\nabla \cdot \sigma\nabla\Phi = \nabla \cdot \boldsymbol{J}^p \tag{2.7}$$

which describes the dependence between the electric potential Φ in the volume conductor induced by event-related and/or spontaneous brain activity. The conductivity tensor $\sigma : \Omega \to \mathbb{R}^{3\times3}$ is a 3×3 tensor.

In a next step, the boundary conditions are derived. As the human head consists of several tissue compartments and the final goal is to allow optimization in multi-compartment volume conductor models, the head domain Ω is divided into a disjunct set of tissue compartments

$$\Omega = \Omega_1 \,\dot\cup\, \ldots \,\dot\cup\, \Omega_{N_C}$$

with varying conductivity profiles $\sigma_i \in \Omega_i, i = 1, \ldots, N_C$. Since the conductivity values differ in terms of tissue type, the conductivity tensor σ has jumps at tissue interfaces (e.g., the brain/CSF interface with conductivity values of $0.33\,\mathrm{Sm}^{-1}$ and $1.79\,\mathrm{Sm}^{-1}$). The conductivity distribution is thus not in C^1, but in the Sobolev space $L^\infty(\Omega)$, i.e., $\sigma \in L^\infty(\Omega)^{3\times3}$.

On the other hand, the electric potential Φ is continuous at tissue interfaces

$$\lim_{\Omega_l \ni \boldsymbol{p} \to \boldsymbol{p}^*} \Phi_l(\boldsymbol{p}) = \lim_{\Omega_k \ni \boldsymbol{p} \to \boldsymbol{p}^*} \Phi_k(\boldsymbol{p})$$

with $\boldsymbol{p}^*$ being an arbitrary point on the interface between the l-th and k-th tissue compartment Ω_l and Ω_k, respectively.

Moreover, the current density distribution $\sigma\nabla\Phi$ is continuous in the volume conductor and

along tissue interfaces

$$\lim_{\Omega_l \ni \boldsymbol{p} \to \boldsymbol{p}^*} \langle \sigma_l(\boldsymbol{p}) \nabla \Phi_l(\boldsymbol{p}), \boldsymbol{n} \rangle = \lim_{\Omega_k \ni \boldsymbol{p} \to \boldsymbol{p}^*} \langle \sigma_k(\boldsymbol{p}) \nabla \Phi_k(\boldsymbol{p}), \boldsymbol{n} \rangle$$

As the air is non-conductive, the conductivity tensor σ is identically zero outside the outer boundary Γ. Therefore, a *homogeneous Neumann boundary condition* at the model surface is given

$$\lim_{\Omega \ni \boldsymbol{p} \to \boldsymbol{p}^*} \langle \sigma(\boldsymbol{p}) \nabla \Phi(\boldsymbol{p}), \boldsymbol{n} \rangle = 0. \tag{2.8}$$

The EEG forward problem is then defined as

Definition 2.2 (Partial differential equation for the EEG forward problem)**.** The EEG forward problem is described by the following elliptic boundary value problem

$$\begin{aligned} \nabla \cdot \sigma \nabla \Phi &= \nabla \cdot \boldsymbol{J}^p \quad in\ \Omega \\ \langle \sigma \nabla \Phi, \boldsymbol{n} \rangle &= 0 \qquad on\ \Gamma \setminus \Gamma_D \\ \Phi &= 0 \qquad on\ \Gamma_D \end{aligned}$$

where a homogeneous Dirichlet boundary condition is used to ensure that the solution to the EEG forward problem is unique.

Remark 2.1 (Regularity of the current density distribution)**.** As discussed before, the conductivity tensor fulfills $\sigma \in L^\infty(\Omega)^{3\times 3}$ and the potential $\Phi \in H^1(\Omega)$. Therefore, $\nabla\Phi \in L^2(\Omega)$ and the current density distribution $\sigma\nabla\Phi \in L^2(\Omega)$. See the Appendix for further details about Sobolev and Lebesgue spaces.

Remark 2.2 (Classical solution of the EEG forward problem)**.** A classical solution $\tilde{\Phi}$ to the EEG forward problem is not achievable since $\tilde{\Phi} \in \mathcal{C}^2(\Omega) \cap \mathcal{C}^0(\overline{\Omega})$ has to be fulfilled. As σ is discontinuous at tissue interfaces when assuming a multi-compartment model and the current density $\sigma\nabla\tilde{\Phi}$ is continuous inside the volume conductor, $\nabla\tilde{\Phi}$ has to be discontinuous at tissue interfaces (to cancel the jumps of σ). Thus, $\tilde{\Phi} \notin \mathcal{C}^1(\Omega)$ is not a classical solution to the EEG forward problem.

Under appropriate regularity assumptions, however, the solution is in the Sobolov space $H^1(\Omega)$:

Theorem 2.1. Let Ω be a volume conductor with Lipschitz continuous boundary and let $\sigma \in L^\infty$ with $\sigma > 0$. Furthermore, let the right-hand side vector $\nabla \cdot \boldsymbol{J}^p \in L^2(\Omega)$. Then a weak solution $\Phi \in H^1(\Omega)$ to the EEG forward problem exists 3.2.

In a next step, the right hand side vector $\boldsymbol{J}^p$ representing brain activity is defined. De Munck and colleagues [31] were able to demonstrate that an equivalent point dipole is a good approximation to the electric brain activity with respect to position, orientation and strength. As a main result of their study, they proposed the following representation for the current density $\boldsymbol{J}^p$

Definition 2.3 (Characterization of current density $\boldsymbol{J}^p$ [31])**.** Let us consider a mathematical dipole at location $\boldsymbol{x}_0$ with dipolar moment $\boldsymbol{q}$. The current density $\boldsymbol{J}^p$ can be characterized as follows

$$\boldsymbol{J}^p = \delta(\boldsymbol{x} - \boldsymbol{x}_0)\boldsymbol{q} \tag{2.9}$$

with δ being the *Dirac delta distribution* and $\boldsymbol{q}$ being the *dipole moment* for a current dipole at location $\boldsymbol{x}$. Applying the divergence operator to both sides yields

$$\nabla \cdot \boldsymbol{J}^p = \nabla \cdot \delta(\boldsymbol{x} - \boldsymbol{x}_0)\boldsymbol{q} \tag{2.10}$$

As the Dirac-delta distribution $\delta(\boldsymbol{x} - \boldsymbol{x}_0) \in H^{-\frac{3}{2}-\epsilon}(\Omega)\ \forall \epsilon > 0$, the right-hand side $\nabla \cdot \boldsymbol{J}^p \in H^{-\frac{1}{2}-\epsilon}(\Omega)\ \forall \epsilon > 0$. When using standard finite element approaches (e.g., Partial integration approach), a solution in the Sobolev space $H^1(\Omega)$ cannot be achieved. In order to theoretically cope with the singularity, a full subtraction approach can be used (see Section 2.4.1).

2.2. Lead field theory

2.2.1. EEG lead field

In this section, a set $\boldsymbol{S} = \{s_1, \ldots, s_l\}$ of surface electrodes is fixed. Due to the linearity of the PDE, the principle of superposition can be applied, as will be discussed in the following:
Let $\boldsymbol{c} \in \mathbb{R}^{3\times 1}$ be the potentials at an arbitrary position $\boldsymbol{p} \in \Omega$ generated by unit vectors located at $\boldsymbol{x}_0$ and oriented parallel to the three cartesian axis, respectively. In order to estimate the *potential vector* $\boldsymbol{c}$, the PDE for the EEG forward problem has to be solved three times (i.e., once for each unit vector). The potential generated by a dipole is then simply given by the inner product of the dipole moment $\boldsymbol{q}$ and the potential vector

$$\Phi(\boldsymbol{p}) = \langle \boldsymbol{c}, \boldsymbol{q} \rangle$$

In a next step, two electrode locations s_i and s_j are fixed at the surface of the volume conductor. In the following, the pair of surface electrodes is called a *lead*. The *lead vector* and the *lead field matrix* is described in the following
Definition 2.4 (Potential difference, lead vector and lead field)**.** Let $\Phi(s_i)$ and $\Phi(s_j)$ be the potentials at electrode locations s_i and s_j generated by a dipole at $\boldsymbol{x}_0$ with moment $\boldsymbol{q}$. Let furthermore $\boldsymbol{c}_{s_i}$ and $\boldsymbol{c}_{s_j}$ be the potentials along the three cartesian axis. The *potential difference* at the surface electrodes can be simply calculated as

$$\Phi(s_i) - \Phi(s_j) = \langle \boldsymbol{c}_{s_i}, \boldsymbol{q} \rangle - \langle \boldsymbol{c}_{s_j}, \boldsymbol{q} \rangle = \langle \boldsymbol{c}_{s_i} - \boldsymbol{c}_{s_j}, \boldsymbol{q} \rangle := \langle \boldsymbol{l}_{s_i s_j}, \boldsymbol{q} \rangle$$

with $\boldsymbol{l}_{s_i,s_j}$ being the so-called *lead vector*.

In order to calculate the so-called *lead field*, the lead vector is calculated for each element in the

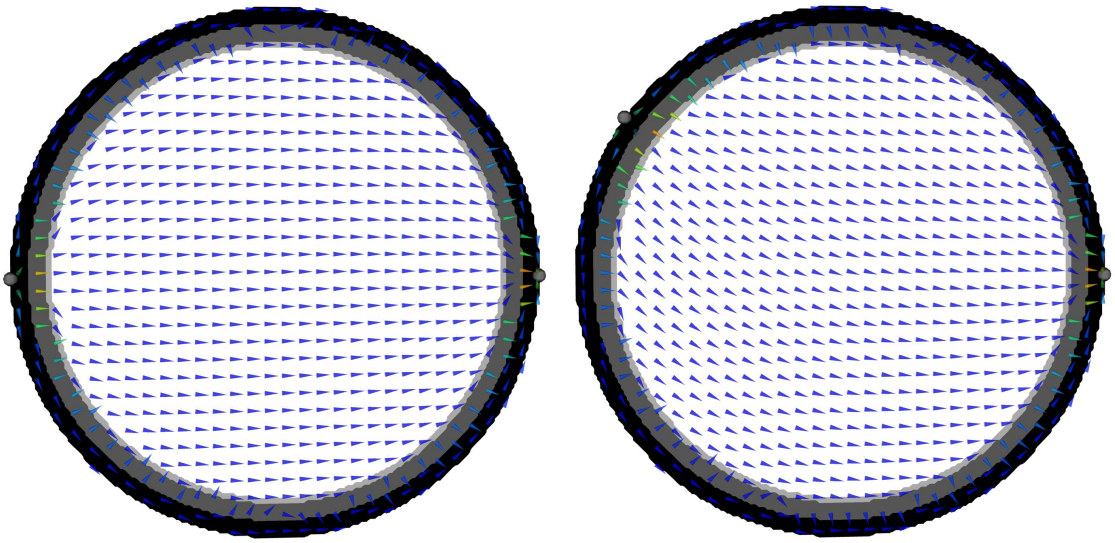

Figure 2.1.: EEG lead field (Vm^{-1}) for two fixed pairs of surface electrodes in a spherical shell model consisting of four concentric shells with outer shell radii of 92, 86, 80 and 78 mm, respectively. Conductivity values of $0.43\,\mathrm{Sm}^{-1}$, $0.0042\,\mathrm{Sm}^{-1}$ and $1.79\,\mathrm{Sm}^{-1}$ are used for the compartments skin, skull and CSF, and a fixed anisotropy ratio of 1:10 between longitudinal and transversal conductivities is employed for the brain compartment, respectively (see Table 2.1). Size-normalized cones are used to present vector orientation and the cones are color-coded to present vector field amplitudes. Sub-sampled versions of the vector fields, where only the middle cone of each $4\,\mathrm{mm} \times 4\,\mathrm{mm}$ block is visualized, are shown here. The locations of the EEG electrodes are depicted by the grey balls.

source space, resulting in a lead field vector $\boldsymbol{L}_{i,j} \in \mathbb{R}^{3M}$ with M being the number of source space nodes. Fixing the first electrode as reference, the lead field matrix $\mathbf{L} \in \mathbb{R}^{(S-1)\times 3M}$ is obtained by calculating the lead fields $\boldsymbol{L}_{i,1}$ for $i = 2, \ldots, l$ and by setting $\mathbf{L} = [\boldsymbol{L}_{2,1}, \ldots, \boldsymbol{L}_{l,1}]$.

As the lead field matrix is completely specified by the geometry and conductivity of the volume conductor model as well as the individual electrode montage, the lead field matrix is independent from the source orientation and strength. Consequently, the potential difference caused by arbitrary sources in the source space can be calculated very efficiently. Because the lead field is linear, changing the amplitude of the source results in an identical pattern of lead field vectors with the amplitude to be changed accordingly.

Considering a set $\boldsymbol{J}_1^p, \ldots, \boldsymbol{J}_k^p$ of active sources in the source space, the potential difference between two surface electrodes can be calculated as

$$\Phi(s_i) - \Phi(s_j) = \int_\Omega \langle \boldsymbol{L}_{i,j}, \sum_{l=1}^{k} \boldsymbol{J}_l^p \rangle \, \mathrm{d}\boldsymbol{x} = \sum_{l=1}^{k} \langle \boldsymbol{L}_{i,j}(\boldsymbol{x}_l), \boldsymbol{q}_l \rangle \, \mathrm{d}\boldsymbol{x}$$

with $\boldsymbol{q}_l$ being the dipole moment of source $\boldsymbol{J}_l^p$, respectively.

Figure 2.1 depicts the lead field for two fixed electrode montages in a spherical model. As shown

in the figure, the lead field vectors are mainly oriented tangentially in the well-conducting compartments scalp and CSF, while they are mainly oriented radially in the poorly conducting skull compartment. In the brain compartment, a mainly homogeneous lead field distribution can be seen. The orientation of the lead field vectors thus strongly depends on the tissue compartments and on the individual conductivity profile.

The sensitivity of a volume conductor model with regard to the source space is discussed in the following

Remark 2.3 (Sensitivity distribution)**.** The lead field vector $\boldsymbol{L}_{i,j}$ describes the sensitivity distribution for a fixed electrode montage at electrode locations s_i and s_j. The potential difference between the electrodes is maximal when the source is oriented parallel to the lead field vector and decreases as the cosine of the lead field vector and the dipole moment, see Equation 2.9. When both vectors are perpendicular, the potential difference is identical to zero.

Figure 2.2 depicts the sensitivity distribution for two fixed surface electrodes in a realistically shaped finite element head model. While the lead field is mainly quasi-tangentially oriented in the skin and CSF compartments, a mainly radial orientation can be seen in the low-conductive skull regions. In the brain compartment, lead field vectors in lower-conductive regions tend to be oriented towards the nearest better conducting regions. This leads to a less homogeneous lead field distribution in the brain compartments.

To summarize, given a specific primary current density distribution $\boldsymbol{J}^p = \delta(\boldsymbol{x} - \boldsymbol{x}_0)\boldsymbol{q}$ and the lead vector field $\boldsymbol{L}_{i,j}$, the potential difference between two surface electrodes can be calculated very efficiently

$$\Phi(s_i) - \Phi(s_j) = \int_\Omega \langle \boldsymbol{L}_{i,j}, \boldsymbol{J}^p \rangle \, \mathrm{d}\boldsymbol{x} = \langle \boldsymbol{L}_{i,j}(\boldsymbol{x}_0), \boldsymbol{q} \rangle \tag{2.11}$$

with $\boldsymbol{x}_0$ being the source location.

For lead field calculation, the EEG forward problem has to be solved three times per element in the source space. The number of forward computations crucially depends on the chosen source grid spacing. In practice, sparse source grids with grid spacing of 5 millimeters [32] or restriction to some thousand source locations (e.g., 5000 possible locations in [137]) have been used to circumvent the excessive computational burden. A further possibility to reduce the source space is to use geometrical constraints like fixing the dipoles to be oriented perpendicular to the cortical surface [24]. In this way, the number of forward computations can be substantially reduced.

2.2.2. MEG lead field

Similar to EEG, the MEG lead field describes the magnetic flux through an MEG sensor induced by an arbitrary source in the source space. The MEG lead field matrix $\boldsymbol{L}_{\mathrm{MEG}}$ thus describes the forward solutions at each sensor for each element in the source space.

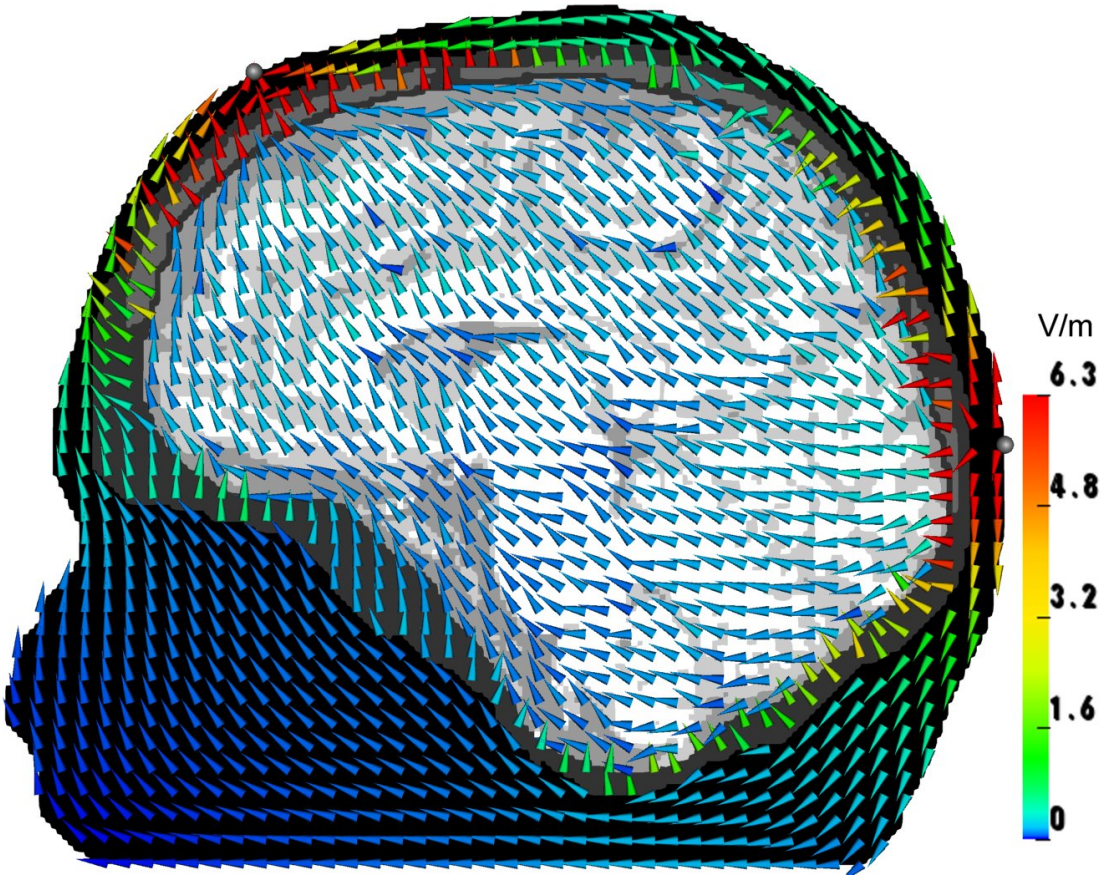

Figure 2.2.: EEG lead field (Vm^{-1}) for two fixed pairs of surface electrodes in a six compartment finite element head model. Conductivity values of $0.43\,\mathrm{Sm}^{-1}$, $0.025\,\mathrm{Sm}^{-1}$, $0.007\,\mathrm{Sm}^{-1}$, $1.79\,\mathrm{Sm}^{-1}$, $0.33\,\mathrm{Sm}^{-1}$ are assigned to the compartments skin, skull compacta, skull spongiosa, CSF and gray matter and an anisotropic white matter conductivity tensor is employed. Size-normalized cones are used to present vector orientation and the cones are color-coded to present vector field amplitudes. Sub-sampled versions of the vector fields, where only the middle cone of each $4\,\mathrm{mm} \times 4\,\mathrm{mm}$ block is visualized, are shown here. The locations of the EEG electrodes are depicted by the grey balls.

According to Ruohonen and colleagues [111], the magnetic flux through a coil element Ψ_i induced by a given dipolar source $\boldsymbol{J}^p = \delta(\boldsymbol{x} - \boldsymbol{x}_0)\boldsymbol{q}$ can be calculated very efficiently with a pre-computed MEG lead field $\mathbf{L}^i_{\mathrm{MEG}}$

$$\Psi_i = \langle \boldsymbol{q}, \mathbf{L}^i_{\mathrm{MEG}}(\boldsymbol{x}_0) \rangle \tag{2.12}$$

with $\boldsymbol{L}^i_{MEG}$ being the lead field matrix at coil i.

Nolte [87] derived an equation for the magnetic lead field for a given MEG channel and a frequency $\omega = 0$. Nolte reported that the transpose of the conductivity times the lead field is divergence-free, and that the lead field differs from the one in any other volume conductor by a gradient of a scalar function. Nolte [87] concluded that for a piecewise homogeneous and isotropic volume conductor, the lead field is always tangential at the outermost surface.

In 2007, Schimpf [119] described a linear-algebraic and a reciprocal approach to calculate the MEG lead-field matrix and presented implementation details using the finite element method. Moreover, Vallaghe and colleagues [135] used the adjoint method to derive EEG and MEG sensor-based lead field equations. They were able to re-derive lead field equations for point-like sensors and to extend these equations to incorporate the geometry of the sensors in the lead field equation. The extension to non-point-like sensors is very similar to the concept of the complete electrode model, which has been deeply investigated for the EEG forward problem [100].

As a further application, the MEG lead field can be used to calculate the current flow field $\sigma \boldsymbol{E}$ induced by transcranial magnetic stimulation (see Chapter 6.1). Ruohonen and colleagues [111] were able to demonstrate that the electric field $\boldsymbol{E}$ induced by a stimulating coil i can be calculated as follows

$$\langle \boldsymbol{q}, \boldsymbol{E} \rangle = -\frac{\partial I_i}{\partial t} \Psi_i \tag{2.13}$$

with $\frac{\partial I_i}{\partial t}$ being the rate of change of current in the stimulating coil. Using Equation 2.12, the electric field can be calculated as follows

$$\boldsymbol{E} = -\frac{\partial I_i}{\partial t} \mathbf{L}^i_{MEG} \tag{2.14}$$

For multi-channel transcranial magnetic stimulation using a set of C coil elements, the electric field $\boldsymbol{E}$ can be calculated as

$$\boldsymbol{E} = \sum_{k=1}^{C} \frac{\partial I_k}{\partial t} \mathbf{L}^k_{MEG} \tag{2.15}$$

2.3. Helmholtz' principle of reciprocity

In this section Helmholtz' principle of reciprocity [53] is introduced.

Theorem 2.2 (Helmholtz' reciprocity theorem, [80], page 20, Theorem 1)**.** Two cases in a volume conductor model Ω are considered:
In a given volume conductor model, a source at position $\boldsymbol{p}_{source}$ and a sink at position $\boldsymbol{p}_{sink}$ are generating a source I

$$I = I^* \delta(\boldsymbol{p}_{source} - \boldsymbol{x}_0) - I^* \delta(\boldsymbol{p}_{sink} - \boldsymbol{x}_0)$$

Secondly, on the boundary of the volume conductor Γ, a current density $\boldsymbol{J}$ is introduced and removed at locations $\boldsymbol{p}_{in}$ and $\boldsymbol{p}_{out}$

$$\boldsymbol{J} = \boldsymbol{J}^* \delta(\boldsymbol{p}_{in} - \boldsymbol{x}_0) - \boldsymbol{J}^* \delta(\boldsymbol{p}_{out} - \boldsymbol{x}_0)$$

Then, the resulting potential fields are directly related

$$I^* [\Phi_2(\boldsymbol{p}_{source}) - \Phi_2(\boldsymbol{p}_{sink})] = \boldsymbol{J}^* [\Phi_1(\boldsymbol{p}_{in}) - \Phi_1(\boldsymbol{p}_{out})] \tag{2.16}$$

with Φ_1 and Φ_2 being the potential field generated by the volume current source I and the surface current density $\boldsymbol{J}$, respectively.

When the amplitude of the current source I^* is identical to the amplitude of the current density $\boldsymbol{J}^*$, the potential difference $\Phi_2(\boldsymbol{p}_{source}) - \Phi_2(\boldsymbol{p}_{sink})$ is identically to the potential difference between $\Phi_1(\boldsymbol{p}_{in}) - \Phi_1(\boldsymbol{p}_{out})$. Otherwise, the ratio is directly given by the ratio of the current source and the surface current density.

2.3.1. Lead field calculation using reciprocity

As shown before, a current injected at an active electrode and grounded at the reference electrode generates a reciprocal potential field Φ_{rec}. Accordingly, the reciprocal electric and current density fields are given as $\boldsymbol{E}_{rec} = -\nabla\Phi_{rec}$ and $\boldsymbol{J}_{rec} = \sigma\boldsymbol{E}_{rec}$, respectively.

Lemma 2.1. Let Φ_{rec} be the reciprocal potential field and let us consider a current source and sink generating a current dipole with strength I^*. Let us furthermore assume a given dipole moment $\boldsymbol{q}$ to be oriented from the current source to sink

$$\boldsymbol{q} = I^*(\boldsymbol{p}_{source} - \boldsymbol{p}_{sink}) \tag{2.17}$$

Then, the following identity can be shown

$$I^*(\Phi_{rec}(\boldsymbol{p}_{source}) - \Phi_{rec}(\boldsymbol{p}_{sink})) = \langle\nabla\Phi_{rec}(\boldsymbol{p}_{source}), \boldsymbol{q}\rangle$$

Proof. Because the volume conductor is source-free under reciprocal conditions, a Taylor expansion of the potential field Φ_{rec} can be applied

$$\Phi_{rec}(\boldsymbol{p}_{source}) = \Phi_{rec}(\boldsymbol{p}_{sink}) + \langle\nabla\Phi_{rec}(\boldsymbol{p}_{source}), (\boldsymbol{p}_{source} - \boldsymbol{p}_{sink})\rangle + \dots \tag{2.18}$$

When decreasing the distance between $\boldsymbol{p}_{source}$ and $\boldsymbol{p}_{sink}$ while keeping the dipole moment constant (by increasing I^*), the higher order terms in Equation 2.3.1 are sufficiently small to be neglected. This leads to

$$\begin{aligned} I^*(\Phi_{rec}(\boldsymbol{p}_{source}) - \Phi_{rec}(\boldsymbol{p}_{sink})) &\overset{(2.18)}{=} I^*(\langle\nabla\Phi_{rec}(\boldsymbol{p}_{source}), (\boldsymbol{p}_{source} - \boldsymbol{p}_{sink})\rangle) \\ &\overset{(2.17)}{=} \langle\nabla\Phi_{rec}(\mathbf{p}_{source}), \boldsymbol{q}\rangle \end{aligned}$$

□

Let Φ be the potential field generated by a dipolar source. In the following theorem, the relationship between Φ and Φ_{rec} is described

Theorem 2.3 (Relationship between potential field and reciprocal potential field)**.** Let Φ and Φ_{rec} be the potential field and the reciprocal potential field, respectively. Furthermore, let $\Phi_{in,out} = \Phi(\boldsymbol{p}_{in}) - \Phi(\boldsymbol{p}_{out})$ be the potential difference at the surface electrodes. Then, the

following equation can be shown

$$\Phi_{in,out} = \langle -\nabla\Phi_{rec}(\boldsymbol{p}_{source}), \boldsymbol{q}\rangle$$

Proof. Theorem 2.2 is applied with $I^* = 1, \Phi_{rec} = \Phi_2, \Phi = \Phi_1$

$$\begin{aligned}\Phi_{in,out} &= \Phi(\boldsymbol{p}_{out}) - \Phi(\boldsymbol{p}_{in}) \\ &\overset{Theorem.2.2}{=} -\Phi_{rec}(\boldsymbol{p}_{source}) - \Phi_{rec}(\boldsymbol{p}_{sink}) \\ &\overset{Lemma2.1}{=} \langle -\nabla\Phi_{rec}(\boldsymbol{p}_{source}), \boldsymbol{q}\rangle\end{aligned}$$

□

Theorem 2.3 allows to calculate the lead field vector from a sensor-point of view. Comparing the main result of Theorem 2.3 with the straight-forward lead field calculation, the lead field vector $\mathbf{L}_{i,j}$ is identical to the gradient of the reciprocal potential field Φ_{rec}. For a lead field matrix computation $\mathbf{L}$, the number of forward computations is thus bounded by the number of surface electrodes and not by the number of nodes in the source space (see Section 2.2). When the number of EEG or MEG sensors is substantially smaller than the number of source space nodes, the reciprocal approach outperforms the straight-forward lead field computations with regard to computation time. In most applications, the number of EEG or MEG sensors is smaller than 10^3, while the source space contains more than 10^5 nodes. Wolters and colleagues [150] were able to demonstrate in a five tissue tetrahedral FE head model with 147,287 nodes and 892,115 elements and a source space of 30,357 possible source locations that the calculation of the whole lead field matrix requires 774,331s $\approx$ 215 h when using the straight-forward way as presented in Section 2.2. They fixed the number of EEG and MEG sensors to be 150 and reported that their transfer matrix approach, which is similar to the reciprocal approach, requires only 3,812 s $\approx$ 1 h of computation time for EEG or MEG lead field computation. While nowadays the number of EEG or MEG sensors remains mainly constant (commonly below 500), source spaces with hundreds of thousands nodes are used in modern and highly-realistic anisotropic volume conductor models [34, 142]. Therefore, the computational complexity of EEG and/or MEG lead field matrix computation can substantially be reduced using reciprocity. From now on, the reciprocal and dipolar electric fields and current flow fields are denoted as $\boldsymbol{E}$ and $\boldsymbol{J}$, respectively.

Weinstein and colleagues [147] presented two efficient methods for realistic lead field computation in EEG source analysis, namely an element-based and a node-based approach. They compared both approaches and discussed their time requirements for lead field matrix computations. They reported that the time to generate both matrices is nearly identical (9 minutes to calculate the element-based EEG lead field matrix compared to 8 minutes for calculating the node-based lead field matrix). In their study, Weinstein and colleagues [147] used tetrahedral meshes, where the number of elements is about 6 times higher as compared to the number of nodes. When considering hexahedral volume conductor models, however, the number of

volume conductor nodes and elements is nearly identical. For this reason, the setup time for the node-based and element-based approaches should be identical. In this thesis, the node-based approach is used for lead field matrix computation.

2.3.2. Transfer matrix approach

The transfer matrix approach was introduced to EEG source analysis by Weinstein and colleagues [147] and Wolters and colleagues [150].

When solving the EEG forward problem for an arbitrary dipolar source, the potential Φ is calculated in the whole volume conductor. However, in many cases one is only interested in the potential at the few FE nodes that are identified with the electrode positions. Thus, a restriction matrix $\mathbf{R} \in \mathbb{R}^{(S-1)\times N}$ (with N being the number of volume conductor nodes) is introduced, mapping Φ to the $S-1$ non reference electrodes

$$\Phi_{EEG} = \mathbf{R}\Phi \tag{2.19}$$

The *transfer matrix* $\mathbf{T}$ is defined as follows [150]

$$\mathbf{T} := \mathbf{R}\mathbf{K}^{-1} \in \mathbb{R}^{(S-1)\times N} \tag{2.20}$$

with $\mathbf{K}$ being the finite element stiffness matrix.
The calculation of $\mathbf{T}$ requires to solve only $S-1$ large FE equation systems. Furthermore, $\mathbf{T}$ can be pre-computed in many practical applications, enabling a fast and robust computation of many forward solutions whenever desired. Once the transfer matrix is calculated, the solution Φ of the EEG forward problem is given by the product of $\mathbf{T}$ with the right-hand side vector $\boldsymbol{b}$

$$\mathbf{T}\boldsymbol{b} = \mathbf{T}\mathbf{K}\Phi \overset{(2.20)}{=} \mathbf{R}\mathbf{K}^{-1}\mathbf{K}\Phi = \mathbf{R}\Phi \overset{(2.19)}{=} \Phi_{EEG} \tag{2.21}$$

2.4. Numerical EEG forward approaches

In this section, three numerical approaches for solving the EEG forward problem are introduced, namely the boundary element method (BEM), the finite difference method (FDM) and the finite element method.

For the boundary element method, the volume conductor is approximated by a model with realistically shaped tissue compartments with constant and isotropic conductivities [39, 40, 41, 79]. The PDE for the EEG forward problem is transformed to an integral equation on the boundaries of the domain. The main advantage of the BEM is that the computational complexity for generating the volume conductor model is relatively low. On the contrary, anisotropic conductivity profiles cannot be taken into account. Moreover, complex geometries (e.g., the thin cortical foldings or the thin spongiosa compartment) cannot be

accurately modeled. For this reason, taking into account the three-layered structure of the skull compartment (skull compacta and spongiosa) and the highly conductive CSF compartment might lead to high computational complexity [129].

Secondly, finite difference methods [47, 51, 64, 136] and finite volume methods [22, 153] to solve the EEG forward problem have been presented. Both methods discretize the volume conductor model into a set of uniform elements and the solution is calculated in each grid element.

Another widely-used method is the finite element method [71, 135, 141, 149] which is a well-established method for solving partial differential equations. The FEM decomposes the domain into a finite set of elements (e.g., tetrahedras or cubes) and approximates the solution with finite element ansatz functions in each element. The FEM, FDM and FVM are very well understood and allow to deal with anisotropic and inhomogeneous conductivity profiles. In this thesis, all simulations are performed with the FEM.

The analytical solution to the EEG forward problem is presented in the following
Lemma 2.2. Let us consider a constant and anisotropic conductivity tensor σ in an unbounded and homogeneous volume conductor model Ω. The solution to $\Delta\Phi = \frac{\boldsymbol{J}^p}{\sigma}$ with $\boldsymbol{J}^p = \delta(\boldsymbol{x}-\boldsymbol{x}_0)\boldsymbol{q}$ is given as

$$\Phi(\boldsymbol{x}) = \frac{1}{4\pi\sqrt{det\ \sigma(\boldsymbol{x}_0)}} \frac{\langle \boldsymbol{q}(\boldsymbol{x}), \sigma^{-1}(\boldsymbol{x}-\boldsymbol{x}_0)\rangle}{\langle \sigma^{-1}(\boldsymbol{x}-\boldsymbol{x}_0), \boldsymbol{x}-\boldsymbol{x}_0)\rangle^{\frac{3}{2}}}$$

and the gradient of Φ can be calculated as

$$\begin{aligned} \nabla\Phi(\boldsymbol{x}) &= \frac{1}{4\pi\sqrt{det\ \sigma(\boldsymbol{x}_0)}} \frac{\sigma^{-1}(\boldsymbol{x}_0)\boldsymbol{q}(\boldsymbol{x})}{\langle \sigma^{-1}(\boldsymbol{x}-\boldsymbol{x}_0), \boldsymbol{x}-\boldsymbol{x}_0)\rangle^{\frac{3}{2}}} \\ &- \frac{1}{4\pi\sqrt{det\ \sigma(\boldsymbol{x}_0)}} \frac{3\langle \boldsymbol{q}(\boldsymbol{x}), \sigma^{-1}(\boldsymbol{x}-\boldsymbol{x}_0)\rangle \sigma^{-1}(\boldsymbol{x}-\boldsymbol{x}_0)}{\langle \sigma^{-1}(\boldsymbol{x}-\boldsymbol{x}_0), \boldsymbol{x}-\boldsymbol{x}_0\rangle^{\frac{5}{2}}} \end{aligned}$$

Proof. See Wolters and colleagues [151] and Drechsler and colleagues [34]. □

As can be seen, the potential Φ and $\nabla\Phi$ have a strong singularity at the dipole location $\boldsymbol{x} = \boldsymbol{x}_0$.

2.4.1. Subtraction approach

In this section, the full subtraction approach for the EEG forward problem is presented. Further information can be found in the publication by Drechsler and colleagues [34].

In order to remove the singularity from the source space, the potential Φ is split into a singularity potential Φ^{∞} and a correction potential Φ^{corr} with Φ^{∞} being the potential of a dipolar source in an unbounded and homogeneous volume conductor (see Lemma 2). In order to remove the singularity from the source space, a *homogeneity assumption* has to be fulfilled. The homogeneity assumption supposes that a constant conductivity tensor can be found in a

small subregion Ω_ϵ around the dipolar source. Under this assumption, the correction potential Φ^{corr} can be calculated as a solution of the so-called *subtraction forward problem*

$$\nabla \cdot \sigma(\boldsymbol{x})\nabla(\Phi^{\infty}(\boldsymbol{x}) + \Phi^{corr}(\boldsymbol{x})) = \nabla \cdot \boldsymbol{J}^p(\boldsymbol{x}) \qquad \boldsymbol{x}\ in\ \Omega \tag{2.22}$$

$$\langle \sigma(\boldsymbol{x})\nabla(\Phi^{\infty}(\boldsymbol{x}) + \Phi^{corr}(\boldsymbol{x})), \boldsymbol{n}(\boldsymbol{x})\rangle = 0 \qquad \boldsymbol{x}\ on\ \Gamma \tag{2.23}$$

$$\int_\Omega (\Phi^{\infty}(\boldsymbol{x}) + \Phi^{corr}(\boldsymbol{x}))\, dx = 0 \tag{2.24}$$

Rearranging the terms leads to

$$\nabla \cdot \sigma(\boldsymbol{x})\nabla\Phi^{corr}(\boldsymbol{x}) = f(\boldsymbol{x}) \qquad \boldsymbol{x}\ in\ \Omega \tag{2.25}$$

$$\langle \sigma(\boldsymbol{x})\nabla\Phi^{corr}(\boldsymbol{x}), \boldsymbol{n}(\boldsymbol{x})\rangle = g(\boldsymbol{x}) \qquad \boldsymbol{x}\ on\ \Gamma \tag{2.26}$$

$$\int_\Omega \Phi^{\infty}(\boldsymbol{x})\, \mathrm{d}\boldsymbol{x} = -\int_\Omega \Phi^{corr}(\boldsymbol{x})\, \mathrm{d}\boldsymbol{x} \tag{2.27}$$

with $f(\boldsymbol{x})$ and $g(\boldsymbol{x})$ given as

$$\begin{aligned} f(\boldsymbol{x}) &= \nabla \cdot (\sigma(\boldsymbol{x}_0) - \sigma(\boldsymbol{x}))\nabla\Phi^{\infty}(\boldsymbol{x}) \quad \boldsymbol{x}\ in\ \Omega \\ g(\boldsymbol{x}) &= -\langle \sigma(\boldsymbol{x})\nabla\Phi^{\infty,\boldsymbol{x}_0}(\boldsymbol{x}), \boldsymbol{n}(\boldsymbol{x})\rangle \quad \boldsymbol{x}\ on\ \Gamma \end{aligned}$$

Because the homogeneity assumption is used, the conductivity in a small subregion around the source is constant. Therefore, $\sigma(\boldsymbol{x}) - \sigma(\boldsymbol{x}_0) = 0$ in Ω_ϵ which implies that the right-hand side vector $f(\boldsymbol{x})$ in Equation 2.25 is equally zero.

The existence and uniqueness of a solution to the full subtraction approach was proven by Wolters and colleagues [151]. Therefore, the full subtraction approach is well defined and thus appropriate for a variational finite element formulation. The projection of Φ^{corr} into the FE space using

$$\Phi^{corr}(\boldsymbol{x}) \approx \Phi_h^{corr}(\boldsymbol{x}) = \sum_{j=1}^{N} \psi_j(\boldsymbol{x})\Phi_j^{SUB} \quad \text{with } \Phi_j^{SUB} = \Phi^{corr}(\boldsymbol{x}_j)$$

yields a linear equation system $\mathbf{K}\Phi^{SUB} = \boldsymbol{b}$ with the *stiffness matrix* $\mathbf{K} \in \mathbb{R}^{N\times N}$

$$\mathbf{K} = (K_{i,j})_{i,j=1,\ldots,N} = (\int_\Omega \langle \sigma\nabla\psi_i, \nabla\psi_j\rangle\, \mathrm{d}\boldsymbol{x})_{i,j=1,\ldots,N} \tag{2.28}$$

the right-hand side vector $\boldsymbol{b} \in \mathbb{R}^N$

$$\boldsymbol{b} = (b_i)_{i=1,\ldots,N} = (\int_\Omega \langle (\sigma(\boldsymbol{x}_0) - \sigma(\boldsymbol{x}))\nabla\Phi^{\infty}(\boldsymbol{x}), \nabla\psi_i(\boldsymbol{x})\rangle\, \mathrm{d}\boldsymbol{x} - \int_\Gamma \psi_i(\boldsymbol{x})\langle \sigma(\boldsymbol{x}_0)\nabla\Phi^{\infty}(\boldsymbol{x}), \boldsymbol{n}(\boldsymbol{x})\rangle\, \mathrm{d}\boldsymbol{s})_{i=1,\ldots,N}$$

and the coefficient vector $\Phi^{SUB} = [\Phi_1^{SUB}, \ldots, \Phi_N^{SUB}] \in \mathbb{R}^N$.
Finally, the solution to the EEG forward problem $\Phi = \Phi^{\infty} + \Phi^{corr}$ is calculated using the solution vector Φ^{SUB}.

2.4.2. Partial integration approach

The partial integration approach was introduced to EEG source analysis by Yan and colleagues [154].

First, Equation 2.9 is multiplied with a finite element ansatz function $\psi_i \in C^\infty$ and integrated over Ω

$$\int_\Omega \nabla \cdot \sigma \nabla \Phi \psi_i \, \mathrm{d}\boldsymbol{x} = \int_\Omega \nabla \cdot \boldsymbol{J}^p \psi_i \, \mathrm{d}\boldsymbol{x}$$

and second, integration-by-parts is applied

$$-\int_\Omega \langle \sigma \nabla \Phi, \nabla \psi_i \rangle \, \mathrm{d}\boldsymbol{x} + \int_\Gamma \langle \sigma \nabla \Phi, \boldsymbol{n} \rangle \psi_i \, \mathrm{d}\boldsymbol{x} = -\int_\Omega \langle \boldsymbol{J}^p, \nabla \psi_i \rangle \, \mathrm{d}\boldsymbol{x} + \int_\Gamma \langle \boldsymbol{J}^p, \boldsymbol{n} \rangle \psi_i \, \mathrm{d}\boldsymbol{s}$$

As the current sources are restricted to the source space, $\boldsymbol{J}^p$ is zero on Γ. Moreover, the homogeneous Neumann boundary condition 2.9 is used, leading to

$$\int_\Omega \langle \sigma \nabla \Phi, \nabla \psi_i \rangle \, \mathrm{d}\boldsymbol{x} = \int_\Omega \langle \boldsymbol{J}^p, \nabla \psi_i \rangle \, \mathrm{d}\boldsymbol{x}$$

Finally, Equation 2.9 is used to rewrite the primary current density $\boldsymbol{J}^p$

$$\int_\Omega \langle \sigma \nabla \Phi, \nabla \psi_i \rangle \, \mathrm{d}\boldsymbol{x} = \langle \boldsymbol{q}, \nabla \psi_i(\boldsymbol{x}_0) \rangle$$

Projecting the potential Φ into the FE space using

$$\Phi(\boldsymbol{x}) \approx \Phi_h(\boldsymbol{x}) = \sum_{j=1}^{N} \psi_j(\boldsymbol{x}) \Phi_j^{PI} \quad \text{with } \Phi_j^{PI} = \Phi(\boldsymbol{x}_j)$$

yields a linear equation system

$$\mathbf{K} \Phi^{PI} = \boldsymbol{b}$$

with the Stiffness matrix 2.28, the right-hand side vector $\boldsymbol{b}$

$$\boldsymbol{b} = (b_i)_{i=1,\ldots,N} = \langle \boldsymbol{q}, \nabla \psi_i(\boldsymbol{x}_0) \rangle \tag{2.29}$$

and the coefficient vector $\Phi^{PI} = [\Phi_1^{PI}, \ldots, \Phi_N^{PI}] \in \mathbb{R}^N$.

Remark 2.4 (Regularity of $\boldsymbol{J}^p$)**.** As described above, the right-hand side $\nabla \cdot \boldsymbol{J}^p \notin L^2(\Omega)$ when using the source representation $\boldsymbol{J}^p = \delta(\mathbf{x} - \mathbf{x}_0)\boldsymbol{q}$. Despite the lack of regularity, integration-by-parts was formally applied. Theoretically, one should not use a point source at the dipole location, but might use a mollifier function $\lim_{\epsilon \to 0} \psi_\epsilon(\boldsymbol{x} - \boldsymbol{x}_0) = \delta(\boldsymbol{x} - \boldsymbol{x}_0)$ to approximate the non-smooth function $\boldsymbol{J}^p$ by a smooth one. As the limit of ψ_ϵ is exactly the Dirac-delta function, the numerical results will be identical. Practically, the partial integration approach has been shown to be highly accurate in sphere models [141].

2.4.3. Adjoint approach

The adjoint approach for the EEG forward problem is given as [135]

$$\begin{aligned} \nabla \cdot \sigma \nabla \boldsymbol{w}_i &= 0 && in \quad \Omega && (2.30)\\ \langle \sigma \nabla \boldsymbol{w}_i, \boldsymbol{n} \rangle &= \delta_{\boldsymbol{s}_i} - \delta_{\boldsymbol{s}_0} && on \quad \Gamma \setminus \Gamma_D && (2.31)\\ \boldsymbol{w}_i &= 0 && on \quad \Gamma_D && (2.32) \end{aligned}$$

with $\boldsymbol{s}_i$ and $\boldsymbol{s}_0$ being the position of the scalp and reference electrode, respectively. Compared to the EEG forward problem, the current source in the source space is removed ($\boldsymbol{J}^p = 0$) and an inhomogeneous Neumann boundary condition is introduced to inject a current to a scalp electrode and to remove it from a given reference electrode.

Integrating Equation 2.30 over Ω and multiplying it with a FE ansatz function $\psi_j \in C^\infty$ yields

$$\int_\Omega (\nabla \cdot \sigma \nabla \boldsymbol{w}_i) \psi_j \, \mathrm{d}\boldsymbol{x} = 0$$

Integration-by-parts yields

$$-\int_\Omega \langle \sigma \nabla \boldsymbol{w}_i, \nabla \psi_j \rangle \, \mathrm{d}\boldsymbol{x} + \int_\Gamma \langle \sigma \nabla \boldsymbol{w}_i, \boldsymbol{n} \rangle \psi_j \, \mathrm{d}\boldsymbol{s} = 0$$

Next, the boundary condition 2.31 is used

$$\int_\Omega \langle \sigma \nabla \boldsymbol{w}_i, \nabla \psi_j \rangle \, \mathrm{d}\boldsymbol{x} = \int_\Gamma (\delta_{\boldsymbol{s}_i} - \delta_{\boldsymbol{s}_0}) \psi_j \, \mathrm{d}\boldsymbol{s}$$

Projecting $\boldsymbol{w}_i$ into the FE space using

$$w_i(\boldsymbol{x}) \approx w_{i,h}(\boldsymbol{x}) = \sum_{j=1}^{N} \psi_j(\boldsymbol{x}) W_j^i \quad \text{with } W_j^i = w_i(\boldsymbol{x}_j)$$

yields a linear equation system $\mathbf{K}\boldsymbol{W}^i = \boldsymbol{b}$, with the stiffness matrix from (2.28), the right-hand side vector $\boldsymbol{b}$

$$\boldsymbol{b} = (b_i)_{i=1,\dots,N} = (\int_\Gamma (\delta_{\boldsymbol{s}_i} - \delta_{\boldsymbol{s}_0}) \psi_j \, \mathrm{d}\boldsymbol{s})_{i=1,\dots,N}$$

and the coefficient vector $\boldsymbol{W}^i = [W_1^i, \dots, W_N^i] \in \mathbb{R}^N$.
The adjoint approach can be used to calculate the lead field matrix in a reciprocal manner. Vallaghe and colleagues [135] were able to demonstrate that the lead field can be calculated as

$$\mathbf{L}_i = \nabla \boldsymbol{W}^i \tag{2.33}$$

Using the precomputed lead field and Riesz representation theorem, the solution $\boldsymbol{W}^i$ of the

adjoint approach can be related to the solution Φ of the EEG forward problem

$$\Phi(\boldsymbol{s}_i) - \Phi(\boldsymbol{s}_0) \overset{(2.11)}{=} \int_\Omega \langle \boldsymbol{J}^p, \nabla \boldsymbol{W}^i \rangle \, \mathrm{d}\boldsymbol{s} \overset{(2.9)}{=} \langle \boldsymbol{q}, \nabla \boldsymbol{W}^i(\boldsymbol{x}_0) \rangle$$

In order to obtain a solution Φ_{EEG} of the EEG forward problem, the linear equation system $\mathbf{K}\boldsymbol{W}^i = \boldsymbol{b}$ has to be solved for $i = 1, \ldots, S-1$ different right hand sides $\boldsymbol{b}$, i.e., in each step, it is used that $\boldsymbol{b}(s_i) = 1$ and $\boldsymbol{b}(s_0) = -1$. In a next step, the potential differences $\Phi(\boldsymbol{s}_i) - \Phi(\boldsymbol{s}_0)$ have to be calculated for $i = 1, \ldots, S-1$. Finally, a common average reference is used, i.e., the additional constraint $0 = \sum_{i=0}^{S-1} \Phi(\boldsymbol{s}_i)$ is used.
For numerical realization of the adjoint approach for EEG source analysis, Vallaghe and colleagues [135] assumed the primary current density distribution $\boldsymbol{J}^p$ to be in the Sobolev space $L^2(\Omega)$. This regularity, however, is not given for point-like sources, see Section 2.1. In a recent validation study, however, the adjoint approach was shown to be highly accurate in sphere models, see Wagner [141].

2.4.4. Analytical EEG forward solutions

De Munck and Peters [30] derived analytical formulas for the EEG forward potentials in multi-layer sphere models. As the series expansion will be frequently used in this thesis for numerical validation, a review of the most important formulas and ideas is given. Further details can be found in the original publication [30].

De Munck and Peters [30] divided the multi-compartment shell model into N_C shells with radii of $r_{N_C} < r_{N_C-1} < \ldots < r_1$ and defined tangential $\sigma_{tang}(r) = \sigma^j_{tang}$ as well as radial $\sigma_{rad}(r) = \sigma^j_{rad}$ conductivity values for each shell $r_{j+1} < r < r_j$. Moreover, the radial coordinate of the source r_0, the radial coordinate of the electrode r_e and the angular distance $\omega_{0,e}$ between the electrode and source point is defined. Furthermore, it is assumed that the source lies in a more interior shell as compared to the electrode, i.e., $r_0 < r_e$. Using this notation, the potential induced by the dipolar source can be expressed in terms of the monopole potential Φ_{mon} at the source location

$$\Phi_{ana} = \langle \boldsymbol{q}, \nabla_0 \Phi_{mon}(\boldsymbol{x}_0, \boldsymbol{x}) \rangle$$

with $\boldsymbol{x}_0$ and $\boldsymbol{x}$ being the source point and the field point, respectively. As the volume conductor is assumed to be spherical and symmetric, the conductivity tensor σ is uniquely defined by the radial and tangential conductivity values.
The monopole potential can be calculated using only the radial components of the source and the electrode [30]

$$\Phi_{mon} = \frac{1}{4\pi} \sum_{n=0}^{N} (2n+1) R_n(r_0, r_e) P_n(\cos \omega_{0,e})$$

with P_n being the Legendre polynomials and R_n being the solution of the following PDE

$$\frac{\partial}{\partial_r}(r^2\sigma_{rad}(r)\frac{\partial}{\partial_t}R_n(r_0,r)) - n(n+1)\sigma_{tang}(r)R_n(r_0,r) = \delta(r_0 - r)$$

In order to solve this inhomogeneous PDE, De Munck and Peters [30] used the product of two linear independent solutions of a homogeneous equation. However, for a superficial source, when r_0 approaches r_e, a very slow convergence rate was reported for the homogeneous equations. In order to deal with the slow convergence rate for superficial sources, De Munck and Peters [30] introduced an *addition-subtraction method* to increase the convergence rate. Using the identities

$$\nabla_0 r_0 = \frac{\boldsymbol{x}_0}{r_0} \qquad \nabla_0 cos\omega_{0,e} = \nabla_0 \frac{\langle \boldsymbol{x}_0, \boldsymbol{x} \rangle}{r_0 r_e} = \frac{1}{r_0}(\boldsymbol{x} - \cos\omega_{0,e}\frac{\boldsymbol{x}_0}{r_0})$$

the analytical potential Φ_{ana} can be calculated as

$$\begin{aligned}\Phi_{ana} &= \langle \boldsymbol{q}, \frac{1}{4\pi}\nabla_0 \sum_{n=0}^{N}(2n+1)R_n(r_0,r_e)P_n(\cos\omega_{0,e})\rangle \\ &= \langle \boldsymbol{q}, \frac{\boldsymbol{x}_0}{r_0}(S_1 - \cos\omega_{0,e}S_0) + \frac{\boldsymbol{x}}{r_e}S_0\rangle\end{aligned}$$

where S_0 and S_1 are given as

$$\begin{aligned}S_0 &= \frac{1}{r_0}\sum_{n=1}^{\infty}(2n+1)R_n(r_0,r_e)P_n'(\cos\omega_{0,e}) \\ S_1 &= \sum_{n=1}^{\infty}(2n+1)R_n'(r_0,r_e)P_n(\cos\omega_{0,e})\end{aligned}$$

Finally, in order to reduce the number of terms required for the calculation of S_0 and S_1, an asymptotic approximation is applied

$$\begin{aligned}S_0 &= \frac{1}{r_0}\sum_{n=1}^{\infty}((2n+1)R_n(r_0,r_e) - F_0\Lambda^n)P_n'(\cos\omega_{0,e}) + \frac{F_0}{r_0}\frac{\Lambda\cos\omega_{0,e} - \Lambda^2}{1 - 2\Lambda\cos\omega_{0,e} + \Lambda^2} \\ S_1 &= \sum_{n=1}^{\infty}((2n+1)R_n'(r_0,r_e) - F_1 n\Lambda_n)P_n(\cos\omega_{0,e}) + \frac{F_1\Lambda}{1 - 2\Lambda\cos\omega_{0,e} + \Lambda^2}\end{aligned}$$

More details about the formulas F_0, F_1 and Λ, can be found in the original literature. In the following, Φ_{ana} is called to be the analytical computed EEG forward solution. For numerical validation, Φ_{ana} is evaluated at the EEG electrodes and compared to the numerically computed potentials, see Section 2.5.1 for two error measures in multi-layer spherical shell models.

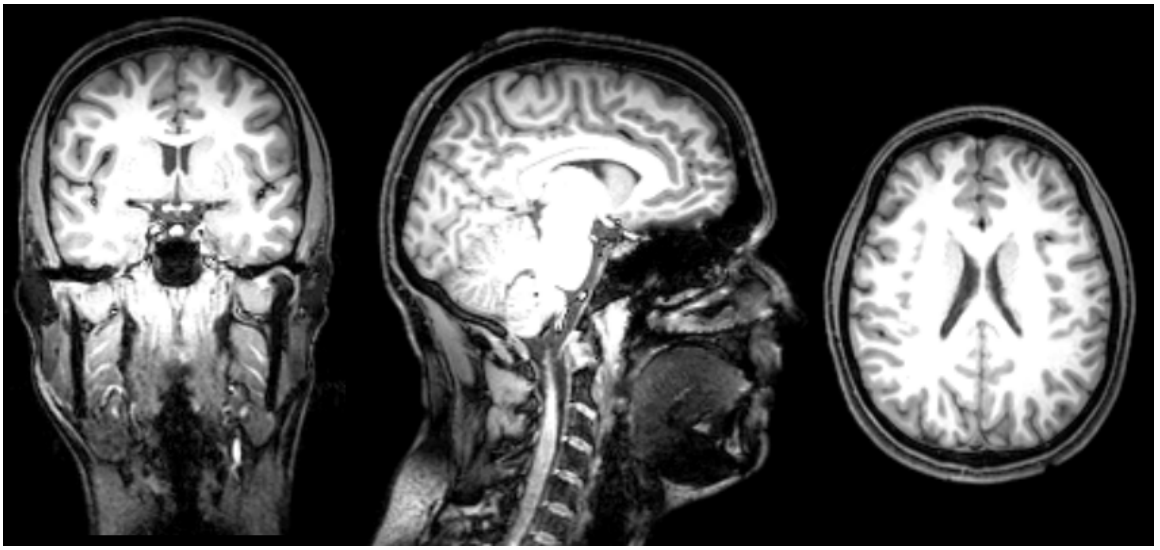

Figure 2.3.: Coronal (left), sagittal (middle) and axial (right) slice of a T1-image. The image was recorded on a 3T scanner (Contrast parameters: TR = 7546 ms, TE = 67 ms).

2.5. Volume conductor modeling

2.5.1. Spherical shell models

Numerical validation is performed in a regular hexahedral, a geometry-adapted hexahedral and a tetrahedral sphere model. Each model consists of four nested compartments (scalp, skull, CSF and brain) with radii of 92, 86, 80 and 78 mm, respectively (Table 2.1). Isotropic conductivity values of $0.43\,\mathrm{Sm}^{-1}$, $0.0042\,\mathrm{Sm}^{-1}$ and $1.79\,\mathrm{Sm}^{-1}$ are assigned to the scalp, skull and CSF, respectively and an anisotropic conductivity tensor is used for the brain compartment (Table 2.1). 748 EEG electrodes are evenly distributed across the surface of the sphere and 77 tangential and 77 radial dipoles are placed on a line from the center of the sphere to the brain/CSF interface in steps of 1 mm. Thus, the dipoles are placed up to only 1 mm below the conductivity jump. For each dipole, the source eccentricity is defined as the percentage of the difference between the dipole location and the sphere midpoint divided by the radius of the inner shell. The topography error (*relative difference measure* (RDM)) and the *magnitude error* (MAG) of the computed potential Φ_{num} with respect to the analytical potential Φ_{ana} are computed as follows

$$\begin{aligned} \mathrm{RDM} &= \left\| \frac{1}{\|\Phi_{ana}\|_2}\Phi_{ana} - \frac{1}{\|\Phi_{num}\|_2}\Phi_{num} \right\|_2 \cdot \frac{100\,\%}{2} \\ \mathrm{MAG} &= \frac{\|\Phi_{num}\|_2}{\|\Phi_{ana}\|_2} \cdot 100\,\%. \end{aligned}$$

Constrained Delaunay tetrahedralization FE approach

In a first step, a suitable boundary discretization of the model is prepared. Then, for a selected

Table 2.1.: Radii and conductivity values for the tissue types used.

Tissue type	**Radii** [mm]	**Conductivity** $[\mathrm{S\,m^{-1}}]$	
	Radii	**tangential cond.**	**radial cond.**
Skin	92	0.43	0.43
Skull	86	0.0042	0.0042
CSF	80	1.79	1.79
Brain	78	0.33	0.033

triangle edge length (here 1.75 mm), in each of the four layers, nodes are distributed in a most-regular way and connected through triangles, resulting in a valid triangular surface mesh for each layer. Importantly to note, it is not allowed that different layers intersect each other. In a next step, a tetrahedralization conforming to the surface meshes is constructed using a Constrained Delaunay tetrahedralization (CDT) approach [124]. First, a Delaunay tetrahedralization of the vertices of the surface meshes is built, and second, a local degeneracy removal algorithm combining vertex perturbation and vertex insertion is used. Finally, a fast facet recovery algorithm is applied [124]. In order to control the size and shape of the tetrahedra, two additional constraints can be applied. The volume constraint restricts the volume of the generated tetrahedra in a certain compartment. In this thesis, a volume constraint of $0.63\,\mathrm{mm}^3$ is applied. The second constraint controls the radius-edge ratio of the tetrahedron. Finally, an additional mesh smoothing and optimization step was used to remove the slivers and improve the overall mesh quality. The CDT meshing procedure resulted in a tetrahedral mesh $tet503k$ with 503,180 nodes and 3,1 million elements. The software package TetGen is used for tetrahedral FE mesh generation [123, 124].

Regular and geometry adapted hexahedral FE approaches

While regular hexahedral FE approaches have been used in many simulation studies [26, 28], an isoparametric FE approach for EEG source analysis [139] and for tCS modeling [142] that is specifically tailored to geometry-adapted hexahedral models is used. First, a hexahedral FE mesh was constructed out of the labeled volume of the four compartment sphere model using an edge length of 1 mm. This resulted in a regular hexahedral FE model $hex3.2m$ with 3,2 million nodes and 3,24 million elements. To increase conformance to the real geometry and to mitigate the staircase effects of the regular hexahedral mesh, a technique to shift nodes on material interfaces [18, 142] was applied. To ensure that interior angles at element vertices remained convex and the Jacobian determinant in the FEM computations remained positive, a nodeshift factor of 0.49 was used. This procedure resulted in a geometry-adapted hexahedral FE model $gahex3.2m$ with 3,2 million nodes and 3,24 million elements. The freely available software SimBio-VGRID [1] was used for hexahedral mesh generation.

[1] The SimBio-Vgrid mesh generator

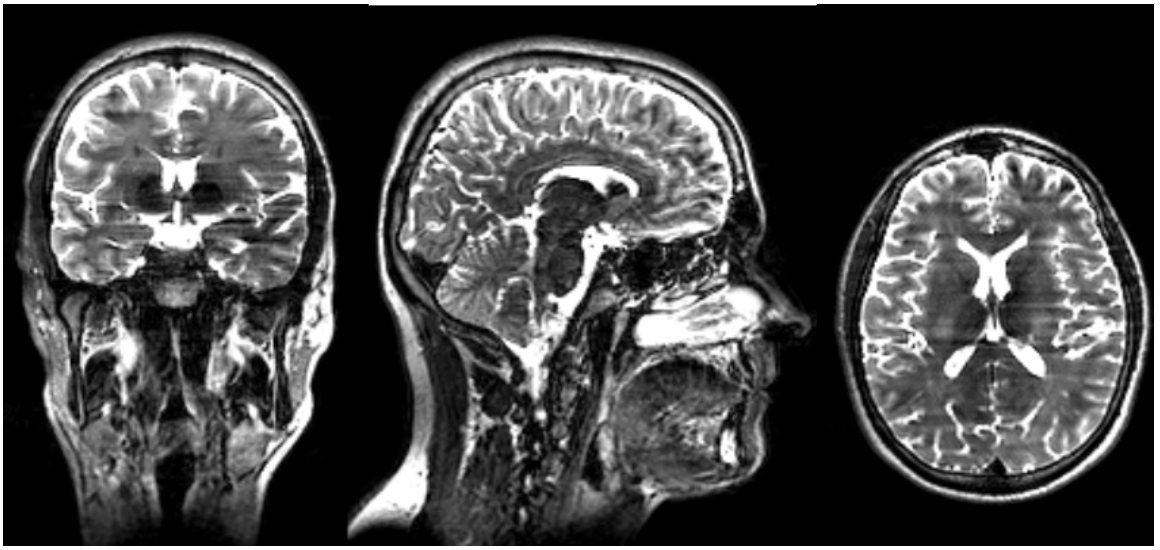

Figure 2.4.: Coronal (left), sagittal (middle) and axial (right) slice of a T2-image. The image was recorded on a 3T scanner (Contrast parameters: TR = 7546 ms, TE = 67 ms).

2.5.2. Highly realistic, six-compartment head model

MRI data acquisition

T1-, T2- and DW-MRI scans of a healthy, 26-year old male subject were measured, see Figures 2.3 and 2.4. After signing the written consent form approved by the ethical committee of the University of Erlangen, the measurements were performed on a 3T scanner (Gyrocan Intera/Achieva, 3.0T, System Release 2.5 (Philips, Best, NL)). A T1w pulse sequence with water selective excitation and a T2w pulse sequence with minimal water-fat-shift were measured using an isotropic resolution of 1.17 mm × 1.17 mm × 1.17 mm.

To measure the diffusion weighted MRI, a Steijskal-Tanner spin-echo EPI sequence (Geometry parameters: FOV 240 mm × 240 mm for 70 transversal slices, 1.875 mm thick, without gap and a square matrix of 128, leading to a voxel size of 1.875 mm x 1.875 mm x 1.875 mm. Contrast parameters: TR = 7546 ms, TE = 67 ms with a SENSE parallel imaging scheme in AP direction (acceleration factor 2)) was used. First, one volume was acquired with diffusion sensitivity $b = 0\,\mathrm{s(mm)^{-2}}$. Next, 20 volumes were measured with diffusion sensitivity $b = 1000\,\mathrm{s(mm)^{-2}}$ using diffusion weighted gradients in 20 directions (equally distributed on a sphere according to [65]). For susceptibility artefact correction, reversed encoding gradients were used to acquire an additional b_0 data set. The pixel bandwidth was 2873 Hz per pixel and the bandwidth in phase encoding direction was 20.3 Hz per pixel.

Registration and segmentation of MRI images

The T1w-MRI was used as the reference image for the registration procedure. An affine registration approach and mutual information as a cost function were used to register the T2w-MRI onto the T1w-MRI. Next, skin and brain masks and inner skull and outer skull surfaces were obtained from the registered images [63, 127]. While the gray and white matter

compartments were segmented from the T1w image, the CSF compartment was segmented from the T2w image. For the segmentation of the CSF compartment, a hidden Markov random field model [156] was used. All computation steps were performed using the FSL [2] software package. After the automatized segmentation procedure, the segmentation was visually inspected and manually corrected using CURRY [3]. For skull spongiosa modeling, the inner and outer skull masks were mapped on the T2w-MRI. Next, one voxel erosion was carried out to guarantee that the inner and outer skull compacta are at least one voxel thick [2]. Finally, a thresholding based region-growing segmentation constraint was used in CURRY to differentiate between skull spongiosa and compacta.

Generation of the geometry-adapted hexahedral FE mesh

The registration and segmentation approach provided a labeled volume of the MRI scans. The labeled MRIs were used to construct a geometry-adapted hexahedral FE mesh. Based on the study of Camacho and colleagues [18], interior nodes of the head model were shifted at material interfaces. This allows to increase conformance to the real head structure and to mitigate the stair-case effects of a regular hexahedral head model. This approach has been shown to reduce the modeling error as compared to regular hexahedral models in multi-layer sphere models ([149], nodeshift-factor 0.33), leading to high numerical accuracies especially for high-resolution meshes [138]. This procedure resulted in a geometry-adapted hexahedral FE model with 2,238,470 nodes and 2,178,209 elements.

Adding white matter tissue anisotropy

The diffusion weighted MR images were corrected for eddy current artefacts by an affine registration of the directional images to the b_0 image using the FSL routine FLIRT. After this procedure, the gradient directions were reoriented using the rotational part of the transformation matrix [70]. Then, a new diffeomorphic approach for correction of susceptibility artefacts using a reversed gradient approach and multiscale nonlinear image registration was applied to the DW-MRI datasets [112]. This approach is implemented in the freely-available FAIR [4] image registration toolbox. After eddy current artefact and susceptibility correction, the b_0 image was rigidly registered to the T2 image using FLIRT and the transformation matrix obtained in this step was used for the registration of the directional images, while taking care that the corresponding gradient directions were reoriented accordingly. The tensors were then calculated using the FSL routine DTIFIT [10]. In a last step, conductivity tensors were calculated from the artefact-corrected and registered diffusion-tensor-MRI using the effective medium approach as described in [110, 134] and embedded in the geometry-adapted hexahedral FE head model. Figure 2.5 shows a coronal cutplane of a commonly-used six-compartment, geometry-adapted hexahedral finite element head model for an auditory cortex stimulation.

[2] www.fmrib.ox.ac.uk/fsl
[3] www.neuroscan.com/curry.cfm
[4] Flexible Algorithms for Image Registration (FAIR) www.mic.uniluebeck.de/people/jan-modersitzki/software/fair.html

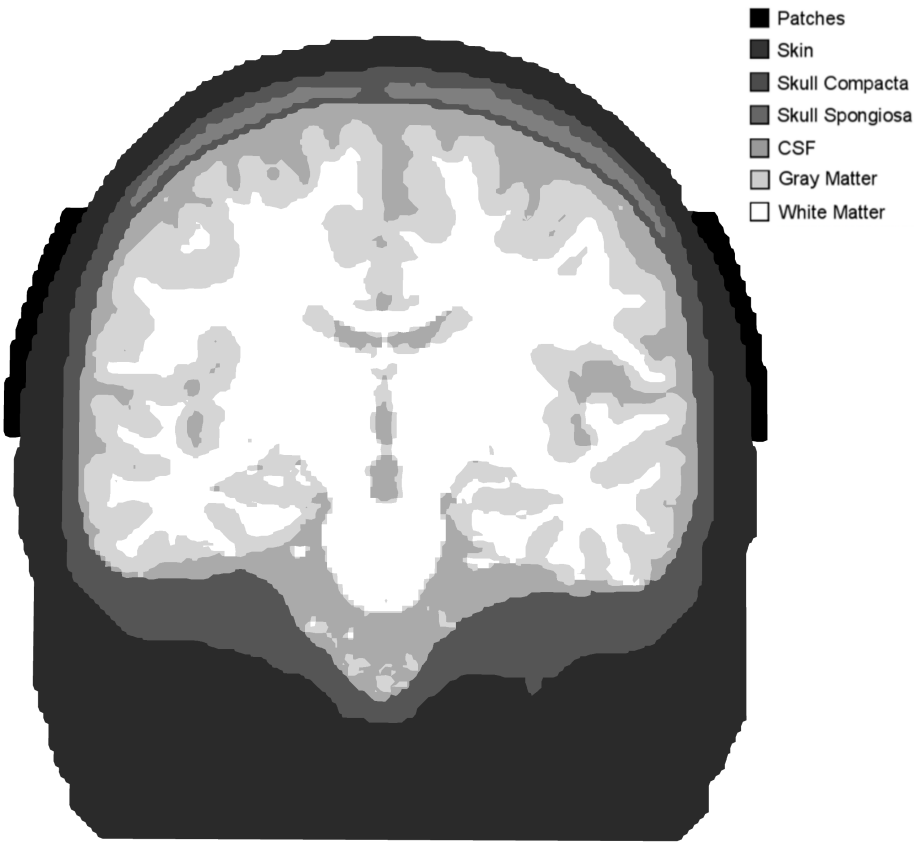

Figure 2.5.: Geometry-adapted six-compartment realistically shaped finite element hexahedral head model for auditory cortex stimulation. Stimulating electrodes with a size of $7\,\mathrm{cm} \times 5\,\mathrm{cm}$, thickness of $4\,\mathrm{mm}$ and saline-like conductivity of $1.4\,\mathrm{Sm}^{-1}$ are positioned above the auditory cortices.

Time requirement for head model generation

In order to generate a highly realistic six-compartment head model with white matter anisotropy, T1w-, T2w- and DT-MRI scans of the patients are required. For the measurement of the MRI scans, the total amount of acquisition time is about 27 minutes. Optionally, simultaneously measured auditory evoked potentials (AEP) and fields (AEF) are used to appropriately estimate the target vector for auditory cortex stimulation. A measurement of AEPs and AEFs requires approximately 24 minutes of measurement time. The measurement of somatosensory evoked potentials (SEP) and fields (SEF) requires an additional measurement time of 7 min per subject. While the generation of a highly accurate and realistically shaped head model takes approximately 10 hours, most parts are automatized as described above. Fully automatized, button-press head model generation tools like BESA MRI [5] might be used in order to further reduce efforts for head model generation.

[5] BESA MRI 2.0, http://www.besa.de/products/besa-mri/besa-mri-overview/

3

Transcranial direct current stimulation

3.1. Current flow modeling in transcranial direct current stimulation

3.1.1. Partial differential equation

For modeling the tDCS current flow vector fields, the quasistatic approximation to Maxwell's equations is used [97]. This yields the *tDCS forward problem*

$$\begin{aligned} \nabla \cdot \sigma \nabla \Phi &= 0 \quad && in\ \Omega && (3.1)\\ \langle \sigma \nabla \Phi, \boldsymbol{n} \rangle &= \boldsymbol{I} \quad && on\ \Gamma && (3.2)\\ \Phi &= 0 \quad && on\ \Gamma_D && (3.3) \end{aligned}$$

with Φ being the electric potential, $\sigma \in (L^\infty)^{3\times 3}$ being an anisotropic conductivity tensor, $\boldsymbol{I}$ being the applied current pattern with non-zero values only at the electrode surfaces, $\boldsymbol{n}$ being the outward normal vector and Γ being the boundary of the domain Ω. Furthermore, a Dirichlet boundary condition on Γ_D is used to ensure that a solution to the tDCS forward problem is unique. The Sobolev space

$$H_\diamond^{-\frac{1}{2}}(\Gamma) := \{u \in H^{-\frac{1}{2}}(\Gamma) : \int_\Gamma u(s)\, \mathrm{d}\boldsymbol{s} = 0\} \subset H^{-\frac{1}{2}}(\Gamma)$$

with $H^{-\frac{1}{2}}(\Gamma)$ being the standard Sobolev space related to Neumann traces of H^1-functions on Γ is introduced. The integral in the above definition has to be interpreted as a duality

product with the constant function equal to one, which is in $H^{\frac{1}{2}}(\Gamma)$.

Under standard and naturally satisfied regularity assumptions, there exists a unique solution $\Phi \in H^1(\Omega)$ to the tDCS forward problem

Theorem 3.1. Let $\sigma \in (C^\infty)^{3\times 3}$ with $\sigma \geq \sigma_0 I_{3\times 3}$ and let $\boldsymbol{I} \in H_\diamond^{-\frac{1}{2}}(\Gamma)$. Then, there exists a unique solution $\Phi \in H^1(\Omega)$ to the tDCS forward problem and the following norm estimate holds

$$\|\Phi\|_{H^1} \leq C \|\boldsymbol{I}\|_{H_\diamond^{-\frac{1}{2}}}$$

Before the existence of a unique solution to the tDCS forward problem is shown, basic definitions and the Lax-Milgram Theorem are presented.

Definition 3.1 (Bounded and coercive bilinearform, [17])**.** A bilinearform $B(u, v)$ on a normed space V is called *bounded* (or *continuous*), if there exists a constant $C < \infty$ such that

$$|B(u, v)| \leq C \|u\|_V \|v\|_V \quad \forall u, v \in V$$

and coercive on $V^* \subset V$ if there exists $\alpha > 0$ such that

$$B(u, u) \geq \alpha \|u\|_V^2 \qquad \forall u \in V^*$$

Theorem 3.2 (Lax-Milgram Theorem, [35] p. 297, Theorem 1)**.** Assume that $B : H^1(\Omega) \times H^1(\Omega) \to \mathbb{R}$ is a bilinear mapping which fulfills the coercivity condition and is also bounded by a constant C. Let us furthermore consider $f : H^1(\Omega) \to \mathbb{R}$ to be a bounded and linear functional in $H^1(\Omega)$. Then there exists a unique element $u \in H^1(\Omega)$ such that

$$B(u, v) = \langle f, v \rangle \qquad \forall v \in H^1(\Omega)$$

Proof of Theorem 3.1. See [35] page 297, Theorem 1 □

The existence of a unique solution $\Phi \in H^1(\Omega)$ to the tDCS forward problem will now be shown

Proof. Multiplying Equation 3.1 with $v \in H^1(\Omega)$, integrating over Ω and applying integration-by-parts yields

$$0 = \int_\Omega (\nabla \cdot \sigma \nabla \Phi) v \, \mathrm{d}\boldsymbol{x} = -\int_\Omega \langle \sigma \nabla \Phi, \nabla v \rangle \, \mathrm{d}\boldsymbol{x} + \int_\Gamma \langle \sigma \nabla \Phi, \boldsymbol{n} \rangle v \, \mathrm{d}\boldsymbol{x}$$

using boundary condition 3.2 implies that

$$\int_\Omega \langle \sigma \nabla \Phi, \nabla v \rangle \, \mathrm{d}\boldsymbol{x} = \int_\Gamma \boldsymbol{I} v \, \mathrm{d}\boldsymbol{x}$$

Therefore, a bilinearform $B(\Phi, v)$ is defined as follows

$$B(\Phi, v) = \int_\Omega \langle \sigma \nabla \Phi, \nabla v \rangle \, \mathrm{d}\boldsymbol{x} \tag{3.4}$$

and a linear functional $f(v)$ is introduced

$$f(v) = \int_\Gamma \boldsymbol{I} v \, \mathrm{d}\boldsymbol{x} \tag{3.5}$$

An easy calculation reveals that the linear functional is bounded in H^1

$$|f(v)| = \int_\Gamma |\boldsymbol{I} v| \, \mathrm{d}\boldsymbol{x} \leq C \int_\Gamma |v| \, \mathrm{d}\boldsymbol{x} \leq \tilde{C} \left\| v \right\|_{L^2} \leq \tilde{C} \left\| v \right\|_{H^1}$$

Furthermore, the bilinearform is also bounded in H^1:
Let σ_{max} be the largest eigenvalue of the conductivity tensor σ. Then one obtains

$$\begin{aligned} |B(\Phi, v)| &= |\int_\Omega \langle \sigma \nabla \Phi, \nabla v \rangle \, \mathrm{d}\boldsymbol{x}| \\ &\leq \sigma_{max} \int_\Omega |\langle \nabla \Phi, \nabla v \rangle| \, \mathrm{d}\boldsymbol{x} \\ &\leq \sigma_{max} \left\| \nabla \Phi \right\|_2 \left\| \nabla v \right\|_2 \\ &\leq \sigma_{max} \left\| \Phi \right\|_{H^1(\Omega)} \left\| v \right\|_{H^1(\Omega)} \\ &:= C \left\| \Phi \right\|_{H^1(\Omega)} \left\| v \right\|_{H^1(\Omega)} \end{aligned}$$

where *Hölder's Inequality* was used, see also Appendix A.2. For the sake of simplicity and to avoid technical details, the coercivity condition is not proven which follows immediately from the Friedrichs inequality, see also [151].
As the linear functional is bounded and the bilinearform is coercive and bounded, the existence of a unique solution $\Phi \in H^1(\Omega)$ directly follows from the Lax-Milgram Theorem. □

In order to fulfill the compatibility condition for bipolar tDCS modeling, the boundary condition 3.2 is exchanged by the following conditions

$$\int_{\Gamma_a} \langle \sigma \nabla \Phi, \boldsymbol{n} \rangle \, \mathrm{d}\boldsymbol{x} = \boldsymbol{I} \quad on \ \Gamma_a \tag{3.6}$$

$$\int_{\Gamma_c} \langle \sigma \nabla \Phi, \boldsymbol{n} \rangle \, \mathrm{d}\boldsymbol{x} = -\boldsymbol{I} \quad on \ \Gamma_c \tag{3.7}$$

$$\langle \sigma \nabla \Phi, \boldsymbol{n} \rangle = 0 \quad on \ \Gamma_r = \Gamma \setminus (\Gamma_a \cup \Gamma_c \cup \Gamma_D) \tag{3.8}$$

with Γ_a and Γ_c being the surface of anode and cathode, respectively.

In order to show the existence of a unique solution $\Phi \in H^1(\Omega)$ to the *extended tDCS forward problem*

$$\nabla \cdot \sigma \nabla \Phi = 0 \quad in \ \Omega \tag{3.9}$$

$$\int_{\Gamma_a} \langle \sigma \nabla \Phi, \boldsymbol{n} \rangle \, \mathrm{d}\boldsymbol{x} = \boldsymbol{I} \quad on \ \Gamma_a \tag{3.10}$$

$$\int_{\Gamma_c} \langle \sigma \nabla \Phi, \boldsymbol{n} \rangle \, \mathrm{d}\boldsymbol{x} = -\boldsymbol{I} \quad on \ \Gamma_c \tag{3.11}$$

$$\langle \sigma \nabla \Phi, \boldsymbol{n} \rangle = 0 \quad on \ \Gamma_r = \Gamma \setminus (\Gamma_a \cup \Gamma_c \cup \Gamma_D) \tag{3.12}$$

$$\Phi = 0 \qquad on\ \Gamma_D \tag{3.13}$$

a right-hand side vector $I \in H^{-\frac{1}{2}}(\Gamma)$ is sufficient

Theorem 3.3. Let $\sigma \in (C^\infty)^{3\times 3}$ with $\sigma \geq \sigma_0 I_{3\times 3}$ and let $\boldsymbol{I} \in H^{-\frac{1}{2}}(\Gamma)$. Then, there exists a unique solution $\Phi \in H^1(\Omega)$ to the extended tDCS forward problem 3.9 - 3.13.

Proof. It is now shown that condition $\int_\Gamma \langle \sigma \nabla \Phi, \boldsymbol{n} \rangle \, \mathrm{d}\boldsymbol{x} = 0$ is always fulfilled. An easy calculation reveals

$$\begin{aligned} \int_\Gamma \langle \sigma \nabla \Phi, \boldsymbol{n} \rangle \, \mathrm{d}\boldsymbol{x} &= \int_{\Gamma_a} \langle \sigma \nabla \Phi, \boldsymbol{n} \rangle \, \mathrm{d}\boldsymbol{x} + \int_{\Gamma_c} \langle \sigma \nabla \Phi, \boldsymbol{n} \rangle \, \mathrm{d}\boldsymbol{x} + \int_{\Gamma_r} \langle \sigma \nabla \Phi, \boldsymbol{n} \rangle \, \mathrm{d}\boldsymbol{x} \\ &= \boldsymbol{I} - \boldsymbol{I} + 0 \\ &= 0 \end{aligned}$$

which ensures that $\boldsymbol{I} \in H_\diamond^{-\frac{1}{2}}(\Gamma)$. Therefore, the existence of a unique solution directly follows from Theorem 3.1. □

In the following, the Laplace equation with inhomogeneous Neumann boundary conditions 3.9 - 3.13 will be called the tDCS forward problem. It fulfills the *compatibility condition*

$$\int_\Omega \nabla \cdot \sigma \nabla \Phi \, \mathrm{d}\boldsymbol{x} - \int_\Gamma \langle \sigma \nabla \Phi, \boldsymbol{n} \rangle \, \mathrm{d}\boldsymbol{x} = 0$$

3.1.2. A finite element approach for tDCS modeling

In order to solve the tDCS forward problem, a finite element method based approach for calculating the current flow fields induced by direct current stimulation is presented. The FEM was also used in many other simulation studies for tDCS [26, 33, 115, 144].

Integrating Equation 3.9 over Ω and multiplying it with a finite element ansatz function $\psi_i \in \mathcal{C}^\infty$ yields

$$\int_\Omega \nabla \cdot \sigma \nabla \Phi \psi_i \, \mathrm{d}\boldsymbol{x} = 0$$

Integration-by-parts leads to

$$-\int_\Omega \langle \sigma \nabla \Phi, \nabla \psi_i \rangle \, \mathrm{d}\boldsymbol{x} + \int_\Gamma \langle \sigma \nabla \Phi, \boldsymbol{n} \rangle \psi_i \, \mathrm{d}\boldsymbol{x} = 0$$

Next, the boundary conditions 3.10, 3.11 and 3.12 are used to obtain

$$\begin{aligned} \int_\Omega \langle \sigma \nabla \Phi, \nabla \psi_i \rangle \, \mathrm{d}\boldsymbol{x} &= \int_{\Gamma_a} \langle \sigma \nabla \Phi, \boldsymbol{n} \rangle \psi_i \, \mathrm{d}\boldsymbol{x} + \int_{\Gamma_c} \langle \sigma \nabla \Phi, \boldsymbol{n} \rangle \psi_i \, \mathrm{d}\boldsymbol{x} \\ &\quad + \int_{\Gamma \setminus (\Gamma_a \cup \Gamma_c \cup \Gamma_D)} \langle \sigma \nabla \Phi, \boldsymbol{n} \rangle \psi_i \, \mathrm{d}\boldsymbol{x} \\ &= \int_{\Gamma_a} \psi_i \boldsymbol{I} \, \mathrm{d}\boldsymbol{x} - \int_{\Gamma_c} \psi_i \boldsymbol{I} \, \mathrm{d}\boldsymbol{x} \end{aligned}$$

The potential Φ is projected into the FE space

$$\Phi(x) \approx \Phi_h(\boldsymbol{x}) = \sum_{j=1}^{N} \psi_j(\boldsymbol{x}) \Phi_j^{tDCS}, \quad \text{with } \Phi_j^{tDCS} = \Phi(x_j).$$

leading to a linear equation system

$$\mathbf{K}\Phi^{tDCS} = \boldsymbol{b}$$

with $\mathbf{K}$ being the FE stiffness matrix (see Equation 2.28), the right-hand side vector $\boldsymbol{b}$

$$\boldsymbol{b} = \begin{cases} \int_{\Gamma_a} \psi_i \boldsymbol{I} \, \mathrm{d}\boldsymbol{x}, & \text{if } supp(\psi_i) \cap \Gamma_a \neq 0 \\ -\int_{\Gamma_c} \psi_i \boldsymbol{I} \, \mathrm{d}\boldsymbol{x}, & \text{if } supp(\phi_i) \cap \Gamma_c \neq 0 \\ 0 & \text{otherwise} \end{cases}$$

and the coefficient vector $\Phi^{tDCS} = [\Phi_1^{tDCS}, \ldots, \Phi_N^{tDCS}] \in \mathbb{R}^N$.

Finally, the current density $\boldsymbol{J}$

$$\boldsymbol{J} = \sigma \nabla \Phi \tag{3.14}$$

is calculated using the solution vector Φ^{tDCS}.

3.2. Relationship between EEG source analysis and tDCS

The goal of this section is to give insight into the relationship between EEG source analysis and tDCS simulation studies by providing analytical forward expressions for the adjoint and the partial integration approach. This relation clarifies that quasi-analytical EEG forward formulas in sphere models (see Section 2.4.4) can be used to investigate numerical accuracies of commonly-used FE approaches for tDCS modeling.

3.2.1. Algebraic formulas for adjoint and partial integration EEG approach

It is now proven that $\Phi_{AA} \in \mathbb{R}^{S-1}$, i.e., the potential vector at the non-reference electrodes resulting from the adjoint approach, and $\Phi_{PI} \in \mathbb{R}^{S-1}$, the potential resulting from the partial integration approach in conjunction with the FE transfer matrix concept, are algebraically identical even for generalized head models.

Lemma 3.1 (Matrix formulation for the adjoint approach solution vector)**.** Let $(\boldsymbol{b}_i)_{i=1,\ldots,S-1} = B \in \mathbb{R}^{N \times (S-1)}$ be the matrix containing the right-hand sides of the adjoint approach. Let furthermore $(\boldsymbol{W}^i)_{i=1,\ldots,S-1} = \mathbf{W} \in \mathbb{R}^{N \times (S-1)}$ be the matrix containing the electric potential solution vectors of the adjoint approach. In addition, let us define $D\Psi(\boldsymbol{x}) := [\nabla\psi_1(\boldsymbol{x}), \ldots, \nabla\psi_N(\boldsymbol{x})] \in \mathbb{R}^{3 \times N}$ with ϕ_i being the FE ansatz functions and let us assume

a current dipole at location $\boldsymbol{x}_0$ with dipolar moment $\boldsymbol{q}$. The potential Φ_{AA} is then given as

$$\Phi_{AA} = \tilde{R}\boldsymbol{u} \tag{3.15}$$

with

$$\boldsymbol{u} := K^{-1}(D\Psi(\boldsymbol{x}_0))^{tr}\boldsymbol{q} \in \mathbb{R}^N \tag{3.16}$$

and $\tilde{R} := B^{tr} \in \mathbb{R}^{(S-1)\times N}$.

Proof. The ith entry of the adjoint approach potential vector $\Phi_{AA} \in \mathbb{R}^{S-1}$ for a single lead is given as

$$\begin{aligned}
(\Phi_{AA})_i &\overset{(2.32)}{=} \langle \boldsymbol{q}, \sum_{j=1}^{N} \nabla\psi_j(\boldsymbol{x}_0)(\boldsymbol{W}^i)_j \rangle \\
&= \langle \boldsymbol{q}, D\Psi(\boldsymbol{x}_0)\boldsymbol{W}^i \rangle \\
&= \langle \boldsymbol{q}, D\Psi(\boldsymbol{x}_0)K^{-1}B_{(\cdot,i)} \rangle \\
&= (D\Psi(\boldsymbol{x}_0)K^{-1}B_{(\cdot,i)})^{tr}\boldsymbol{q} \\
&= (B_{(\cdot,i)})^{tr}(K^{-1})^{tr}(D\Psi(\boldsymbol{x}_0))^{tr}\boldsymbol{q} \\
&= (B^{tr})_{(i,\cdot)}K^{-1}(D\Psi(\boldsymbol{x}_0))^{tr}\boldsymbol{q} \\
&= \tilde{R}_{(i,\cdot)}K^{-1}(D\Psi(\boldsymbol{x}_0))^{tr}\boldsymbol{q} \\
&= \tilde{R}_{(i,\cdot)}\boldsymbol{u}
\end{aligned}$$

and thus $\Phi_{AA} = \tilde{R}\boldsymbol{u}$. □

Lemma 3.2 (Matrix formulation for the partial integration approach in conjunction with an FE transfer matrix)**.** Let $R \in \mathbb{R}^{(S-1)\times N}$ be the restriction matrix from Equation 2.19. Then it reads

$$\Phi_{PI} = R\boldsymbol{u} \tag{3.17}$$

with the same $\boldsymbol{u}$ as in Lemma 3.1.

Proof. Φ_{PI} is simply given by

$$\Phi_{PI} \overset{(2.21)}{=} RK^{-1}\boldsymbol{b} \overset{(2.29)}{=} RK^{-1}\left(\boldsymbol{q}^{tr}D\Psi(\boldsymbol{x}_0)\right)^{tr} = RK^{-1}\left(D\Psi(\boldsymbol{x}_0)\right)^{tr}\boldsymbol{q} \overset{(3.16)}{=} R\boldsymbol{u} \tag{3.18}$$

□

Theorem 3.4 relates the solution of the AA to the solution of the PI approach.

Theorem 3.4. Let $\Phi_{AA} \in \mathbb{R}^{S-1}$ and $\Phi_{PI} \in \mathbb{R}^{S-1}$ be the EEG forward potentials calculated with the adjoint approach and the partial integration approach in conjunction with the FE transfer matrix, respectively. Then, both EEG forward potential vectors are identical, whereas only the exact type of referencing is different.

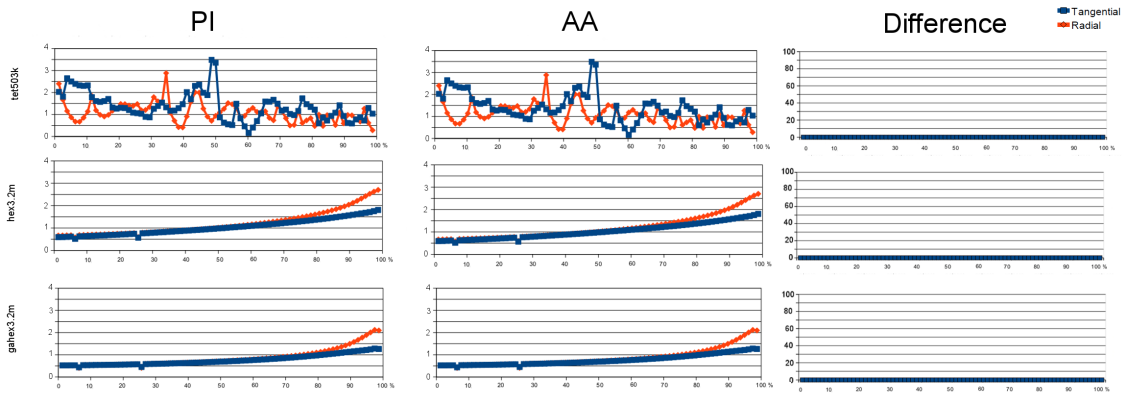

Figure 3.1.: Validations in spherical shell model: RDM errors for PI (left column) and AA (middle column) in CDT model $tet503k$ (first row), in regular hexahedral model $hex3.2m$ (second row) and in geometry-adapted hexahedral model $gahex3.2m$ (third row) at different source eccentricities (x-axis). The right column displays the difference (PI - AA) between both approaches. Errors for tangential (blue) and radial sources (red) are color-coded. Note that the scaling on the y-axes is identical to allow an easy comparison of numerical errors.

Proof. Because $\tilde{R} \in \mathbb{R}^{(S-1)\times N}$ and $R \in \mathbb{R}^{(S-1)\times N}$ only differ in column i_{ref} (the FE node of the reference electrode), one obtains

$$\tilde{R} = R - \mathbf{1}^{S-1}(\boldsymbol{e}_{i_{ref}}^{N})^{tr} \tag{3.19}$$

with $\mathbf{1}^{S-1} \in \mathbb{R}^{S-1}$ a vector filled with 1 and $\boldsymbol{e}_{i_{ref}}^{N} \in \mathbb{R}^{N}$ the unit vector with 1 only at position i_{ref}. Therefore, the following equation holds:

$$\Phi_{AA} \overset{Lemma\ 3.1}{=} \tilde{R}\boldsymbol{u} \overset{(3.19)}{=} R\boldsymbol{u} - \mathbf{1}^{S-1}(\boldsymbol{e}_{i_{ref}}^{N})^{tr}\boldsymbol{u} \overset{Lemma\ 3.2}{=} \Phi_{PI} - (\boldsymbol{u})_{i_{ref}}\mathbf{1}^{S-1} \tag{3.20}$$

□

3.2.2. Results

3.2.2.1. Validation in four layer sphere model

Figure 3.1 and 3.2 show RDM and MAG errors for the partial integration in combination with the FE transfer matrix approach (PI), the adjoint approach (AA) and the difference (PI-AA) using CDT model $tet503k$, the regular hexahedral model $hex3.2m$ and the geometry-adapted hexahedral model $gahex3.2m$, respectively.
Most importantly and as can be easily extracted from both figures, AA and PI perform identically with respect to numerical accuracy, independent of depth and orientation of the sources and number, size and shape of the elements to be considered.

The arithmetic operations count (see also [141]) in Table 3.1 shows that PI and AA require the same amount of operations to solve the EEG forward problem for all three models. The

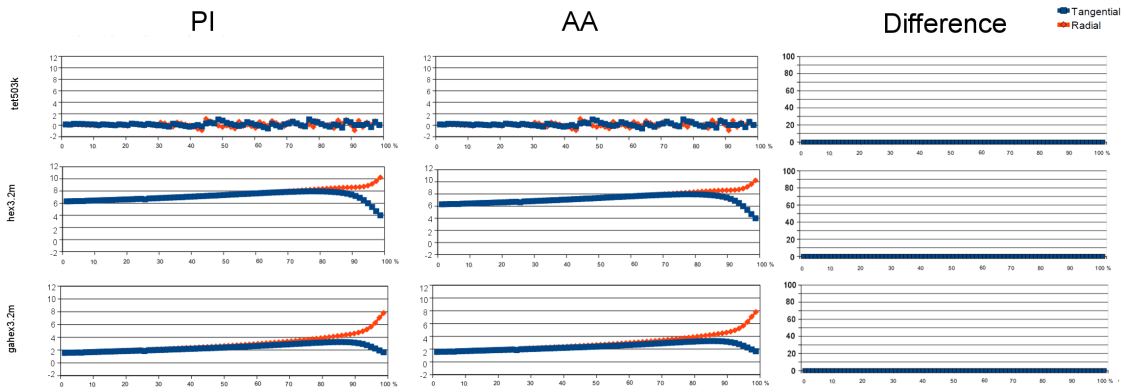

Figure 3.2.: Validations in spherical shell model: MAG errors for PI (left column) and AA (middle column) in CDT model $tet503k$ (first row), in regular hexahedral model $hex3.2m$ (second row) and in geometry-adapted hexahedral model $gahex3.2m$ (third row) at different source eccentricities (x-axis). The right column displays the difference (PI - AA) between both approaches. Errors for tangential (blue) and radial sources (red) are color-coded. Note that the scaling on the y-axes is identical to allow an easy comparison of numerical errors.

combination of Figures 3.1, 3.2 and Table 3.1 points out that PI and AA are identical for the four-layer sphere scenario, even if the way of computation is quite different.
In Theorem 3.4 , it was even proven algebraically that, up to the reference potential, PI and AA will lead to the same results, even for general head models. With regard to the reference, PI fixes the potential at a reference electrode to be exactly zero ($\Phi(\mathbf{s}_0) = 0$), while AA calculates the potential at the measurement sites with respect to the potential at a reference electrode ($\Phi(\mathbf{s}_i) - \Phi(\mathbf{s}_0)$). However, after re-referencing, both PI and AA will lead to the same results.

In Sections 2.4.3 and 3.1 it was shown that, as a substep of the overall calculations, in Equations 2.33 and 3.14 the AA numerically computes the electric potential solution for a tDCS simulation when using point-electrodes at $\mathbf{s}_i$ and $\mathbf{s}_0$. Therefore, the validation results presented in Figures 3.1 and 3.2 do not only show the numerical errors in the EEG forward problem, but also allow conclusions about the accuracy in calculating the electric potential underlying tDCS simulations.

As shown in Figure 3.1, with regard to the RDM and for eccentricities between 0% and 70%, the geometry-adapted hexahedral approach performs best ($\leq 1\%$) when compared to the regular hexahedral approach ($\leq 1.4\%$) and the CDT approach ($\leq 3.5\%$). For the higher

Approach / model	$tet503k$	$hex3.2m$	$gahex3.2m$
AA	$1{,}90 \cdot 10^{12}$	$2{,}84 \cdot 10^{13}$	$2{,}84 \cdot 10^{13}$
PI	$1{,}90 \cdot 10^{12}$	$2{,}84 \cdot 10^{13}$	$2{,}84 \cdot 10^{13}$

Table 3.1.: Arithmetic operations needed for PI and AA to solve the EEG forward problem in tetrahedral model $tet503k$ and in regular and geometry-adapted hexahedral models $hex3.2m$ and $gahex3.2m$, respectively.

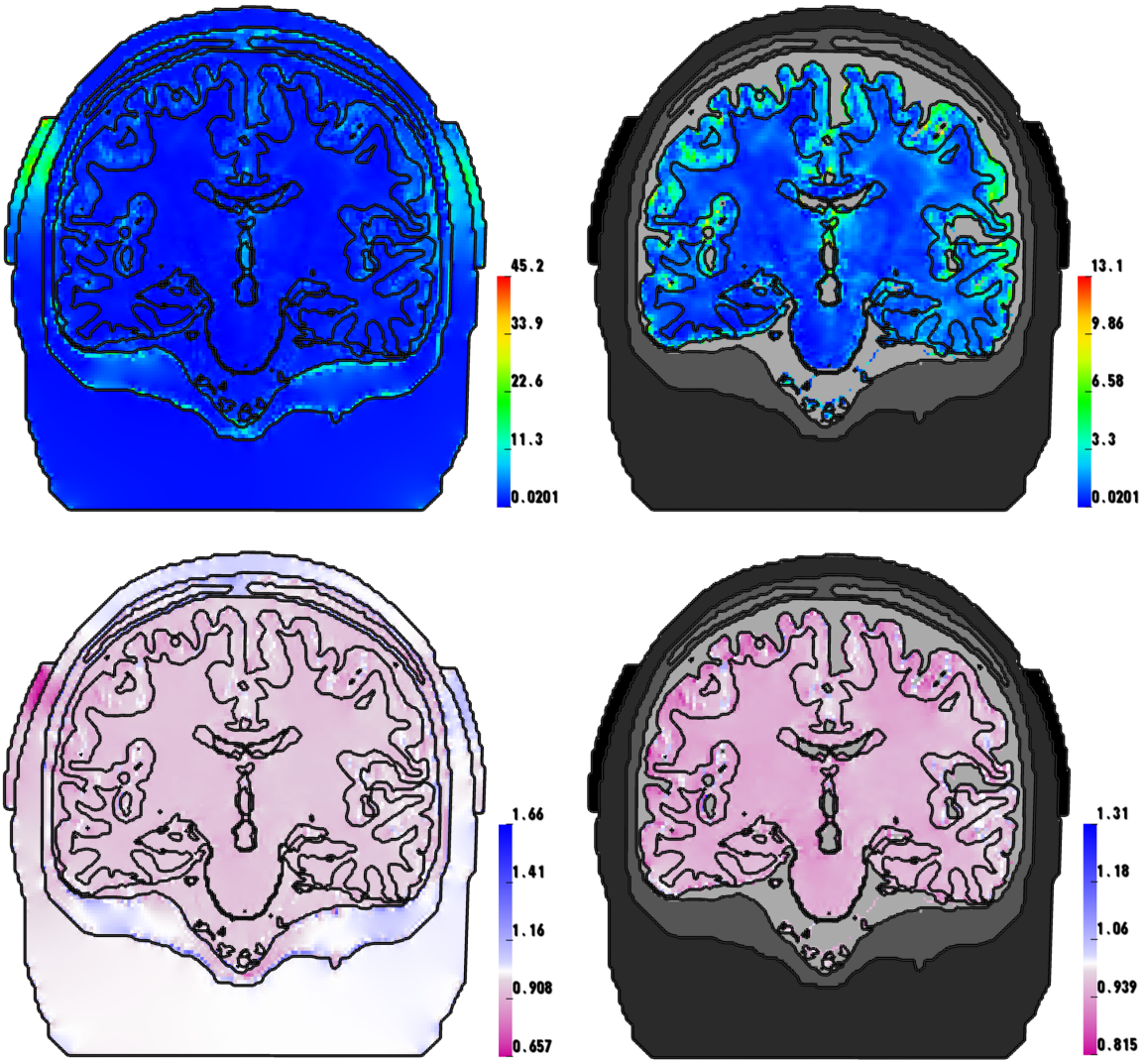

Figure 3.3.: Differences in the resulting current density vector field between an isoparametric geometry-adapted hexahedral FE approach as compared to a standard regular hexahedral approach for auditory cortex stimulation: Changes in orientation (first row) and magnitude (second row) in the whole volume conductor (first column) and only in the brain compartment (second column).

eccentricities between 70% and 98.72%, with RDM errors below 1.8%, the CDT is slightly better than the geometry-adapted ($\leq$ 2.1%) and the regular hexahedral approach ($\leq$ 2.8%). For both hexahedral modeling approaches and for higher eccentricities between 70% and 98.72%, RDM errors are higher for radial than for tangential sources, while they are very similar for eccentricities below 70%.

As shown in Figure 3.2, with errors below 1.1%, the CDT approach performs best with regard to the MAG, as expected. It is followed by the geometry-adapted hexahedral approach ($\leq$ 4% for eccentricities below 80% and $\leq$ 8% for eccentricities below 98.72%) and the regular hexahedral approach ($\leq$ 8.2% for eccentricities below 80% and $\leq$ 11% for eccentricities below 98.72%). For both hexahedral modeling approaches and for higher eccentricities between 70%

and 98.72%, MAG errors are higher for radial than for tangential sources, while they are very similar for eccentricities below 70%.

As deeper discussed in Section 3.2.3, a comparison between the CDT and the hexahedral approaches is rather difficult, while with regard to realistic head models both hexahedral models can directly be compared. Therefore, and as a preparation for Section 3.2.2.2, the hexahedral model validation results are now summarized. The geometry-adapted approach outperforms the standard regular approach by a factor of 1.3 with regard to RDM and MAG (from a maximal RDM of 2.8% down to 2.1% and from a maximal MAG of 11% down to 8%), further motivating the use of geometry-adaptation in combination with an isoparametric hexahedral FE approach for practical applications.

3.2.2.2. Regular and geometry-adapted hexahedral approaches in a realistic tDCS model

Figure 3.3 depicts changes in orientation and magnitude of the current density vector field (Equation 3.14) in the whole volume conductor and only in the brain compartment when using the geometry-adapted hexahedral approach as compared to the standard regular one. As can be seen, with orientation changes up to 45.2 degrees, changes are largest in the electrodes (upper left subfigure). Moreover, significant changes in orientation can be seen in skin, skull and CSF compartments. In superficial cortical areas, maximal current density orientation changes up to 13.1 degrees can be found (upper right). The change in magnitude is depicted on a pink-white-blue scale (lower subfigures), i.e., magnitude decreases in pink areas, remains constant in white regions and increases in blue regions. For auditory cortex stimulation, both an increase (up to 66%) and a decrease (up to 44%) in current density magnitude can be seen in electrodes, skin and skull (lower left). Moreover, magnitude mainly decreases in the CSF (lower left) and, with values up to 18.5%, in the brain compartment (lower right).

3.2.3. Discussion

In this study, accuracy and efficiency of a reciprocal and a direct EEG forward approach were investigated, namely the adjoint approach (AA) [47, 76, 87, 119, 135] and the partial integration approach in conjunction with an FE transfer matrix concept (PI) [120, 147, 150, 154]. In a four compartment sphere model, where quasi-analytical series expansion formulas exist [30], the numerical accuracy were analyzed with regard to RDM and MAG numerical errors for both approaches. A CDT FE approach, a standard hexahedral FE approach based on regular hexahedral and an isoparametric FE approach using geometry-adapted hexahedral was used and analyzed.

Vallaghe and colleagues [135], who derived the AA for source analysis using a combination of Riesz representation theorem and Helmholtz' principle of reciprocity, hypothesized that the two approaches PI and AA are very similar, as they both change the forward problem from a source point of view to a sensor point of view, but that the difference is that one

does it in a discrete space (PI), whereas the other keeps the original continuous space (AA). This validation study in a multilayer sphere model revealed that the numerical accuracy and computational complexity for calculating the EEG forward problem is identical for the AA and the PI approach. Moreover, it could be proven algebraically that AA and PI are identical even for general head models. With regard to improving the numerical accuracy and efficiency of FE-based EEG forward modeling, it is thus sufficient to only validate one of the approaches and compare it with other source modeling approaches [71, 120, 140, 151]. Even if AA can thus not contribute new numerical aspects to the EEG forward problem, it allows to calculate electrode lead vector fields $\boldsymbol{L}_i$ for given electrode pairs (Equation 2.33) and visualize the sensitivity of this electrode pair to sources in the brain using just a single image for $\boldsymbol{L}_i$ and having Equation 2.32 in mind.

Furthermore, as shown in this paper, the AA can also be used to bridge EEG source analysis and tDCS simulation (Equations 2.32, 2.33 and 3.14). Therefore, quasi-analytical EEG forward solutions in multilayer sphere models [30] can not only be used to investigate numerical accuracies of different FE approaches for the EEG forward problem, but also to reciprocally validate the approaches for tDCS simulation. For tDCS modeling, tetrahedral approaches have been presented in [77, 148], regular hexahedral approaches in [26, 28, 95] and the geometry-adapted hexahedral approach in [142].

As shown in Figures 3.1 and 3.2, the geometry-adapted approach is more accurate by a factor of 1.3 than the standard regular hexahedral approach. The gain in accuracy by means of a better approximation of smooth compartment surfaces thus outweighs the possible numerical disadvantage of less regular elements at tissue boundaries. The result presented here is in line with the EEG forward simulation study of [151], which showed that topography and magnitude errors can be reduced by even more than a factor of 2 and 1.5 for tangential and radial sources, respectively, when using an isoparametric FE approach with geometry-adapted hexahedral meshes with a nodeshift factor of 0.49 and Venant and subtraction source modeling approaches in 2 and 3 mm hexahedral models. In this study, besides the higher resolution (1 mm) and the different source modeling approach (PI), only a nodeshift factor of 0.33 was used, which explains the smaller factor of error-reduction. The more conservative nodeshift-factor ensures that interior angles at element vertices remain convex and the Jacobian determinants in the FEM computations remain positive also in highly realistic six-compartment head models [5, 142]. therefore it was also used here for the spherical model validation study. In summary, the geometry-adapted approach does not involve any additional difficulties for the user and thus has to be preferred to the regular standard approach for modeling both the EEG forward problem and tCS.

The comparison between the CDT approach and the geometry-adapted hexahedral approach is more difficult. First of all, model $gahex3.2m$ has about 6 times more degrees of freedom when compared to model $tet503k$. When knowing that the computational complexity for FE modeling in both source analysis and tDCS simulation using an algebraic multigrid conjugate gradient solver (AMG-CG) increases mainly linearly with the number of unknowns (see also

Section 3.3), $gahex3.2m$ leads to 6 times higher computational costs than $tet503k$. Even if for eccentricities between 0% and 70%, with $\leq 1\%$ compared to $\leq 3.5\%$ RDM error, the $gahex3.2m$ based approach outperformed the $tet503k$ based approach, for the higher eccentricities between 70% and 98.72% the less-computationally expensive tetrahedral approach even slightly took the lead with RDM errors $\leq 1.8\%$ compared to $\leq 2.1\%$. With regard to the MAG, the CDT ($\leq 1.1\%$) outperformed the geometry-adapted hexahedral approach ($\leq 4\%$ for eccentricities below 80% and $\leq 8\%$ for eccentricities below 98.72%). With regard to multilayer sphere modeling, where non-intersecting surfaces can accurately be constructed, CDT FE approaches are thus advisable. However, with regard to the modeling of a realistic head volume conductor from voxel-based MRI data, numerical errors of a few percent are most probably negligible when compared to remaining model errors. This has been shown by [140], who concluded that a reduction of the model error will have a much higher impact than a further increase of the numerical accuracy. A CDT FE approach for realistic head geometries is difficult to generate in practice and might lead to unrealistic model features like artificially closed skull compartments that ignore skull holes like the foramen magnum and the optic canals. Furthermore, CDT modeling necessitates nested surfaces, while in reality surfaces might touch each other, e.g., the inner and outer surface of the cerebrospinal fluid compartment. As discussed below, it might thus be advisable to focus on further reducing model errors. Therefore, for realistic head modeling, voxel-based methods like the isoparametric geometry-adapted hexahedral FE approach were considered as more advisable than purely surface-based ones because of their convenient generation from MRI data and the accompanying topological advantages.

In Equation 3.14, it was shown that lead vector fields in EEG source analysis and tDCS current flow fields are directly related as the latter is identical to the product of the conductivity tensor σ and the lead vector field $\boldsymbol{L}_i$ (when considering identical electrode montages). Therefore, the results also link head volume conductor model sensitivity investigations in EEG source analysis to tDCS modeling and vice versa. For this reason, in Section 4.1 tDCS computer simulations were performed, starting with a homogenized three-compartment head model and extending this step by step to a six-compartment anisotropic model. Thereby, important tDCS volume conduction effects were shown and a guideline for efficient yet accurate volume conductor modeling was presented. Vorwerk and colleagues [139] investigated the influence of modeling/not modeling the compartments skull spongiosa, skull compacta, CSF, gray matter, and white matter and of the inclusion of white matter anisotropy on the EEG forward solutions. The effect sizes in terms of orientation and magnitude differences are very similar to those that were found in tDCS in Section 4.1. This indicates that the results of studying volume conduction effects in EEG source analysis also allow conclusions on the outcome of tDCS simulations, and vice versa, and the theory for this relationship was presented here.

A last aim of this study was to compare tDCS simulation in a geometry-adapted and a regular hexahedral FE approach in a highly realistic volume conductor model with white matter anisotropy. Significant changes in orientation up to 13.1 degrees and a decrease in current density amplitude of about 20 % occurred in the gray matter compartment when

using the numerically more accurate geometry-adapted hexahedral approach as compared to the regular one. The effect sizes are similar to those of neglecting the distinction between skull compacta and spongiosa in skull modeling for tDCS [142]. In clinical practice, the exact knowledge of current density orientation and magnitude is very important. Minor changes in the cortical current density vector field might even strongly influence the decision with respect to placement of the electrodes and/or strength of stimulation [33, 142]. Therefore, using a geometry-adapted FE approach might substantially increase accuracy and reliability of tDCS simulation results and help to find optimized stimulation protocols. Current density amplitudes in the brain and CSF compartment were significantly reduced (up to 20 %) when using a geometry-adapted as compared to a regular hexahedral approach. Moreover, current density in the skin underneath the edges of the electrodes was decreased (up to 15 %). Thus, commonly-used regular hexahedral FE approaches [26, 28, 95] might overestimate current densities in the brain and in the skin underneath the electrodes. In Section 4.1 it is shown that strongest current densities always occur in the skin compartment underneath the edges of the electrodes, which might cause skin irritations or skin burn [104]. In summary, because skin and brain current magnitudes might have been overestimated in former regular hexahedral FE modeling studies, the proposed geometry-adapted approach suggests that higher stimulation magnitudes might be needed to accordingly modulate neural activity at brain level.

3.3. Iterative solvers for FEM-based tDCS

In this section, three iterative solver methods for tDCS are introduced and their numerical accuracy as well as their computational complexity are investigated and compared. Based on the results, an optimal solver method for efficient and accurate current density modeling in transcranial direct current stimulation is selected.

The variation of one stimulation parameter (inter-individual conductivity profile; location and/or size of the electrodes/coils; individual subject; multi-array tDCS or TMS array) leads to different FE equation systems which have to be solved to estimate the current flow fields. For algorithmic-based sensor optimization approaches, the number of forward calculations is given by $S-1$, where S is the number of surface electrodes [33]. Hence, for an extended 10-10 EEG electrode configuration with 74 electrodes, 73 large equation systems have to be solved. As the final goal in modeling brain stimulation techniques is to calculate optimized stimulation protocols for individual patients and their specific disease, the equation systems should be solved in a computationally efficient but accurate way.

In order to solve the large and sparse discretized FE equation system $\mathbf{K}\Phi = \boldsymbol{b}$ (here $\Phi^{tDCS} =: \Phi \in \mathbb{R}^N$), direct or preconditioned iterative solver methods can be used. While direct methods often lead to substantially lower numerical errors, their excessive memory consumption and computational burden for large equation systems are major drawbacks. On the contrary, iterative solver methods are rather cheap with respect to memory consumption and computational burden and even allow to automatically adapt to the new conditions in

each iteration step. For these reasons, an iterative solver method is used in this thesis. In the following section, the conjugate gradient (CG) iterative solver method, which is in the class of Krylov subspace methods, is shortly introduced. Further details and implementation issues for the CG method can be found in Nocedal and Wright [86] and Shewchuk [122]

3.3.1. Conjugate gradient iterative method

Let $\mathbf{K} \in \mathbb{R}^{N \times N}$ and $\boldsymbol{b} \in \mathbb{R}^N$ be the FE stiffness matrix and the right-hand side vector, respectively. The CG method minimizes the following quadratic minimization problem in an iterative way

$$f(\boldsymbol{x}) = \Phi^{tr}\mathbf{K}\Phi - \Phi^{tr}\boldsymbol{b} \tag{3.21}$$

whose minimum is also a unique solution to the linear equation system $\mathbf{K}\Phi = \boldsymbol{b}$

Lemma 3.3. Let Φ^* be a minimizer of the quadratic minimization problem 3.21 with $\mathbf{K}$ being the symmetric and positive definite stiffness matrix and $\boldsymbol{b}$ being the right-hand side vector. Then Φ^* is also a unique solution to the linear equation system $\mathbf{K}\Phi = \boldsymbol{b}$

Proof. Let Φ^* be a minimum of Equation 3.21, then by definition $\nabla f(\Phi^*) = 0$. Therefore

$$0 = \nabla f(\Phi^*) = \frac{1}{2}\mathbf{K}^{tr}\Phi^* + \frac{1}{2}\mathbf{K}\Phi^* - \boldsymbol{b}$$

Since $\mathbf{K}$ is symmetric (i.e. $\mathbf{K}^{tr} = \mathbf{K}$), the term $\frac{1}{2}\mathbf{K}^{tr}\Phi^* + \frac{1}{2}\mathbf{K}\Phi^*$ reduces to $\mathbf{K}\Phi^*$. This implies that a minimizer of Equation 3.21 is also a solution to the linear equation system $\mathbf{K}\Phi = \boldsymbol{b}$. The solution Φ^* is unique if the Hessian $H(f(\Phi^*)) = \mathbf{K}$ is positive. As $\mathbf{K}$ is positive-definite (i.e., $\Phi^{tr}\mathbf{K}\Phi > 0$) which implies that $\mathbf{K} > 0$, Φ^* is a unique solution to the linear equation system. □

The main idea of the CG method is to use a set of orthogonal vectors $\boldsymbol{d}_0, \ldots, \boldsymbol{d}_{n-1}$ and to consecutively scale the solution vector Φ in each iteration step. In this way, the solution is obtained after maximal n iteration steps.

The $i+1$-th iteration step of the CG method is defined as

$$\Phi_{i+1} = \Phi_i + \alpha_i d_i \tag{3.22}$$

with α_i to be defined in the following. In order to calculate α_i, two variables are introduced

- The error term $\boldsymbol{e}_i = \Phi_i - \Phi$
- The residual error $\boldsymbol{r}_i = \boldsymbol{b} - \mathbf{K}\Phi_i$

which can be used to obtain the following identities

$$\boldsymbol{r}_{i+1} = \boldsymbol{b} - \mathbf{K}\Phi_{i+1} = \boldsymbol{b} - \mathbf{K}(\boldsymbol{e}_{i+1} - \Phi) = \boldsymbol{b} - \mathbf{K}\boldsymbol{e}_{i+1} - \mathbf{K}\Phi = -\mathbf{K}\boldsymbol{e}_{i+1} \tag{3.23}$$

$$\boldsymbol{e}_{i+1} = \Phi_{i+1} - \Phi = \Phi_i + \alpha_i\boldsymbol{d}_i - \Phi = \boldsymbol{e}_i + \alpha_i\boldsymbol{d}_i \tag{3.24}$$

Note that $\boldsymbol{e}_{i+1}$ is orthogonal to $\boldsymbol{d}_i$ as the scaling vectors $\boldsymbol{d}_i$ are assumed to be orthogonal. Therefore

$$0 = \boldsymbol{d}_i^{tr}\boldsymbol{e}_{i+1} \overset{(3.24)}{=} \boldsymbol{d}_i^{tr}(\boldsymbol{e}_i + \alpha_i \boldsymbol{d}_i)$$

and α_i can be calculated as

$$\alpha_i = -\frac{\boldsymbol{d}_i^{tr}\boldsymbol{e}_i}{\boldsymbol{d}_i^{tr}\boldsymbol{d}_i}$$

The term α_i thus depends on the error term which implies that the exact solution Φ is needed to calculate the α_i. In order to calculate the scaling factors without knowing the exact solution vector Φ, the concept of *K-orthogonality* is introduced

Definition 3.2 (K-orthogonality [122])**.** The vector $\boldsymbol{d}_i$ and the error term $\boldsymbol{e}_j$ are called to be *K-orthogonal* or *conjugate*, if there exists a matrix $\mathbf{K}$ such that

$$\boldsymbol{d}_i^{tr}\mathbf{K}\boldsymbol{e}_j = 0$$

Let us now assume that $\boldsymbol{e}_{i+1}$ is $\mathbf{K}$-orthogonal to $\boldsymbol{d}_i$, i.e., $\boldsymbol{d}_i^{tr}\mathbf{K}\boldsymbol{e}_{i+1} = 0$. Then the following equation is fulfilled

$$0 = \boldsymbol{d}_i^{tr}\mathbf{K}\boldsymbol{e}_{i+1} = \boldsymbol{d}_i^{tr}\mathbf{K}(\boldsymbol{e}_i + \alpha_i \boldsymbol{d}_i)$$

and therefore

$$\alpha_i = -\frac{\boldsymbol{d}_i\mathbf{K}\boldsymbol{e}_i}{\boldsymbol{d}_i^{tr}\mathbf{K}\boldsymbol{d}_i} \overset{(3.23)}{=} \frac{\boldsymbol{d}_i\boldsymbol{r}_i}{\boldsymbol{d}_i^{tr}\mathbf{K}\boldsymbol{d}_i} \tag{3.25}$$

Therefore, only $\mathbf{K}$-orthogonal vectors $\boldsymbol{d}_i$ are required to calculate the scaling vectors α_i. In the following, the *Gram-Schmidt process* is used to calculate the $\mathbf{K}$-orthogonal vectors $\boldsymbol{d}_i$.

Let us assume linear independent vectors $\boldsymbol{v}_1, \ldots, \boldsymbol{v}_{n-1} \in \mathbb{R}^n$ and define $\boldsymbol{d}_0 = \boldsymbol{v}_0$. Then a $\mathbf{K}$-orthogonal system can be calculated in the following way

$$\boldsymbol{d}_i = \boldsymbol{v}_i + \sum_{k=0}^{n-1} \beta_{ik}\boldsymbol{d}_k \tag{3.26}$$

with β_{ik} to be derived in the following. The following equation can be derived

$$\boldsymbol{d}_i^{tr}\mathbf{K}\boldsymbol{d}_j \overset{(3.26)}{=} \boldsymbol{v}_i^{tr}\mathbf{K}\boldsymbol{d}_j + \sum_{k=0}^{n-1} \beta_{ik}\boldsymbol{d}_k^{tr}\mathbf{K}\boldsymbol{d}_j$$

Note that $\boldsymbol{d}_i$ is K-orthogonal for all $i < j$, i $\boldsymbol{d}_i^{tr}\mathbf{K}\boldsymbol{d}_j = 0$ for all $i < j$. Using this fact β_{ik} can be calculated as follows

$$\beta_{ik} = -\frac{\boldsymbol{v}_i^{tr}\mathbf{K}\boldsymbol{d}_k}{\boldsymbol{d}_j^{tr}\mathbf{K}\boldsymbol{d}_k} \tag{3.27}$$

This method is called the *method of conjugate directions*. In the following the method of conjugate directions is modified such that the number of iterations to calculate the β_{ik} is substantially reduced from $\mathcal{O}(n^2)$ to $\mathcal{O}(m)$ with m being the number of nonzero entries of $\mathbf{K}$ [122].

The conjugate gradient method uses the residuals $\boldsymbol{r}_i = \boldsymbol{b} - \mathbf{K}\Phi_i$ as linear independent vectors for the Gram-Schmidt process. The advantage of the residual $\boldsymbol{r}_i$ is that it is orthogonal to the directions $\boldsymbol{r}_j$ with $j < i$. Consequently, the new directions $\boldsymbol{d}_i$ are also orthogonal to $\boldsymbol{d}_j$ with $j < i$. Since the residual is orthogonal to the previous search directions, each residual is also orthogonal to the previous residuals, i.e., $\boldsymbol{r}_i^{tr}\boldsymbol{r}_j = 0$ for $i \neq j$. Let us now assume the n-dimensional subspace $\mathcal{D}_i = span\{r_0, \ldots, r_{n-1}\}$. It follows that each residual is a linear combination of the previous residuals and $\mathbf{K}\boldsymbol{d}_i$. Therefore, the subspace $\mathcal{D}_{i+1}$ can be defined as $\mathcal{D}_{i+1} = \mathcal{D}_i \cup \mathbf{K}D_i = \text{span}\ \{\boldsymbol{r}_0, \mathbf{K}\boldsymbol{r}_0, \ldots, \mathbf{K}^{n-1}\boldsymbol{r}_0\}$.

Definition 3.3 (Krylov subspace [45])**.** The subspace $\mathcal{D}_{i+1}$ is called a *Krylov subspace*. A subspace is called to be a n-th Krylov subspace $\mathcal{K}$ generated by a matrix $\mathbf{K} \in \mathbb{R}^{n\times n}$ and a vector $\boldsymbol{r} \in \mathbb{R}^n$ if

$$\mathcal{K} = span\{\boldsymbol{r}, \mathbf{K}^1\boldsymbol{r}, \ldots \mathbf{K}^{n-1}\boldsymbol{r}\}$$

Using the identity

$$\boldsymbol{r}_i^{tr}\boldsymbol{r}_{j+1} = \boldsymbol{r}_i^{tr}(\boldsymbol{r}_j - \alpha_j \boldsymbol{r}_i^{tr}\mathbf{K}\boldsymbol{d}_j)$$

the term $\boldsymbol{r}_i^{tr}\mathbf{K}\boldsymbol{d}_j$ can be calculated as follows

$$\boldsymbol{r}_i^{tr}\mathbf{K}\boldsymbol{d}_j = \begin{cases} \frac{1}{\alpha_i}\boldsymbol{r}_i^{tr}\boldsymbol{r}_i & \text{if } i = j \\ -\frac{1}{\alpha_{j-1}}\boldsymbol{r}_i^{tr}\boldsymbol{r}_i & \text{if } i = j+1 \\ 0 & \text{else} \end{cases}$$

and the β_{ij} can be calculated as:

$$\beta_{ij} \overset{(3.27)}{=} -\frac{\boldsymbol{v}_i^{tr}\mathbf{K}\boldsymbol{d}_j}{\boldsymbol{d}_j^{tr}\mathbf{K}\boldsymbol{d}_j} = \begin{cases} \frac{1}{\alpha_{i-1}}\frac{\boldsymbol{r}_i^{tr}\boldsymbol{r}_i}{\boldsymbol{d}_{i-1}^{tr}\mathbf{K}\boldsymbol{d}_{i-1}} & \text{if } i = j+1 \\ 0 & \text{i >j+1} \end{cases}$$

Using $\beta_i = \beta_{i(i-1)}$ and $\alpha = \frac{\boldsymbol{d}_i\boldsymbol{r}_i}{\boldsymbol{d}_i^{tr}\mathbf{K}\boldsymbol{d}_i}$, the following term can be derived for β_i

$$\beta_i = \frac{\boldsymbol{r}_i^{tr}\boldsymbol{r}_i}{\boldsymbol{d}_{i-1}^{tr}\boldsymbol{r}_{i-1}} = \frac{\boldsymbol{r}_i^{tr}\boldsymbol{r}_i}{\boldsymbol{r}_{i-1}\boldsymbol{r}_{i-1}}$$

One of the main advantages is that only the previous residual vectors $\boldsymbol{r}_j$ with $j < i$ are needed to calculate the new β_i. This procedure allows to calculate the β_i in a very efficient way. In order to enhance efficiency of the CG-method, three preconditioner methods for the CG-method are introduced.

3.3.2. Preconditioner methods

The accuracy of the simulation and the computational complexity of the CG method is coupled to the *condition number* of the stiffness matrix $\mathbf{K}$, which is defined as the ratio of the

Algorithm 1 Conjugate gradient iterative solver

Input: $\mathbf{K}, \boldsymbol{b}, \Phi_0, k_{max}, TOL, \boldsymbol{r}_{prev}$
$k = 0$
$\boldsymbol{d}_0 = \boldsymbol{r}_0 = \boldsymbol{b} - \mathbf{K}\Phi_0$
while $\|\boldsymbol{r}_k - \boldsymbol{r}_{prev}\| > TOL$ and $k < k_{max}$ **do**
  $\alpha_k = \frac{\boldsymbol{r}_k^{tr}\boldsymbol{r}_k}{\boldsymbol{d}_k\mathbf{K}\boldsymbol{d}_k}$
  $\Phi_{k+1} = \Phi_k + \alpha_k\boldsymbol{d}_k$
  $\boldsymbol{r}_{k+1} = \boldsymbol{r}_k - \alpha_k\mathbf{K}\boldsymbol{d}_k$
  $\beta_{k+1} = \frac{\boldsymbol{r}_{k+1}^{tr}\boldsymbol{r}_{k+1}}{\boldsymbol{r}_k^{tr}\boldsymbol{r}_k}$
  $\boldsymbol{d}_{k+1} = \boldsymbol{r}_{k+1} + \beta_{k+1}\boldsymbol{d}_k$
  $\boldsymbol{r}_{prev} = \boldsymbol{r}_{k+1}$
end while
return Φ

largest and smallest eigenvalues. For large condition numbers, the matrix $\mathbf{K}$ is called to be *ill-conditioned*. Large condition numbers lead to inaccurate simulation results and very slow residual convergence.

In EEG source analysis, large condition numbers of the order of 10^7 have been reported [71]. In order to reduce large condition numbers, a frequently-used approach is to introduce a preconditioner matrix $\mathbf{P} \in \mathbb{R}^{N\times N}$ such that the preconditioned matrix $\mathbf{P}^{-1}\mathbf{K}$ has a substantially smaller condition number for the preconditioned equation system $\mathbf{P}^{-1}\mathbf{K}\Phi = \mathbf{P}^{-1}\boldsymbol{b}$. The improved condition number for the preconditioned conjugate gradient method (PCG) is investigated in the following

Theorem 3.5 (Error estimate for PCG method [71])**.** Let $\mathbf{K}$ and $\mathbf{P}$ be positive definite matrices. Let Φ^* be the exact solution of $\mathbf{P}^{-1}\mathbf{K}\Phi^* = \mathbf{P}^{-1}\boldsymbol{b}$, then the k-th iterative of the PCG method Φ^k fulfills the following norm estimate

$$\left\|\Phi^k - \Phi^*\right\|_K \leq c^k \frac{2}{1+c^{2k}} \left\|\Phi^0 - \Phi^*\right\|_K \quad c := \frac{\sqrt{\kappa(\mathbf{P}^{-1}\mathbf{K})} - 1}{\sqrt{\kappa(\mathbf{P}^{-1}\mathbf{K})} + 1}$$

Proof. See Lew and colleagues [71], Theorem 2.1 and Hackbusch [46] Theorem 9.4.14. □

The objective of the next section is to investigate the efficacy and accuracy of incomplete Cholesky without fill-in (IC(0)), Jacobi and algebraic multigrid preconditioners for the conjugate gradient method. A very similar work was presented by Lew and colleagues [71], who investigated accuracy and run-time for different EEG forward approaches and three solver methods (IC(0)-CG, Jacobi-CG and AMG-CG).

3.3.2.1. Jacobi preconditioner

As only the diagonal elements of the stiffness matrix $\mathbf{K}$ are used as preconditioner (i.e., $\mathbf{P} = diag(\mathbf{K})$) the Jacobi-CG method is a very simple and cheap preconditioner. The Jacobi-CG is thus very efficient when the matrices are *diagonally dominant*. A matrix is called to be

diagonally dominant when every diagonal entry is larger than the sum of the non-diagonal entries in the corresponding row, i.e., $\sum_{i \neq j} |a_{ij}| \leq |a_{ii}| \quad \forall i$. When splitting the Jacobi preconditioner between left and right, the following equation system is solved with $\tilde{\mathbf{P}} = \sqrt{\mathbf{P}}$

$$\underbrace{\tilde{\mathbf{P}}^{-1}\mathbf{K}\tilde{\mathbf{P}}^{tr}}_{:=\tilde{\mathbf{K}}}\Phi = \tilde{\mathbf{P}}^{-1}\tilde{\mathbf{P}}^{tr}\boldsymbol{b}$$

The scaled stiffness matrix $\tilde{\mathbf{K}}$ is also SPD with unit diagonal entries, as row and column scaling preserves symmetry [71]. The improved condition number κ for the Jacobi-CG method is given in the following theorem

Theorem 3.6. Let $\mathbf{K}$ be the stiffness matrix and $\tilde{\mathbf{P}}$ be the Jacobi-preconditioner. Assume that each row of $\mathbf{K}$ does not contain more than d non-zero entries. Then the following error bound can be shown for all diagonal matrices $\mathbf{D}^{-1}$

$$\kappa(\mathbf{P}^{-1}\mathbf{K}) \leq d\kappa(\mathbf{D}^{-1}\mathbf{K})$$

Proof. See Lew and colleagues [71]. □

3.3.2.2. Incomplete Cholesky without fill-in preconditioner

The incomplete Cholesky preconditioner decomposes the stiffness matrix $\mathbf{K}$ into $\mathbf{K} = \mathbf{L}\mathbf{L}^{tr}$ where $\mathbf{L}$ is a lower triangular matrix [133]. Such a decomposition of $\mathbf{K}$, however would lead to a matrix $\mathbf{L}$ which is substantially less sparse as compared to $\mathbf{K}$. An Incomplete Cholesky preconditioner without fill-in (IC(0)-CG) is thus used, which is given as $\mathbf{K} \approx \mathbf{L}_0\mathbf{L}_0^{tr}$ with $\mathbf{L}_0$ being the Cholesky decomposition of the scaled stiffness matrix $\tilde{\mathbf{K}}$.

Remark 3.1. When splitting $\tilde{\mathbf{K}} = Id + \frac{1}{1+\eta}(E + E^{tr})$ with E being the strict lower triangular part of $\tilde{\mathbf{K}}$, the existence of a preconditioner is guaranteed for sufficient large values of η, see Lew and colleagues [71].

3.3.2.3. AMG preconditioner

A detailed introduction to the AMG-CG method can be found in Reitzinger and colleagues [105] and Lew and colleagues [71], who implemented their AMG method for numerical simulations of high-voltage insulators and for the EEG forward problem, respectively.

3.3.3. Results and Discussion

Numerical errors versus AMG-CG accuracy level

Figures 3.4 and 3.5 (left column) depict the numerical errors RDM and MAG versus AMG-CG solver accuracy levels (see Lew and colleagues [71] for further detials about the solver accuracy level) using the spherical shell models $tet503k$ and $gahex3.2m$, respectively. As shown in

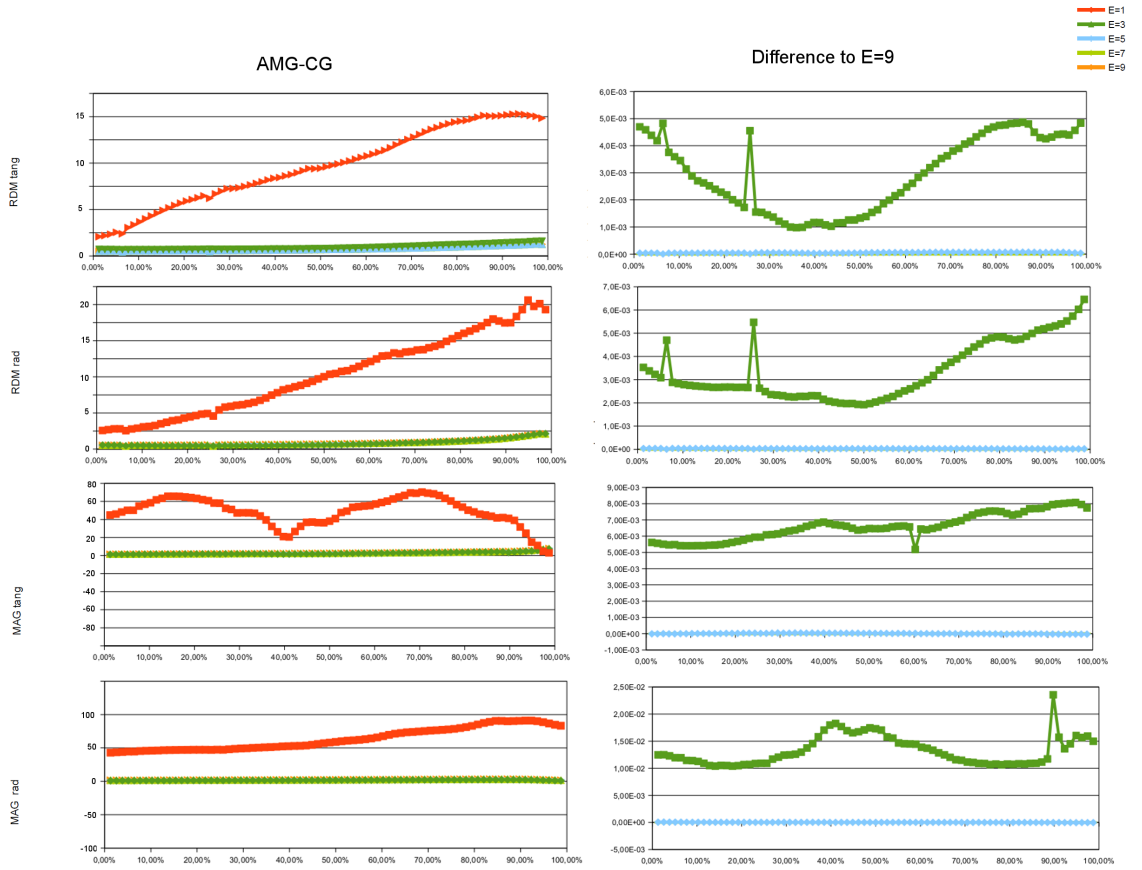

Figure 3.4.: Left column shows RDM (first and second row) and MAG (third and fourth row) errors versus vector eccentricity for AMG-CG accuracy levels of 10^{-1} = red, 10^{-3} = green, 10^{-5} = light blue, 10^{-7} = light green and 10^{-9} = orange, respectively, in model *tet*503*k*. Right column displays difference in RDM and MAG errors between the highest accuracy level (10^{-9}) and accuracy levels of 10^{-7}, 10^{-5} and 10^{-3}, respectively. Moreover, the first and third rows show the accuracy for tangential current flow vectors while the second and fourth rows depict the performance for radial current flow vectors, respectively.

Figures 3.4 and 3.5, identical RDM and MAG errors can be seen for AMG-CG accuracy levels of 10^{-7} and 10^{-9}, while substantially higher numerical errors can be seen for accuracy levels of 10^{-1} (up to a factor of 20) and 10^{-3} (up to a factor of 1.4). Moreover, only slightly higher numerical errors can be seen for an accuracy level of 10^{-5}. This holds true for the tetrahedral model *tet*503*k* (Figure 3.4) and the geometry-adapted hexahedral model *gahex*3.2*m* (Figure 3.5). An AMG-CG accuracy level of 10^{-7} is thus sufficient to receive accurate simulation results.

Numerical errors versus preconditioner method

In this section, the numerical performance of the preconditioner methods IC(0), Jacobi and AMG for the conjugate gradient method are investigated. As was shown before, an AMG-CG solver accuracy level of 10^{-7} is sufficient to obtain accurate simulation results and is thus taken as reference solver for this comparison. In order to allow direct comparison of the

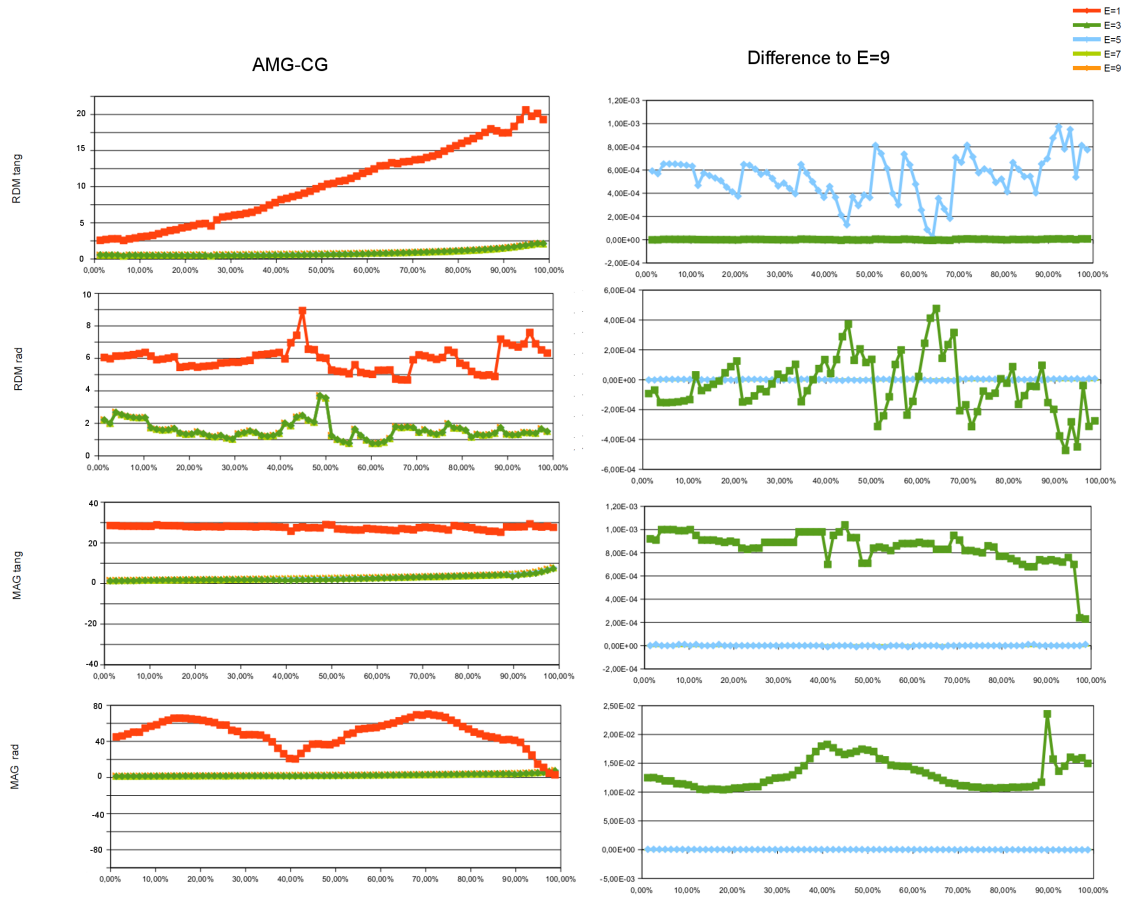

Figure 3.5.: Left column shows RDM (first and second row) and MAG (third and fourth row) errors versus vector eccentricity for AMG-CG accuracy levels of 10^{-1} = red, 10^{-3} = green, 10^{-5} = light blue, 10^{-7} = light green and 10^{-9} = orange, respectively, in model *gahex*3.2*m*. Right column displays difference in RDM and MAG errors between the highest accuracy level (10^{-9}) and the accuracy levels of 10^{-7}, 10^{-5} and 10^{-3}, respectively. Moreover, the first and third rows show the accuracy for tangential current flow vectors while the second and fourth rows depict the performance for radial current flow vectors, respectively.

numerical errors, solver accuracy levels of 10^{-7} are also used for the solver methods IC(0)-CG and Jacobi-CG. Figures 3.6 and 3.7 depict the numerical errors RDM and MAG for the three preconditioner methods. As can be seen in the figures, all three preconditioner methods show identical RDM and MAG errors. This holds true for the tetrahedral spherical shell model *tet*503*k* and the geometry-adapted hexahedral model *gahex*3.2*m*.

Solver time versus AMG-CG accuracy level

A further important aspect in simulation studies is computational efficiency. Table 3.2 depicts the averaged solver time (sec.) over 1496 simulated electrode configurations for AMG-CG solver accuracy levels of $10^{-1}, \ldots, 10^{-9}$. As can be seen, the higher the AMG-CG solver accuracy level, the higher the averaged solver time. This holds true for both, the tetrahedral sphere model *tet*503*k* and the geometry-adapted hexahedral sphere model *gahex*3.2*m*. The accuracy level should thus be as low as possible in order to allow a fast and efficient computation of

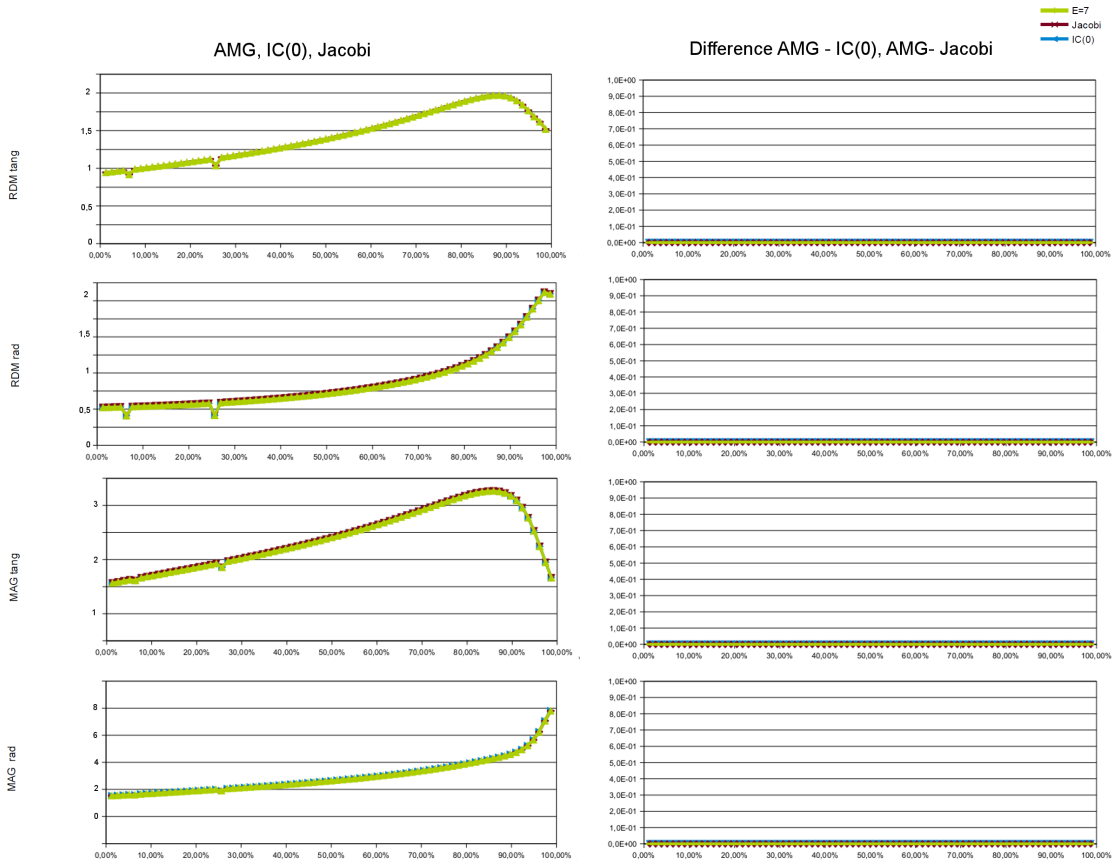

Figure 3.6.: Left column shows RDM (first and second row) and MAG (third and fourth row) errors versus vector eccentricity for AMG-CG (light green), the IC(0)-CG (dark red) and the Jacobi-CG (blue) methods with an accuracy level of 10^{-7}, respectively, in model $tet503k$. Right column displays difference in RDM and MAG errors between the AMG-CG solver and the IC(0)-CG and the Jacobi-CG methods. Moreover, the first and third rows show the accuracy for tangential current flow vectors while the second and fourth rows depict the performance for radial current flow vectors, respectively.

the solution to the linear equation system $\mathbf{K}\Phi = \boldsymbol{b}$. On the other hand, the numerical errors should be as low as possible in order to achieve as high as possible solver accuracy. As both accuracy levels of 10^{-7} and 10^{-9} lead to identical numerical accuracies, a solver accuracy level of 10^{-7} is sufficient to receive accurate, fast and robust simulation results.

Solver time versus preconditioner method

In a last investigation, the solver clock time versus preconditioner methods AMG, Jacobi and IC(0) for the conjugate gradient method is investigated. Table 3.3 depicts the average solver time (sec.) over 1496 stimulated electrode configurations using the spherical shell models $tet503k$ and $gahex3.2m$, respectively. Again, an accuracy level of 10^{-7} is used for all solver methods. While the numerical performance of all three solver methods is identical, the solver clock time substantially differs between them. In all models, the AMG-CG method is the fastest solver, followed by the IC(0)-CG method and the Jacobi-CG method is the slowest solver. The AMG-CG solver thus turns out to be more efficient with regard to time

Figure 3.7.: Left column shows RDM (first and second row) and MAG (third and fourth row) errors versus vector eccentricity for AMG-CG (light green), the IC(0)-CG (dark red) and the Jacobi-CG (blue) methods, respectively, in model *gahex*3.2*m*. Right column displays difference in RDM and MAG errors between the AMG-CG solver and the IC(0)-CG and the Jacobi-CG methods. Moreover, the first and third rows show the accuracy for tangential current flow vectors while the second and fourth rows depict the performance for radial current flow vectors, respectively.

Table 3.2.: Average solver time (sec.) over all simulated electrode configurations (1496) for spherical shell models *tet*503*k* and *gahex*3.2*m*. AMG-CG accuracy levels of 10^{-1}, 10^{-3}, 10^{-5}, 10^{-7} and 10^{-9} are employed.

	Sphere models	
Solver accuracy level	*tet*503*k*	*gahex*3.2*m*
10^{-1}	1.78	17.73
10^{-3}	4.64	40.17
10^{-5}	5.78	70.41
10^{-7}	8.52	112.53
10^{-9}	10.19	144.728

requirements as compared to the IC(0)-CG and Jacobi-CG solver methods.

Table 3.3.: Average solver time (sec.) over all simulated electrode configurations (1496) for spherical shell models $tet503k$ and $gahex3.2m$ for the AMG-CG, Jacobi-CG and IC(0)-CG, respectively.

	Head model	
Solver method	$tet503k$	$gahex3.2m$
AMG-CG	8.52	112.53
IC(0)-CG	17.42	230.79
Jacobi-CG	22.14	261.48

Guideline for fast and efficient solver method

In this study, numerical accuracy and efficiency for the Jacobi, IC(0) and AMG preconditioner methods for the conjugate gradient method were studied. The numerical errors RDM and MAG were investigated and a solver accuracy level of 10^{-7} was shown to be sufficient to obtain an accurate numerical accuracy for the three solver methods. However, the investigation of the solver clock time revealed that the AMG-CG solver outperformed the Jacobi-CG and IC(0)-CG solvers with regard to computational efficacy.

Because a similar sparse equation system $\mathbf{K}\Phi = \boldsymbol{b}$ with a different right-hand side vector has to be solved in TMS modeling, the main findings of this investigation are also valid for TMS. Therefore, it is recommendable to use an AMG-CG solver method with solver accuracy level of 10^{-7} to solve the large sparse equation system in TMS and tDCS modeling.

3.4. A complete electrode model for tDCS

In the here developed geometry-adapted modeling pipeline for tDCS, the contact impedance of the electrodes and the contact impedance between electrode and skin tissue was not modeled. As the shunting currents between electrodes and skin can affect the current density distribution, a complete electrode model [100] might be useful for tDCS. In this respect, a complete electrode model could increase accuracy of the simulation, especially in the skin and electrode compartments. This might be especially important for a combination of EEG measurement and transcranial alternating current stimulation, where the stimulation artefact has to be filtered from the raw EEG signal before evaluation. The complete electrode model for tDCS is very similar to the one that is used in electrical impedance tomography (EIT). In EIT, a set of electrodes is attached to a surface of a device and an alternating current is injected to some of the electrodes. Moreover, the potential differences between the other electrodes are measured simultaneously. This principle can be used to estimate the conductivities of certain tissue compartments or to reconstruct the surfaces of objects.

The complete electrode model for tDCS consists of a Laplace equation with inhomogeneous

Neumann boundary conditions

$$\begin{aligned} \nabla \cdot \sigma \nabla \Phi &= 0 \qquad && \boldsymbol{x} \in \Omega && (3.28)\\ \int_{e_l} \langle \sigma \nabla \Phi, \boldsymbol{n} \rangle \, \mathrm{d}\boldsymbol{x} &= \boldsymbol{I}_l \qquad && \boldsymbol{x} \in e_l, l = 1, \ldots, L && (3.29)\\ \Phi + Z_l \langle \sigma \nabla \Phi, \boldsymbol{n} \rangle &= U_l \qquad && \boldsymbol{x} \in e_l, l = 1, \ldots, L && (3.30)\\ \langle \sigma \nabla \Phi, \boldsymbol{n} \rangle &= 0 \qquad && \boldsymbol{x} \in \Gamma \setminus \bigcup_{l=1}^{L} e_l && (3.31) \end{aligned}$$

with Z_l being the contact impedance between the l-th electrode and the skin tissue. Here Φ describes the potential distribution in the whole volume conductor model and U_l the potential at the fixed electrodes. The following two equations are required to ensure the existence of a unique solution (compatibility condition has to be fulfilled)

$$\sum_{l=1}^{L} \boldsymbol{I}_l = 0 \qquad \text{and} \qquad \sum_{l=1}^{L} U_l = 0$$

The existence and uniqueness of a solution $(\tilde{\Phi}, U_l)$ to Equations (3.28) - (3.31) was shown by Somersalo and colleagues [128].

For numerical realization, let $v \in H^1(\Omega)$ be a test function and $V_l \in \mathbb{R}^L$ be a constant. Equation (3.28) is multiplied with $v \in H^1(\Omega)$ and integrated over Ω

$$\begin{aligned} & \int_\Omega \nabla \cdot \sigma \nabla \Phi v \, \mathrm{d}\boldsymbol{x} = 0 \\ \Leftrightarrow \quad & -\int_\Omega \langle \sigma \nabla \Phi, \nabla v \rangle \, \mathrm{d}\boldsymbol{x} + \int_\Gamma \langle \sigma \nabla \Phi, \boldsymbol{n} \rangle v \, \mathrm{d}\boldsymbol{x} = 0 \\ \Leftrightarrow \quad & -\int_\Omega \langle \sigma \nabla \Phi, \nabla v \rangle \, \mathrm{d}\boldsymbol{x} + \sum_{l=1}^{L} \int_{e_l} \langle \sigma \nabla \Phi, \boldsymbol{n} \rangle v \, \mathrm{d}\boldsymbol{x} = 0 \\ \overset{(3.30)}{\Leftrightarrow} \quad & -\int_\Omega \langle \sigma \nabla \Phi, \nabla v \rangle \, \mathrm{d}\boldsymbol{x} + \sum_{l=1}^{L} \int_{e_l} \frac{1}{Z_l} (U_l - \Phi) v \, \mathrm{d}\boldsymbol{x} = 0 \\ \Leftrightarrow \quad & -\int_\Omega \langle \sigma \nabla \Phi, \nabla v \rangle \, \mathrm{d}\boldsymbol{x} + \sum_{l=1}^{L} \int_{e_l} \frac{1}{Z_l} (U_l - \Phi)(v - V_l) \, \mathrm{d}\boldsymbol{x} = -\sum_{l=1}^{L} I_l V_l \\ \Leftrightarrow \quad & +\int_\Omega \langle \sigma \nabla \Phi, \nabla v \rangle \, \mathrm{d}\boldsymbol{x} + \sum_{l=1}^{L} \int_{e_l} \frac{1}{Z_l} (\Phi - U_l)(v - V_l) \, \mathrm{d}\boldsymbol{x} = \sum_{l=1}^{L} I_l V_l \end{aligned}$$

where the boundary conditions (3.29) and (3.30) are used to obtain the following identities

$$\begin{aligned} \int_{e_l} \langle \sigma \nabla \Phi, \boldsymbol{n} \rangle \mathrm{d}\boldsymbol{x} &= \int_{e_l} \frac{1}{Z_l} (U_l - \Phi) \, \mathrm{d}\boldsymbol{x} && (3.32)\\ \sum_{l=1}^{L} \frac{1}{Z_l} \int_{e_l} (U_l - \Phi) V_l \, \mathrm{d}\boldsymbol{x} &= \sum_{l=1}^{L} I_l V_l && (3.33) \end{aligned}$$

Using the Ritz-Galerkin method and defining $\Phi = \sum_{i=1}^{N} z_i \phi_i$ leads to

$$\begin{aligned}\sum_{i=1}^{N}\Big(\int_\Omega \langle \sigma \nabla \phi_i, \nabla v\rangle \,\mathrm{d}\boldsymbol{x} \quad &+ \quad \sum_{l=1}^{L}\int_{e_l}\frac{1}{Z_l}\phi_i v \,\mathrm{d}\boldsymbol{x}\Big) z_i \\ &- \quad \sum_{i=1}^{N}\sum_{l=1}^{L}\int_{e_l}\frac{1}{Z_l}(\phi_i V_l + U_l v + U_l V_l)\,\mathrm{d}\boldsymbol{x} - \sum_{l=1}^{L} I_l V_l = 0\end{aligned}$$

$$\overset{(3.33)}{\Leftrightarrow} \sum_{i=1}^{N}\Big(\int_\Omega \langle \sigma \nabla \phi_i, \nabla v\rangle \,\mathrm{d}\boldsymbol{x} + \sum_{l=1}^{L}\int_{e_l}\frac{1}{Z_l}\phi v \,\mathrm{d}\boldsymbol{x}\Big) z_i - \sum_{l=1}^{L}\int_{e_l}\frac{1}{Z_l} U_l v \,\mathrm{d}\boldsymbol{x} = 0$$

Using $v = \phi_j$ for $j = 1, \ldots, N$, the following system has to be solved

$$\sum_{i,j=1}^{N}\Big(\int_\Omega \langle \sigma \nabla \phi_i, \nabla \phi_j\rangle \,\mathrm{d}\boldsymbol{x} + \sum_{l=1}^{L}\int_{e_l}\frac{1}{Z_l}\phi_i\phi_j \,\mathrm{d}\boldsymbol{x}\Big) z_i - \sum_{l=1}^{L}\Big(\sum_{j=1}^{N}\int_{e_l}\frac{1}{Z_l}\phi_j \,\mathrm{d}\boldsymbol{x}\Big) U_l = 0 \tag{3.34}$$

Moreover, the following equation can be derived from the boundary conditions

$$I_l = \sum_{i=1}^{N}\int_{e_l}\frac{1}{Z_l}(U_l - \phi_i)\,\mathrm{d}\boldsymbol{x} = \frac{1}{Z_l}U_l|e_l| - \sum_{i=1}^{N}\Big(\int_{e_l}\frac{1}{Z_l}\phi_i \,\mathrm{d}\boldsymbol{x}\Big) z_i,\ l = 1, \ldots, L \tag{3.35}$$

Using Equations 3.34 and 3.35 and defining vectors $\boldsymbol{u} = (U_1, \ldots, U_L) \in \mathbb{R}^L$, $\boldsymbol{z} = (z_1, \ldots, z_N) \in \mathbb{R}^N$ and $\boldsymbol{I} = (I_1, \ldots, I_L)\mathbb{R}^L$ the vectors $\boldsymbol{u}$ and $\boldsymbol{z}$ are coupled through the linear matrix equation

$$\begin{pmatrix} \boldsymbol{A} & \boldsymbol{B} \\ \boldsymbol{B}^{tr} & \boldsymbol{C} \end{pmatrix} \begin{pmatrix} \boldsymbol{z} \\ \boldsymbol{u} \end{pmatrix} = \begin{pmatrix} 0 \\ \boldsymbol{I} \end{pmatrix}$$

with $\boldsymbol{A} \in \mathbb{R}^{N\times N}$, $\boldsymbol{B} \in \mathbb{R}^{N\times L}$ and $\boldsymbol{C} \in \mathbb{R}^{L\times L}$ defined as

$$\begin{aligned}
\boldsymbol{A}(i,j) &= \int_\Omega \langle \sigma \nabla \phi_i, \nabla \phi_j\rangle \,\mathrm{d}\boldsymbol{x} + \sum_{l=1}^{L}\int_{e_l}\frac{1}{Z_l}\phi_i\phi_j \,\mathrm{d}\boldsymbol{x}, && i,j = 1, \ldots, N \\
\boldsymbol{B}(i,l) &= \int_{e_l}\frac{1}{Z_l}\phi_i \,\mathrm{d}\boldsymbol{x} && i = 1, \ldots, N,\ l = 1, \ldots, L \\
\boldsymbol{C}(s,l) &= \begin{cases} \frac{1}{Z_l}|e_l|, & \text{if } s = l \\ 0, & \text{else} \end{cases}, && s,l = 1, \ldots, L
\end{aligned}$$

This matrix equation system leads to the following solutions for $\boldsymbol{u}$ and $\boldsymbol{z}$

$$\begin{aligned}\boldsymbol{u} &= (-\boldsymbol{B}^{tr}\boldsymbol{A}^{-1}\boldsymbol{B} + \boldsymbol{C})^{-1}\boldsymbol{I} \\ \boldsymbol{z} &= (\boldsymbol{B}^{tr} - \boldsymbol{C}\boldsymbol{B}^{-1}\boldsymbol{A})^{-1}\boldsymbol{I}\end{aligned}$$

The objective of this study is to investigate the CEM-based current density distribution $\sigma\boldsymbol{z}$ and to compare it to the PEM-based simulation method for transcranial direct current stimulation. A highly-realistic five-compartment (skin, skull compacta, skull spongiosa, CSF, and brain

tissue) tetrahedral finite element head model is used and the complete electrode model for tDCS is employed. An anodal current of 1 mA is injected at a round-shaped electrode with a diameter of 1.2 cm located above the left auditory cortex and removed at a round-shaped electrode with a diameter of 1.2 cm located above the right auditory cortex. In order to allow simultaneous EEG measurements, 74 EEG scalp electrodes with a diameter of 1.2 cm are centered at the locations of an extended 10-10 EEG system.

Results

Figures 3.8 and 3.9 depict the CEM-based and PEM-based current density distributions in the whole model and only in the brain compartment, respectively. As can be seen in Figures 3.8-A1 and 3.8-B1 and Figures 3.9-A1 and 3.9-B1, the CEM-based and PEM-based current flow fields are very similar. For both vector fields, a peak current density of 2.1 Am^{-2} can be observed in the skin compartment underneath the edges of the stimulating electrodes. A large amount of the current density is tangentially conducted along the scalp from the anode to the cathode. The currents that enter the skull flow mainly radially in compacta and slightly more tangentially in spongiosa. After penetrating the low-conductive skull compartments, a large amount of the current is channeled along the highly-conductive CSF compartments towards farther away brain areas in the direction of the cathode. Current vectors in white matter regions close to the cortex tend to be oriented towards the more conductive cortical tissue close-by. The peak current density in the brain is 0.054 Am^{-2}, see Figures 3.9-A1 and 3.9-B1.

The resulting current flow field orientation and magnitude changes between the CEM-based and PEM-based current flow fields are shown in Figures 3.8-A2 and 3.8-B2 (3.9-A2 and 3.9-B2 only in the brain compartment). Very low changes in orientation up to 0.88 degrees can be seen in the skin and skull compacta compartments, especially underneath the electrodes, while hardly any change in orientation can be seen in the CSF and brain compartments. In the brain, tiny modifications with regard to orientation (up to 0.022 degrees) are found in superficial cortical regions, while no change in orientation can be seen in deeper white matter structures, see Figures 3.8-A2 and 3.9-A2. The magnitude difference between the CEM-based and PEM-based current density is depicted in Figures 3.8-B2 and 3.9-B2. The factor shows the deviation (in %) between the PEM-based and CEM-based current density amplitudes. While a positive value (> 0) indicates that the PEM-based current density amplitude is bigger, a negative value (< 0) shows that the CEM-based current density amplitude is bigger. In the skull, CSF and brain compartments hardly any change in current density amplitude can be seen between both current flow fields, see Figure 3.8-B2. In the skin compartment, both areas with increased (up to 1.12 %) and decreased (up to 1.11 %) current density amplitude can be seen. This indicates that the CEM-based current density decreases underneath the measuring EEG electrodes and increases at the edges of the electrodes.

The CEM-based and PEM-based current flow field orientation and magnitude differences are one order of magnitude smaller as compared to the numerical errors of the FEM-based tDCS forward approach (Section 3.2). These results showed that with regard to the current flow

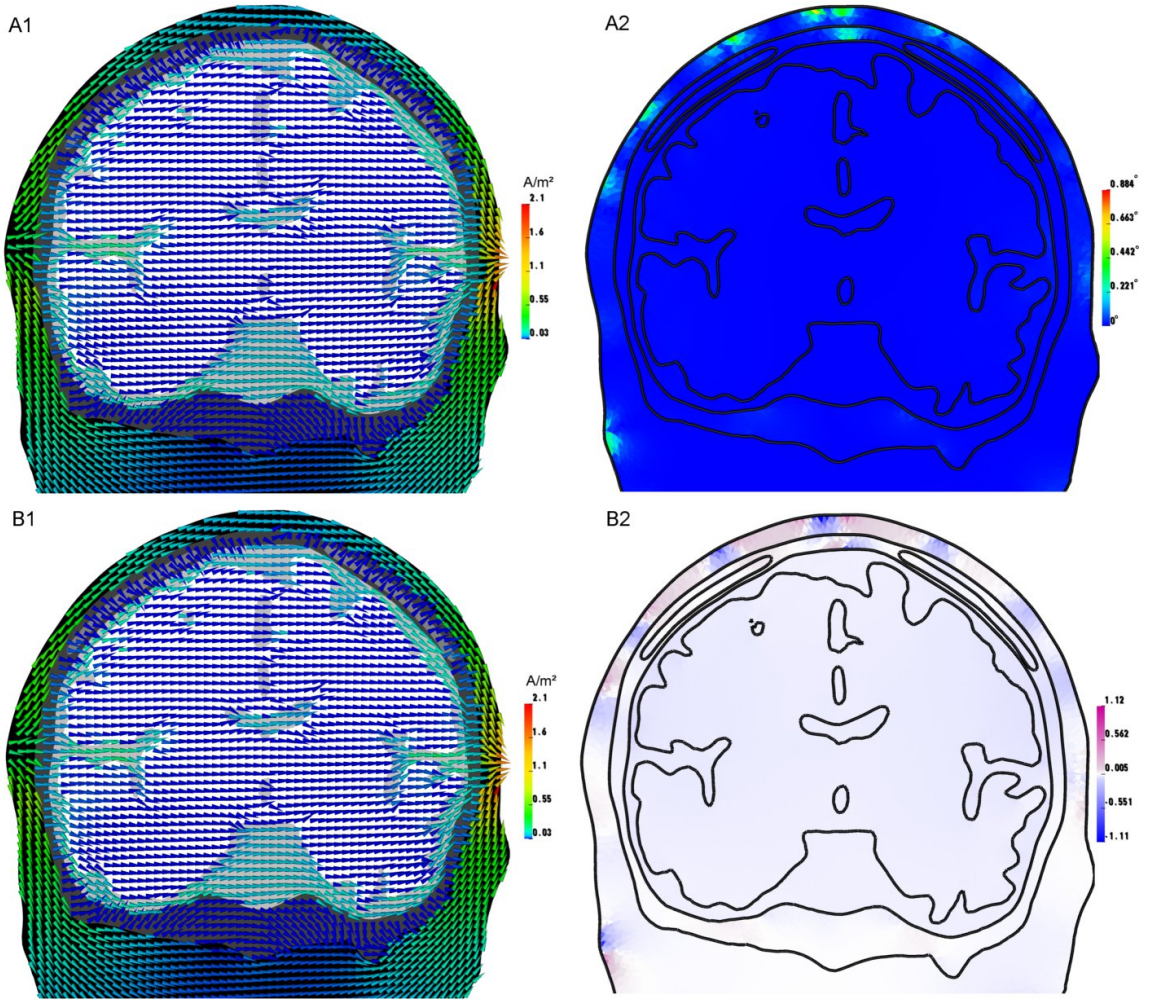

Figure 3.8.: CEM- (-A1) and PEM-based (-B1) current density distribution on a coronal slice through the model. The top right (-A2) and top bottom (-B2) figures display change in orientation and magnitude between the CEM-based and the PEM-based current density distributions. The color scale in the top figure shows changes in orientation, while the color scale in the bottom figure displays the deviation (in %) between the PEM-based and CEM-based current density amplitudes.

field calculation for standard bipolar electrode montages or multi-array stimulation devices, the standard PEM is a sufficiently accurate model.

For simultaneous tDCS/tACS stimulations and EEG measurements, however, the CEM can be a promising method and might outperform the PEM-based modeling pipeline. As can be seen in Figure 3.8, a bipolar stimulation with 1 mA leads to current flow field amplitudes between 0.2 Am^{-2} and 2.1 Am^{-2} in the skin compartment. Taking into account the minimal cortical current source strength of about 10 nAm required to induce electric fields which can be measured by the EEG electrodes, the small difference below 1 % between the CEM-based and PEM-based current flow fields in the skin compartment field might be highly significant. In order to investigate this issue, two sources in the auditory cortices with a source strength of 10 nAm are simulated and differences in CEM-based and PEM-based potential fields at the measurement EEG electrodes are investigated. Potential field amplitudes between −42.7 mV and 42.8 mV can be measured at the EEG scalp electrodes for the two sources in the auditory

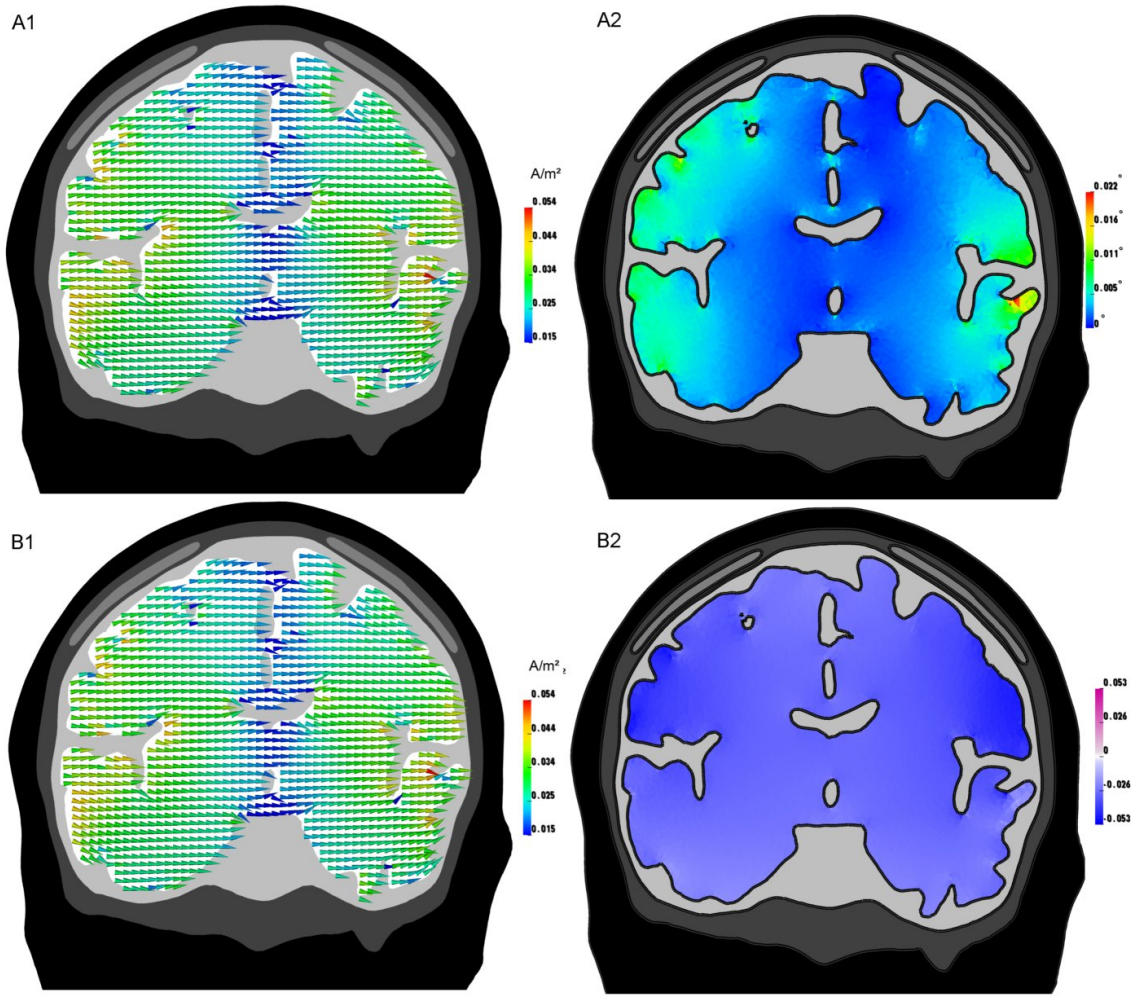

Figure 3.9.: CEM- (-A1) and PEM-based brain current density distribution (-B1) on a coronal slice through the model. The top right (-A2) and top bottom (-B2) figures display change in orientation and magnitude between the CEM-based and the PEM-based current density distributions. The color scale for the top figure shows changes in orientation, while the color scale in the bottom figure displays the deviation (in %) between the PEM-based and CEM-based current density amplitudes.

cortices (not shown here). In a next step, the difference between the CEM-based and PEM-based potential fields at the measurement electrodes divided by the strength of the sources in the auditory cortices is investigated. With difference values above 70 %, the difference between the CEM-based and PEM-based potential fields is thus substantially higher as compared to the numerical errors of the modeling approaches. In conclusion, the results clearly indicated that with regard to the tDCS forward computation, the PEM-based modeling pipeline is a sufficiently accurate model. However, for simultaneous tDCS/tACS stimulations and EEG measurements, the CEM-based forward problem clearly outperforms the simple PEM-based modeling approach and should thus be used. This work has been conducted with Britte Agsten, University of Münster [1].

4

Simulation studies for transcranial direct current stimulation

4.1. tDCS volume conduction effects

During this thesis, a simulation study for transcranial direct current stimulation was conducted as first and corresponding author. In this section, the most important results of this study and a discussion with existing literature are presented. Many parts are directly transferred from the original publication with some additional parts that have been added. Further results of this simulation study can be found in the original publication, see Wagner and colleagues [142].

The objective of this study was to provide insight into the sophisticated interplay between stimulation and the induced current density distribution in the individual subject. Furthermore, the sensitivity of the current density in the brain towards the most important tissue compartments to be modeled in tDCS computer simulation studies was investigated. For this reason, a low-parametric three compartment finite element head model (skin, skull, brain) which constitutes a simplification of the brain anatomy was evaluated. In further steps, this head model was extended step-by-step to a more realistic six-compartment FE head model (skin, skull compacta, skull spongiosa, CSF, gray and white matter) with white matter anisotropy. In each consecutive step, the effects of the increased accuracy of the volume conductor model on the tDCS current density distribution was investigated by quantifying the current orientation and magnitude changes. Along this line, the influence of each individual tissue compartment was analyzed, providing a deeper insight into volume conduction effects in transcranial direct current stimulation. It was thus investigated which tissue compartments

are important to be modeled in tDCS computer simulation studies. Keeping this in mind, a guideline for efficient yet accurate volume conductor modeling in tDCS was presented.

Two commonly-used bipolar electrode montages for targeting the auditory cortex and the motor cortex were used to investigate volume conduction effects in tDCS. Each bipolar electrode montage consisted of two sponge-like rubber electrodes with a commonly used size of $5\,\text{cm} \times 7\,\text{cm}$, thickness of $4\,\text{mm}$ and saline-like conductivity of $1.4\,\text{Sm}^{-1}$ attached to the scalp [85, 155].

4.1.1. Methods

A highly realistic geometry-adapted hexahedral finite element head model consisting of six compartments (skin, skull spongiosa, skull compacta, CSF, gray and white matter) and white matter anisotropy is generated following the newly-invented pipeline as presented in Section 2.5. As the aim of this study is to investigate volume conduction effects in tDCS, a step-by-step approach is used and a set of simplified head models is introduced. Each simplified head model is generated by re-labeling tissue compartments, i.e., the three-compartment head model relabels the CSF, gray matter and white matter compartments to a single brain compartment and the skull compacta and spongiosa to an isotropic skull compartment.

Setup of the step-by-step approach

The model labels represent the number of compartments and whether isotropic or anisotropic conductivity profiles (I for isotropic, A for anisotropic white matter) are used (e.g., 3CI is used for the three-compartment head model with isotropic conductivities).

Three-compartment isotropic head model (3CI)

The standard three-compartment head model 3CI [91, 108] consists of the isotropic compartments skin, skull and brain. Classically, the scalp is defined as the outermost compartment while the skull is defined as the region between the scalp and the interior skull boundary. The brain is specified as the region inside the interior skull boundary. For the compartments skin, skull and brain, isotropic conductivity values of $0.43\,\text{Sm}^{-1}$, $0.001\,\text{Sm}^{-1}$ and $0.33\,\text{Sm}^{-1}$ are selected [142]. The conductivity value of the skull is chosen both to be in the range of the conductivity values that best approximate the three-layered structure [2] of the human skull [25] and to be identical to the conductivity value that was used in previous tDCS simulation studies [27, 33, 144].

Four compartment head model (4CI)

In a first step, the isotropic skull compartment is split into compact and spongy bone. Akhtari and colleagues [2] performed physical measurements with excised human skull fragments and reported that the spongy bone is in average 3.6 times more conductive than the compact bone (with a maximal factor of 8.2). Based on the physical measurement of Akhtari and colleagues

[2], conductivity values of $0.025\,\mathrm{Sm}^{-1}$ and $0.007\,\mathrm{Sm}^{-1}$ are thus used for skull compacta and spongiosa, respectively.

Five compartment head model (5CI)

In a next step, the brain compartment is split into brain proper and CSF. The conductivity of human CSF at body temperature was measured by Baumann and colleagues [8] to be $1.79\,\mathrm{Sm}^{-1}$ (average over 7 subjects, ranging in age from 4.5 months to 70 years, with a standard deviation of less than 2.4 % between subjects and for frequencies between 10 and 10.000 Hz) which is to be used in head model 5CI. A conductivity value of $1.79\,\mathrm{Sm}^{-1}$ for the CSF compartment was also used in the tDCS simulation study of Salvador and colleagues [116].

Six compartment head model (6CI)

The homogenized brain proper compartment is split into brain gray matter and white matter. For brain gray and white matter, isotropic conductivity values of $0.33\,\mathrm{Sm}^{-1}$ and $0.14\,\mathrm{Sm}^{-1}$ are used [102].

Six compartment head model with white matter anisotropy (6CA)

In a last step, white matter anisotropy is added to model 6CI. Similar to Rullmann and colleagues [110], the effective medium approach [134] results in a mean conductivity value of $0.14\,\mathrm{Sm}^{-1}$ for the white matter compartment (see [110], Table 2, here scaling factor s = 0.254). The 6CA model is thus the most realistic model used in this tDCS computer simulation study.

Localization of auditory and motor cortex

For appropriate electrode placement, the auditory and motor cortex of the subject of this study is localized using combined 74-channel EEG and 274-channel MEG experiments. The localization results are thus used to define the target areas for auditory and motor cortex stimulation and to position the center of the electrodes (see further description below and Figures 4.1-A2,A3 and Figure A.1-A2,A3 in the appendix). Furthermore, the location of the coronal cut planes for visualization of the stimulation results (see Figures 4.1, 4.2, A.1 and A.3) are selected based on the localization results.

In order to define the target areas for auditory cortex stimulation, a source analysis of the measured auditory evoked fields and auditory evoked potentials is performed: 350 Hz sinusoidal tones with 800 ms duration and a stimulus onset asynchrony (SOA) of 3.5 s - 4.5 s to avoid habituation are presented, overall 120 trials. After preprocessing, the dipole solution for the auditory N1 component is calculated from the averaged AEF and AEP using CURRY.

The central sulcus is a prominent landmark of the brain, separating the primary motor cortex from the primary somatosensory cortex. For the localization of the central sulcus, somatosensory evoked field data of the subject are used. The medianus nerve is stimulated with 0.5 ms square pulses applied from two surface electrodes. The amplitude is increased until a clear movement of the thumb is observed. An SOA randomized between 350 and

450 ms is used to avoid habituation and 950 trials are measured. After preprocessing and averaging of the SEF data, a source analysis for the localization of the somatosensory N20 component at the posterior wall of the central sulcus is performed using CURRY. The motor cortex is then determined at the nearby anterior wall of the central sulcus.

Modeling of stimulating electrodes

For the modeling of the stimulating electrodes, two rectangular sponge-like rubber patches with a commonly used size of 7 cm × 5 cm, thickness of 4 mm and saline-like conductivity of $1.4\,\mathrm{Sm}^{-1}$ are used, in line with [26, 114]. This bipolar electrode montage is referred to as the *standard tDCS montage* in this thesis. A total current of 1 mA is applied to the anode. To simulate auditory cortex stimulation, the electrodes are positioned symmetrically around the localized auditory cortices (above the area of the TP9, TP10, P7, P8, T7, T8, CP5 and CP6 electrodes using a 10/10 EEG system). The location of the tDCS electrodes for auditory cortex stimulation can be seen in Figures 4.1-A2 and 4.1-A3. To simulate motor cortex stimulation, the anode is placed above the primary motor cortex (M1) and the cathode above the right eyebrow [84]. The standard tDCS electrode montage for motor cortex stimulation is shown in Figures A.1-A2 and A.1-A3.

Visualization of current density vector fields

For the visualization of the current density, size-normalized cones are used to represent current flow orientation and their color-code is used to present current density amplitude. As the full resolution vector fields are too fine to be visualized over the whole cut plane, sub-sampled versions of the current flow field, where only the middle cone of each 4 mm × 4 mm block is visualized (see Figures 4.1 and 4.2, left column), are presented. Moreover, the change in orientation Ang (degree) and magnitude Mag (factor) is calculated for each incorporated feature (see Figures 4.1 and 4.2, second and third column) as

$$Ang(i) = \arccos \frac{< \boldsymbol{J}_1(i), \boldsymbol{J}_2(i) >}{\|\boldsymbol{J}_1(i)\|_2 \, \|\boldsymbol{J}_2(i)\|_2} \tag{4.1}$$

$$Mag(i) = \frac{\|\boldsymbol{J}_2(i)\|_2}{\|\boldsymbol{J}_1(i)\|_2} \tag{4.2}$$

with $\boldsymbol{J}_1(i)$ and $\boldsymbol{J}_2(i)$ being the calculated current densities in the reference and expanded model in the i-th element, respectively.

Furthermore, the directional agreement Par between the fiber directions in white matter compartment and the current flow fields is calculated

$$Par(i) = acos(< \boldsymbol{J}(i), \boldsymbol{v}(i) >) \tag{4.3}$$

with $\boldsymbol{v}(i)$ being the primary eigenvector of the conductivity tensor in the white matter compartment in the i-th element. While a Par value of 1 indicates directional agreement, a Par value of 0 represents orthogonality.

4.1.2. Results

First, the current density distribution in the low-parametric isotropic three-compartment head model is discussed, and second, the changes in current density that occurs as the simpler head model is extended step by step to a more realistic six compartment head model with white matter anisotropy are expounded. Finally, the current density distribution within the most realistic head model is evaluated. As the results for auditory and motor cortex did not essentially differ, the main differences with respect to auditory cortex stimulation will be discussed; important data will be presented in parentheses following the auditory cortex data. The figures for motor cortex stimulation can be found in the Appendix A.3.

Isotropic three-compartment model (3CI model)

Figure 4.1-A1 (A.1-A1 for motor cortex stimulation) depicts the current flow field in the 3CI model on a coronal cutplane through the localized auditory cortex region. Peak current densities of $1.2\,\mathrm{Am}^{-2}$ ($1.3\,\mathrm{Am}^{-2}$) can be seen in the skin compartment, especially underneath the edges of the electrodes. Most of the current that enters the skin is deflected by the low conductive skull compartment and tangentially channeled along the skin from anode to cathode. In the skull, mainly radial current flow can be seen, while in the isotropic brain compartment a homogeneous current density orientation is shown. As can be seen, changes in the brain current flow fields are rendered indistinguishable as Figure 4.1 is scaled to the full range of current density amplitudes in the model. Therefore, Figure 4.2 shows an identically structured plot, showing only the current flow fields in the brain compartment. In the brain, peak current densities of $0.11\,\mathrm{Am}^{-2}$ ($0.078\,\mathrm{Am}^{-2}$) can be seen in brain regions directly underneath the simulating electrodes.

The interplay between median current density amplitude in the brain and the distance to the nearest electrode node is displayed in Figure 4.3 (A.4). A correlation between distance and current density amplitude can be seen, i.e., median brain current density decreases smoothly with increasing distance to the stimulating electrodes.

Including the layered skull structure (4CI model)

The first feature that is added to the low-parametric three-compartment head model is the distinction between skull compacta and spongiosa. The corresponding current flow field orientation and magnitude changes can be seen in Figures 4.1-B and 4.2-B (A.1-B and A.3-B). While the first column (Figure -B1) shows the current density vector field in the 4CI model, the second (Figure -B2) and third (Figure -B3) columns displays changes in current flow field orientation (Ang, Equation 4.1.1) and magnitude (Mag, Equation 4.1.1) between the 3CI and 4CI models. Changes in orientation of up to 64 (31) degrees can be seen in the skull, while minor changes can be observed in the skin and brain. Because the conductivity of the spongiosa is strongly increased (from $0.01\,\mathrm{Sm}^{-1}$ to $0.025\,\mathrm{Sm}^{-1}$), changes in orientation of up to 9.2 (12.2) degrees do occur in the cortex, mostly underneath the electrodes. For motor cortex stimulation, major changes in orientation (up to 12.2 degrees) can be seen in the target

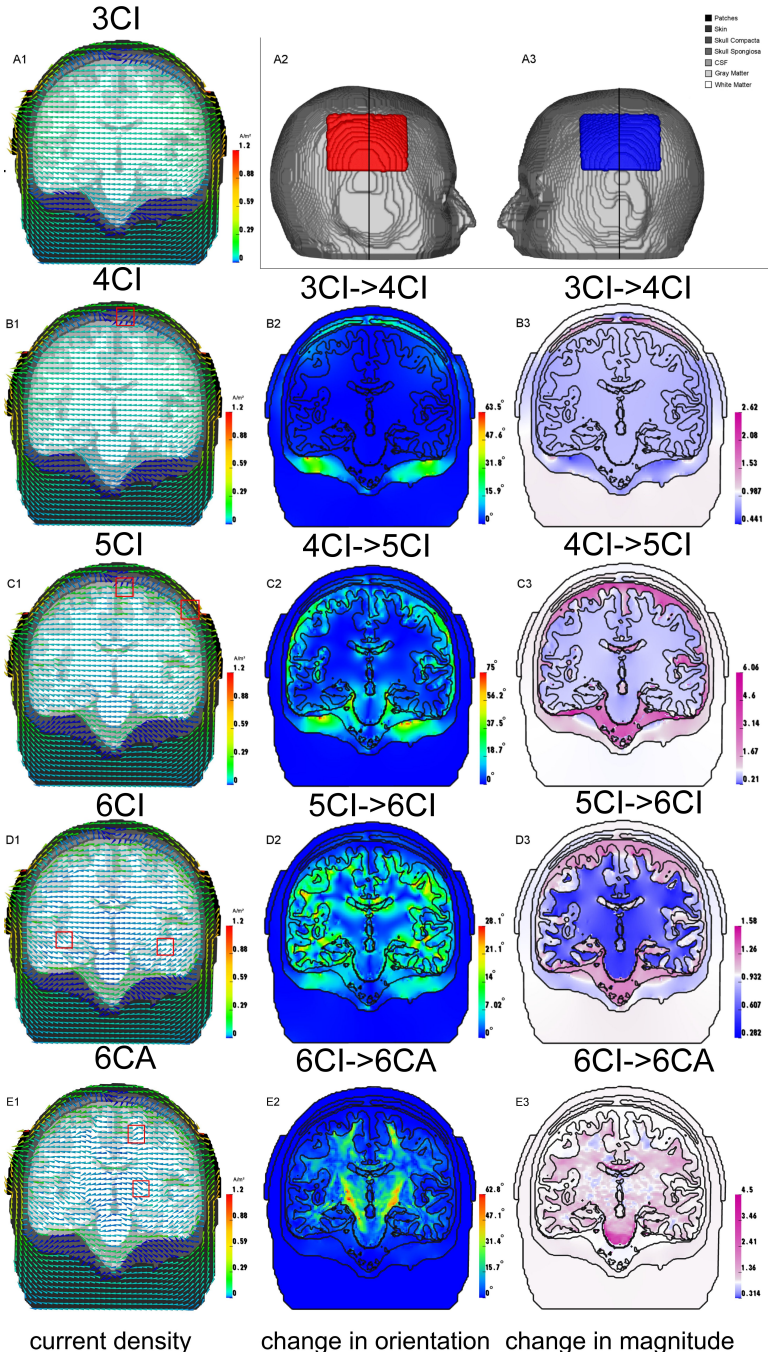

Figure 4.1.: Current flow fields for auditory cortex stimulation. The stimulating electrodes are shown in A2 (anode in red) and A3 (cathode in blue). Left column shows the vector field for the 3CI (A), 4CI (B), 5CI(C), 6CI (D) and 6CA (E) head models on a coronal slice through the model as shown in A2 and A3. The middle and right columns display change in orientation and magnitude that resulted from adding one feature to the model (each model is compared to the one in the row above: Figures B2 and B3 show difference between A1 and B1). The color scale for the middle column shows changes in orientation, while the color scale for the right column displays the factor resulting from dividing magnitudes. Red boxes in B1, C1, D1 and E1 show magnified samples that are used in Figure 4.4. Adapted from [142]

region (see Figure A.3-B2), while the target region is hardly affected for auditory cortex stimulation (see Figure 4.2-B2). Current density decreases ($Mag < 1$) in the whole brain

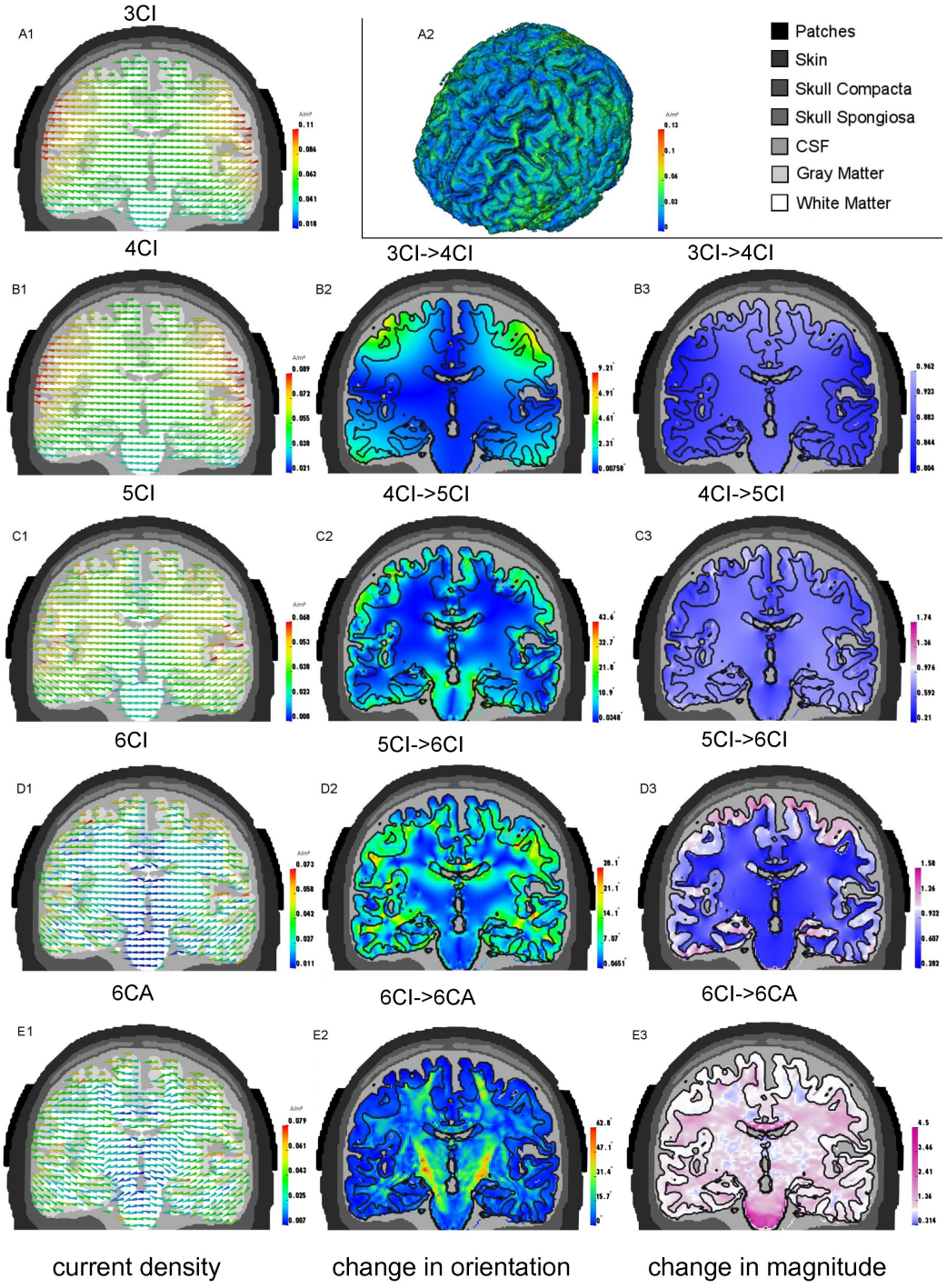

Figure 4.2.: Current flow fields only in the brain compartment for auditory cortex stimulation. This structure of the figure is identical to Figure 4.1, whereas the scale is adapted to the current density amplitudes in the brain compartment. In A2, a volume rendering of the current density is presented on the brain surface in the 6CA model. Adapted from [142]

and most compacta regions (Figures 4.2-B3 and 4.1-B3 (A.3-B3 and A.1-B3)) and increases ($Mag > 1$) in the lower resistive spongiosa compartment (Figure 4.1-B3 (A.1-B3)) and in a

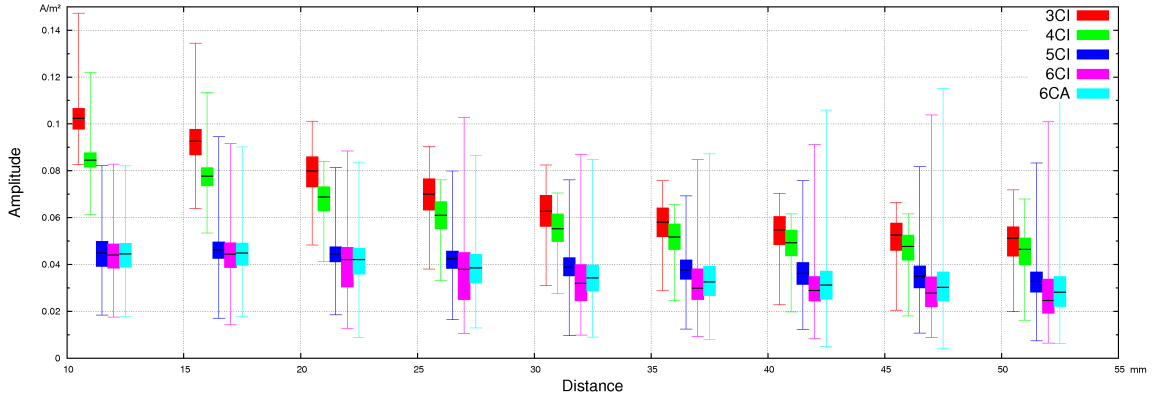

Figure 4.3.: Boxplot for each of the five models with auditory cortex stimulation. Current density amplitudes are presented in the brain elements located at a specific distance (+ or - 2.5 mm) to the nearest electrode nodes. While the black dash marks the median current density, the box comprises the upper and lower quartile and the error bars show the maximal and minimal current densities. See also [142]

cortical region underneath a large portion of spongiosa above the motor cortex stimulation site (Figure A.3-B3). The pattern of peak cortical current density distribution does not change with respect to the 3CI model in auditory cortex stimulation and slightly changes for motor cortex stimulation. For motor cortex stimulation, the current flow field in the target brain region is substantially affected by the presence of the spongiosa compartment (see Figures A.3-B2 and A.3-B3). Similar to the 3CI model, median brain current density increases with decreasing distance to the nearest electrode node.

Figure 4.4 (A.2) depicts the percentage of elements within a given range of angular and magnitude changes for the whole volume conductor and for the gray matter compartment separately. Changes in orientation below 9 degrees in the whole volume conductor and below 6 degrees in the gray matter compartment can be seen for more than 95 % (97 %) of the elements. However, changes up to 126 (59.7) degrees and 56.4 (14.5) degrees do occur in the whole volume conductor and in the gray matter compartment, respectively. Changes in magnitude between 0.8 and 1.2 occur for over 90 % (94 %) of the elements in the whole volume conductor and for 99.9 % (100 %) of the elements in the gray matter compartment, respectively. In the whole model, magnitude differences range from 0.2 to 3.92 (0.3 to 3.83).

Magnified samples (see red box in Figure 4.1) of the current density vector fields containing major changes in orientation are displayed in full resolution in Figure 4.5-A. While the current flow field in the skull compartment is mainly radially oriented in the 3CI model (Figure 4.5-A1), far more tangentially oriented vector field components can be seen in the skull spongiosa in the 4CI model (Figure 4.5-A2) for a compacta-to-spongiosa conductivity ratio of 1:3.6. When using the maximal reported compacta-to-spongiosa ratio of 1:8.2 (Akhtari and colleagues [2]), a correlation between the tangential behavior in the spongiosa layer and the increase in compacta-to-spongiosa ratio can be seen. Mainly tangentially current flow components in the spongiosa compartment can be seen when a compacta-to-spongiosa ratio of 1:23 is used, see Figure 4.5-A4. The direction of the current flow field in the spongiosa is thus strongly

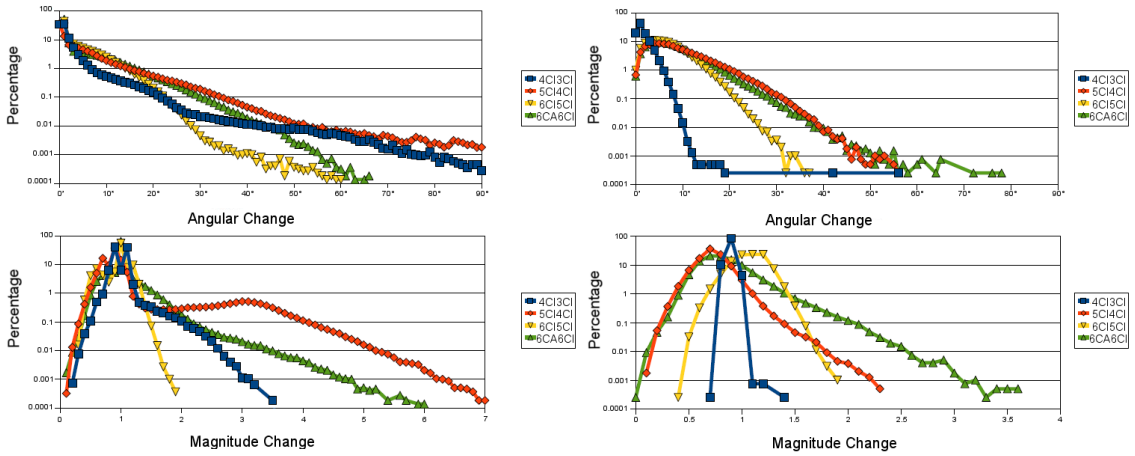

Figure 4.4.: Statistical evaluation of the current flow field orientation (Ang) and magnitude (Mag) changes for auditory cortex stimulation. For each added model component (e.g. 3CI to 4CI model), the percentage of elements that show a change within a given range is presented. The analysis is performed for the whole head model (left) and only the gray matter compartment (right). The percentage is depicted on a logarithmic scale with minimum at 0.0001.

influenced by the compacta-to-spongiosa-ratio, leading to strong spongiosa channeling effects for higher ratios.

Including the CSF compartment (5CI) model

Adding the highly conductive CSF compartment to the 4CI model does not affect the current density orientation in the skin (Figure 4.1-C2 (A.1-C2)), but influences the current flow field orientation in the skull and CSF (up to 75 (72) degrees) and in the brain (up to 44 (56) degrees). In the brain, modifications with regard to orientation are found in most cortical regions bordering CSF, with major changes close to the stimulation site. Compared to the current density amplitudes in the 4CI model, the current density in the CSF increases by a maximal factor of 6.1 (5.21) (Figure 4.1-C3 (A.1-C3)). However, in white matter and most cortical regions, the current density amplitude is decreased substantially, especially close to the stimulation site (Figure 4.2-C3 (A.3-C3)). There is hardly any change in the skin compartment, see Figure 4.1-C3 (A.1-C3). While the median brain current density increases between distances of 10 and 15 mm, median brain current density decreases with increasing distance to the nearest electrode node in regions farther away, see Figure 4.3. Moreover, there is a strong decrease in median current density of about 50 % between the 5CI and 4CI models in regions close to the stimulating electrodes and a minor decrease in regions farther away. Furthermore, a strong increase in maximal current density is visible in sensor-remote brain regions.

Figure 4.4 shows orientation changes below 20 degrees for more than 94 % (94 %) of the elements in the whole model and maximal changes of 146 (91) degrees. In the gray matter compartment, changes below 20 degrees occur in over 94 % (91 %) of the elements and maximal changes are 56 (72) degrees. Changes in magnitude are between 0.14 and 9.87 (0.1 and 7.64) in the whole volume conductor and between 0.14 and 2.33 (0.18 and 1.82) and in the gray

matter compartment. The current density in the gray matter compartment decreases in over 95 % (97 %) of the elements and for over 92 % (93 %) of the elements the magnitude change lies between 0.5 and 1. In the whole volume conductor, the magnitude change is between 0.5 and 1.2 for over 90 % (91 %) of the elements.

Figures 4.5-B1 and -B3 and 4.5-B2 and -B4 show the current flow fields at two different locations (see boxes in Figure 4.1-C1) in the 4CI and 5CI models, respectively. A large amount of current density that passed the skull is tangentially channeled along the highly conductive CSF compartment from anode to cathode, see Figure 4.5-B2. The bottom row of Figure 4.5 shows a sulcus in both the 4CI (Figure 4.5-B3) and the 5CI (Figure 4.5-B4) model. While a homogeneous current density distribution can be seen in head model 4CI, currents travel mainly along and towards the CSF in the 5CI model, leading to higher amplitudes in sensor-remote cortical regions and at sulci walls and bottoms. This leads to a less homogeneous and irregular current flow pattern.

Differentiating between gray and white matter (6CI) model

Figures 4.1-D (A.1-D) and 4.2-D (A.3-D) display the current flow vector field and the orientation and magnitude changes after adding a white matter compartment to head model 5CI. Changes in orientation (up to 28 (36) degrees) do occur mostly in inferior parts of the CSF and near the boundary between gray and white matter. Current density amplitude increases in the CSF and decreases in the white matter, see Figures 4.1-D3 and 4.2-D3 (A.1-D3 and A.3-D3). In the gray matter compartment, current density decreases slightly close the the simulation site and increases in regions farther away. Close to the stimulation site, the median current density remains nearly constant, while it decreases in brain regions farther away from the electrodes.

The current flow in more than 94 % of all and 91 % of the gray matter elements shows orientation changes of less than 12 (13) degrees, see Figure 4.4 (A.2). Orientation changes up to 71 (60) degrees and 37 (49) degrees can be found in the whole model and in the gray matter compartment, respectively. Magnitude changes are less than 40 % in 95 % of all volume conductor elements and in 98 % (99 %) of gray matter elements. Maximal changes are between 0.25 and 1.95 (0.29 and 2.1).

Figure 4.5 depicts two regions including boundaries between gray and white matter within the 5CI (C1,C3) and the 6CI (C2,C4) models, see red boxes in Figure 4.1-D1. In the white matter, current density tends to be oriented towards the neighboring gray matter boundary, see Figure 4.2-D1.

Adding white matter anisotropy (6CA model)

Figure 4.1-E1 (A.1-E1) shows the current flow field in a model in which white matter anisotropy is added to the 6CI model. While changes in orientation up to 64 (62.3) degrees occur all over both gray and white matter compartments, they are largest in central white matter regions. Current density in the gray matter compartment is decreased, while both areas with increased

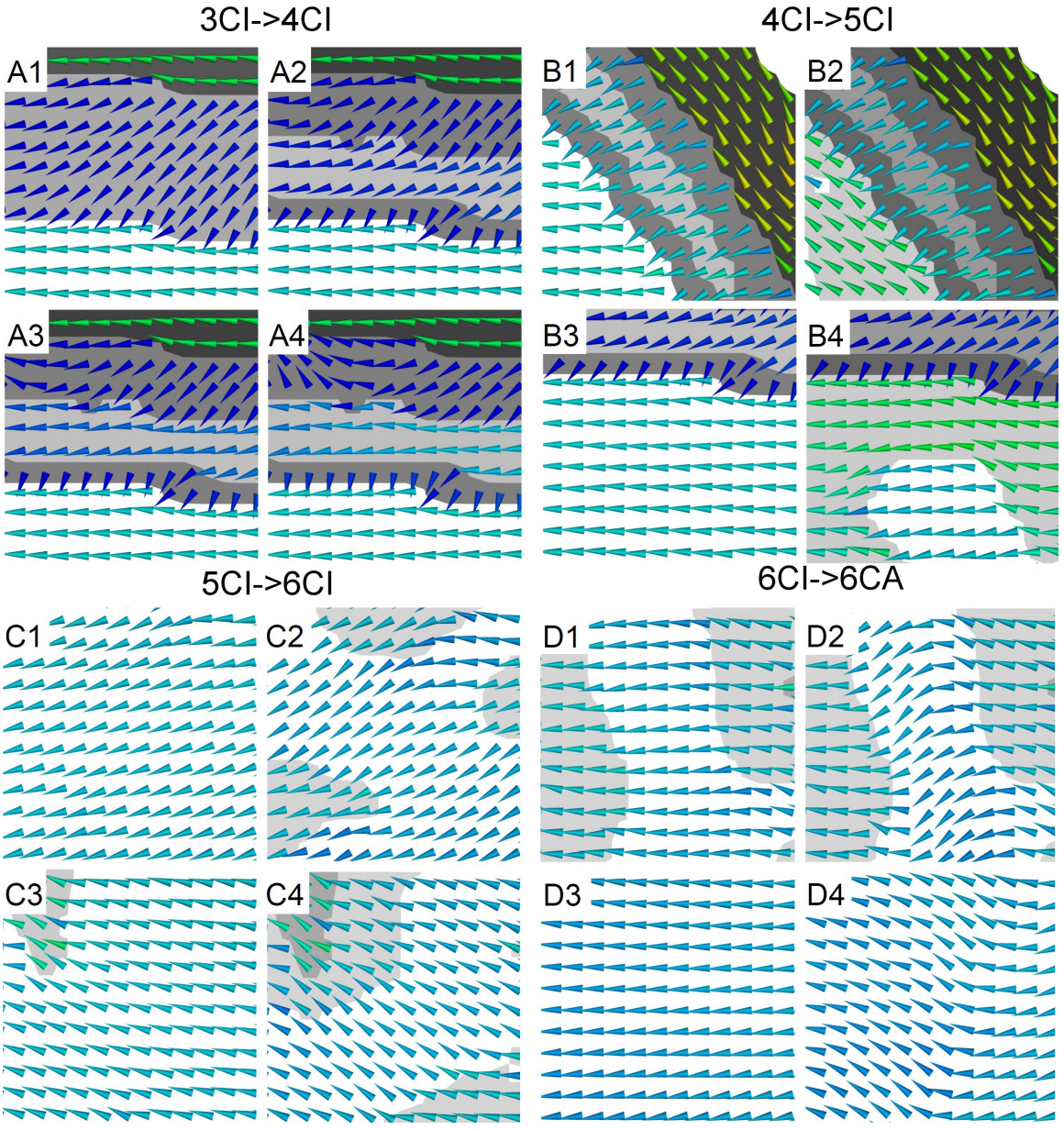

Figure 4.5.: Selected details of the current flow vector fields in full resolution (1mm). Figures A depict the effects of including skull spongiosa, by comparing the 3CI (A1) to model 4CI with compacta-to-spongisa conductivity ratios of 1:3.6 (A2), 1:8.2 (A3) and 1:23 (A4). Figures B show the changes caused by including the CSF compartment at two locations in the 4CI (B1,B3) and 5CI (B2,B4) models. Figures C present the differences that resulted from including a white matter compartment at two locations in the 5CI (C1,C3) and 6CI (C2,C4) models. Figures D present the current density distribution caused by incorporating white matter anisotropy at two locations in the 6CI (D1,D3) and 6CA (D2,D4) models. Tissue labels are adapted to the tissues contained in the model and color-coded and size-normalized cones are used to present current flow field magnitude and orientation, respectively. Adapted from [142]

and decreased current density amplitude can be seen in the white matter compartment. Major changes in orientation and magnitude can be seen in central white matter regions. The median brain current density decreases between distances of 10 and 25 mm from the electrodes, while in deeper regions it remains mainly unchanged, see Figure 4.3 (A.4).

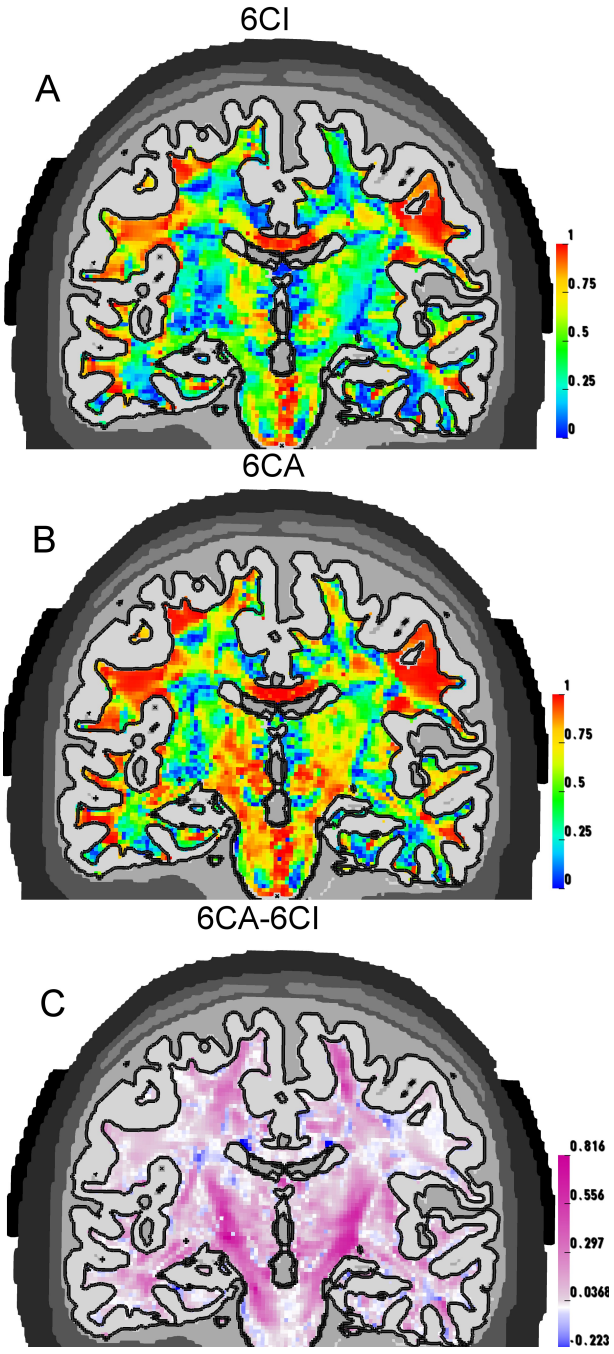

Figure 4.6.: Directional agreement (PAR) between first eigenvector of the conductivity tensor in anisotropic white matter and current density in the 6CI (A) and 6CA (B) models. Figure C displays differences in parallelity between both models, i.e., C = B - A. Adapted from [142]

As can be seen in Figure 4.4 (A.2), more than 94 % of all and 91 % of gray matter elements show orientation changes under 15 (17) degrees, while maximal changes are up to 79 (120) degrees. Current density magnitude changes less than 40 % (30 %) in 95 % of all and 90 % of gray matter elements. In the whole model, magnitude differences range from 0.02 to 7.15 (0.02 to 6.51).

Magnified samples of a thalamocortical projection fiber (Figure 4.5-D1,D2) and a pyramidal

tract region (Figure 4.5-D3,D4) in the 6CI (D1,D3) and 6CA (D2,D4) models are shown in Figure 4.5. In both thalamocortical projection fibers as well as pyramidal tract areas, the current flow field is mainly homogeneous in the 6CI model, while major changes in orientation occur in the 6CA model.

The directional agreement (*Par*, Equation 4.1.1) between the main fiber directions in the white matter compartment (primary eigenvector of the conductivity tensor) and the current density is depicted in Figure 4.6. The current density in the 6CI model does not show high directional agreement to the pyramidal tracts (Figure 4.6-A), whereas the current flow in the 6CA model is oriented far more parallel to the pyramidal tracts (Figure 4.6-B). Figure 4.6-C reveals large differences in parallelity in central white matter regions.

Current density distribution in most realistic model

As can be seen in Figure 4.1-E1, a peak current density of $1.2\,\mathrm{Am}^{-2}$ ($1.3\,\mathrm{Am}^{-2}$) can be observed at the skin surface underneath the edges of the tDCS electrodes. A large amount of current is conducted along the scalp from the anode to the cathode. The currents that enter the skull flow mainly radially in compacta and slightly more tangentially in spongiosa. After passing the skull, a large part of the current is channeled along the CSF towards farther away brain areas in the direction of the cathode. Figure 4.2-E1 shows that highest current densities in the brain occur in small cortical structures surrounded by CSF. Current vectors in white matter regions close to the cortex tend to be oriented towards the more conductive cortical tissue close-by. The peak current density in Figure 4.2-E1 is $0.078\,\mathrm{Am}^{-2}$ ($0.053\,\mathrm{Am}^{-2}$).

4.1.3. Discussion

Three-compartment head model

In all models, a large fraction of the current was short-circuited through the scalp because of the less resistive scalp pathway as compared to the skull and brain pathway. This is in agreement with previous tDCS modeling studies [77, 116]. In the three-compartment model, strongest current densities in the brain compartment were found at the brain/skull interface directly underneath the stimulating electrodes. Because of the homogeneous isotropic conductivity of the brain, currents flowed straight from anode to cathode inside the interior skull surface. As the electrodes were placed symmetrically on the scalp, the strongest intensities can thus be seen in the target region (see Figure 4.2-A2). For motor cortex stimulation, however, the maximum did not lie underneath the electrode, but more anteriorly towards the reference electrode (see Figure A.3-A2). So for both configurations, the maximum current density in the brain lay in between the electrodes, a result in accordance with other tDCS studies [27, 36, 77].

Skull compacta and spongiosa modeling

Because of the low conductivity of $0.01\,\mathrm{Sm}^{-1}$ of the skull compartment [28, 144], the low-parametric 3CI model showed mainly radial current flow in the skull. Including spongiosa to

this model slightly changed this behavior. Current became tangentially channeled along the better conductive spongiosa, leading to an overall decrease in brain current density and a small effect on the current density orientation. The spongiosa shunting effect was also observed in previous studies [57, 103] and increases in size for higher compacta-to-spongiosa conductivity ratios, in agreement with Rampersad and colleagues [103]. The only studies modeling separate skull layers for electrical stimulation were performed with two-dimensional and/or spherical models [57, 103], making this study the first to investigate the effects of including separate skull layers in a realistic three-dimensional tDCS model.

For motor cortex stimulation, the target area is where the orientation change was largest, while for auditory cortex stimulation the target area was hardly affected by the presence of the spongiosa. This is due to the distribution of the spongiosa relative to the placement of the electrodes. The closer the electrodes were to the spongiosa, the more current was channeled along the spongiosa. Therefore, realistic modeling of the skull is very important when large parts of spongiosa are located underneath the stimulating electrodes.

Influence of CSF compartment

When including CSF, current density increased in the CSF and decreased in the brain compartment. Current density was shunted away from the target brain area via the CSF. This effect is due to the substantially better conductivity of CSF as compared to the brain compartment (5.4 times higher conductivity) and is in agreement to the findings of others [26, 27, 116, 144]. The CSF channeled currents both into deeper lying sulci and towards sensor-remote cortical regions. The current flow field all along the CSF/brain boundary became less homogeneous. In cortical regions close to the CSF, currents were relative strong and directed to the more conductive CSF compartment. Within 10 to 15 mm to the electrodes, an increase in median brain current density was shown (see Figure 4.3). This is due to channeling of current density from the cortical crown to the walls and bottoms of sulci underneath the electrodes (see Figures 4.2-B2 and -C2), in agreement with Salvador and colleagues [116]. Of the four added features that were investigated, the inclusion of the CSF had by far the largest effect on the relation between brain current density amplitude and distance to the nearest electrode node. Therefore, an exact and accurate modeling of the CSF compartment and the brain surface is essential for realistic tDCS simulation studies.

Including white matter

When adding a white matter compartment, the conductivity in the white matter compartment was decreased substantially, leading to a strong overall decrease in current density in the white matter compartment. As the brain condutivitiy was thus lower, there was a larger conductivity disparity between CSF and brain tissues as compared to the five-compartment head model. Therefore, a larger quantity of current was shunted along the CSF, leading to weaker current density in the cortical tissue nearby the stimulation site and stronger current density in sensor-remote cortical regions. Current vectors in white matter close to the gray matter compartment tended to be oriented towards the more conductive gray matter, because

of the less resistive current pathway offered by the gray matter. Because the conductivity disparity between CSF and brain tissue is only marginally bigger than the disparity that was introduced by including the CSF, the pattern of peak cortical current density distribution was very similar to the distribution that was seen in the five-compartment head model. Previously, the distinction between gray and white matter was modeled by others [28, 114, 116, 144], but only Sadleir and colleagues [114] discussed the effect of this distinction. They also reported that changing the conductivity of the white matter led to small changes in the brain current density vector field. Moreover, this study design allowed to describe and investigate the effect of the white matter compartment in comparison to the other investigated effects, a very important point to setup a guideline for efficient yet accurate volume conductor modeling in transcranial direct current stimulation.

Salvador and colleagues [116] applied an anodal current of 1 mA to a 25 cm^2-sized electrode above the motor cortex and placed the cathode above the right frontopolar cortex. A five-compartment head model (skin, skull, CSF, gray and white matter) was used with comparable conductivities as in this study. Highest current densities of 1.6 Am^{-2} in the skin, 0.33 Am^{-2} in the CSF and 0.068 Am^{-2} in the cortex were reported. Wagner and colleagues [144] and Parazzini and colleagues [95] were able to demonstrate that maximal skin and cortical current densities did not vary essentially between 25 cm^2 and 35 cm^2-sized electrodes. Hence, maximal skin and cortical current densities obtained for motor cortex stimulation are of the same order of magnitude as the values presented by Salvador and colleagues [116]. Maximal cortical current densities calculated in both auditory and motor cortex stimulation are of the same order of magnitude as the values discussed previously by Wagner and colleague [144] and Datta and colleagues [28].

Effect of white matter anisotropy

When adding white matter anisotropy, current density strongly increased in large parts of the white matter, especially in the thalamocortical fiber tracts and the pyramidal tract regions. On the contrary, only minor changes in orientation and magnitude occurred in superficial cortical regions, while larger changes were demonstrated in deeper gray matter regions. More importantly, current flow in white matter was oriented far more parallel to the anisotropic fiber bundles, especially in the thalamocortical fiber and pyramidal tract regions in agreement with the results of others [57, 90, 130]. While the study of Holdefer and colleagues [57] was performed on a two-dimensional single coronal MRI slice including the motor cortex with a two-dimensional white matter anisotropy, a highly realistic three-dimensional MRI-derived head model was used. Moreover, realistically shaped electrodes were modelled, while Holdefer and colleagues [57] and Suh and colleagues [130] used point electrodes to model anode and cathode. Moreover, this is the first study to use the linear effective medium approach for computing the white matter anisotropy, while other groups [90, 130] used fixed anisotropy ratios of 1:10 longitudinally to transversally to the fiber bundles. Lastly, while other studies were performed in a two-dimensional model with 150,000 tetrahedral elements [57] or in tetrahedral models with 147,287 [90] or 160,231 FE nodes [130], with more than 2 million FE

nodes, high resolution geometry-adapted hexahedral FE modeling was performed, which is the currently most realistic hexahedral modeling procedure for tDCS (see Section 3.2).

General discussion

This study revealed the significance and influence of MRI-derived realistic volume conductor modeling for tDCS simulations. The results clearly showed that realistically shaped multi-compartment FE head models are required to receive accurate and realistic simulation results. A novel full step-by-step approach for realistic tDCS modeling was performed. This concept allows to directly compare the effect sizes of neglecting important head tissue compartments, which was considered to be important by others [26, 57, 95, 144]. Keeping the main results of this simulation study in mind, a guideline for efficient yet accurate volume conductor modeling in tDCS can be formulated:
All important tissue compartments between the electrodes and the target brain area should be modeled as accurately as possible. Isotropic representations of the skin, skull, CSF and brain gray and white matter are essential for any simulation study. If a significant portion of spongiosa is in between the electrodes and the target brain region, the skull should be distinguished into its compact and spongy bone. For deeper target regions, white matter anisotropy is important while it seems to be less important for superficial target regions. This is, however, only true under the assumption that mainly the cortical structures are sensitive to polarization, as reported by Radman and colleagues [101], who showed layer V pyramidal neuronal soma to be individually the most sensitive to polarization by optimally oriented subtreshold fields. The supratreshold electric field action potential threshold was shown to reflect both direct cell polarization and synaptic (network) activation. In the related area of deep brain stimulation, the most realistic predictions of axonal thresholds were shown to be achieved with the most detailed model that contained diffusion-tensor based three-dimensional tissue anisotropy and inhomogeneity and that the more simplistic models substantially overestimated the spatial extent of neural activation [19].

This simulation study showed that in the most realistic head model, highest median current densities occur in brain regions close to the stimulation site; the smaller the distance to the nearest electrode node, the bigger the median brain current density. Although the current flow field is irregular, brain regions close to the simulation site receive strongest median current densities. When there is no individual head model of the patient available, the stimulation electrodes should be placed above the target region. To achieve either excitation or inhibition in a target region, the anode or cathode should be placed there, respectively [3]. It should be noted, however, that the stimulation always requires both electrodes. Therefore, the use of different electrode sizes has been suggested. For example, in order to achieve local excitation a small anode should be placed above the target region and a larger return electrode elsewhere - thus minimizing the effect of inhibition [83].

While some studies used point electrodes [57, 130], conventional sponge-based electrodes are better suited in clinical practice and simulation studies. Therewith, peak currents of more than $1.1\,\mathrm{Am}^{-2}$ were found in the skin under the edges of the electrodes. This effect occurs

because of the better conductivity of the electrodes as compared to the scalp compartment and has been reported before in spherical shell models [77, 103] and realistically shaped FE head models [26, 28]. As the electrode to skin conductivity ratio, the electrode size and the total current injected are equal, the here presented maximum current densities in the skin are mainly the same in all models (3CI-6CA). According to Reilly and colleagues [104], maximal currents in the skin are at the level to induce skin sensation, in line with experimental studies of Nitsche and colleagues [83] and Wassermann and Grafman [146] who reported a mild sensation under the stimulating electrodes during current injection, independent of the polarity and location of the electrodes.

The final outcome of the simulation study is strongly influenced by the individual head and the distribution of the electrodes. As individual anatomical differences strongly influence the simulation, ideally one would generate a highly realistic and subject-specific MRI-derived FE head model of each patient following the guideline for efficient and yet accurate volume conductor modeling for tDCS. Along this line one could adjust electrode placement and calculate individually optimized stimulation setups for specific target regions.

The strongest electric field in the six-compartment head model with white matter anisotropy are between 236 μVmm^{-1} and 167 μVmm^{-1} for auditory and motor cortex stimulation, respectively. Miranda and colleagues [77] simulated maximal cortical current densities of about 0.1 Am^{-2}. With this procedure, Miranda and colleagues depicted electric fields of 220 μVmm^{-1}. One has to take into account that the introduced current was doubled compared to this simulation study. However, a significant higher skin to skull conductivity ratio (75:1 compared to 43:1) was used. Therefore, stronger currents were tangentially channeled along the scalp and only minor currents penetrated the skull. Thus, the current density magnitudes in both studies were comparable.

Until now, mainly the current density amplitudes in the target regions was investigated. Not only the current density amplitude, but also the orientation is an important factor in brain stimulation. Anodal stimulation of the primary motor cortex enhance cortical excitability in the motor cortex, whereas cathodal stimulation inhibits it [84]. However, there is further need for more research to better understand the relationship between current density orientation, individual cortical folding, orientation of the neurons and effects of stimulation.

As described in Section 2.1, the quasi-static approximation to Maxwell's equations is justified for modeling in the low-frequency regime. Logothetis and colleagues [73] used in vivo direct measurements of the cortical impedance spectrum in the primary cortex of monkeys and were able to demonstrate that the impedance is independent of frequency, is homogeneous and tangentially isotropic within the gray matter compartment. In the related field of transcranial magnetic stimulation, Bossetti and colleagues [14] showed that the quasi-static approximation to Maxwell's equations is fairly good even for rapid stimulation pulses with stimulation frequencies above 1 kHz. They concluded that the modeling error was much less dependent on the permittivity of the medium than on the conductivity. For this reasons, the main findings of this chapter should also be valid for at least low-frequency (below 100 Hz)

transcranial alternating current stimulation. A detailed review of the underlying mechanisms and modulation of cognitive processes of tACS can be found in Herrmann and colleagues [54]. Two further facts of the method are important. Firstly, changing the polarity of the electrodes results in an identical pattern of current density with the vector field orientation flipped by 180 degrees. Secondly, as the lead field matrix is linear, the stimulation intensity can be scaled to any desired input current simply by multiplying the current flow pattern with the new current strength. The current density during one half cycle of tACS can be derived from tDCS simply by scaling and for the other half cycle simply by scaling and flipping the orientation by 180 degrees. In the following, tDCS/tACS are denoted as transcranial current stimulation (tCS).

Recently, a very similar study investigating the influence of modeling/not modeling the conductive compartments skull spongiosa, skull compacta, CSF, gray matter, and white matter and of the inclusion of white matter anisotropy on the EEG/MEG forward solution has been presented by Vorwerk and colleagues [139]. Vorwerk and colleagues were able to demonstrate that the inclusion of the highly-conductive CSF compartment had the strongest influence on both signal topography and magnitude in both modalities. Furthermore, they found the effect of gray/white matter distinction to be nearly as big as that of the CSF inclusion. In comparison to these two steps, the introduction of white matter anisotropy leaded to a clearly weaker, but still strong, effect. Finally, the distinction between skull spongiosa and compacta caused the weakest effects in both modalities when using an optimized conductivity value for the homogenized compartment.

4.2. Electrode montages for targeting the frontal and occipital lobe

In collaboration with Toralf Neuling from Oldenburg [82], a simulation study investigating the applicability of commonly used clinical electrode montages for targeting the frontal lobe and the occipital lobe was conducted (as shared first author). In this section, the most important results of the simulation study are presented. Further information can be found in the original publication by Neuling and colleagues [82].

The PEM-based current density vector fields are calculated in a six-compartment FE head model with white matter anisotropy, see Section 2.5. For stimulation, two rectangular electrodes with a size of $7\,\mathrm{cm} \times 5\,\mathrm{cm}$ are positioned on the head surface and a total current of $1\,\mathrm{mA}$ is applied to the anode. As the maximal current density in the skin compartment is about 20 times higher as compared to the maximum current densities in the brain ($1.3\,\mathrm{Am}^{-2}$ in the skin compartment and $0.078\,\mathrm{Am}^{-2}$ in the brain compartment on the saggital slice through the model) the current flow fields are only visualized in the brain. Using the conventions of an extended 10-10 EEG system, the following frequently-used electrode montages are simulated

- The medial electrode configuration for stimulating the frontal lobe: Electrodes centered at locations FPz and Oz
- The lateral electrode configuration for stimulating the frontal lobe: Electrodes centered at locations F7 and F8
- The medial electrode configuration for stimulating the occipital lobe: Electrodes centered at locations Cz and Oz
- The lateral electrode configuration for stimulating the occipital lobe: Electrodes centered at locations P7 and P8

Figures 4.7 and 4.8 depict the brain current flow fields when the medial and lateral electrode configurations for stimulating the frontal lobe are used, respectively. For the medial electrode configuration, a very widespread current flow field pattern with relatively high current densities located in nearly all cortical lobes can be seen. Moreover, occipital lobes receive stronger current densities as compared to the frontal lobes (Figure 4.7). The medial configuration is thus not very well suited for a focused and targeted stimulation of the frontal lobes.

On the contrary, when using the lateral bipolar electrode montage, strongest current density amplitudes can be seen in the frontal lobes (Figure 4.8). Moreover, temporal and parietal lobes receive substantially weaker current densities and nearly no current densities can be seen in the occipital lobes. This electrode montage is thus very well suited for a targeted and focused stimulation of the frontal lobes. Taking together, the lateral electrode montage is better suited for stimulating the frontal lobe as will be discussed in the following: First, when using the lateral configuration, strongest current densities of about $0.095\,\mathrm{Am}^{-2}$ can be seen in the frontal lobes, while for the medial configuration, very weak current densities of about $0.03\,\mathrm{Am}^{-2}$ can be seen in the frontal lobes. Second, the lateral configuration leads to a very

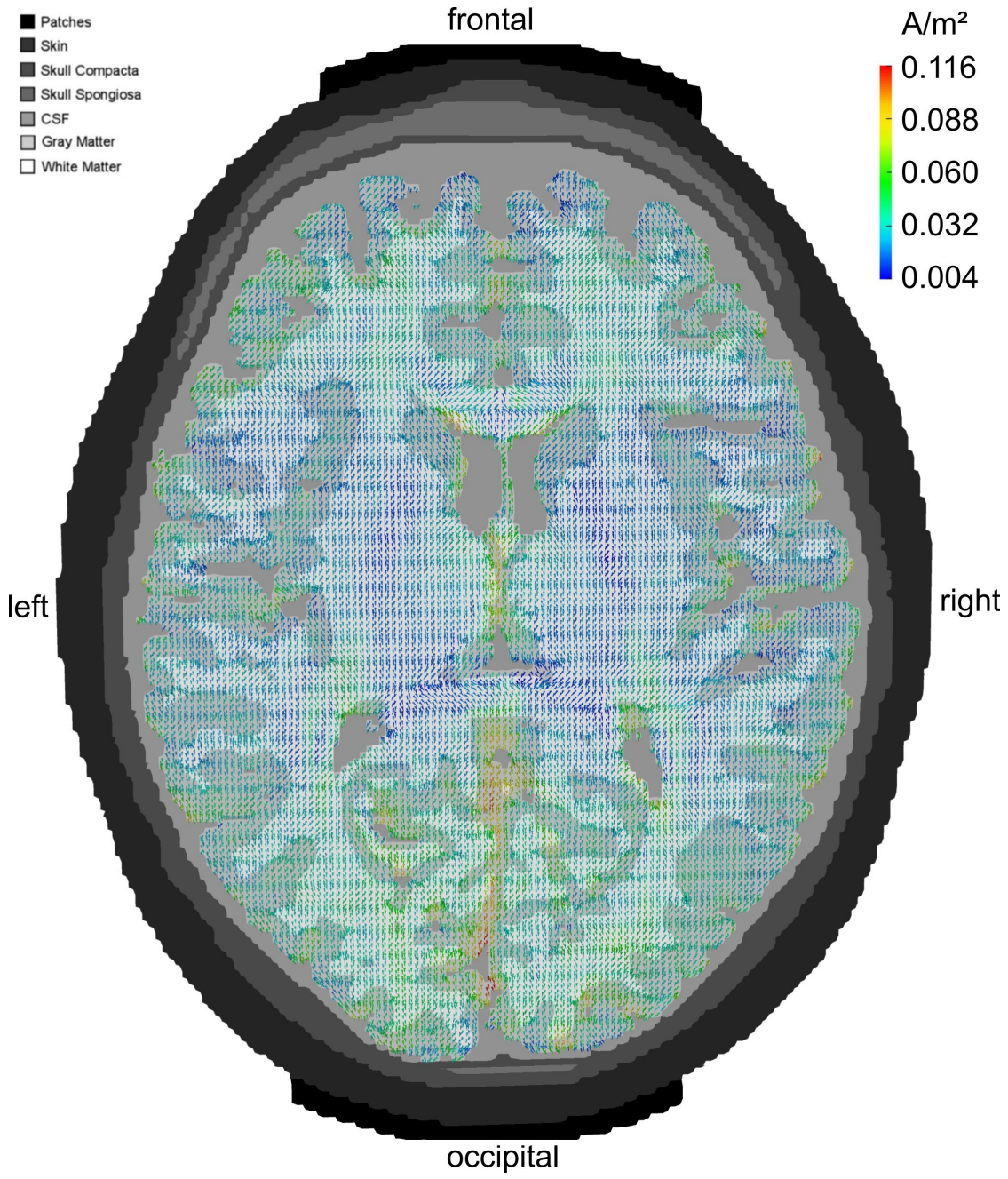

Figure 4.7.: Axial view of current flow field. The stimulation electrodes are centered around electrode positions FPz and Oz, resulting in a widespread current flow pattern with strongest current density in the occipital cortex. Current density amplitudes above 0.07 A/m^2 can be seen in nearly all cortical lobes. Adapted from [82].

focal and targeted stimulation of the frontal lobes, while the medial configuration induces a very widespread current flow pattern with the strongest intensities located in the non-target brain regions. Third, for the medial configuration, both frontal hemispheres receive nearly an identical pattern of cortical current density. The excitatory stimulation of the left dorsolateral prefrontal cortex (dlPFC) is of special importance for the treatment of mayor depression [13, 38]. In most clinical studies, an unsymmetric electrode montage was used, i.e., the anode was placed above the left frontal lobe and the cathode over the right orbit [13, 38]. Based on

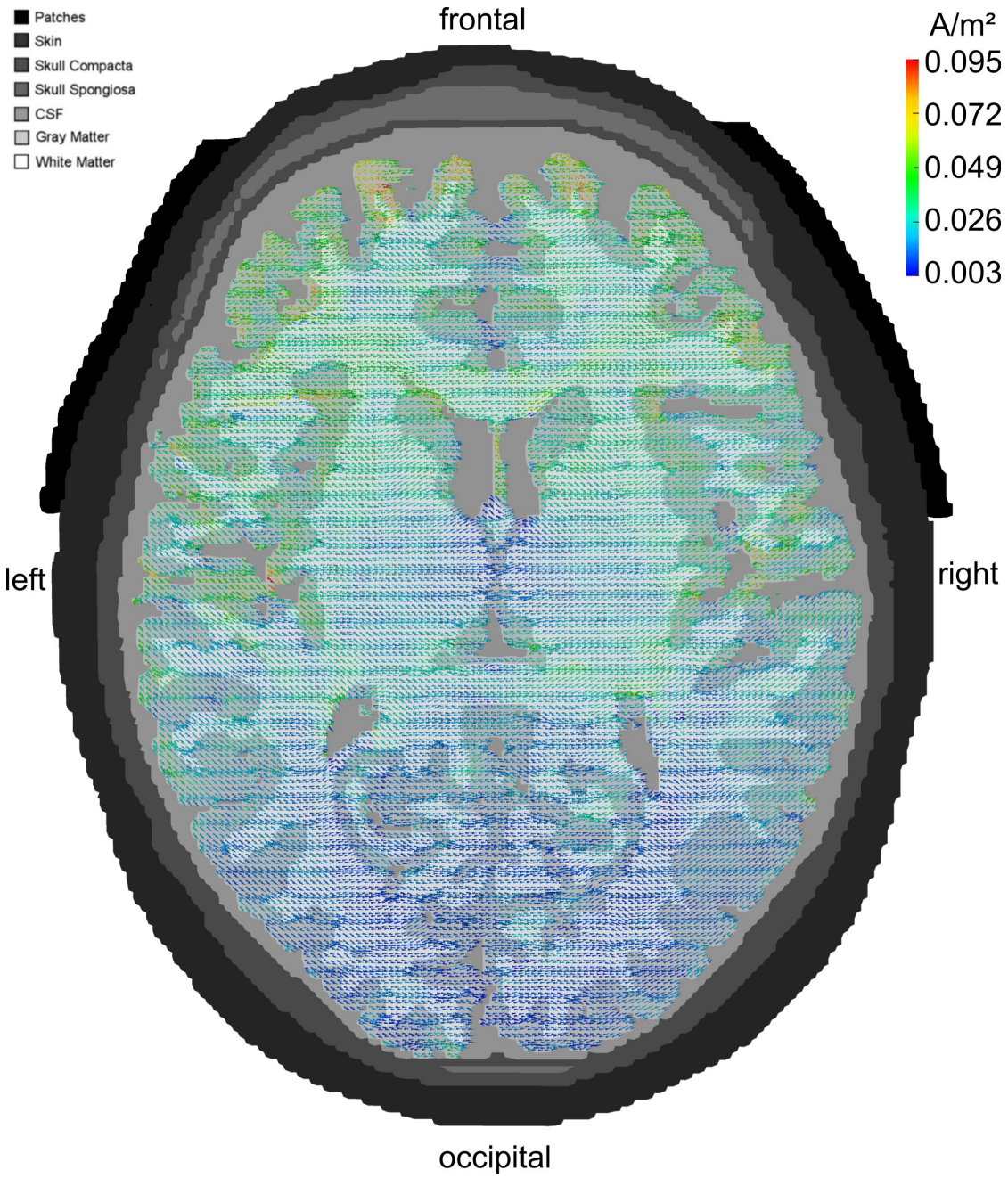

Figure 4.8.: Axial view of current flow field. The stimulation electrodes are centered around electrode positions F7 and F8. While strong current densities can be seen in the frontal lobe, only weak current density amplitudes can be found in the temporal and parietal lobes. The occipital lobe receives nearly no current density. Adapted from [82].

the findings of this simulation study, the lateral electrode montage might be better suited for the treatment of major depression as compared to the electrode montages that was used by Boggio and colleagues [13] and Fregni and colleagues [38]. However, the stimulation of the left dlPFC without stimulating other parts of the frontal lobe is not possible with standard bipolar tCS electrode montages (Figures 4.7 and 4.8). For this reason, a novel algorithmic-based optimization approach, which can be used to optimize the current density in a specific target region, while minimizing current density in the remaining brain, is presented in Section 5.

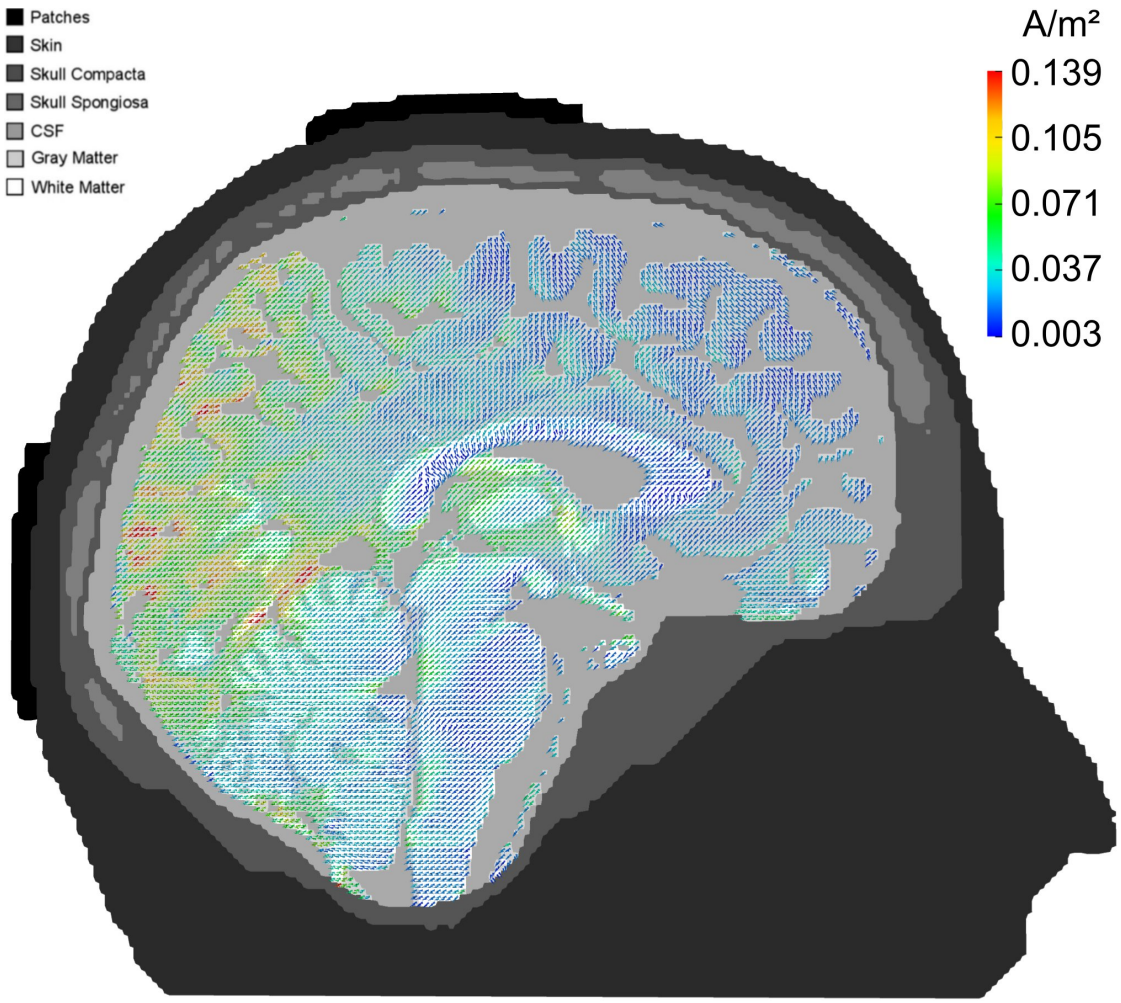

Figure 4.9.: Sagittal view of current flow field. The stimulation electrodes were centered around electrode positions Cz and Oz, resulting in maximal current density amplitudes in posterior brain regions, especially in the occipital cortex. Adapted from [82].

Figures 4.9 and 4.10 depict the cortical current density distributions when the medial and lateral electrode configurations for stimulating the occipital lobes are used, respectively. As can be seen in Figures 4.9 and 4.10, both electrode configurations show strongest cortical current flow field amplitudes in posterior brain regions, especially in the occipital part. The medial configuration leads to strongest current densities of about $0.13\,\mathrm{Am}^{-2}$ in the occipital lobe, while maximal current densities of about $0.09\,\mathrm{Am}^{-2}$ can be seen when the lateral electrode configuration is used for stimulation. Moreover, when using the medial configuration, strongest current densities can be seen in the medial part of the occipital cortex, whereas the lateral configuration leads to current density which are not restricted to the medial part of the occipital cortex but also reach the more lateral parts. However, both electrode montages are well suited for a stimulation of the occipital cortex. This has also been confirmed by several experimental studies investigating lateral and medial electrode configurations for occipital cortex stimulation, see Antal and colleagues [4] and Herrmann and colleagues [54] for an overview of the existing literature.

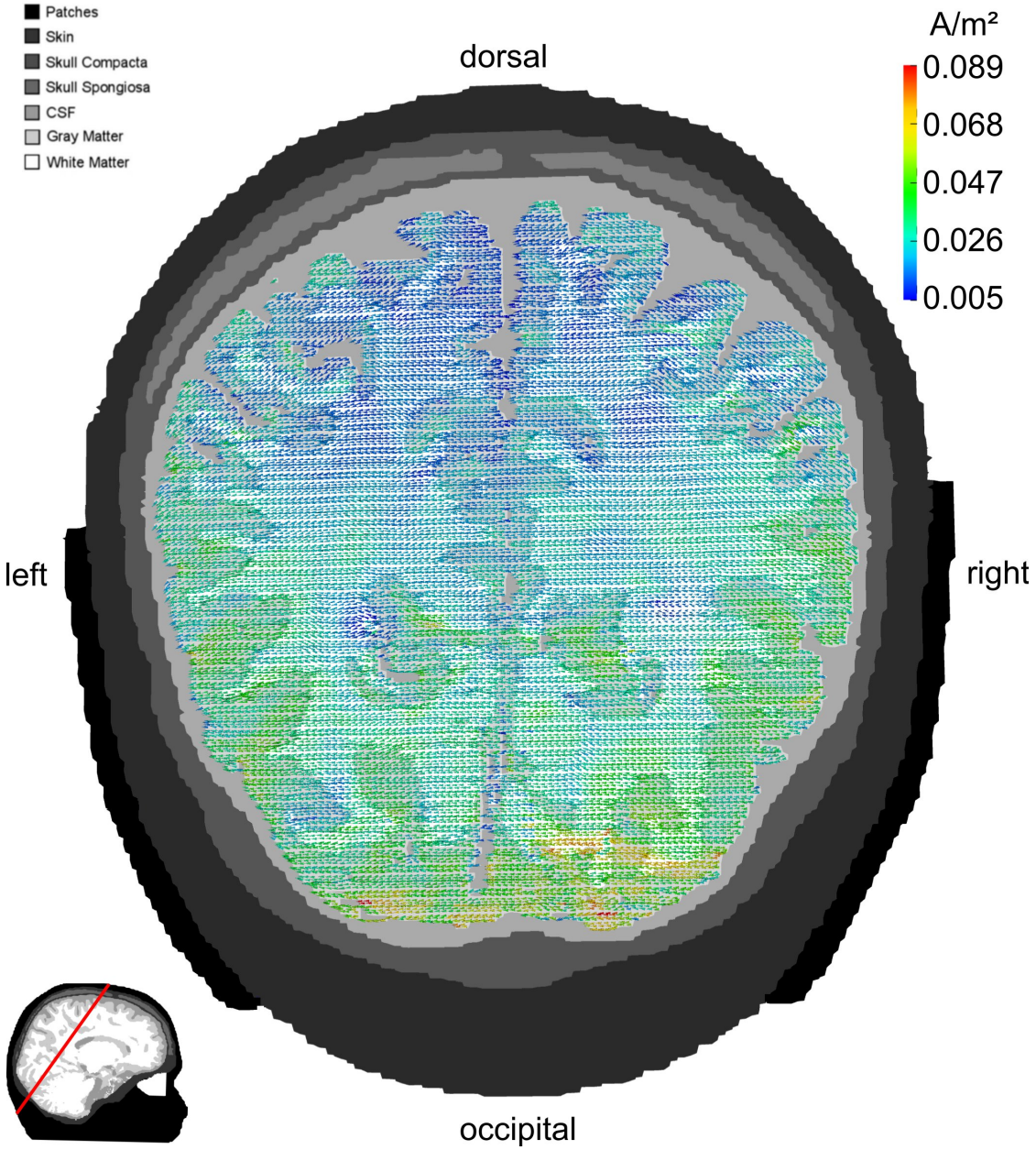

Figure 4.10.: Transversal view of current flow field. The stimulation electrodes were centered around electrode positions P7 and P8. The current flow field pattern shows a clear maximum over posterior brain regions, but also reaches parietal and temporal cortex regions. The slice is indicated on the upper left figure. Adapted from [82].

4.3. Electrode montages for auditory cortex stimulation

In Neuling and colleagues [81], an auditory detection experiment with humans was conducted, the EEG was recorded concurrently and simultaneously oscillating transcranial direct current stimulation with 10 Hz ($\alpha - tDCS$) was applied. The detection thresholds were found to depend on the phase of the oscillation that was entrained by the $\alpha - tDCS$. For stimulation, the standard tCS bipoloar electrode montage that was investigated deeply in Section 4.1

was used. The induced cortical current flow field in a highly-realistic six-compartment FE head model with white matter anisotropy is depicted in Figure 4.1-E1. While relative strong currents reach both auditory cortices, the current density amplitude in nearly all cortical lobes is of the same order of magnitude. Moreover, cathodal stimulation of the left auditory cortex might lead to inhibitory effects, whereas anodal stimulation of the right auditory cortex might induce excitatory effects. Therefore, it remains to be investigated whether the effects of stimulation, which were found to be highly significant, are elicited by the stimulation of the auditory cortices or driven by stimulation of other cortical regions. For this reasons, the practicability of four electrode montages for targeting the auditory cortices is investigated.

For appropriate estimation of the primary auditory cortex locations and orientations, the auditory cortices of the subject of this study are localized in combined 74-channel EEG and 274-channel MEG experiments. For localization of the primary auditory cortices and to get the orientation of the auditory N1 component correctly, a source analysis of the measured auditory evoked fields and potentials is performed. After preprocessing, the dipole solution for the auditory N1 component is calculated from the averaged AEF and AEP using CURRY. By combining the AEF and AEP, the location and orientation of the primary N1 component can be fairly accurately be determined and is used as target vectors for bi-hemispheric auditory cortex stimulation.

In this study, four electrode montages for bi-hemispheric auditory cortex stimulation (size of the electrodes is 25 mm $\times$ 25 mm) are introduced

- *Electrode montage 1:* Two anodes are positioned above the area of the primary auditory cortices and a total current of 0.5 mA is applied to each anode. The cathode is centered around electrode location Cz, see Figure 4.11-A.
- *Electrode montage 2:* Similar to electrode montage 1, but a larger cathode with a size of 70 mm $\times$ 70 mm is used, see Figure 4.11-B.
- *Electrode montage 3:* A four-by-one electrode montage on both hemispheres: The anodes are positioned above the areas of the auditory cortices and are surrounded by four return electrodes, see Figure 4.11-C. A total current of 1 mA is applied to each anode.
- *Electrode montage 4:* Two-by-one electrode montage on both hemispheres: The anodes are positioned 2 cm anterior and the cathode 2 cm posterior to the regions of the primary auditory cortices, respectively, see Figure 4.11-D. A total current of 1 mA is applied to both anodes.

Results

Electrode montage A1/Cz

Figure 4.12 shows the brain current density vector field when two anodes are placed above the auditory cortices and the cathode is centered around electrode location Cz. As can be seen in the figure, the current flow field is rather widespread. While both auditory cortices receive

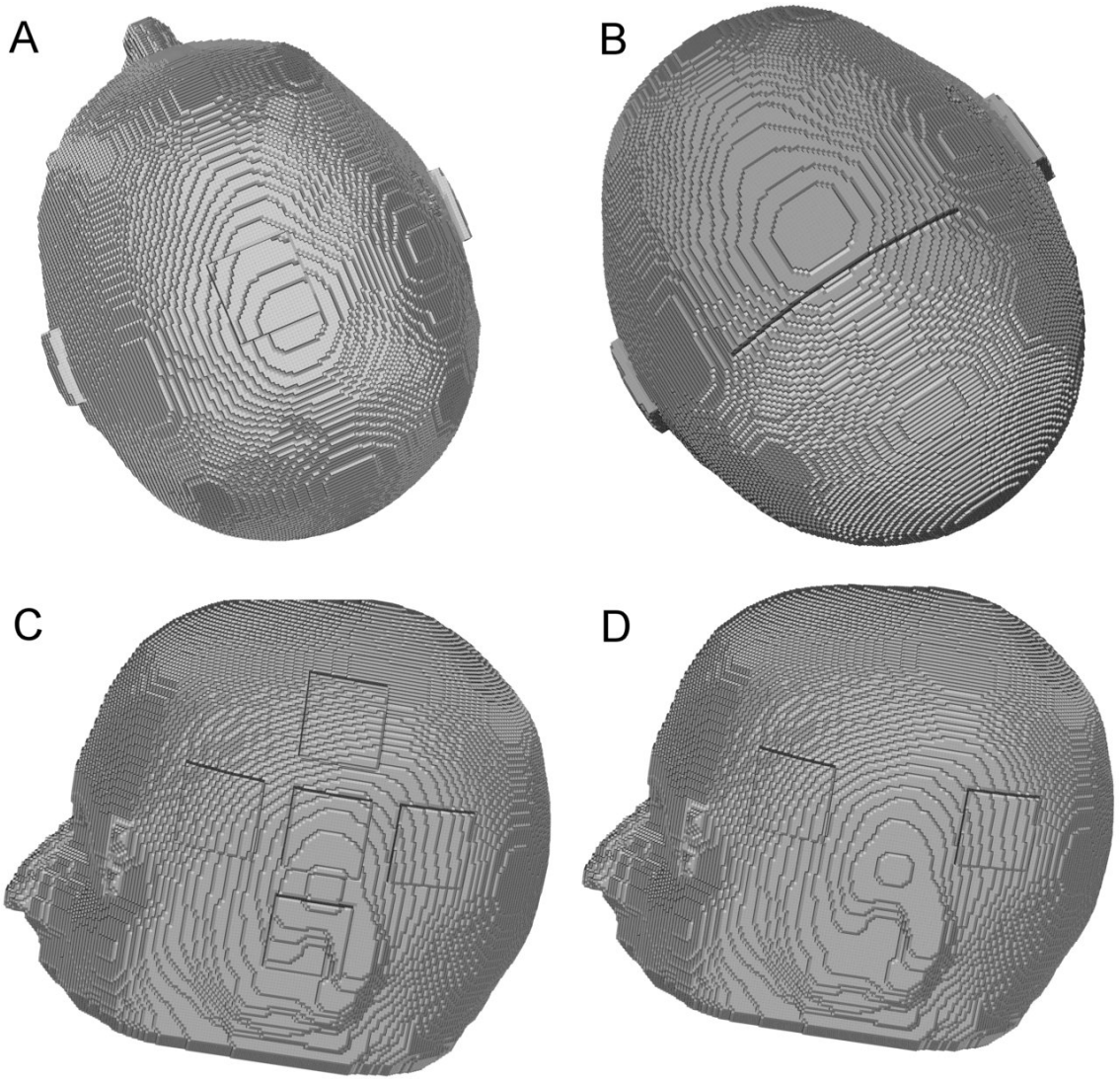

Figure 4.11.: Four electrode montages for targeting the auditory cortices. Figures -A, -B, -C and -D depict electrode montages 1 ,2 ,3 and 4, respectively.

current densities of about $0.05\,\mathrm{Am}^{-2}$, a peak cortical current density of about $0.1\,\mathrm{Am}^{-2}$ occur in non-target cortical lobes in between the anodes and the cathode (Figure 4.12). Moreover, current densities of about $0.06\,\mathrm{Am}^{-2}$ can be seen in the white matter compartment, especially in the corpus callosum region. Inferior brain regions receive nearly no current densities, see Figure 4.12.

Table 4.1 depicts the parallelity between the induced current flow fields and the auditory cortex target vectors. With *par* values of 65.65 % and 48.28 % on the left and right hemispheres, the current flow field shows only little parallelity with the target vectors.

Electrode montage A1/ large Cz

Figure 4.13 depicts the pattern of cortical current density when two active electrodes are

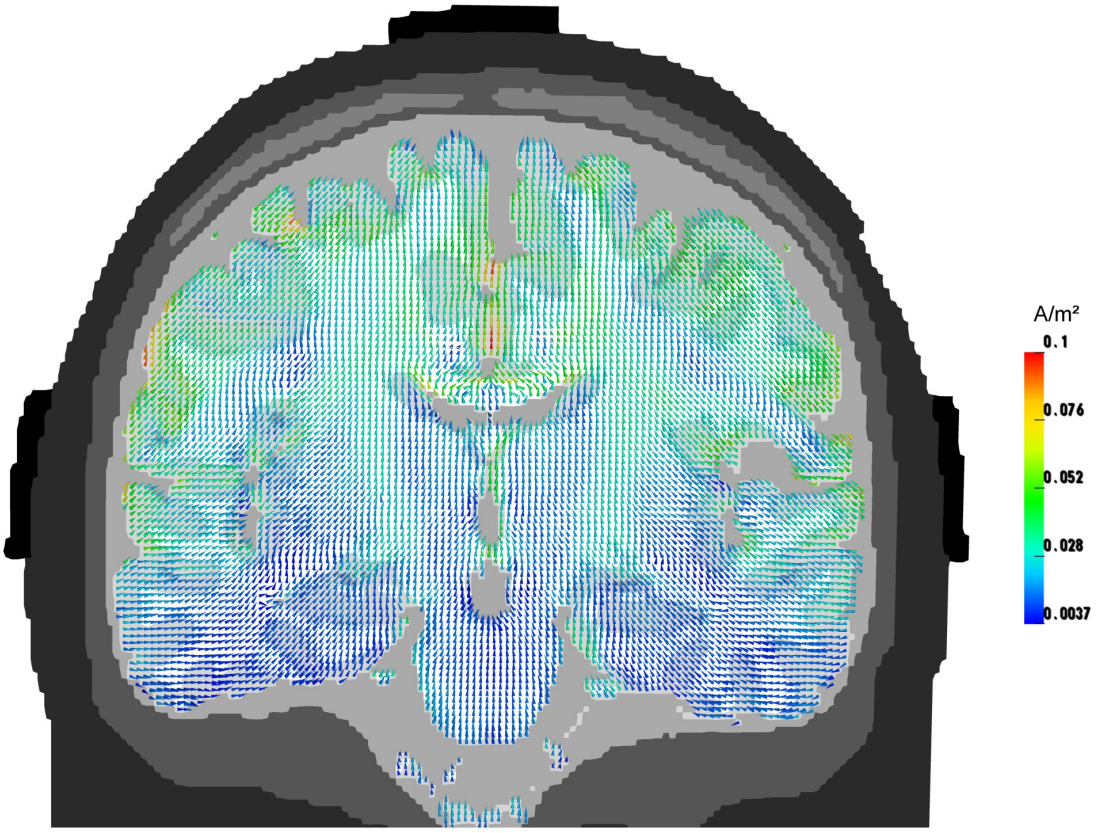

Figure 4.12.: Electrode montage 1 for auditory cortex stimulation. Two anodes are positioned above the area of the primary auditory cortices and a total current of 0.5 mA is applied to each anode. The cathode is centered around electrode location Cz.

positioned above the auditory cortices and a larger cathode is located at electrode location Cz. The current flow pattern is very similar to the pattern that was induced by electrode montage 1, but the maximal current density amplitude in the brain is decreased by 10 % (from 0.1 Am^{-2} to 0.09 Am^{-2}). Similarly, cortical current densities of about 0.05 Am^{-2} and 0.06 Am^{-2} occur in the auditory cortices and in the white matter compartment, respectively (Figure 4.13).

With *par* values of 65.43 % and 48.83 % on the left and right hemispheres, the current flow field only shows minor directional agreement with the auditory cortex target vectors.

Four-by-one electrode montage

Figure 4.14 displays the brain current density vector field when four-by-one electrode montages are placed above the auditory cortices. Current density is not restricted to, but focused to auditory cortex regions. Superior and inferior brain regions receive almost no current densities (Figure 4.14). The current density in the auditory cortices is 0.045 Am^{-2}, see Figure 4.14.

With a PAR value of 42.96 % and 25.53 % for right- and left-hemispheric auditory cortex stimulation, the induced current density vector fields are mainly oriented orthogonally to the target vectors, see Table 4.1. The four-by-one electrode montage is thus very focused in terms of current density amplitude, but the orientation component of the primary auditory

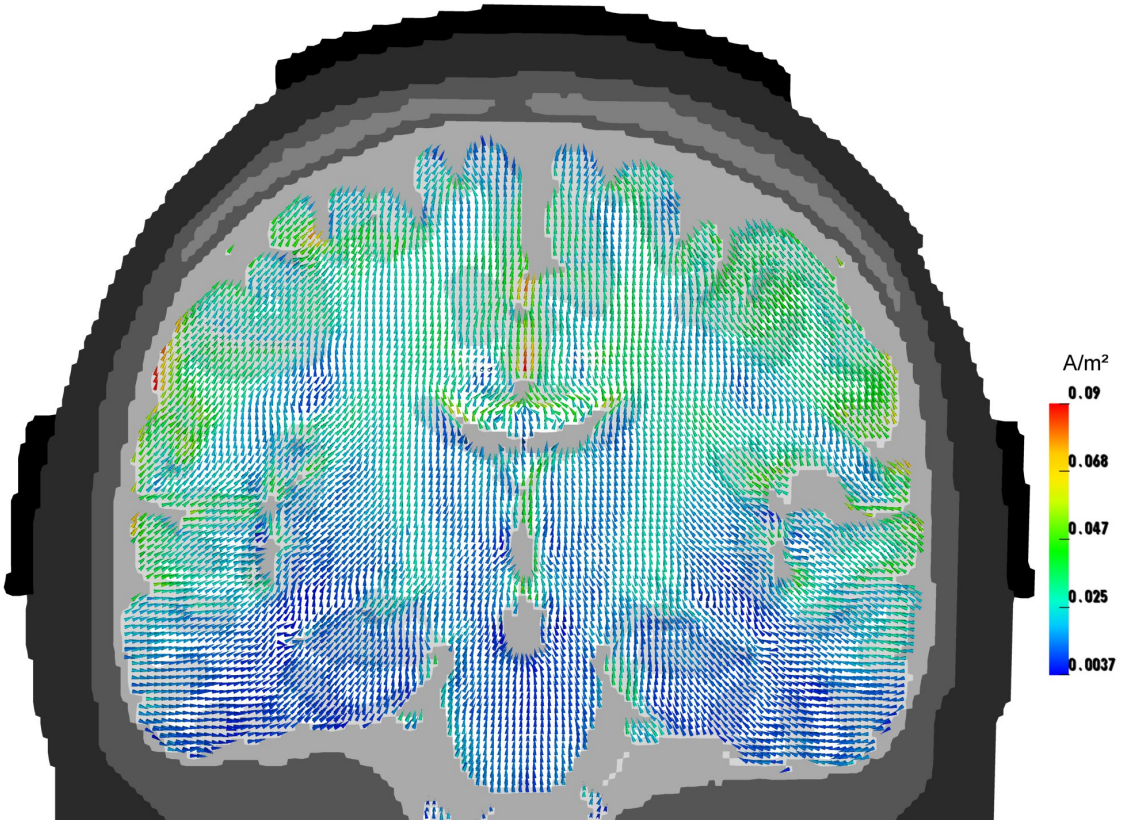

Figure 4.13.: Electrode montage 2 for auditory cortex stimulation. Two anodes are positioned above the area of the primary auditory cortices and a total current of 1 mA is applied to each anode. A large cathode with a size of 70 cm × 70 cm is centered around electrode location Cz.

cortices cannot be appropriately stimulated. The four-by-one electrode configuration is thus only suitable for stimulating radial target vectors.

Anterior-Posterior electrode montage

Figure 4.15 displays the pattern of cortical current density for electrodes being centered 2 cm anterior and 2 cm posterior to the location of the auditory cortices. Current density is not restricted to, but focused to auditory cortex regions. Strongest current density amplitudes of about 0.099 Am^{-2} occur in both auditory cortices (Figure 4.15). Moreover, also weaker current densities of about 0.05 Am^{-2} can be seen in deeper brain structures. Non-auditory cortical regions receive nearly no current densities (Figure 4.15). With *par* values of 80.92 % and 78.74 %, the current density is oriented mainly parallel to the auditory cortex target vectors (Table 4.1).

Discussion

Electrode montages A1/Cz and A1/large Cz

Electrode montages 1 and 2 showed a very widespread current flow pattern with the strongest intensities located in between the anodes and the cathode (Figures 4.12 and 4.13). The maximum current density in the brain thus lies in between the stimulating electrodes, in line

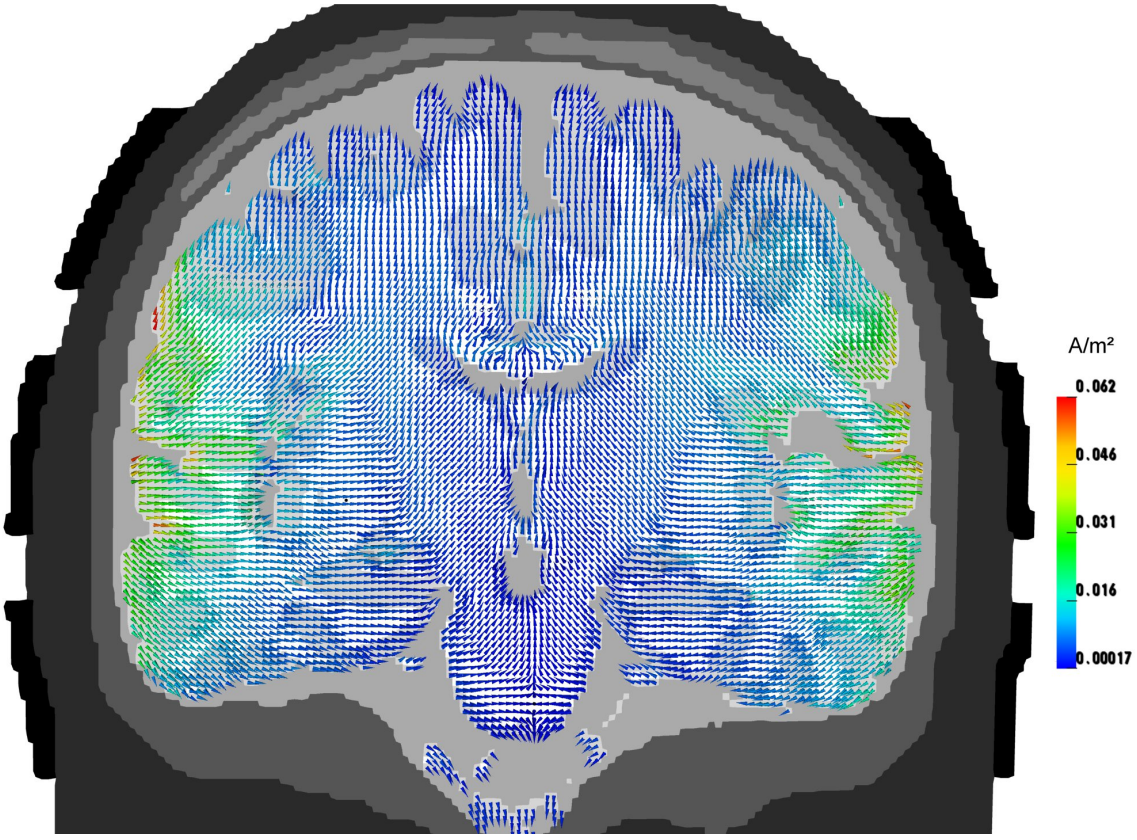

Figure 4.14.: Four-by-one electrode montage for auditory cortex stimulation. Two anodes are positioned above the area of the primary auditory cortices and a total current of 1 mA is applied to each anode. Four cathodes are positioned on the neighboring electrode locations.

with the findings of Section 4.1. With target current densities of about $0.05\,\mathrm{Am}^{-2}$, the current density in the auditory cortices is relatively low. On the contrary, relatively high current densities of about $0.1\,\mathrm{Am}^{-2}$ and $0.09\,\mathrm{Am}^{-2}$ occurred in non-auditory cortex regions. This might lead to inhibitory/excitatory side effects of stimulation.

Moreover, for effective stimulation, the optimized current density distribution should be oriented perpendicularly to the cortical surface [11, 23]. Also, the direction is important as shown by Bindman and colleagues [11] and Creutzfeldt and colleagues [23] who were able to demonstrate in physical measurements in rats and cats, respectively, that the neural firing rate is strongly influenced by the direction of the field to the cortical surface. Perpendicularly-

Table 4.1.: Directional agreement (in %) between the current flow fields $\boldsymbol{J}$ and the auditory cortex target vectors $\boldsymbol{e}$.

Electrode montage	Left auditory cortex	Right auditory cortex
1	65.65	48.28
2	65.43	48.83
3	42.96	25.35
4	80..92	78.74

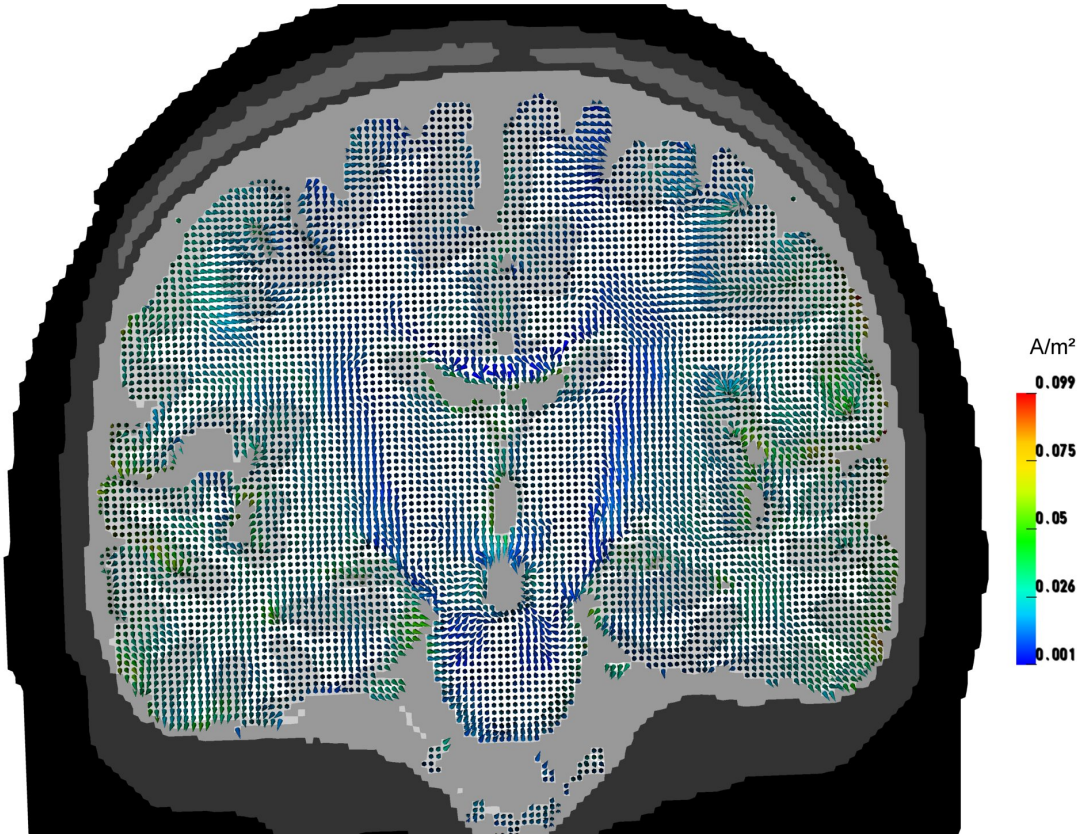

Figure 4.15.: Two-by-one electrode montage on both hemispheres. The anodes are positioned 2 cm anterior and the cathode 2 cm posterior to the regions of the primary auditory cortices

inwards (and parallel to the long apical dendrites of the large pyramidal cells in cortical layer V) stimulation, i.e. anodal stimulation, strongly enhanced the activity of the cortical neurons, whereas radially-outwards stimulation, i.e. cathodal stimulation, inhibited it. The orientation of the electric field to the target is thus also a very important aspect for an efficient and focused stimulation. As the current flow pattern show only minor parallelity to the target vectors and strongest current density amplitudes occurred in non-auditory cortex regions, both electrode montages are not suitable for a targeted and focused stimulation of the auditory cortices.

Four-by-one electrode montage

The four-by-one electrode montage induced a rather focal current flow pattern in brain regions underneath the stimulating anodes. As the anodes were centered above the auditory cortex regions, strongest current flow field amplitudes can thus be seen in the target regions. However, the current flow field was mainly oriented orthogonally to the auditory cortex target vectors. Because the primary auditory N1 component is mainly oriented tangentially to the scalp surface (see Figure 5.11), the four-by-one electrode montage is not suitable for a targeted stimulation of the auditory cortices.

As was shown, the four-by-one electrode montage induced a radial and rather focal current flow field underneath the anodes, in line with Dmochowski and colleagues [33]. When there is

no multi-array tCS device available for sensor optimization, a four-by-one electrode montage can thus be used for a focused stimulation of radial target vectors. This is also possible with a standard bipolar electrode montages as the current at the cathodes might be divided into four currents of $-0.25\,\mathrm{mA}$.

Anterior-Posterior electrode montage

As the electrodes were positioned 2 cm anterior and 2 cm posterior to the target region, strongest cortical current densities can be seen in the auditory cortices. Again, the maximum current density in the brain thus lies in between the stimulating electrodes. Strongest current density amplitudes of about $0.1\,\mathrm{Am}^{-2}$ can be seen in the target regions. In comparison to the other investigated electrode montages, the current flow field shared much more directional agreement with the auditory cortex target vectors. As the induced cortical current flow field was oriented inwards and mainly parallel to both auditory cortices, excitatory effects of stimulation can be expected on both hemispheres. As an identical applied current pattern (e.g. 1 mA) was used for both anodes and cathodes, a standard two-channel tCS stimulator might thus also be used to simultaneously induce excitatory effects in both auditory cortices. While the slightly inwards orientation component of the target vector cannot be approximated appropriately and mild inhibitory/excitatory effects induced by side-stimulation might occur, the anterior-posterior electrode montage clearly outperformed the other bipolar electrode montages for auditory cortex stimulation and the electrode montage that was used by Neuling and colleagues [81].

5

Current density optimization in transcranial current stimulation

As was shown in a highly-realistic volume conductor model (see Figure 4.2-E1), conventional bipolar electrode montages induce a rather broad cortical current flow field with the largest intensities often located in the non-target brain regions. Moreover, inter-individually varying conductivity profiles (see Section 4.1 and [81, 142]), variation in brain anatomy [26, 33, 144], the size, form and location of the stimulating electrodes (see Sections 4.2 and 4.3 and [77, 144, 142]) and brain abnormalities [26, 144] strongly influence the cortical current flow fields. While significant effects of stimulation as compared to sham were reported in clinical studies [38, 81, 84], it is rather unclear whether the effects are driven by the stimulation of the target brain region or elicited by the stimulation of non-target regions.

In order to investigate this issue, current density optimization approaches might be used to calculate current flow fields which are maximal in a presumed target region and comparably low in non-target regions. The simplest solution might be to use a set of bipolar electrode montages at fixed locations and calculate the induced current density distribution in the volume conductor model [60]. These simple solutions, however, do not minimize current densities in non-target regions, control current density in the skin compartment (might cause skin burns) or compensate exhibitory/inhibitory side effects of stimulation. Moreover, as the CSF channels current density away from the target region (see Figure 4.1-C1 and Figure 4.5-B), radially oriented target vectors can most often not be appropriately stimulated with conventional bipolar electrode montages. Keeping in mind the disadvantages of simple trial-and-error methods, algorithmic-based optimization approaches for multi-array transcranial direct current stimulation were introduced [33, 60, 96, 115]. Im and colleagues [60] used an

evolution strategy algorithm to search for two electrode locations which generate maximal current flow towards a certain target direction. They used structural MRI data of a standard brain atlas and tessellated it into 118,433 tetrahedral elements and 19,981 nodes. Im and colleagues reported that they could calculate optimal bipolar scalp electrode montages which can stimulate target brain regions with minimal injection currents. Recently, Park and colleagues [96] calculated optimal injection current/potential at 12 electrodes by solving a constrained optimization problem. They evaluated the current density distribution in a realistic head model using the finite element method adopting the superposition principle. Park and colleagues [96] reported that the average current density values at the target area were increased (between 35 % and 78 %) after the optimization. Also, averaged current density in non-target regions was shown to be reduced by a maximal factor of 14.2 % by controlling the input values of the electrodes.
Dmochowski and colleagues [33] used a multi-array consisting of 64 fixed electrode locations to calculate optimized stimulation protocols for presumed target regions. They applied *least square*, *Weighted least squares with individual L_1 constraint*, *linearly constrained minimum variance* and *optimization for intensity* optimization approaches for this purpose. In order to analyze their optimization methods, Dmochowski and colleagues [33] employed radial and tangential targets and reported that compared with conventional bipolar electrode montages their optimization approach achieved electric fields which exhibit simultaneously greater focality and target intensity at cortical targets using the same total current applied.
Sadleir and colleagues [115] devised a method of steering current towards a selected area by reference to a 19-electrode montage applied to a high-resolution FE head model. They used a non-linear optimization procedure to maximize mean current densities inside the left inferior frontal gyrus while simultaneously restricting overall current and median current densities within the accumbens.

In this thesis, a novel optimization approach for safe (currents can be controlled both at the skin and brain levels) and well-targeted multi-array transcranial current stimulation is proposed. Existence of at least one minimizer and residual and objective convergence results are proven for the proposed optimization methods. For discretization of the respective optimization problems, the finite element method is employed and the existence of at least one minimizer to the discretized optimization problems is shown. For numerical solution of the corresponding discretized problem, the alternating direction method of multipliers is employed.

5.1. Methods

5.1.1. Motivation and objective functional

Let us reconsider a volume conductor model Ω, its boundary $\Gamma \in C^1$ and a number S of fixed scalp electrodes. In order to calculate optimized stimulation protocols for presumed

target vectors, a multi-channel tCS array consisting of $S = 74$ fixed electrode locations (the locations of an extended 10-10 EEG electrode system, see Figure 5.2) is generated. Figure 5.1 depicts an overview of the optimization setting in a two-dimensional model. In an optimal stimulation, the induced current flow field is maximal in a presumed target region Ω_t and zero in non-target regions $\Omega_r = \Omega \setminus \Omega_t$. Physically, a focused stimulation without stimulating non-target regions is not possible as the current has to flow through the volume conductor to reach the target region. For this reason, the current flow field is restricted by a constant $\epsilon > 0$ such that

$$|\sigma \nabla \Phi| \leq \epsilon \qquad \text{in } \Omega_r$$

As was shown in Section 4.1, the maximal current density in the skin is substantially higher as compared to the maximal current density in the brain. When the size of the scalp electrodes is reduced, the ratio is even more increased [144]. For this reason, using an identical safety constraint ϵ for scalp and brain is not feasible as will be discussed in the following: When using a very high safety value ϵ for the scalp (e.g. $2\,\mathrm{Am}^{-2}$), the optimization method will not minimize current densities in non-target brain regions as all currents in the brain are below $2\,\mathrm{Am}^{-2}$. On the other hand, when using a very low threshold value of $0.04\,\mathrm{Am}^{-2}$, the optimizer might calculate very weak applied current pattern at the fixed electrodes in order to minimize current density in the scalp. Therefore, different values ϵ for scalp and brain are used, allowing to account for patient safety both at the scalp and brain levels and a focused stimulation in the brain. As the currents in the skull and CSF are weaker as compared to the current densities in the scalp (see Section 4.1) and not important for patient safety, the threshold value for the skin compartment is also used for the skull and CSF compartments. The new threshold vector ϵ is thus defined in the following

Definition 5.1 (Threshold vector ϵ)**.** Let $\Omega_s \subset \Omega$ being a subset of Ω containing the volume conductor elements in the skin, skull and CSF compartments. Furthermore, let us assume $\Omega_b \subset \Omega$ to be a subset representing the elements in the brain compartments. The combined threshold vector ϵ for a well-targeted and safe stimulation is then defined as

$$\epsilon = \begin{cases} \epsilon_1, & \text{if } i \in \Omega_s \\ \epsilon_2, & \text{if } i \in \Omega_b \end{cases}$$

Secondly, the total current applied to all electrodes is limited to 2 mA, a commonly used safety criteria [33].

As discussed before, for effective stimulation, the optimized current density distribution should be oriented perpendicularly to the cortical surface [11, 23]. Also, the direction is important as shown by Bindman and colleagues [11] and Creutzfeldt and colleagues [23] who were able to demonstrate in physical measurements in rats and cats, respectively, that the neural firing rate is strongly influenced by the direction of the field to the cortical surface. In order to force the current density to be oriented mainly parallel to the target vector, the integral $\int_{\Omega_t} \langle \sigma \nabla \Phi, \boldsymbol{e} \rangle \, \mathrm{d}\boldsymbol{x}$

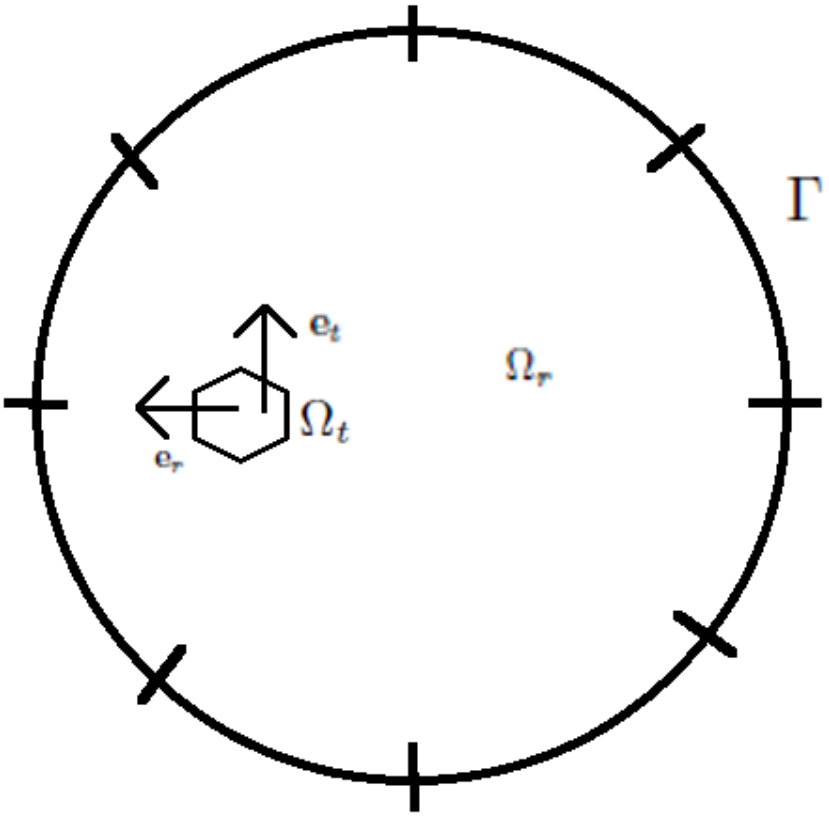

Figure 5.1.: Optimization setup in a two-dimensional model. The target region Ω_t, a radial ($\boldsymbol{e}_r$) and tangential ($\boldsymbol{e}_t$) target vector and the boundary Γ of the volume conductor model Ω are depicted. The electrodes are represented by radial lines.

with $\boldsymbol{e} \subset \Omega_t$ being a vector parallel and radially-inwards-oriented to the cortical surface is thus maximized.

In the following, the current flow field constraint in the whole domain is reformulated as $\omega|\sigma\nabla\Phi| \leq \epsilon$ with a weight $\omega = 1$ in Ω_r and $0 < \omega \ll 1$ in Ω_t.

A constrained optimization problem is considered

$$
\begin{aligned}
(\mathbf{P}_{tCS}) \qquad & -\textstyle\int_{\Omega_t}\langle\sigma\nabla\Phi, \boldsymbol{e}\rangle \,\mathrm{d}\boldsymbol{x} \;\rightarrow \min_{\boldsymbol{I}\in H_{\diamond}^{-\frac{1}{2}}(\Gamma)} \\
& \text{subject to} \quad \omega|\sigma\nabla\Phi| \leq \epsilon \\
& \int_{\Gamma}|\boldsymbol{I}| \,\mathrm{d}\boldsymbol{x} \;\leq 4 \\
& \nabla\cdot\sigma\nabla\Phi = 0 \qquad \textit{in } \Omega \\
& \langle\sigma\nabla\Phi, \boldsymbol{n}\rangle = \boldsymbol{I} \qquad \textit{on } \partial\Gamma \\
& \Phi = 0 \qquad \textit{on } \Gamma_D
\end{aligned}
$$

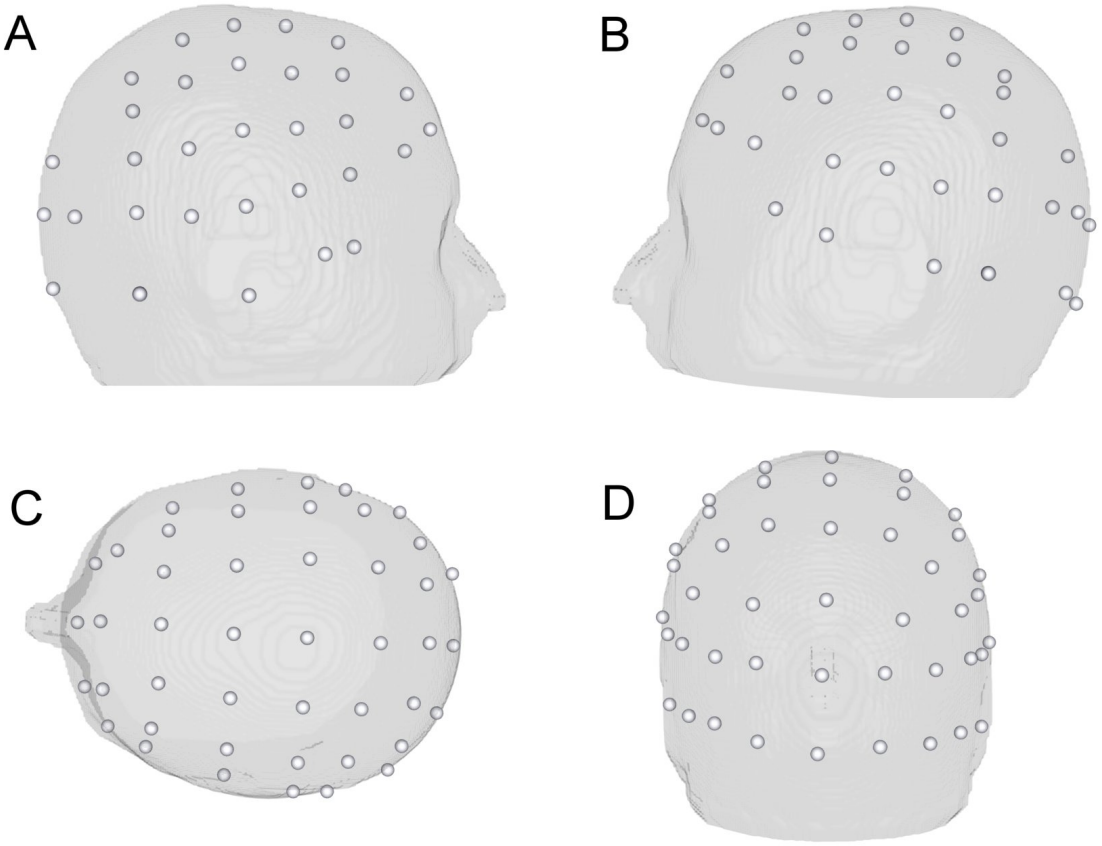

Figure 5.2.: Location of the stimulating electrodes using an extended 10-10 EEG system. Figures A, B, C and D show the electrodes on the right hemisphere, left hemisphere, anterior and posterior parts of the volume conductor model, respectively.

which is a control problem with Neumann boundary conditions [72]. Note that the safety limitation on the inflow current is a *control constraint*, while the limit on the current flow outside the target region is a *state constraint*. The state constraint ensures that $\langle \sigma \nabla \Phi, \boldsymbol{n} \rangle$ is bounded in $H^{-\frac{1}{2}}(\Gamma)$

Theorem 5.1. Let us consider the optimization problem $(\mathbf{P}_{tCS})$ with $\epsilon > 0$. The state constraint $\omega |\sigma \nabla \Phi| \leq \epsilon$ ensures that $\langle \sigma \nabla \Phi, \boldsymbol{n} \rangle$ is bounded in $H^{-\frac{1}{2}}(\Gamma)$.

Proof. Let $U_{\tilde{\epsilon}}$ be a neighborhood of Γ. Since $\omega \neq 0$ in Ω, it follows that $\omega \neq 0$ in $U_{\tilde{\epsilon}}$. The state constraint $\omega |\sigma \nabla \Phi| \leq \tilde{\epsilon}$ ensures that $|\sigma \nabla \Phi| \leq \frac{\tilde{\epsilon}}{\omega}$ in $U_{\tilde{\epsilon}}$ which implies that $\sigma \nabla \Phi$ is bounded in $U_{\tilde{\epsilon}}$. Since $\sigma \in (\mathcal{L}^{\infty})^{3\times 3}$ it follows that $\nabla \Phi$ is bounded in $U_{\tilde{\epsilon}}$. Consequently, $\Phi \in H^1(U_{\tilde{\epsilon}})$ and the trace theorem ensures that $\Phi \in H^{\frac{1}{2}}(\Gamma)$. Therefore, $\langle \nabla \Phi, \boldsymbol{n} \rangle \in H^{-\frac{1}{2}}(\Gamma)$ and it follows that $\nabla \Phi$ is bounded in $H^{-\frac{1}{2}}(\Gamma)$. Finally, from $\sigma \in (\mathcal{L}^{\infty})^{3\times 3}$ one obtains that $\langle \sigma \nabla \Phi, \boldsymbol{n} \rangle$ is bounded in $H^{-\frac{1}{2}}(\Gamma)$. □

The constrained optimization problem $(\boldsymbol{P}_{tCS})$ is a rather challenging optimal control problem. First, the current density distribution $\sigma \nabla \Phi$ is optimized, while many other applications require to optimize the potential field Φ. Second, a point-wise gradient state constraint is used. While optimal control problems with state constraints were frequently used [48] not much attention

was given to gradient state constraints only until recently [118]. Third, one looks for a control function $\boldsymbol{I}$ vanishing on large parts of the boundary, known as *sparsity optimal control problem* [55]. Indeed, one rather looks for $\boldsymbol{I}$ as a combination of concentrated measures rather than an L^1-function, so the above integral formulation has to be understood as formal notation for the total variation of the Radon measure identified with $\boldsymbol{I}$. This will be made precise in the next section.

Applying Gauss' Theorem to $\int_{\Omega_t}\langle\sigma\nabla\Phi,\boldsymbol{e}\rangle\,\mathrm{d}\boldsymbol{x}$ provides a further motivation for the proposed objective functional. Assuming σ and $\boldsymbol{e}$ locally constant, one obtains

$$\int_{\Omega_t}\langle\sigma\nabla\Phi,\boldsymbol{e}\rangle\,\mathrm{d}\boldsymbol{x}=\int_{\Omega_t}\sigma\Phi\nabla\cdot\boldsymbol{e}+\boldsymbol{e}\nabla\sigma\Phi\,\mathrm{d}\boldsymbol{x}=\int_{\Omega_t}\nabla\cdot(\sigma\Phi\boldsymbol{e})\,\mathrm{d}\boldsymbol{x}=\int_{\Gamma_t}\langle\sigma\Phi\boldsymbol{e},\boldsymbol{n}\rangle\mathrm{d}\sigma$$

In order to maximize the current densities along the target direction, the potential should be maximized where the target vector $\boldsymbol{e}$ is oriented parallel to the outward normal vector $\boldsymbol{n}$ on Γ_t.

5.1.2. Optimal control problem

5.1.2.1. Continuous formulation

The optimization problem $(\mathbf{P}_{tCS})$ is now reconsidered. In order to provide a rigorous formulation of the safety constraint, $\boldsymbol{I}$ is interpreted as a Radon measure in the space $\mathcal{M}(\Gamma)$. The norm of $\mathcal{M}(\Gamma)$, this is the total variation of a measure, is an appropriate replacement for the L^1-norm. The constraint then becomes

$$\|\boldsymbol{I}\|_{\mathcal{M}(\Gamma)}\leq 4$$

In order to obtain a unified formulation also allowing for other design constraints respectively a discrete electrode setup, a feasible set $\mathcal{D}(\Gamma)\subset H_\diamond^{-\frac{1}{2}}(\Gamma)$ is introduced. To further simplify notation, an operator A is defined via

$$A:\quad H_\diamond^{-\frac{1}{2}}(\Gamma)\to L^2(\Omega)^3,\quad \boldsymbol{I}\mapsto\sigma\nabla\Phi.$$

Since $\boldsymbol{I}\in\mathcal{D}(\Gamma)\subset H_\diamond^{-\frac{1}{2}}(\Gamma)$, the boundary value problem for the Poisson equation has a unique solution $\Phi\in H^1(\Omega)$ bounded by a multiple of the norm of $\boldsymbol{I}$ as guaranteed by Theorem 3.1. This implies that A is a well-defined linear operator. Hence $\sigma\nabla\Phi=A\boldsymbol{I}$ can be substituted in $(\mathbf{P}_{tCS})$, which leads to the following equivalent reformulation

$$\begin{aligned}(\mathbf{P}^2_{tCS,\epsilon})\qquad -\textstyle\int_{\Omega_t}\langle A\boldsymbol{I},\boldsymbol{e}\rangle\,\mathrm{d}\boldsymbol{x}\ &\to\min_{\boldsymbol{I}\in\mathcal{D}(\Gamma)}\\ \text{subject to}\quad \omega|A\boldsymbol{I}|&\leq\epsilon\\ \|\boldsymbol{I}\|_{\mathcal{M}(\Gamma)}&\leq 4\end{aligned}$$

The existence of at least one minimizer $\boldsymbol{I} \in \mathcal{D}(\Gamma)$ to the minimization problem $(\mathbf{P}^2_{tCS,\epsilon})$ is the topic of the following theorem.

Theorem 5.2. Let $\mathcal{D}(\Gamma)$ be weakly closed in $H_\diamond^{-\frac{1}{2}}(\Gamma)$, let $0 \in \mathcal{D}(\Gamma)$ and let $\epsilon > 0$. Then there exists at least one minimizer $\boldsymbol{I} \in \mathcal{D}(\Gamma)$ of the convex optimization problem $(\mathbf{P}^2_{tCS,\epsilon})$.

Proof. An easy computation reveals that $\boldsymbol{I} = 0 \in \mathcal{D}(\Gamma)$ is feasible for $(\mathbf{P}^2_{tCS,\epsilon})$, i.e., the set of feasible points is not empty. Moreover, it is closed in the weak-star topology of $H_\diamond^{-\frac{1}{2}}(\Gamma) \cap \mathcal{M}(\Gamma)$, which can be seen as follows: First of all the norm in $\mathcal{M}(\Gamma)$ is lower semicontinuous with respect to weak-star convergence in this space, which implies that a limit of feasible points satisfies the safety constraint as well. Moreover, weak convergence of a sequence $\boldsymbol{I}^k$ in $H_\diamond^{-\frac{1}{2}}(\Gamma)$ implies weak convergence of $A\boldsymbol{I}^k$ in $L^2(\Omega)^3$, which implies that the limit satisfies the state constraint due to the weak closedness of pointwise constraints in L^2. Moreover, the feasible set is obviously bounded in $\mathcal{M}(\Omega)$ due to the safety constraint and in $H_\diamond^{-\frac{1}{2}}(\Gamma)$ since any feasible $\boldsymbol{I}$ is the Neumann trace of a function bounded in $W^{1,\infty}(\Omega)$ and thus in $H^1(\Omega)$. Hence, the Banach-Alaoglu Theorem implies compactness in the weak-star topology. Since the objective is a bounded linear functional and in particular weak-star lower semicontinuous the existence of a minimizer is obtained by standard reasoning. □

One can observe that the objective as well as all terms involved in the constraints of the optimal control problem are linear. This allows us to renormalize the unknown and in this way eliminate the safety constraint. This motivates the following simplified version

$$\begin{aligned} (\mathbf{P}_{tCS,\epsilon}) \qquad & -\textstyle\int_{\Omega_t} \langle A\boldsymbol{I}, \boldsymbol{e}\rangle \,\mathrm{d}\boldsymbol{x} && \to \min_{\boldsymbol{I}\in\mathcal{D}(\Gamma)} \\ & \text{subject to} && \omega|A\boldsymbol{I}| \le \epsilon \end{aligned}$$

Residual and objective convergence results and dual and residual feasibility for the simplified optimization problem $(\mathbf{P}_{tCS,\epsilon})$ are shown in the Appendix A.1.

The existence of a minimizer $\boldsymbol{I}$ in $H_\diamond^{-\frac{1}{2}}(\Gamma)$ of $(\mathbf{P}_{tCS,\epsilon})$ can be shown

Theorem 5.3. Let $\mathcal{D}(\Gamma)$ be weakly closed in $H_\diamond^{-\frac{1}{2}}(\Gamma)$, let $0 \in \mathcal{D}(\Gamma)$ and let $\epsilon > 0$. Then there exists at least one minimizer $\boldsymbol{I} \in \mathcal{D}(\Gamma) \cap H_\diamond^{-\frac{1}{2}}(\Gamma)$ of the convex optimization problem $(\mathbf{P}_{tCS,\epsilon})$.

Proof. The existence of at least one minimizer $\boldsymbol{I} \in \mathcal{D}(\Gamma) \cap H_\diamond^{-\frac{1}{2}}(\Gamma)$ follows by similar reasoning as in Theorem 5.2. □

By renormalizing a minimizer of $(\mathbf{P}_{tCS,\epsilon})$ a minimizer for the full optimization problem $(\mathbf{P}^2_{tCS,\epsilon})$ with safety constraint for the control can be obtained, which of course only holds if the total variation of the minimizer is finite.

Theorem 5.4. Let $\epsilon > 0$ be a threshold parameter and $\boldsymbol{I} \in \mathcal{M}(\Gamma) \cap H_\diamond^{-\frac{1}{2}}(\Gamma)$ be a minimizer of the simplified minimization problem $(\mathbf{P}_{tCS,\epsilon})$. Then $\tilde{\boldsymbol{I}} = \frac{4\boldsymbol{I}}{\|\boldsymbol{I}\|_{\mathcal{M}(\Gamma)}}$ is a minimizer of $(\mathbf{P}^2_{tCS,\delta})$ with $\delta = \frac{4\epsilon}{\|\boldsymbol{I}\|_{\mathcal{M}(\Gamma)}}$ and vice versa.

Proof. As $\frac{4\epsilon}{\|\boldsymbol{I}\|_{\mathcal{M}(\Gamma)}}$ is constant, one obtains

$$\langle A\tilde{\boldsymbol{I}}, \boldsymbol{e}\rangle = \langle A\frac{4\epsilon}{\|\boldsymbol{I}\|_{\mathcal{M}(\Gamma)}}, \boldsymbol{e}\rangle = \frac{4\epsilon}{\|\boldsymbol{I}\|_{\mathcal{M}(\Gamma)}}\langle A\boldsymbol{I}, \boldsymbol{e}\rangle$$

which implies that the minimization problems are equivalent. The constraints are also equivalent:

" $\Rightarrow$ "

Let $\epsilon > 0$ be a threshold parameter and $\boldsymbol{I} \in \mathcal{M}(\Gamma) \cap H_{\diamond}^{-\frac{1}{2}}(\Gamma)$ be a minimizer of the simplified minimization problem $(\mathbf{P}_{tCS,\epsilon})$ which implies that $|\omega A\boldsymbol{I}| \leq \epsilon$. It is shown that this implies $|\omega A\tilde{\boldsymbol{I}}| \leq \delta$ and $\left\|\tilde{\boldsymbol{I}}\right\|_{\mathcal{M}(\Gamma)} \leq 4$ for $\tilde{\boldsymbol{I}} = \frac{4\boldsymbol{I}}{\|\boldsymbol{I}\|_{\mathcal{M}(\Gamma)}}$ and $\delta = \frac{4\epsilon}{\|\boldsymbol{I}\|_{\mathcal{M}(\Gamma)}}$.

$$\begin{aligned}
|\omega A\tilde{\boldsymbol{I}}| &= |\omega A\frac{4\boldsymbol{I}}{\|\boldsymbol{I}\|_{\mathcal{M}(\Gamma)}}| \\
&\leq |\omega A\boldsymbol{I}||\frac{4}{\|\boldsymbol{I}\|_{\mathcal{M}(\Gamma)}}| \\
&\leq \epsilon|\frac{4}{\|\boldsymbol{I}\|_{\mathcal{M}(\Gamma)}}| \\
&= \frac{4\epsilon}{\|\boldsymbol{I}\|_{\mathcal{M}(\Gamma)}} \\
&= \delta
\end{aligned}$$

where the fact that $\|\boldsymbol{I}\|_{\mathcal{M}(\Gamma)}$ is positive was used. Furthermore

$$\begin{aligned}
\left\|\tilde{\boldsymbol{I}}\right\|_{\mathcal{M}(\Gamma)} &= \left\|\frac{4\boldsymbol{I}}{\|\boldsymbol{I}\|_{\mathcal{M}(\Gamma)}}\right\|_{\mathcal{M}(\Gamma)} \\
&\leq 4\left\|\frac{\boldsymbol{I}}{\|\boldsymbol{I}\|_{\mathcal{M}(\Gamma)}}\right\|_{\mathcal{M}(\Gamma)} \\
&\leq 4\frac{\|\boldsymbol{I}\|_{\mathcal{M}(\Gamma)}}{\|\boldsymbol{I}\|_{\mathcal{M}(\Gamma)}} \\
&= 4
\end{aligned}$$

which implies that the control and state constraint of the minimization problem $(\mathbf{P}^2_{tCS,\delta})$ are also fulfilled.

" $\Leftarrow$ "

Let $\delta = \frac{4\epsilon}{\|\boldsymbol{I}\|_{\mathcal{M}(\Gamma)}} > 0$ be a threshold parameter and $\tilde{\boldsymbol{I}} \in \mathcal{M}(\Gamma) \cap H_{\diamond}^{-\frac{1}{2}}(\Gamma)$ be a minimizer of the minimization problem $(\mathbf{P}^2_{tCS,\delta})$. This implies that $|\omega A\tilde{\boldsymbol{I}}| \leq \delta$ and $\left\|\tilde{\boldsymbol{I}}\right\|_{\mathcal{M}(\Gamma)} \leq 4$. It will be shown that this implies that $|\omega A\boldsymbol{I}| \leq \epsilon$ for the simplified minimization problem $(\mathbf{P}_{tCS,\epsilon})$. Because

$$\tilde{\boldsymbol{I}} = \frac{4\boldsymbol{I}}{\|\boldsymbol{I}\|_{\mathcal{M}(\Gamma)}}$$

one obtains

$$\boldsymbol{I} = \frac{\tilde{\boldsymbol{I}} \, \|\boldsymbol{I}\|_{\mathcal{M}(\Gamma)}}{4}$$

and it follows

$$\begin{aligned} |\omega A \boldsymbol{I}| &= |\omega A \frac{\tilde{\boldsymbol{I}} \, \|\boldsymbol{I}\|_{\mathcal{M}(\Gamma)}}{4}| \\ &\leq |\omega A \tilde{\boldsymbol{I}}| |\frac{\|\boldsymbol{I}\|_{\mathcal{M}(\Gamma)}}{4}| \\ &\leq \delta |\frac{\|\boldsymbol{I}\|_{\mathcal{M}(\Gamma)}}{4}| \\ &\leq \delta \frac{\|\boldsymbol{I}\|_{\mathcal{M}(\Gamma)}}{4} \\ &= \frac{4\epsilon}{\|\boldsymbol{I}\|_{\mathcal{M}(\Gamma)}} \frac{\|\boldsymbol{I}\|_{\mathcal{M}(\Gamma)}}{4} \\ &= \epsilon \end{aligned}$$

which implies that the state constraint of the minimization problem $(\mathbf{P}_{tCS,\epsilon})$ is also fulfilled. □

While the minimization problem $(\mathbf{P}_{tCS,\epsilon})$ is thus only used for numerical realization, the scaled stimulation protocol $\tilde{\boldsymbol{I}} = \frac{4\boldsymbol{I}}{\|\boldsymbol{I}\|_{\mathcal{M}(\Gamma)}}$ guarantees patient safety both at the scalp and brain levels, see Theorem 5.4. Furthermore, the maximal current density $|\sigma \nabla \Phi| = |A\boldsymbol{I}| \leq \delta$ in non-target regions is given as $\frac{4\epsilon}{\|\boldsymbol{I}\|_{\mathcal{M}(\Gamma)}}$.

At first glance the usefulness of Theorem 5.4 might appear limited, since the relation between the constraint bounds ϵ and δ is quite implicit, depending on the minimizer of the second problem. However, since there is no natural choice of the bound in either case one can choose δ or ϵ in appropriate ranges equally well. However, it turns out that $(\mathbf{P}_{tCS,\epsilon})$ is somewhat easier in particular with respect to numerical solutions. Moreover, it facilitates the introduction of sparsity constraints on the control by additional penalization, which is the subject of the following discussion.

5.1.2.2. Penalized problem formulation

In order to control the applied current pattern at the fixed electrodes, the minimization problem $(\mathbf{P}_{tCS,\epsilon})$ is extended by two penalties. While an L_2 term $\alpha \int_\Gamma \boldsymbol{I}^2 \, \mathrm{d}\boldsymbol{x}$ is introduced to penalize the energy of the applied current pattern, an L_1 penalty $\beta \, \|\boldsymbol{I}\|_{\mathcal{M}(\Gamma)}$ is used to minimize the number of active electrodes in the minimization procedure. The latter has to be reinterpreted in the same way as the safety constraint in terms of Radon measures. This leads to the following minimization problem

$$\begin{aligned} (\mathbf{P}^{\alpha,\beta}_{tCS,\epsilon}) \qquad & -\textstyle\int_{\Omega_t} \langle A\boldsymbol{I}, \boldsymbol{e} \rangle \, \mathrm{d}\boldsymbol{x} \quad + \alpha \displaystyle\int_\Gamma \boldsymbol{I}^2 \, \mathrm{d}\boldsymbol{x} + \beta \, \|\boldsymbol{I}\|_{\mathcal{M}(\Gamma)} \to \min_{\boldsymbol{I} \in \mathcal{D}(\Gamma)} \\ & \text{subject to} \qquad \omega |A\boldsymbol{I}| \leq \epsilon \end{aligned}$$

The minimization problem $(\mathbf{P}^{\alpha,\beta}_{tCS,\epsilon})$ with $\alpha > 0, \beta = 0$ and $\alpha = 0, \beta > 0$ will be called the L_2 regularized optimization procedure (L2R) and the L_1 regularized optimization procedure (L1R), respectively. If both penalties are active the penalty term is also known as elastic net. Since the L^2 penalty adds strict convexity to the problem, uniqueness of a minimizer together with existence can be shown via analogous arguments as above:

Theorem 5.5. Let $\mathcal{D}(\Gamma)$ be weakly closed in $H_\diamond^{-\frac{1}{2}}$, $0 \in \mathcal{D}(\Gamma)$, and let $\alpha > 0$ and $\beta = 0$. Then there exists a unique minimizer $\boldsymbol{I} \in L^2(\Gamma)$ to the L2R constrained optimization problem $(\mathbf{P}^{\alpha,0}_{tCS,\epsilon})$. The result can even be generalized for $\beta \geq 0$.

For the problem with pure L^1-penalization the proof of existence is almost identical to the one of Theorem 5.4

Theorem 5.6. Let $\mathcal{D}$ be weakly closed in $H_\diamond^{-\frac{1}{2}}$ and let $\alpha = 0$ and $\beta > 0$. Then there exists at least one minimizer $\boldsymbol{I} \in \mathcal{M}(\Gamma) \cap \mathcal{D}(\Gamma)$ to the L1R constrained optimization problem $(\mathbf{P}^{0,\beta}_{tCS,\epsilon})$.

5.1.2.3. Discrete problem

The finite element method is used for numerical discretization of the considered optimization problem. Let us discretize $\boldsymbol{I} = \sum_{i=1}^{S} I_i \phi_i$ with ϕ_i being finite element basis functions. As $\boldsymbol{I}$ has mean zero, I_S can be eliminated. Furthermore, mappings A_1 and A_2 representing the discretizations are introduced

$$A_1 : \mathbb{R}^{S-1}(\Gamma) \to \mathcal{D}(\Gamma), \qquad \boldsymbol{I}_S = (I_i) \mapsto \boldsymbol{I} = \sum_{i=1}^{S} I_i \phi_i$$
$$A_2 : L^2(\Omega)^3 \to \mathbb{R}^{3N}(\Omega), \quad \sigma \nabla \Phi \mapsto (\sigma \nabla \Phi)_i$$

with N the number of elements and define the discretized operator $A_2 \circ A \circ A_1 = B \in \mathbb{R}^{3N \times (S-1)}$.

Remark 5.1 (The discretized optimization matrix B)**.** For sensor optimization, a set S of surface electrodes is used. In this study $S = 74$ fixed electrode locations are used, see Figure 5.2. Fixing the first electrode as reference, 73 pairs of surface electrodes are used to calculate the discretized mapping $B \in \mathbb{R}^{3N \times (S-1)}$. To calculate the i-th row $B_i \in \mathbb{R}^{3N}$, the tCS forward problem with inhomogeneous Neumann boundary conditions at the i-th and the reference electrode and homogeneous Neumann boundary conditions at the remaining model surface is used. As was shown in Section 3.3, an AMG-CG solver with solver accuracy level of 10^{-7} is used which requires approximatively 90 seconds to solve the equation system $\mathbf{K}\Phi^{tDCS} = \boldsymbol{b}$ in a highly realistic six-compartment volume conductor model consisting of 2,2 million nodes and elements. After solving this equation system, the influence matrix $B_i = \sigma \nabla \Phi^{tDCS}$ is computed from the values Φ^{tDCS} at the FE nodes. The whole mapping B can thus be calculated in less than two hours of computation time.

As the target vector $\boldsymbol{e}$ is only defined in the target region, a mapping $\tilde{\boldsymbol{e}}$: $\Omega_t \mapsto \mathbb{R}^{3N}(\Omega)$ is

defined

$$\tilde{\boldsymbol{e}}_i = \begin{cases} \boldsymbol{e}_i, & \text{if } e_i \in \Omega_t \\ 0, & \text{otherwise} \end{cases}$$

and $\langle B\boldsymbol{I}_S, \boldsymbol{e}\rangle$ is replaced by $\langle B\boldsymbol{I}_S, \tilde{\boldsymbol{e}}\rangle$, since $\langle B\boldsymbol{I}_S, \tilde{\boldsymbol{e}}\rangle = 0$ in $\Omega \setminus \Omega_t$. and the discretized optimization problem $(\bar{\mathbf{P}}_\epsilon^{\alpha,\beta})$ is introduced as

$$\begin{aligned} (\bar{\mathbf{P}}_\epsilon^{\alpha,\beta}) \qquad & -\langle B\boldsymbol{I}_S, \tilde{\boldsymbol{e}}\rangle \quad +\alpha\langle \boldsymbol{I}_S, \boldsymbol{I}_S\rangle + \beta \left\|\boldsymbol{I}_S\right\|_1 \to \min_{\boldsymbol{I}_s \in \mathbb{R}^{S-1}} \\ & \text{subject to} \quad \omega_i |(B\boldsymbol{I}_S)_i| \preceq \epsilon \end{aligned}$$

The existence (and potential uniqueness) of minimizers of the discretized optimization problem follows now directly from the above results since the regularity of finite element basis functions implies that the set

$$\mathcal{D}(\Gamma) = \{\boldsymbol{I} = \sum_{i=1}^{S} I_i \phi_i\}$$

satisfies all assumptions needed. For the sake of brevity, the issue of convergence of minimizers as $S \to \infty$ is not shown, which can, e.g., be shown via Γ-convergence of the functionals involved.

5.2. Implementation of the discretized optimization problem

The alternating direction method of multipliers (ADMM) [15] is used to obtain a numerical solution to the corresponding discretized problem. The ADMM is a variant of the *augmented Lagrangian method* for solving constrained optimization problems. The method combines important convergence properties (no strict convergence or finiteness is required) and the decomposability of the dual ascent method [15].
To solve the discretized optimization problem $(\bar{\mathbf{P}}_\epsilon^{\alpha,\beta})$, in a first step, the auxiliary variable $\boldsymbol{z} = \boldsymbol{I}_S \in \mathbb{R}^{S-1}$ is introduced in some terms of the objective functional, leading to the following problem

$$\begin{aligned} & -\langle B\boldsymbol{I}_S, \tilde{\boldsymbol{e}}\rangle \quad +\alpha\langle \boldsymbol{z}, \boldsymbol{z}\rangle + \beta \left\|\boldsymbol{z}\right\|_1 \to \min_{\boldsymbol{I}_S, \boldsymbol{z}} \\ & \text{subject to} \quad \omega_i |(B\boldsymbol{I}_S)_i| \preceq \epsilon \\ & \qquad\qquad\quad \boldsymbol{I}_S = \boldsymbol{z} \end{aligned}$$

In a next step, $B\boldsymbol{I}_S = \boldsymbol{y}$ is introduced

$$-\langle y, \tilde{\boldsymbol{e}}\rangle \quad +\alpha\langle \boldsymbol{z}, \boldsymbol{z}\rangle + \beta \left\|\boldsymbol{z}\right\|_1 \to \min_{\boldsymbol{I}_S, \boldsymbol{z}, \boldsymbol{y}} \tag{5.1}$$

$$\text{subject to} \quad \omega_i |(y)_i| \preceq \epsilon \tag{5.2}$$

$$\boldsymbol{I}_S = \boldsymbol{z} \tag{5.3}$$
$$B\boldsymbol{I}_S = \boldsymbol{y} \tag{5.4}$$

Furthermore, a function v is introduced as

$$v(\boldsymbol{y}) = \begin{cases} 0 & \text{if } \omega_i|(y)_i| \leq \epsilon \\ \infty & \text{else} \end{cases}$$

to make the inequality constraint implicit.

Then, the Lagrange function for the minimization problem reads

$$\begin{aligned} L(\boldsymbol{I}_S, \boldsymbol{y}, \boldsymbol{z}, \boldsymbol{p}_1, \boldsymbol{p}_2) &= \alpha\langle \boldsymbol{z}, \boldsymbol{z}\rangle + \beta \left\|\boldsymbol{z}\right\|_1 + \langle \boldsymbol{z} - \boldsymbol{I}_S, \boldsymbol{p}_1\rangle \\ &\quad -\langle \boldsymbol{y}, \tilde{\boldsymbol{e}}\rangle + \langle \boldsymbol{y} - B\boldsymbol{I}_S, \boldsymbol{p}_2\rangle + v \end{aligned}$$

The augmented Lagrangian $L_{\mu_1,\mu_2}(\boldsymbol{I}_S, \boldsymbol{y}, \boldsymbol{z}, \boldsymbol{p}_1, \boldsymbol{p}_2)$ which is to be minimized is then defined as

$$\begin{aligned} L_{\mu_1,\mu_2}(\boldsymbol{I}_S, \boldsymbol{y}, \boldsymbol{z}, \boldsymbol{p}_1, \boldsymbol{p}_2) &= \alpha\langle \boldsymbol{z}, \boldsymbol{z}\rangle + \beta \left\|\boldsymbol{z}\right\|_1 + \frac{\mu_1}{2}\langle \boldsymbol{z} - \boldsymbol{I}_S, \boldsymbol{z} - \boldsymbol{I}_S\rangle + \langle \boldsymbol{z} - \boldsymbol{I}_S, \boldsymbol{p}_1\rangle - \langle \boldsymbol{y}, \tilde{\boldsymbol{e}}\rangle \\ &\quad + \frac{\mu_2}{2}\langle \boldsymbol{y} - B\boldsymbol{I}_S, \boldsymbol{y} - B\boldsymbol{I}_S\rangle + \langle \boldsymbol{y} - B\boldsymbol{I}_S, \boldsymbol{p}_2\rangle + v(\boldsymbol{y}) \end{aligned}$$

with $\mu_1, \mu_2 \in \mathbb{R}$ and $\boldsymbol{p}_1 \in \mathbb{R}^{S-1}, \boldsymbol{p}_2 \in \mathbb{R}^{3N}$ being the *augmented Lagrangian parameters* and the *dual variables*, respectively [15].
For this Lagrangian, the ADMM iteration consists of updating $\boldsymbol{I}$,$(\boldsymbol{y}, \boldsymbol{z})$ and $(\boldsymbol{p}_1, \boldsymbol{p}_2)$ conditioned on the current values of the other variables. Therefore, for given $L_{\mu_1,\mu_2}(\boldsymbol{I}_S, \boldsymbol{y}, \boldsymbol{z}, \boldsymbol{p}_1, \boldsymbol{p}_2)$ do

$$\begin{aligned} \boldsymbol{I}_S^{k+1} &= argmin_{\boldsymbol{I}_S} \quad L_{\mu_1,\mu_2}(\boldsymbol{I}_S, \boldsymbol{y}^k, \boldsymbol{z}^k, \boldsymbol{p}_1^k, \boldsymbol{p}_2^k) \\ (\boldsymbol{z}, \boldsymbol{y})^{k+1} &= argmin_{(\boldsymbol{z},\boldsymbol{y})} \quad L_{\mu_1,\mu_2}(\boldsymbol{I}_S^{k+1}, \boldsymbol{y}, \boldsymbol{z}, \boldsymbol{p}_1^k, \boldsymbol{p}_2^k) \\ (\boldsymbol{p}_1, \boldsymbol{p}_2)^{k+1} &= argmin_{(\boldsymbol{p}_1,\boldsymbol{p}_2)} \quad L_{\mu_1,\mu_2}(\boldsymbol{I}_S^{k+1}, \boldsymbol{y}^{k+1}, \boldsymbol{z}^{k+1}, \boldsymbol{p}_1, \boldsymbol{p}_2) \end{aligned}$$

Minimization with respect to $\boldsymbol{I}_S$

Neglecting the terms of $L_{\mu_1,\mu_2}(\boldsymbol{I}_S, \boldsymbol{y}, \boldsymbol{z}, \boldsymbol{p}_1, \boldsymbol{p}_2)$ that do not depend on $\boldsymbol{I}_S$, one obtains

$$\begin{aligned} \frac{\mu_1}{2}\langle \boldsymbol{z}^k - \boldsymbol{I}_S^{k+1}, \boldsymbol{z}^k - \boldsymbol{I}_S^{k+1}\rangle &+ \langle \boldsymbol{z}^k - \boldsymbol{I}_S^{k+1}, \boldsymbol{p}_1^k\rangle \\ &+ \frac{\mu_2}{2}\langle \boldsymbol{y}^k - B\boldsymbol{I}_S^{k+1}, \boldsymbol{y}^k - B\boldsymbol{I}_S^{k+1}\rangle + \langle \boldsymbol{y}^k - B\boldsymbol{I}_S^{k+1}, \boldsymbol{p}_2^k\rangle \end{aligned}$$

Rearranging the terms, neglecting the terms that do not depend on $\boldsymbol{I}_S^{k+1}$ and putting the integrals together one gets

$$\frac{\mu_1}{2}\langle \boldsymbol{z}^k - \boldsymbol{I}_S^{k+1} - \frac{1}{\mu_1}\boldsymbol{p}_1^k, \boldsymbol{z}^k - \boldsymbol{I}_S^{k+1} - \frac{1}{\mu_1}\boldsymbol{p}_1^k\rangle + \frac{\mu_2}{2}\langle B\boldsymbol{I}_S^{k+1} - \boldsymbol{y}^k + \frac{1}{\mu_2}\boldsymbol{p}_2^k, B\boldsymbol{I}_S^{k+1} - \boldsymbol{y}^k + \frac{1}{\mu_2}\boldsymbol{p}_2^k\rangle$$

Expanding the equations leads to the following quadratic minimization problem

$$\begin{aligned}\frac{\mu_1}{2}\langle \boldsymbol{I}_S^{k+1}, \boldsymbol{I}_S^{k+1}\rangle &- 2\langle \boldsymbol{z}^k, \boldsymbol{I}_S^{k+1}\rangle + \frac{2}{\mu_1}\langle \boldsymbol{I}_S^{k+1}, p_1^k\rangle \\ &+ \frac{\mu_2}{2}(-2\langle \boldsymbol{y}^k, B\boldsymbol{I}_S^{k+1}\rangle + \langle B\boldsymbol{I}_S^{k+1}, B\boldsymbol{I}_S^{k+1}\rangle + \frac{2}{\mu_2}\langle B\boldsymbol{I}_S^{k+1}, \boldsymbol{p}_2^k\rangle\end{aligned}$$

which can be easily solved by differentiating with respect to $\boldsymbol{I}_S^{k+1}$ and setting the equation system to be zero

$$(\mu_1 Id + \mu_2 B^{tr}B)\boldsymbol{I}_S^{k+1} - (\mu_1 \boldsymbol{z}^k - Id\boldsymbol{p}_1^k + \mu_2 B^{tr}\boldsymbol{y}^k - B^{tr}\boldsymbol{p}_2^k) = 0$$

and solving with respect to $\boldsymbol{I}_S^{k+1}$

$$\boldsymbol{I}_S^{k+1} = (\mu_1 Id + \mu_2 B^{tr}B)^{-1}(\mu_1 \boldsymbol{z}^k - Id\boldsymbol{p}_1^k + \mu_2 B^{tr}\boldsymbol{y}^k - B^{tr}\boldsymbol{p}_2^k)$$

with $Id \in \mathbb{R}^{(S-1)\times(S-1)}$ being the $(S-1)\times(S-1)$ identity matrix.

Minimization with respect to y

Neglecting the terms of $L_{\mu_1,\mu_2}(\boldsymbol{I}_S, \boldsymbol{y}, \boldsymbol{z}, \boldsymbol{p}_1, \boldsymbol{p}_2)$ that do not depend on $\boldsymbol{y}^{k+1}$, rearranging the terms and putting the integrals together leads to

$$\begin{aligned}&\frac{\mu_2}{2}\langle \boldsymbol{y}^{k+1} - B\boldsymbol{I}_S^{k+1} - \frac{1}{\mu_2}\boldsymbol{p}_2^k, \langle \boldsymbol{y}^{k+1} - B\boldsymbol{I}_S^{k+1} - \frac{1}{\mu_2}\boldsymbol{p}_2^k\rangle - \langle \boldsymbol{y}^{k+1}, \tilde{\boldsymbol{e}}\rangle + v(\boldsymbol{y}) \\ = \;& \frac{\mu_2}{2}\langle \boldsymbol{y}^{k+1} - B\boldsymbol{I}_S^{k+1} - \frac{1}{\mu_2}\boldsymbol{p}_2^k - \frac{1}{\mu_2}\tilde{\boldsymbol{e}}, \boldsymbol{y}^{k+1} - B\boldsymbol{I}_S^{k+1} - \frac{1}{\mu_2}\boldsymbol{p}_2^k - \frac{1}{\mu_2}\tilde{\boldsymbol{e}}\rangle + v(\boldsymbol{y})\end{aligned}$$

which can be solved analytically as follows

$$\boldsymbol{y}_i^{k+1} = \begin{cases} \frac{\epsilon}{\omega_i}\frac{(B\boldsymbol{I}_S^{k+1} + \frac{1}{\mu_2}\boldsymbol{p}_2^k + \frac{1}{\mu_2}\tilde{\boldsymbol{e}})_i}{|(B\boldsymbol{I}_S^{k+1} + \frac{1}{\mu_2}\boldsymbol{p}_2^k + \frac{1}{\mu_2}\tilde{\boldsymbol{e}})_i|}, & \text{if } |(B\boldsymbol{I}_S^{k+1} + \frac{1}{\mu_2}\boldsymbol{p}_2^k + \frac{1}{\mu_2}\tilde{\boldsymbol{e}})_i| > \frac{\epsilon}{\omega_i} \\ (B\boldsymbol{I}_S^{k+1} + \frac{1}{\mu_2}\boldsymbol{p}_2^k + \frac{1}{\mu_2}\tilde{\boldsymbol{e}})_i, & \text{otherwise}\end{cases}$$

Minimization with respect to z

Rearranging the terms and putting the integrals together leads to

$$\begin{aligned}&\alpha\langle \boldsymbol{z}^{k+1}, \boldsymbol{z}^{k+1}\rangle + \beta\left\|\boldsymbol{z}^{k+1}\right\|_1 + \frac{\mu_1}{2}\langle \boldsymbol{z}^{k+1} - \boldsymbol{I}_S^{k+1}, \boldsymbol{z}^{k+1} - \boldsymbol{I}_S^{k+1}\rangle + \langle \boldsymbol{z}^{k+1} - \boldsymbol{I}_S^{k+1}, \boldsymbol{p}_1^k\rangle \\ =\;& \alpha\langle \boldsymbol{z}^{k+1}, \boldsymbol{z}^{k+1}\rangle + \beta\left\|\boldsymbol{z}^{k+1}\right\|_1 + \frac{\mu_1}{2}\langle \boldsymbol{z}^{k+1} - \boldsymbol{I}_S^{k+1} - \frac{1}{\mu_1}\boldsymbol{p}_1^k, \boldsymbol{z}^{k+1} - \boldsymbol{I}_S^{k+1} - \frac{1}{\mu_1}\boldsymbol{p}_1^k\rangle \\ =\;& \alpha\langle \boldsymbol{z}^{k+1}, \boldsymbol{z}^{k+1}\rangle + \frac{\mu_1}{2}\langle \boldsymbol{z}^{k+1} - \boldsymbol{I}_S^{k+1} - \frac{1}{\mu_1}\boldsymbol{p}_1^k + \frac{1}{\mu_1}\beta, \boldsymbol{z}^{k+1} - \boldsymbol{I}_S^{k+1} - \frac{1}{\mu_1}\boldsymbol{p}_1^k + \frac{1}{\mu_1}\beta\rangle \\ =\;& \alpha\langle \boldsymbol{z}^{k+1}, \boldsymbol{z}^{k+1}\rangle \\ +\;& \langle \underbrace{\sqrt{\frac{\mu_1}{2}}Id}_{:=\tilde{I}d} z^{k+1} - \sqrt{\frac{\mu_1}{2}}\boldsymbol{I}_S^{k+1} - \frac{1}{\sqrt{2\mu_1}}\boldsymbol{p}_1^k + \frac{1}{\sqrt{2\mu_1}}\beta, \frac{\mu_1}{2}Idz^{k+1} - \sqrt{\frac{\mu_1}{2}}\boldsymbol{I}_S^{k+1} - \frac{1}{\sqrt{2\mu_1}}\boldsymbol{p}_1^k + \frac{1}{\sqrt{2\mu_1}}\beta\rangle\end{aligned}$$

Algorithm 2 Algorithm for the discretized minimization problem ($\bar{\mathbf{P}}_\epsilon^{\alpha,\beta}$)

Input: $B, \epsilon, \mu_1, \mu_2, \alpha, \beta, \omega, \tilde{\boldsymbol{e}}$, $\boldsymbol{I}_S^{prev}$, $\boldsymbol{I}_S^0$, $\boldsymbol{p}_1^0$, $\boldsymbol{p}_2^0$, $\boldsymbol{z}^0$, $\boldsymbol{y}^0$, N, TOL
$k = 0$
while $k < 3$ *or* $\left\|\boldsymbol{I}_S^k - \boldsymbol{I}_S^{prev}\right\| > TOL$ **do**
  $\boldsymbol{I}_S^{prev} = \boldsymbol{I}_S^k$
  $\boldsymbol{I}_S^{k+1} = (\mu_1 Id + \mu_2 B^{tr} B)^{-1}(\mu_1 \boldsymbol{z}^k - \boldsymbol{p}_1^k + \mu_2 B^{tr} \boldsymbol{y}^k - B^{tr} \boldsymbol{p}_2^k)$
  for $i = 1, \cdots, 3N$ **do**
    if $|(B\boldsymbol{I}_S^{k+1} + \frac{1}{\mu_2}\boldsymbol{p}_2^k + \frac{1}{\mu_2}\tilde{\boldsymbol{e}})_i| > \frac{\epsilon}{\omega_i}$ **then**
      $\boldsymbol{y}_i^{k+1} = \frac{\epsilon}{\omega_i} \frac{(B\boldsymbol{I}_S^{k+1} + \frac{1}{\mu_2}\boldsymbol{p}_2^k + \frac{1}{\mu_2}\tilde{\boldsymbol{e}})_i}{|(B\boldsymbol{I}_S^{k+1} + \frac{1}{\mu_2}\boldsymbol{p}_2^k + \frac{1}{\mu_2}\tilde{\boldsymbol{e}})_i|}$
    else
      $\boldsymbol{y}_i^{k+1} = (B\boldsymbol{I}_S^{k+1} + \frac{1}{\mu_2}\boldsymbol{p}_2^k + \frac{1}{\mu_2}\tilde{\boldsymbol{e}})_i$
    end if
  end for
  $\boldsymbol{z}^{k+1} = (\tilde{Id}^{tr}\tilde{Id} + \alpha Id)^{-1}\tilde{Id}^{tr}(\sqrt{\frac{\mu_1}{2}}\boldsymbol{I}_S^{k+1} + \frac{1}{\sqrt{2\mu_1}}\boldsymbol{p}_1^k - \frac{1}{\sqrt{2\mu_1}}\beta)$
  $\boldsymbol{p}_1^{k+1} = \mu_1(\boldsymbol{p}_1^k + \boldsymbol{I}_{tCS}^{k+1} - \boldsymbol{z}^{k+1})$
  $\boldsymbol{p}_2^{k+1} = \mu_2(\boldsymbol{p}_2^k + B\boldsymbol{I}_S^{k+1} - \boldsymbol{y}^{k+1})$
  $k = k + 1$
end while
$\delta = \frac{4\epsilon}{\|\boldsymbol{I}_S^{k+1}\|_{\mathcal{M}(\Gamma)}}$
return $\boldsymbol{I}_S^{k+1}$, δ, k, $\left\|\boldsymbol{I}_S^{k+1}\right\|_{\mathcal{M}(\Gamma)}$

The solution is simply given as

$$\boldsymbol{z}^{k+1} = (\tilde{Id}^{tr}\tilde{Id} + \alpha)^{-1}\tilde{Id}^{tr}(\sqrt{\frac{\mu_1}{2}}\boldsymbol{I}_S^{k+1} + \frac{1}{\sqrt{2\mu_1}}\boldsymbol{p}_1^k - \frac{1}{\sqrt{2\mu_1}}\beta)$$

Dual variable update

Finally, the dual variables can be updated in the following way

$$\begin{aligned} \boldsymbol{p}_1^{k+1} &= \mu_1(\boldsymbol{p}_1^k + B\boldsymbol{I}_S^{k+1} - \boldsymbol{y}^{k+1}) \\ \boldsymbol{p}_2^{k+1} &= \mu_2(\boldsymbol{p}_2^k + \boldsymbol{I}_S^{k+1} - \boldsymbol{z}^{k+1}) \end{aligned}$$

Putting together, the algorithm for the constrained minimization problem can be expressed as shown in Algorithm 2.

In the following, $\boldsymbol{I}_{tCS} = \boldsymbol{I}_S$ and $\mathbf{B}_{tCS} = \mathbf{B}$ are called to be discretized applied current pattern and the discretized optimization matrices for tCS modeling, respectively. Moreover, in all optimizations only the elements corresponding to the gray and white matter compartments are employed for the optimization.

Table 5.1.: Tangential target vector $\tilde{\boldsymbol{e}}$: Averaged (over 924 targets) scaled threshold value δ, the number of iterations k and the scaling factor $\|\boldsymbol{I}_{tCS}\|_{\mathcal{M}(\Gamma)}$ for tangential target vectors $\tilde{\boldsymbol{e}}$ and different input values ϵ.

$\epsilon\left[Am^{-2}\right]$	0.0001	0.0005	0.001	0.005	0.01
$\delta\left[Am^{-2}\right]$	0.00332	0.0085	0.0154	0.0175	0.0208
Iterations k	132	53	33	203	143
$\|\boldsymbol{I}_{tCS}\|_{\mathcal{M}(\Gamma)}$	120.15	233.96	352.279	1312.2	1919.93

Table 5.2.: Radial target vector $\tilde{\boldsymbol{e}}$: Averaged (over 924 targets) scaled threshold value δ, the number of iterations k and the scaling factor $\|\boldsymbol{I}_{tCS}\|_{\mathcal{M}(\Gamma)}$ for radial target vectors $\tilde{\boldsymbol{e}}$ and different input values ϵ.

$\epsilon\left[Am^{-2}\right]$	0.0001	0.0005	0.001	0.005	0.01
$\delta\left[Am^{-2}\right]$	0.0043	0.0114	0.015	0.023	0.025
Iterations k	134	36	35	68	118
$\|\boldsymbol{I}_{tCS}\|_{\mathcal{M}(\Gamma)}$	92.03	176.08	267.06	887.08	1597.73

5.3. Results and Discussion

5.3.1. Spherical shell model

Current density in non-target regions

In this section, the L1R approximated discretized optimization problem ($\bar{\mathbf{P}}_{\epsilon}^{\mathbf{0},\beta}$) is used to calculate optimized stimulation protocols for a set of 924 tangential (parallel to the inner skull surface) and 924 radial (perpendicular to the inner skull surface) target vectors and Theorem 5.4 is applied to estimate the averaged maximal current density in non-target regions. Tables 5.1 and 5.2 depict the averaged maximal current density in non-target regions, the number of iterations until a minimum was found and the scaling factor $\|\boldsymbol{I}_{tCS}\|_{\mathcal{M}(\Gamma)}$. As can be seen in the tables, for a threshold value $\epsilon = 0.001\,\mathrm{Am}^{-2}$, the averaged maximal current density in non-target regions is relatively weak and the number of iterations until a minimum was found is lowest. For this reasons, a threshold value of $\epsilon = 0.001\,\mathrm{Am}^{-2}$ is thus used in this study as it allows safe and well-targeted stimulation and fast and robust computation of the stimulation protocol.

Optimization in spherical models

Figure 5.3 depicts the L1R optimized current flow fields and the corresponding stimulation protocols for four tangential (to the skull surface) target vectors with a target depth of 2 mm, 12 mm, 22 mm and 32 mm. As can be seen, for target vector depths of 2 mm and 12 mm, the optimized brain current flow field show relatively high focality, while for target depths of 22 mm and 32 mm, a slightly more widespread brain current flow field can be seen. For

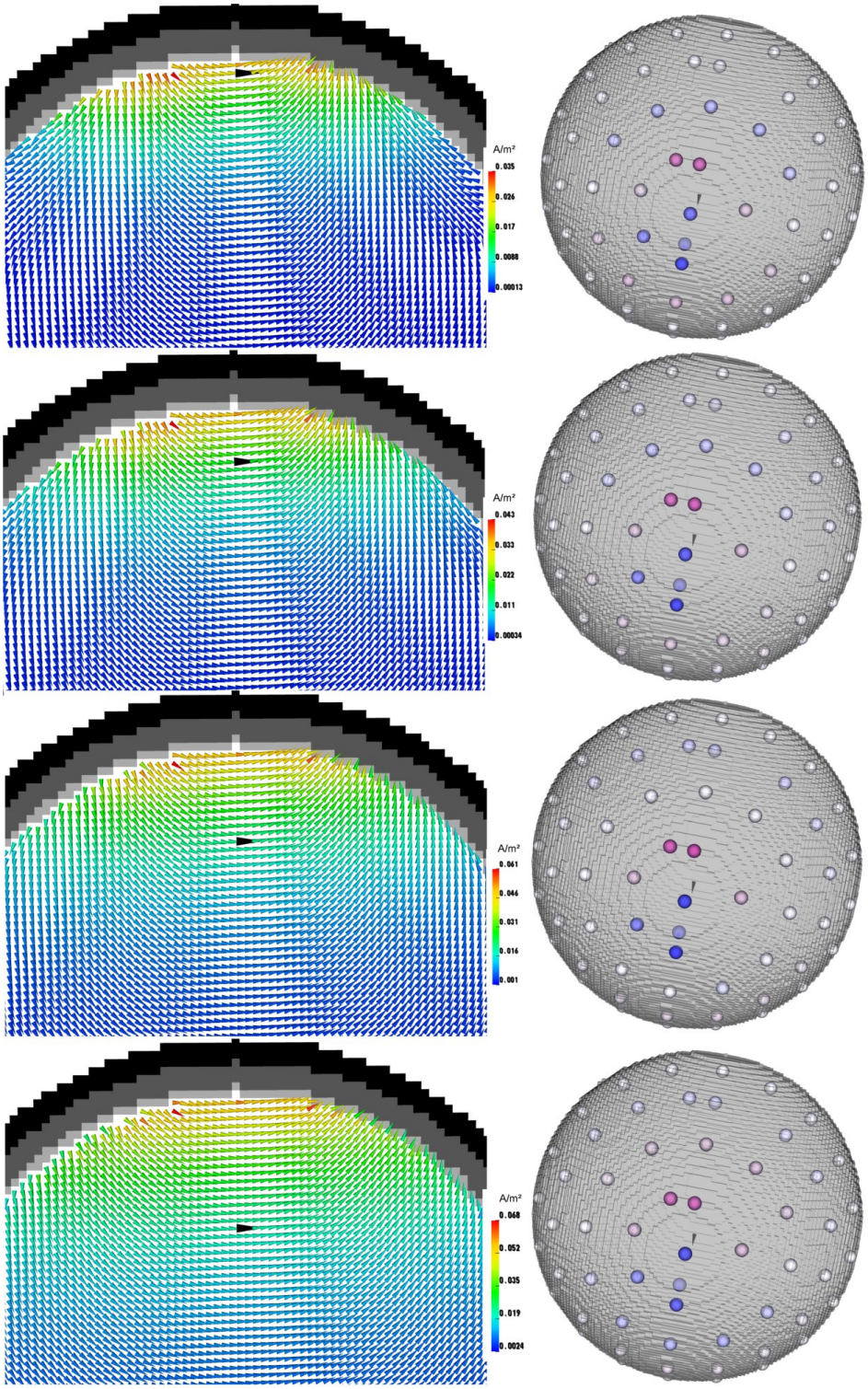

Figure 5.3.: Optimized current density distribution $\boldsymbol{J}$ in a sphere model. The left column displays $\boldsymbol{J}$ on a sagital slice through the hexahedral sphere model and the right column shows the corresponding stimulation protocols. The depth of the target vector in Figures -A, -B, -C and -D is 2 mm, 12 mm, 22 mm and 32 mm, respectively. The target vectors $\tilde{\boldsymbol{e}}$ are depicted by the black cones.

all target vectors, strongest current density amplitudes in the brain compartment always occur at the CSF/brain boundary above the target region. This is due to the fact that the

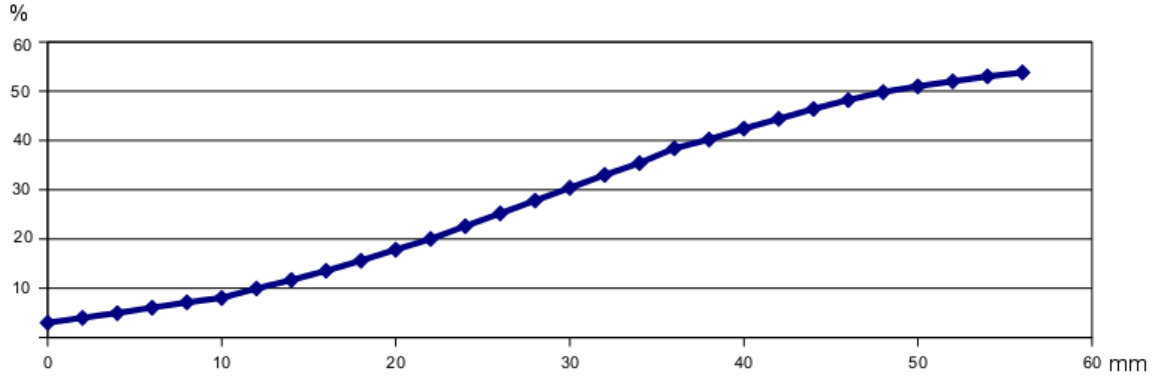

Figure 5.4.: Ratio (in percentage) between the averaged current density in non-target regions divided by the current density in the target region. The stimulation depth (in mm) is depicted on the x-axis.

potential field $\nabla\Phi$ satisfies the maximum principle for harmonic functions which states that a non-constant function always attains its maximum at the boundary of the domain [42, Theorem 14.1].

The corresponding stimulation protocols are depicted in Figure 5.3 (right column). The optimized stimulation protocols show a high focality with mainly four active electrodes, while weak compensating currents are injected at neighboring electrodes. The latter, however, only holds true for stimulation depths up to 12 mm. When deeper target vectors are used, weak supporting currents are injected at the neighboring electrodes (Figure 5.3, third and fourth row).

A quantification of the optimized current densities is shown in Table 5.3. As can be seen, the deeper the target vector is located, the weaker the current density in the target region. While, with target current densities of $0.042\,\mathrm{Am}^{-2}$, the target current density is identical for target vector depths of 22 mm and 32 mm, the averaged current density is a factor of 1.7 (from $0.0084\,\mathrm{Am}^{-2}$ to $0.014\,\mathrm{Am}^{-2}$) higher when the deeper target vector is used. In order to quantify the focality of the current density, Figure 5.4 shows the interaction between the averaged current density in non-target regions and the current density in the target at a specific distance to the CSF/brain boundary (30 target vectors with a target vector depth of 2 mm to 62 mm are used). A correlation between target depth and current density focality can be seen, i.e., the focality of the current flow field decreases smoothly with increasing target depth.

5.3.2. Realistically shaped FE head model

The highly realistic six-compartment FE head model (see Section 2.5) is used and the optimized current densities in the brain compartment are investigated with regard to focality, target intensity and orientation. Four target vectors are used to calculate optimized stimulation protocols. For all simulations, the target area Ω_t always consists of the elements corresponding

Table 5.3.: Quantification of optimized current density in a four-compartment spherical shell model. The averaged current density in the target area (CD_a second column), the averaged current density in non-target regions (third column), the inner product of current density and target vector (CD_t fourth column) and the percentage of current density that is oriented parallel to the target vector (PAR, fifth column) is displayed for different target vector depths (first column).

mm		$[Am^{-2}]$		[%]
Target	$\frac{\int_{\Omega_t}\lvert\boldsymbol{BI}_S\rvert\,\mathrm{d}\boldsymbol{x}}{\lvert\Omega_t\rvert}$	$\frac{\int_{\Omega\setminus\Omega_t}\lvert\boldsymbol{BI}_S\rvert\,\mathrm{d}\boldsymbol{x}}{\lvert\Omega\setminus\Omega_t\rvert}$	$\frac{\int_{\Omega}\langle\boldsymbol{BI}_S,\boldsymbol{e}\rangle\,\mathrm{d}\boldsymbol{x}}{\lvert\Omega_t\rvert}$	$PAR=\frac{CD_t}{CD_a}$
2	0.054	0.00216	0.0484	89.6
12	0.044	0.0039	0.0428	97.3
22	0.042	0.0084	0.0414	98.5
32	0.042	0.014	0.0404	96.2

to the target vectors and only the volume conductor elements in the brain are used for optimization, i.e., $\omega = 1$ only in the brain compartments and $\omega \ll 1$ in the target region and in the CSF, skin and skull compartments.

In order to investigate the current flow field that is induced by an optimized standard bipolar electrode montage, a maximum two electrode (M2E) approach is used. This approach stimulates only the main positive (anode) and the main negative electrode (cathode) of the L1R optimized stimulation protocols with a total current of 1 mA. In order to quantify the optimized current flow fields, the current densities in the direction of the target vectors (CD_t) and the percentage of current density that is oriented parallel to the target vector (PAR) are calculated, as shown in columns 4 and 5 in Table 5.4, respectively.

5.3.2.1. Mainly tangential target vector

Figure 5.5 displays the optimized current densities (for better visibility, a different scaling was used) and the corresponding stimulation protocols (same scaling) for a mainly tangential target vector as shown in Figures 5.5-A1 and -A2. As can be seen in Figures 5.5-B1 and 5.5-C1, the optimized current flow fields using the L2R and L1R approaches, respectively, show high focality and maximal current densities can be observed in the target region. While the L2R and L1R approaches lead to target current densities of $0.022\,\mathrm{Am}^{-2}$ and $0.038\,\mathrm{Am}^{-2}$ (Table 5.4, second column), current densities in non-target brain regions are rather weak (Figures 5.5-B1 and -C1). Overall, due to the rather widespread applied current pattern at the fixed electrodes (Figure 5.5-B2), the L2R optimized current flow field (Figure 5.5-B1) has smaller amplitude when compared to the L1R one (Figure 5.5-C1). On the other hand, the L1R stimulation protocol (Figure 5.5-C2) shows high focality with mainly two active electrodes, while only very weak compensating currents are injected at the neighboring electrodes. The M2E approach results in higher target current densities of $0.071\,\mathrm{Am}^{-2}$ (Table 5.4, second column). However, using the M2E approach, relatively strong current densities can also be

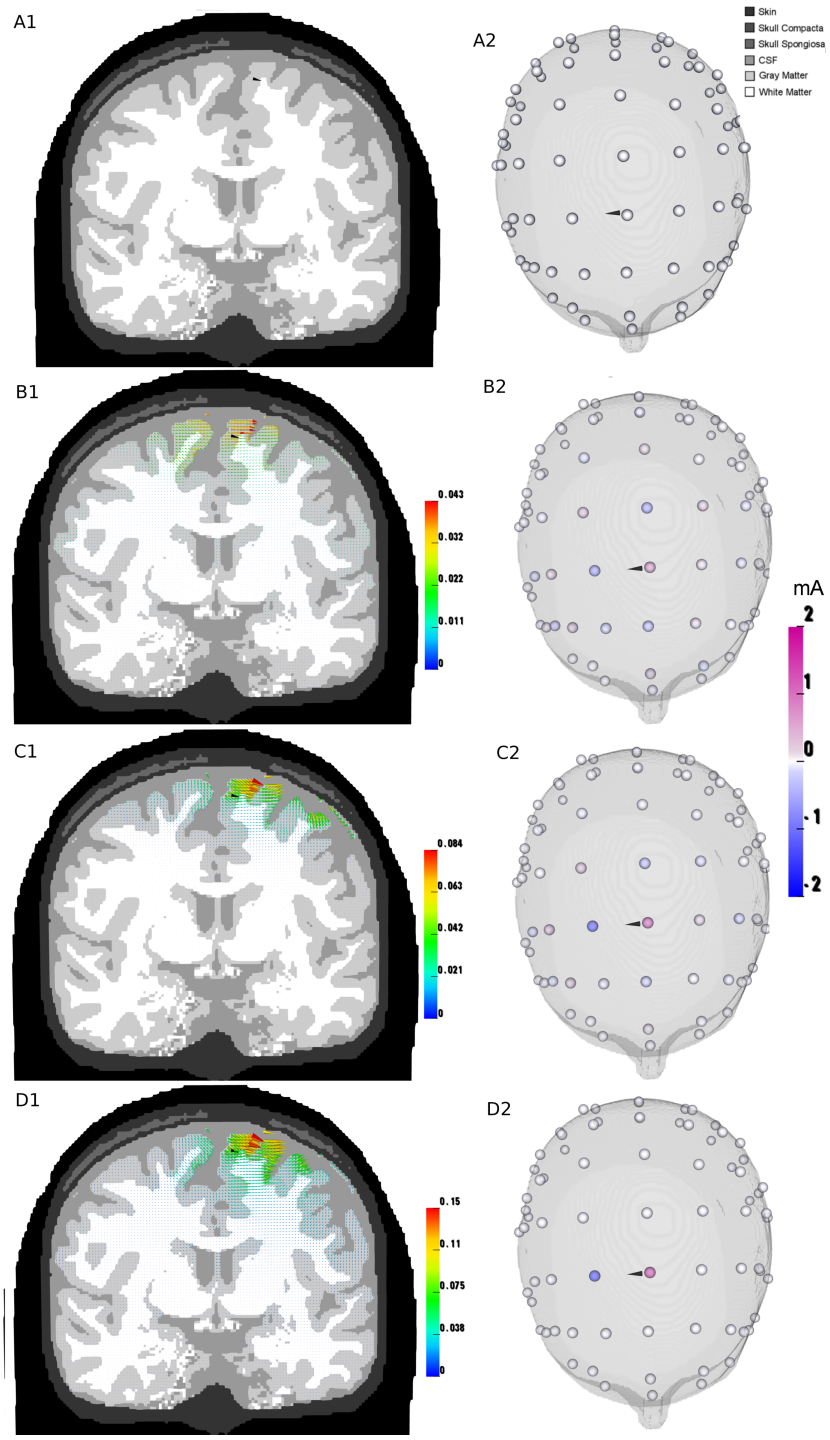

Figure 5.5.: Optimized current density for a mainly tangential (to the skull surface) target vector (Figs. -A1 and -A2). The optimized current densities in the brain compartment and stimulation protocols are depicted in Figures -1 and -2, respectively. Figures -B -C and -D show optimization results for the L2R, L1R and M2E approaches, respectively.

noted in non-target regions, especially in pyramidal tract and deeper white matter regions (Figure 5.5-D1).

With a PAR value of 86.4, 86.8 and 85.9 for L2R, L1R and M2E (Table 5.4, fifth column),

Target	$\frac{\int_{\Omega_t}\lvert \boldsymbol{BI}_S\rvert \,\mathrm{d}\boldsymbol{x}}{\lvert\Omega_t\rvert}$ $\left[Am^{-2}\right]$	$\frac{\int_{\Omega\setminus\Omega_t}\lvert \boldsymbol{BI}_S\rvert \,\mathrm{d}\boldsymbol{x}}{\lvert\Omega\setminus\Omega_t\rvert}$ $\left[Am^{-2}\right]$	$\frac{\int_{\Omega}\langle \boldsymbol{BI}_S,\boldsymbol{e}\rangle \,\mathrm{d}\boldsymbol{x}}{\lvert\Omega_t\rvert}$ $\left[Am^{-2}\right]$	$PAR = \frac{CD_t}{CD_a}$ [%]
tangential L2R	0.022	0.00144	0.019	86.4
tangential L1R	0.038	0.00151	0.033	86.8
tangential M2E	0.071	0.0080	0.061	85.9
radial L2R	0.026	0.00064	0.025	96.1
radial L1R	0.045	0.00071	0.043	95.5
radial M2E	0.063	0.0074	0.048	76.2
patch L2R	0.025	0.00147	0.022	88.0
patch L1R	0.037	0.00157	0.033	89.1
patch M2E	0.071	0.0080	0.062	87.3
deep L2R	0.015	0.00345	0.013	86.7
deep L1R	0.019	0.00249	0.018	94.7
deep M2E	0.052	0.01477	0.049	94.2

Table 5.4.: Quantification of optimized current density. The averaged current density in the target area (CD_a, second column), the averaged current density in non-target regions (third column), the inner product of current density and target vector (CD_t, fourth column) and the percentage of current density that is oriented parallel to the target vector (PAR, fifth column) is displayed for different target vectors (first column).

the current densities of all three approaches are mainly oriented parallel to the target vector, leading to CD_t values, i.e., current densities along the target direction, of 0.019 , 0.033 and $0.061\,\mathrm{Am}^{-2}$, respectively (Table 5.4, fourth column). While the CD_t values between L1R and M2E are thus less than a factor of 2 different, the averaged current density amplitudes in non-target regions is about 5.3 times higher when using the M2E approach (Table 5.4, third column). The L1R optimized current flow field thus shows significantly higher focality and also slightly better parallelity to the target vector in comparison to the bipolar electrode montage M2E. However, if no multi-channel tDCS stimulator is available, the M2E approach provides an optimized bipolar electrode montage for a mainly tangential target vector.

5.3.2.2. Mainly radial target vector

The mainly radially oriented target is shown in Figures 5.6-A1 and -A2. Figures 5.6-B1 and 5.6-C1 depict the optimized current densities for the L2R and L1R approaches, respectively. As shown in Table 5.4 (Column 2), with a value of $0.045\,\mathrm{Am}^{-2}$, the target current density for the L1R approach is more than a factor of 1.7 times stronger than with the L2R approach ($0.026\,\mathrm{Am}^{-2}$). Non-target regions show only weak current densities (Figures 5.6-B1 and -C1). With a value of $0.063\,\mathrm{Am}^{-2}$, the M2E approach yields the largest target intensity (Table 5.4, second column). However, for this approach, the maximal current density in the brain does not occur in the target region, but on a neighboring gyrus in between the stimulating

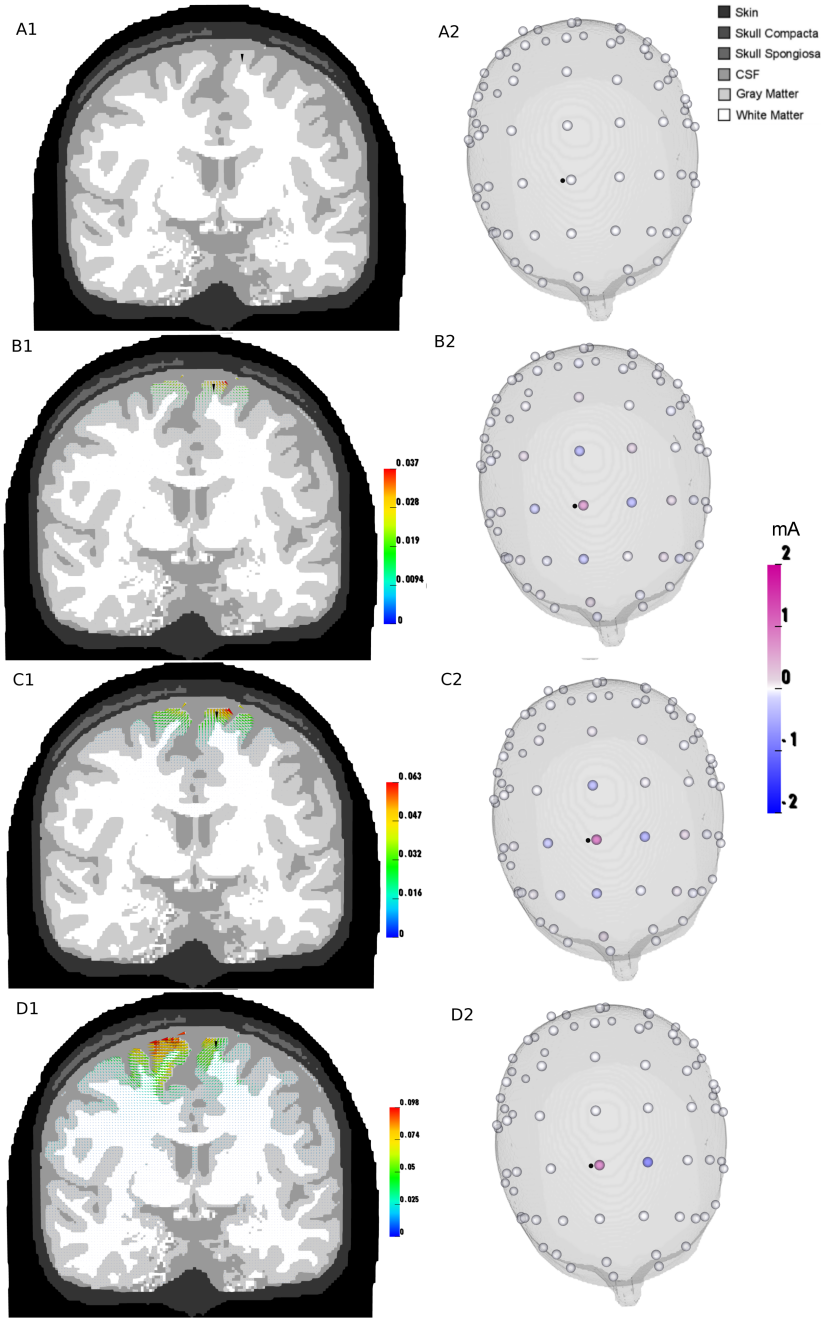

Figure 5.6.: Optimized current densities for a mainly radial target vector (Figs. -A1 and -A2). The optimized current densities in the brain compartment and stimulation protocols are depicted in Figures -1 and -2, respectively. Figures -B -C and -D show optimization results for the L2R, L1R and M2E approaches, respectively.

electrodes and in mainly tangential direction (Figure 5.6-D1). Moreover, the M2E optimized current density shows again an overall much lower focality than the L2R and L1R current flow fields.

The L2R stimulation protocol (Figure 5.6-B2) consists of an anode above the target, surrounded by four cathodes and a ring of very weak positive currents at the second neighboring electrodes, a distribution which might be best described by a sinc-function. As can be seen in Figure

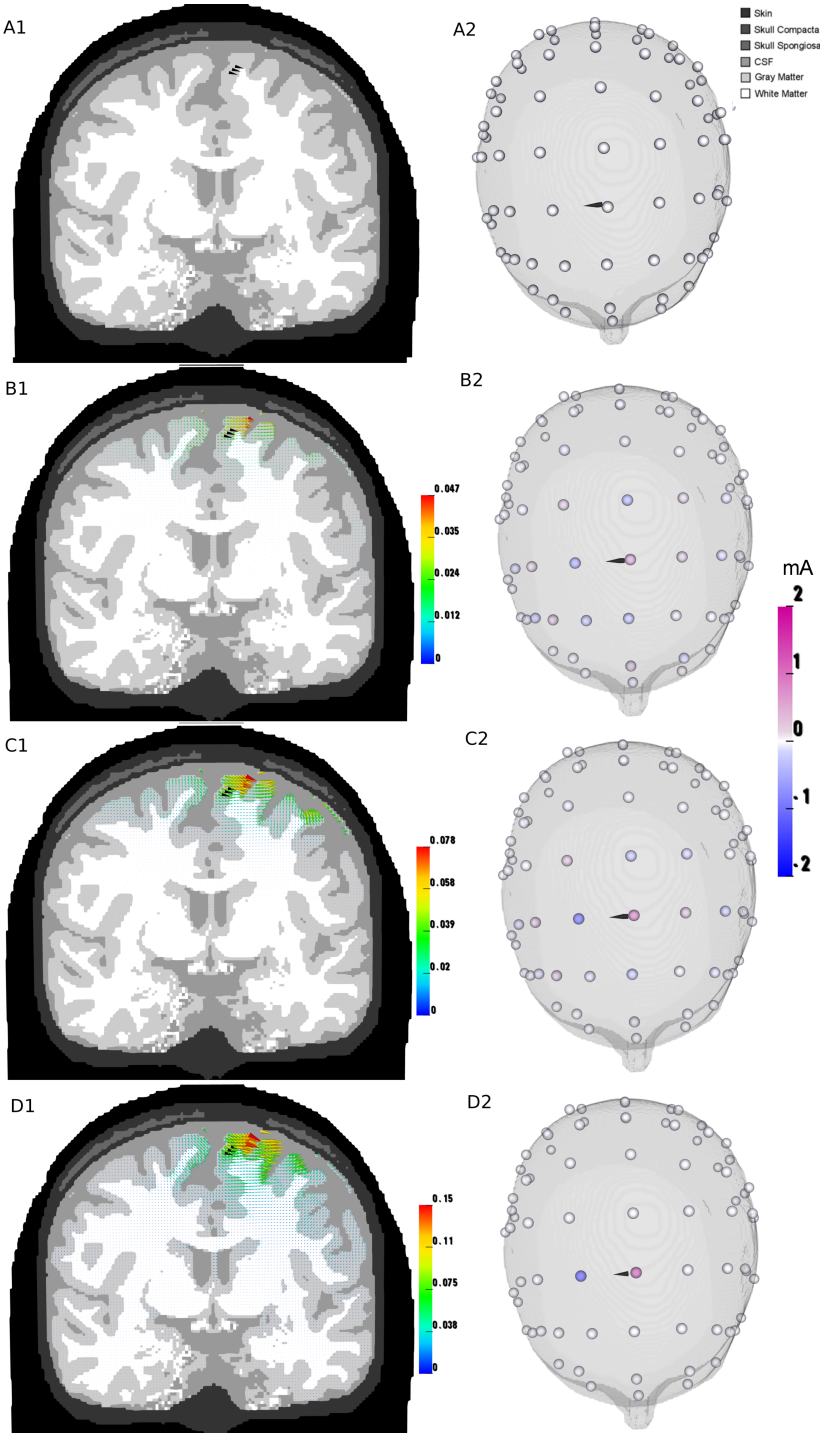

Figure 5.7.: Optimized current densities for an extended target region consisting of 9 tangential vectors (Figs. -A1 and -A2). The optimized current densities in the brain compartment and stimulation protocols are depicted in Figures -1 and -2, respectively. Figures -B -C and -D show optimization results for the L2R, L1R and M2E approaches, respectively.

5.6-C2, the L1R stimulation protocol is mainly composed of a main positive current at the electrode above the target region and four return currents applied to the surrounding electrodes.

The L2R and L1R optimized current flow fields show high directional agreement with the target vector $\boldsymbol{e}$ (PAR value above 95 %), with the L2R slightly outperforming the L1R approach (Table 5.4, fifth column). With a PAR value of only 76.2 % the current flow field in the M2E model shows much less directional agreement with the target vector. This results in CD_t values of 0.025, 0.043 and 0.048 Am^{-2} for the L2R, L1R and M2E approaches, respectively. In order to obtain higher PAR values for the M2E approach, i.e., higher current densities along the target direction, the distance between anode and cathode might be enlarged, in line with Dmochowski and colleagues [33] who reported that the optimal bipolar electrode configuration for a radial target vector consists of an electrode placed directly over the target with a distant return electrode. Another interesting bipolar electrode arrangement for a radial target vector might consist of an anode over the target and a cathodal ring around the anode.

5.3.2.3. Extended target region

In this section, an extended target area of 3 mm × 1 mm × 1 mm is used for current density optimization. The target area is centered around the location of the superficial target vector that was also used in Section 5.3.2.1 and the corresponding target vectors are selected to be mainly tangentially oriented (Figures 5.7-A1 and 5.7-A2). As can be seen in Figures 5.7-B1 and 5.7-C1, the optimized current flow fields of the L2R and L1R approaches show high focality. L2R and L1R yield an averaged target intensity of 0.025 Am^{-2} and 0.037 Am^{-2}, respectively (Table 5.4, second column). Current density is not restricted to but focused to the target area, especially for the L2R approach (Figure 5.7-B1). In comparison to the superficial tangential target vector of Section 5.3.2.1, the L1R optimized averaged current density in the target area is decreased by about 3 % (from 0.038 Am^{-2} to 0.037 Am^{-2}) and the optimized stimulation protocols are also very similar. Because the main two electrodes are taken from the L1R optimization, this implies that also the M2E stimulation protocol remains constant to the stimulation protocol from Section 5.3.2.1. In this way, the M2E approach yields an averaged target intensity of 0.071 Am^{-2} (Table 5.4, second column).

With averaged PAR values of 88.0, 89.1 and 87.3 (Table 5.4, fifth column), the current densities are mainly oriented parallel to the target vectors with L1R performing best. The averaged current flow field intensity along the target direction is 0.022, 0.033 and 0.062 Am^{-2} for the L2R, L1R and M2E approaches, respectively (Table 5.4, fourth column). However, for M2E also non-target regions reach significant current densities, as clearly shown in Figure 5.7-D1. The averaged current density amplitudes in non-target regions is 0.00157 and 0.0080 Am^{-2} for the L1R and M2E approaches (Table 5.4, third column). The L1R optimized current flow field thus shows a factor of 5.1 higher focality in comparison to bipolar electrode montage M2E. However, the M2E approach provides an optimized bipolar electrode montage for an extended target area of tangential target vectors.

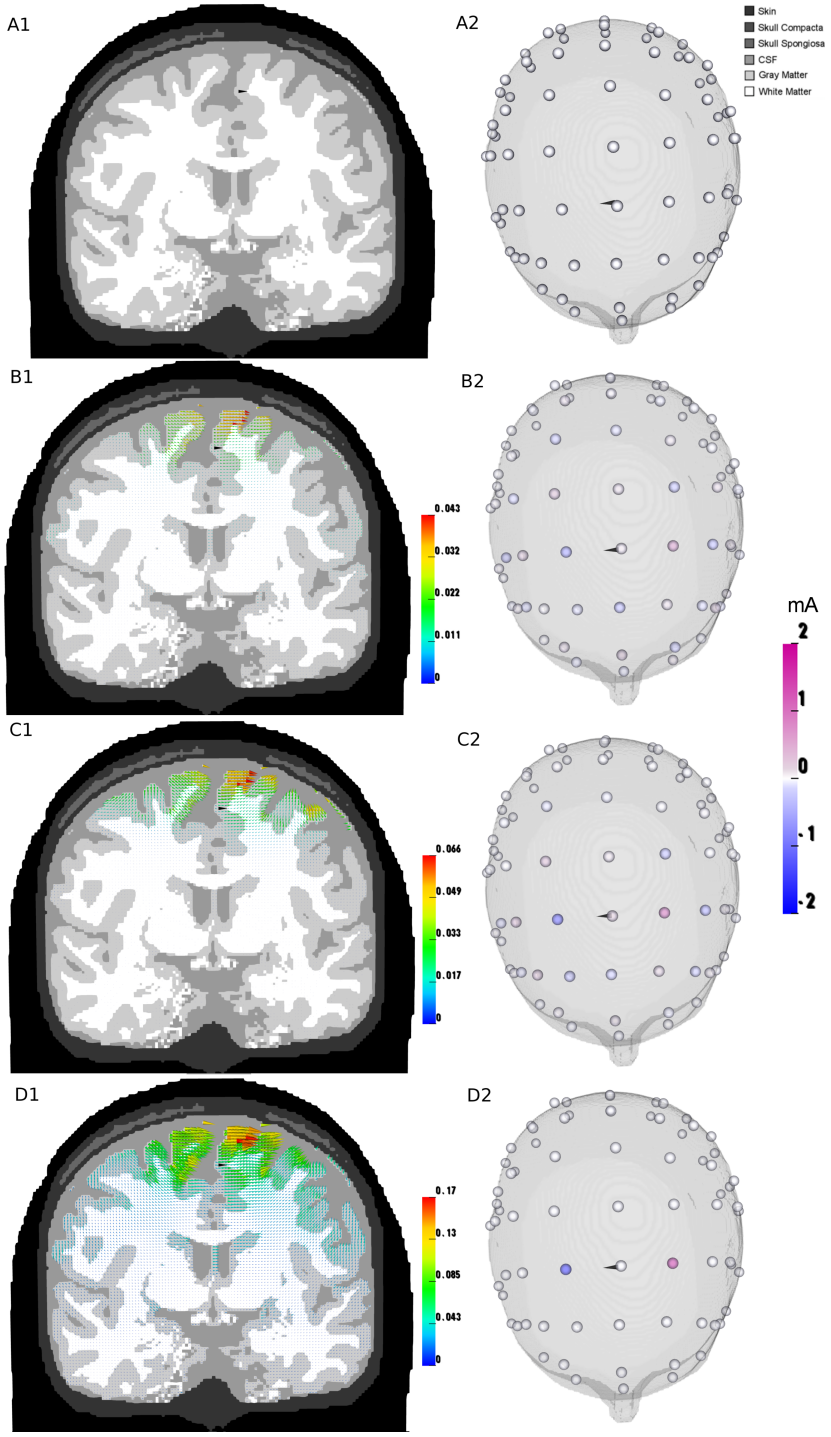

Figure 5.8.: Optimized current densities for a deeper target vector (Figs. -A1 and -A2). The optimized current density distribution in the brain compartment and the corresponding stimulation protocol are depicted in Figures -1 and -2, respectively. Figures -B -C and -D show optimization results for the L2R, L1R and M2E approaches, respectively.

5.3.2.4. Deep and tangential target vector

In the last simulation scenario, optimization for a deeper and mainly tangentially oriented target vector as shown in Figures 5.8-A1 and -A2 was investigated. Figures 5.8-B1 and -C1

depict the optimized current density distributions when using L2R and L1R for optimization, respectively. For those approaches, the target current densities are 0.015 and 0.019 Am^{-2}, respectively. With a value of 0.052 Am^{-2}, which is more than 2.7 times the L1R value, the largest target intensity is, however, achieved with the M2E approach (Table 5.4, second column). CD_t values of 0.013, 0.018 and 0.049 Am^{-2} lead to PAR values of 86.7, 94.7 and 94.2 for the L2R, L1R and M2E approaches (Table 5.4, fourth and fifth column). The target current densities are thus for all three approaches oriented mainly parallel to the target vector.

For all three approaches, strongest current density amplitudes in the brain compartment always occur at the CSF/brain boundary above the target region (Figures 5.8-B1,-C1 and -D1). This is due to the fact that the potential field $\nabla\Phi$ satisfies the maximum principle for harmonic functions which states that a non-constant function always attains its maximum at the boundary of the domain [42, Theorem 14.1]. Nevertheless, in average over all non-target regions, with a value of 0.014 77 Am^{-2} for M2E, the L2R (0.003 45 Am^{-2}) and L1R (0.002 49 Am^{-2}) optimized current flow fields show a factor of about 4.3 and 5.9 times lower current densities, respectively (Table 5.4, third column). Overall, L2R and L1R thus have a much higher focality, which can also easily be seen in Figures 5.8-B1,-C1 and -D1. However, if no multi-channel tDCS device is available, the M2E approach provides an optimized bipolar electrode arrangement for a deep and tangential target vector.

The L2R and L1R stimulation protocols show high focality with mainly two active electrodes, while only weak compensating currents are injected at the neighboring electrodes (Figures 5.5-B2 and -C2). Similar to Section 5.3.2.1, the compensating currents are stronger when using the L2R optimization procedure, leading to weaker target brain current densities as compared to the L1R stimulation. In order to enable current density to penetrate into deeper brain regions, the distance between the two main stimulating electrodes is larger when compared to the superficial mainly tangential target vector from Section 5.3.2.1, i.e., the electrode above the target region is not used for stimulation, while a more distant electrode is used as anode.

5.3.2.5. Discussion

A novel optimization approach for safe and well-targeted multi-channel transcranial direct current stimulation has been proposed. Existence of at least one minimizer and residual and objective convergence results have been proven for the proposed optimization methods. The main advantages of the newly invented optimization approach is that it allows to control the current densities both at the skin and brain levels, while the optimization methods of Dmochowski and colleagues [33] only limit the total current applied to the electrodes. For discretization of the respective optimization problems, the finite element method was employed and the existence of at least one minimizer to the discretized optimization problems has been shown. For numerical solution of the corresponding discretized problem, the alternating direction method of multipliers was employed. A highly-realistic six-compartment head model with white matter anisotropy was generated and optimized current density distributions were

calculated and investigated for a mainly tangential and a mainly radial target vector, an extended target area of 3 mm × 1 mm × 1 mm and a deeper and mainly tangential target vector. The numerical results revealed that, while all approaches fulfilled the patient safety constraint, the optimized current flow fields show significantly higher focality and, with the exception of the L2R for the deep target, higher directional agreement to the target vector in comparison to standard bipolar electrode montages. The higher directional agreement is especially distinct for the radial target vector. In all test cases, because of a more widespread distribution of injected and extracted surface currents, the L2R optimization procedure ($\bar{\mathbf{P}}_{\epsilon}^{\alpha,\mathbf{0}}$) led to relatively weak current densities in the brain compartment. The L1R optimized current density distribution along the target direction was in all test cases stronger than the L2R one and might thus be able to induce more significant stimulation effects. The stimulation will thus enhance cortical excitability especially in the target regions, while it will as good as possible prevent too strong excitability changes in non-target regions.

The M2E approach was shown to provide an optimized bipolar electrode montage as long as the target is mainly tangentially oriented. For radial targets, the M2E approach was unsatisfactory, an optimal bipolar electrode configuration might then consist of a small electrode placed directly above the target region with a distant return electrode or a small electrode over the target encircled by a ring return electrode, as proposed in [33].

5.3.3. Comparison with other optimization methods for tCS

In this section, the L1R optimization method is compared to the optimization methods for multi-array tCS that were presented by Dmochowski and colleagues [33]. The optimization methods least square with individual L1 constraint (LS) and the linearly constrained minimum variance method with individual L1 constraints (LCMV) [33] were implemented and optimized stimulation protocols were calculated in the six-compartment, geometry-adapted, hexahedral FE head model with white matter anisotropy. In order to compare the optimization methods, the mainly tangential target vector (Subsection 5.3.2.1) and the mainly radial target vector (Subsection 5.3.2.2) are used. A quantification of the optimized current flow fields for the three optimization methods LS, L1R and LCMV is shown in Table 5.5.

Mainly tangential target vector

The mainly tangential target vector is depicted in Figures 5.5-A1 and -A2. As can be seen in Table 5.5 (second column), the LS, L1R and LCMV approaches lead to target current densities of 0.091 Am^{-2}, 0.038 Am^{-2} and 0.032 Am^{-2}. Overall, the LS optimized current flow field has higher amplitude as compared to the LCMV and L1R current flow fields, while the LCMV and L1R optimized current field amplitudes are nearly identical. Moreover, the L1R and LCMV stimulation protocols are very similar and mainly composed of two active electrodes, while weaker compensating currents are injected at the neighboring electrodes. The LS stimulation protocol shows very high focality and is mainly comprised of three electrodes (Figure 5.9-A2).

	$\left[Am^{-2}\right]$			[%]	
Target	$\frac{\int_{\Omega_t}\lvert\boldsymbol{BI}_S\rvert\,\mathrm{d}\boldsymbol{x}}{\lvert\Omega_t\rvert}$	$\frac{\int_{\Omega\setminus\Omega_t}\lvert\boldsymbol{BI}_S\rvert\,\mathrm{d}\boldsymbol{x}}{\lvert\Omega\setminus\Omega_t\rvert}$	$\frac{\int_{\Omega}\langle\boldsymbol{BI}_S,\boldsymbol{e}\rangle\,\mathrm{d}\boldsymbol{x}}{\lvert\Omega_t\rvert}$	PAR	**FOC**
tangential LS	0.091	0.00527	0.083	91.2%	17.2
tangential L1R	0.038	0.00151	0.033	86.8%	25.1
tangential LCMV	0.032	000144	0.031	96.9%	22
radial LS	0.071	0.0015	0.069	97.2%	46.7
radial L1R	0.045	0.0007	0.043	95.6%	47.8
radial LCMV	0.033	0.0007	0.033	100%	63.4

Table 5.5.: Quantification of optimized current density. The current density in the target area (second column), the averaged current density in non-target regions (third column), the inner product of current density and target vector (:= CD_t) (fourth column) and the percentage of current density that is oriented parallel to the target vector (:=PAR)(fifth column) and the focality ((:=FOC) Column 2 divided by Column 3) is displayed for two target vectors (first column) and the LS with L1 constraint, LCMV with L1 constraint and the L1R optimization methods, respectively.

With PAR values of 91.2, 86.8 and 96.9 for the LS, L1R and LCMV approaches, the current densities are mainly oriented parallel to the target vector, leading to current densities in the direction of the target vector of 0.033 and 0.031 Am^{-2} for the L1R and LCMV approaches (Table 5.5, fourth column). While the averaged current density amplitude in non-target regions of 0.00144 and 0.00151 Am^{-2} is very similar for the LCMV and L1R approaches (Table 5.5, third column), the current density in the direction of the target vector is about 7 % higher (0.033 Am^{-2} to 0.031 Am^{-2}) when using the L1R optimization method. On the other hand, the LCMV optimized current flow field shows slightly higher parallelity to the target vector (86.8% and 96.9% for the L1R and LCMV approaches) in comparison to the L1R current flow field. A trade-off between current density amplitudes in the target region and parallelity to the target vector can thus be seen, i.e., a higher target intensity leads to weaker parallelity to the target vector. .

The LS approach leads to relatively high current density in the direction of the target vector of 0.083 Am^{-2}. However, when using the LS optimization method, the averaged current density in non-target regions is a factor of about 3.7 (0.00151 Am^{-2} and 0.00527 Am^{-2} for the L1R and LCMV approaches) higher as compared to the L1R optimized current flow field (Table 5.5, third column). Therefore, a trade-off between target current density and averaged current density in non-target regions can be seen, i.e., higher target current densities lead to substantially higher averaged current density in non-target regions of the optimized current flow fields. In conclusion, while the current density in the direction of the target vector is about 2.5 times higher when using the LS optimization approach as compared to the LCMV and L1R approaches, the optimized current flow field shows a factor of about 3.7 lower focality. Moreover, the L1R optimized current flow field shows significantly higher focality in comparison to the LS and LCMV optimized current flow fields (Table 5.5, sixth column).

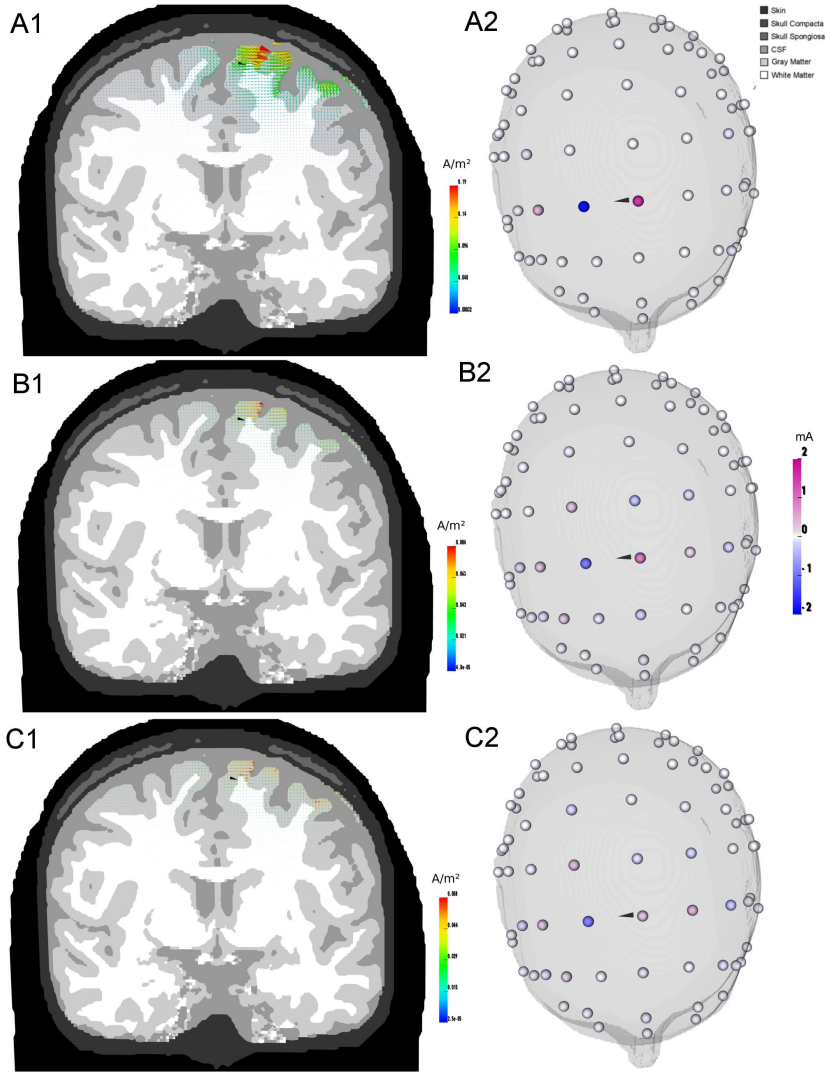

Figure 5.9.: Optimized current densities for a mainly tangential target vector (see Figures 5.5-A1 and -A2). The optimized current densities in the brain compartment and stimulation protocols are depicted in Figures -1 and -2, respectively. Figures -A -B and -C show optimization results for the LS, L1R and LCMV approaches, respectively.

Mainly radial target vector

The mainly radially oriented target is shown in Figures 5.6-A1 and -A2. Figures 5.10-A1, 5.10-B1 and 5.10-C1 depict the optimized current densities for the LS, L1R and LCMV approaches, respectively, when a mainly radial target vector is used for optimization. As shown in Table 5.5 (Column 2), the target current density is $0.071\,\mathrm{Am}^{-2}$, $0.045\,\mathrm{Am}^{-2}$ and $0.033\,\mathrm{Am}^{-2}$ for the LS, L1R and LCVM approaches, respectively.

All three stimulation protocols are mainly composed of a main positive current at the electrode above the target region and four return currents applied to the surrounding electrodes (Figures 5.10-A1, -B2 and -C2). When using the L1R and LCMV approaches, however, additionally weaker compensating currents are injected at the second neighboring electrodes, leading to overall lower current densities in the brain compartment.

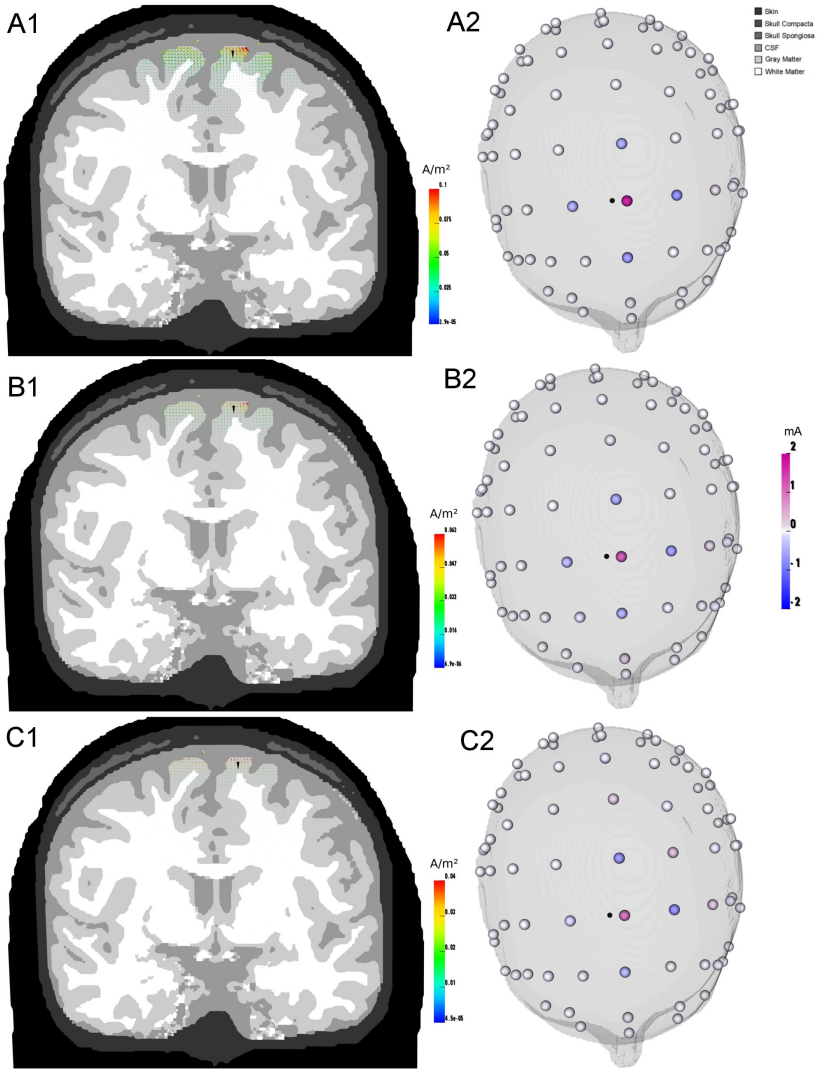

Figure 5.10.: Optimized current densities for a mainly radial target vector (see Figures 5.6-A1 and -A2). The optimized current densities in the brain compartment and stimulation protocols are depicted in Figures -1 and -2, respectively. Figures -A -B and -C show optimization results for the LS, L1R and LCMV approaches, respectively.

The LS, L1R and LCMV optimized current flow fields show high directional agreement with the target vector $\boldsymbol{e}$, with the LCMV approach leading to best results (Table 5.5, fifth column). This results in CD_t values of 0.069, 0.043 and 0.033 Am^{-2} for the LS, L1R and LCMV approaches, respectively. While the CD_t are thus not too different for the LS and L1R approaches, the averaged current density in non-target regions is about 2.3 times higher when using the LS optimization method. For the radial target vector, the L1R optimized current flow fields thus show substantially higher focality in comparison to the LS optimized current flow field. Again, a trade-off between target current density and averaged current density in non-target regions and a trade-off between target current density and parallelity to the target vector can be shown. Moreover, the L1R optimized current flow field shows a factor of 1.5 higher focality in comparison to the LS and LCMV optimized current flow fields (Table 5.5, sixth column). This work has been conducted with Simon Homölle, University of Münster

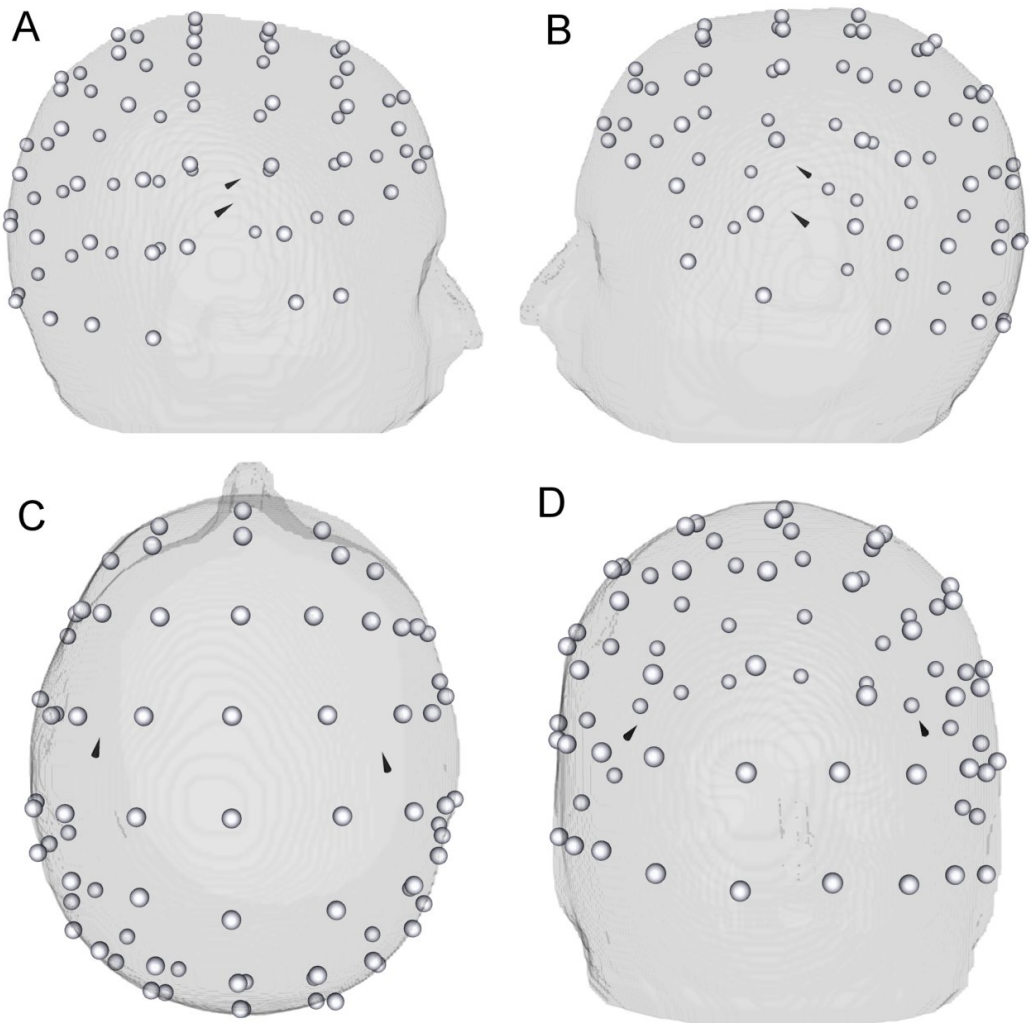

Figure 5.11.: Location and orientation of the target vectors for auditory cortex stimulation. Combined AEP and AEF data is used to appropriately estimate the location and orientation of the auditory cortex target vectors.

[58].

5.3.4. Optimized stimulation protocols for auditory cortex stimulation

In this section, the novel L1R optimization method is used to calculate optimized stimulation protocols for bi-hemispheric auditory cortex stimulation. The highly realistic six-compartment head model with white matter anisotropy is used (see Section 2.5). Moreover, combined AEP and AEF data of the subject are used to appropriately estimate the location and orientation of the auditory cortex target vectors, see Section 4.1 and Figure 5.11. In order to also allow one-hemispheric auditory cortex stimulation, the optimization is split into two parts. First, the target vector in the right-hemisphere is used and an optimized applied current pattern is calculated, and second, an optimal applied current pattern is calculated for left-hemispheric auditory cortex stimulation. Figures 5.12-A1 and -B1 depict the optimized

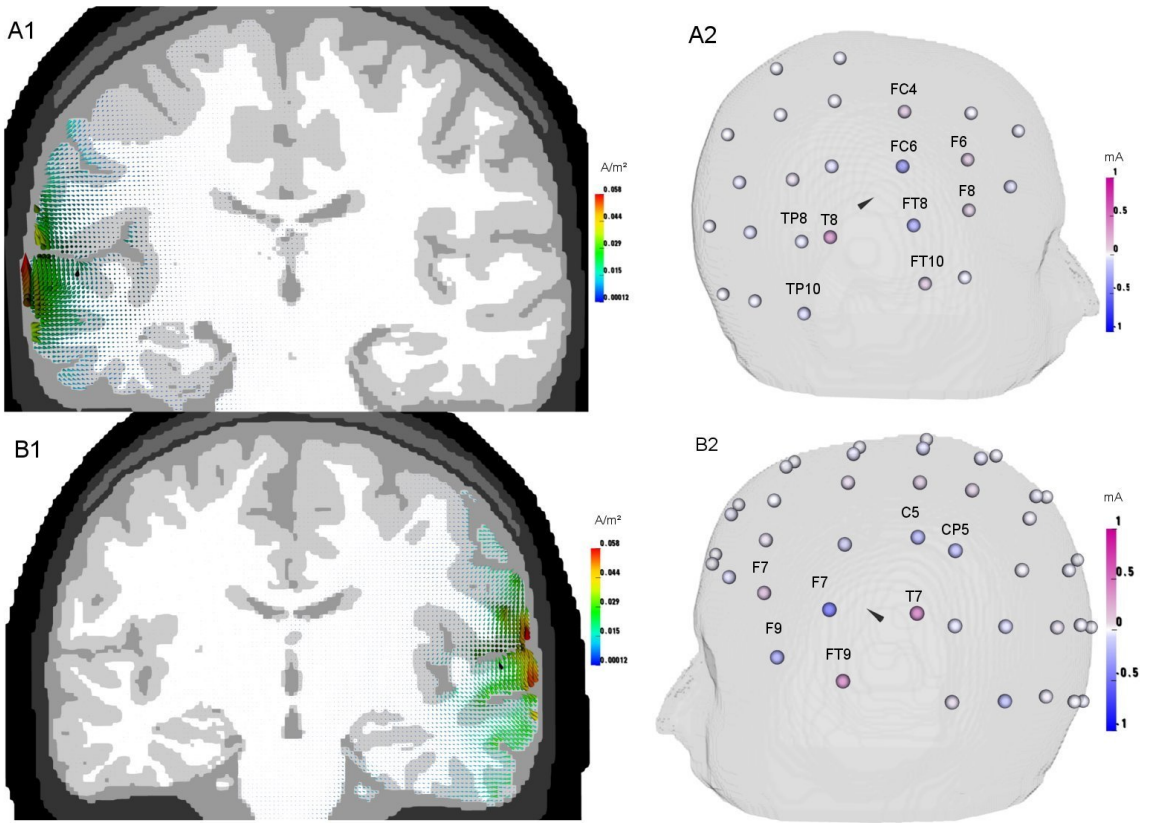

Figure 5.12.: Optimized current flow pattern for bi-hemispheric auditory cortex stimulation (Figures -A1 and -B1). The corresponding stimulation protocols are depicted in Figures -A2 and -B2.

current flow field for right- and left-hemispheric auditory cortex stimulation, respectively. As can be seen in Figures 5.12-A1 and -B1, the optimized current flow fields show a high focality. For both optimized current flow fields, the strongest current densities are located in the auditory cortices. Moreover, current density in non-target regions is substantially smaller as compared to the current densities in the auditory cortices (Figures 5.12-A1 and -B1). The corresponding stimulation protocol are shown in Figures 5.12-A2 and -B2. For right-hemispheric auditory cortex stimulation, the stimulation protocol shows high focality and is mainly comprised of three electrodes, an anodal stimulation at electrode location T8 and two cathodal stimulations at electrode locations FT8 and FC6. In order to reduce current density in non-target regions, the L1R optimization approach injects very weak compensating currents at neighboring electrodes, especially at 10-10 electrode locations TP8, TP10, FC4, F6, F8 and FT10, see Figure 5.12-A2. The stimulation protocol for left-hemispheric auditory cortex stimulation shows great focality with mainly four electrodes to be used, two anodal stimulations at electrode locations FT9 and T7 and two cathodal stimulations at electrode locations F7 and F9. Similarly, weaker compensating currents are injected at neighboring electrodes, especially at electrodes F7, C5 and CP5 (Figure 5.12-B2).

The parallelity between the optimized current flow fields and the auditory cortex target vectors was also investigated. With PAR values of 96.08 and 98.28 in the left and right auditory

cortices, the optimized current flow fields are mainly oriented parallel to the auditory cortex target vectors. The optimized current flow fields for left- and right-hemispheric auditory cortex stimulation thus show substantially higher focality and directional agreement to the target vector in comparison to the standard bipolar electrode montage that was used in Section 4.1 and to the best electrode montage for auditory cortex stimulation that was presented in Section 4.3.

5.4. Impact of uncertain head tissue conductivity

While a guideline for efficient yet accurate volume conductor modeling was presented (Section 4.1) and optimized stimulation protocols for auditory cortex stimulation have been calculated (Section 5.3.4), the influence of inter-individually varying conductivity profiles with regard to optimal electrode configurations of a multi-array tCS stimulation is rather unclear. In [121], we present an uncertainty quantification of the optimal electrode configurations with regard to inter-individually varying conductivity profiles. In the following, the most important results of this study are summarized. Further important details can be found in our original publication by Schmidt and Wagner and colleagues [121].

A multi-variate generalized polynomial chaos technique (gPC) is used to compute the probability density functions and sensitivity of the quantities of interest for the uncertainty in the conductivity of skin, skull, gray matter and white matter. The L1R optimization method is used to calculate optimized stimulation protocols for right-hemispheric auditory cortex stimulation. The target vector for right hemispheric auditory cortex stimulation was shown in Figure 5.11. For the uncertainty quantification, upper and lower resistivity values of the compartments skin, gray matter and white matter are chosen from Haueisen [49]. For the isotropic compartment skull, upper and lower conductivity values are selected to be identical to those used by Aydin and colleagues [5]. They selected minimum and maximum conductivity values of $0.0016\,\mathrm{Sm}^{-1}$ and $0.033\,\mathrm{Sm}^{-1}$ for the skin compartment and used a skull-calibration method for simultaneously measured somatosensory evoked potentials and fields. An overview of the conductivity values is depicted in Table 5.6 [121].

Table 5.6.: Overview of mean, lower and upper boundary, and relative deviation of the conductivity values, see also [121].

Tissue type	Conductivity $\left[\mathrm{S\,m}^{-1}\right]$			
	Min	Mean	Max	Rel. Deviation
Skull	0.00016	0.00173	0.0033	90.8 %
Skin	0.28	0.575	0.87	51.3 %
Gray matter	0.22	0.445	0.67	50.6 %
White matter	0.09	0.19	0.29	52.6 %

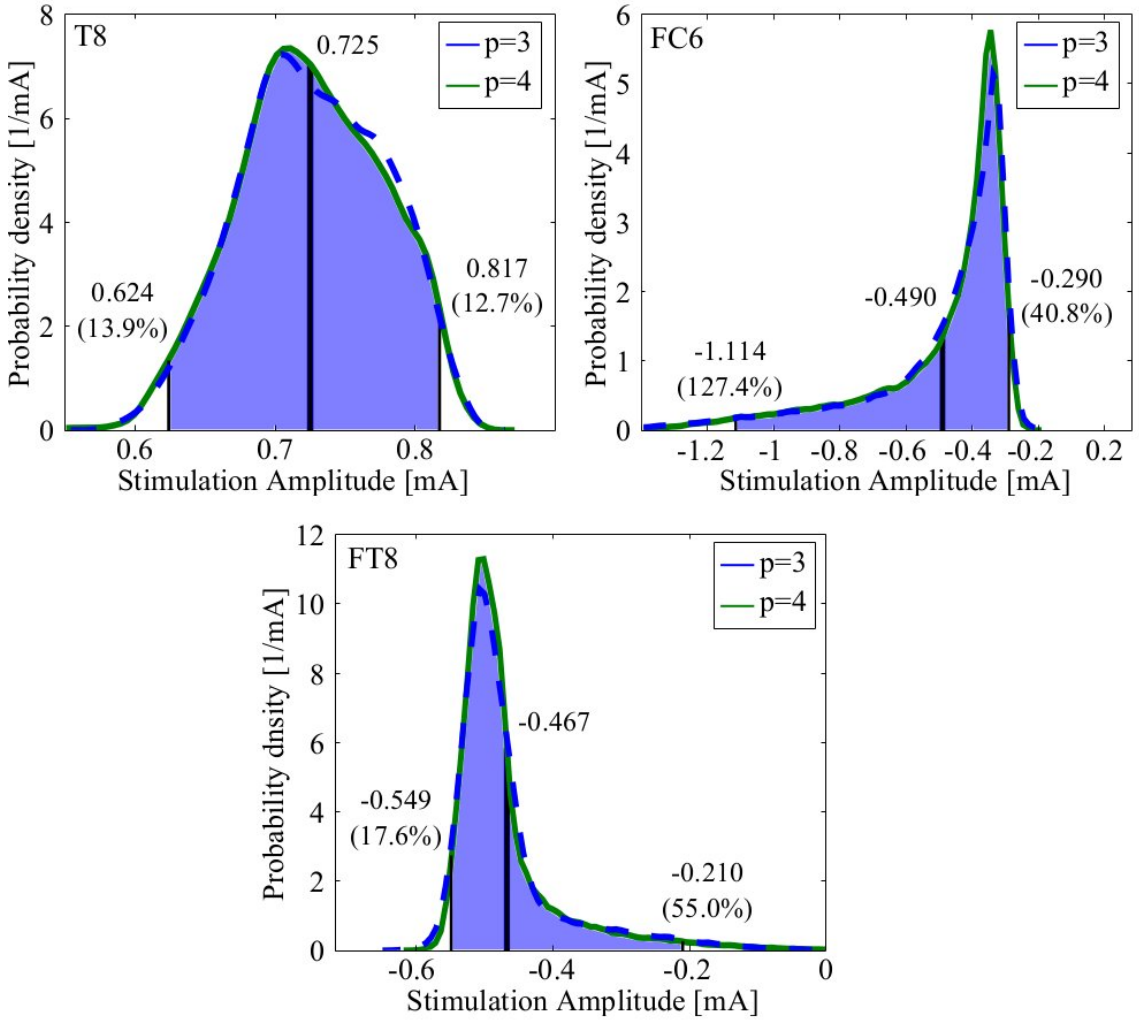

Figure 5.13.: Estimated probability density function for the main anode and the two main cathodes using a gPC expansion order p =3 (blue) and p = 4 (green), modified from [121].

As was shown in Section 5.3.4, the optimized stimulation protocol for right hemispheric auditory cortex stimulation shows great focality and is mainly comprised of three electrodes, an anodal stimulation at electrode location T8 and two cathodal stimulations at electrode locations FT8 and FC6. For this reason, in Figure 5.13 the estimated probability density function for the main anode the main two cathodes using a gPC expansion order of p = 3 and p = 4 are depicted. As can be seen, the probability density functions show a good agreement for expansion orders p = 3 and p = 4, while minor differences can be seen, especially at the peaks of the probability density functions. Moreover, the probability density functions are very sharp. While an asymmetric behavior can be seen for the cathodes, the probability density function for the anode is fairly symmetric, see Figure 5.13. With deviations up to 127.4 % and 55 %, the lower and upper quantities for the cathodes show a considerably larger deviation

Table 5.7.: Sensivitivty on stimulation amplitudes for the main anode and the two main cathodes, see also [121].

	Sensitivity on Stimulation Amplitude		
Parameter	T8 [%]	FC6 [%]	FT8 [%]
σ_{skin}	5.9	7.7	4.0
σ_{skull}	**28.9**	**79.8**	**70.1**
σ_{gm}	16.2	6.9	13.0
σ_{wm}	**27.2**	0.5	3.1
$\sigma_{\mathsf{skin}}, \sigma_{\mathsf{skull}}$	12.0	3.5	6.6
$\sigma_{\mathsf{skull}}, \sigma_{\mathsf{gm}}$	7.3	1.2	2.8
$\sum$	**97.5**	**99.5**	**99.6**

to the mean values as compared to the anode. This shows that inter-individually varying conductivity profiles have a substantial influence on the prediction of optimal stimulation protocols for right-hemispheric auditory cortex stimulation.

In order to investigate to which extent the uncertain tissue conductivities influence the stimulation amplitudes of the three main electrodes, the Sobol' indices for the sensitivity analysis of the three main stimulating electrodes are calculated [121]. Table 5.7 depicts the first order Sobol' indices and the higher order Sobol' indices with values larger than 1 %. A detailed introduction to generalized Sobol' indices can be found in Owen [94].

The sensitivity of the stimulation amplitudes at specified electrodes with respect to each uncertain tissue conductivity is represented by the first order Sobol' indices. The higher order Sobol' indices show interaction effects where only the combination of multiple uncertain parameters results in an uncertain stimulation amplitude [121]. While the stimulation amplitude of the main anode was influenced to a similar extent by the uncertain conductivity of the skull and the white matter, the stimulation amplitudes at the two main cathodes were mainly influenced by the uncertain skull conductivity. This shows that the probability density function of the stimulation protocols at the main anode and cathodes are most sensitive to the uncertainty in the skull conductivity. For this reason, a skull calibration method using simultaneously measured somatosensory evoked potentials and fields [5] might be used to individually estimate the skull conductivity value of the individual subject. Along this line, the skull conductivity can be used as a deterministic model parameter which might reduce the large deviations in the stimulation amplitudes at the main cathodes.

6

Transcranial magnetic stimulation

While tCS simulation studies revealed that the current flow field is rather broad with the largest intensities often located in the non-target regions [82, 142], the current flow field induced by TMS is on a supra-threshold magnitude level (e.g., controlling the thumb movement is possible with TMS, but not with tCS) and the strongest cortical current densities located in brain regions directly under the rim of the stimulating coil [92, 143, 145]. The effects of the individual cortical folding [62, 92], brain tissue anisotropy [74, 93] and brain abnormalities [143] have been recently investigated. Volume conductor models using the highly-conductive CSF compartment [62, 92, 93, 145], a white matter compartment [62, 92, 93, 145] and white matter anisotropy [29, 62, 92, 93] have been employed.

6.1. Computer simulation studies for TMS

6.1.1. Methods and implementation issues

In order to derive the Poisson equation with inhomogeneous Neumann boundary conditions for modeling the electric field induced by transcranial magnetic stimulation, Maxwell's equations are reconsidered (see also Section 2.1)

$$\nabla \times \boldsymbol{E} = -\frac{\partial \boldsymbol{B}}{\partial t} \tag{6.1}$$

$$\nabla \cdot \boldsymbol{B} = 0 \tag{6.2}$$

$$\nabla \times \frac{1}{\mu}\boldsymbol{B} = -\sigma \boldsymbol{E} \tag{6.3}$$

As the magnetic field $\boldsymbol{B}$ is solenoidal, a magnetic vector potential $\mathbf{A}$ is introduced [20] such that (divergence of a curl is zero)

$$\boldsymbol{B} = \nabla \times \mathbf{A} \tag{6.4}$$

Moreover, the magnetic vector potential $\mathbf{A}$ has to fulfill [20]

$$\boldsymbol{E} = -\frac{\partial \mathbf{A}}{\partial t} - \nabla\Phi \tag{6.5}$$

Multiplying Equation 6.5 with the conductivity tensor $\sigma \in (L^\infty(\Omega))^{3\times 3}$ and using Equation 6.3 one obtains

$$\nabla \times \frac{1}{\mu}\boldsymbol{B} = -\sigma\frac{\partial \mathbf{A}}{\partial t} - \sigma\nabla\Phi$$

Applying the divergence operator to both sides and using $\nabla \cdot \nabla \times \frac{1}{\mu}\boldsymbol{B} = 0$, the potential Φ can be calculated as follows

$$\begin{aligned} \nabla \cdot (-\sigma\frac{\partial \mathbf{A}}{\partial t} - \sigma\nabla\Phi) &= 0 && in\ \Omega \\ \Leftrightarrow \nabla \cdot -\sigma\frac{\partial \mathbf{A}}{\partial t} &= \nabla \cdot \sigma\nabla\Phi && in\ \Omega \end{aligned}$$

At the scalp/air boundary inhomogeneous Neumann boundary conditions were used, leading to the following boundary conditions for the potential Φ

$$\begin{aligned} \langle -\sigma\frac{\partial \mathbf{A}}{\partial t} - \sigma\nabla\Phi, \boldsymbol{n}\rangle &= 0 && on\ \Gamma \\ \Leftrightarrow \langle \sigma\nabla\Phi, \boldsymbol{n}\rangle &= -\langle \sigma\frac{\partial \mathbf{A}}{\partial t}, \boldsymbol{n}\rangle && on\ \Gamma \end{aligned}$$

The time-dependent magnetic vector potential $\mathbf{A}(\boldsymbol{x}, t)$ is given as follows [107]

$$\mathbf{A}(\boldsymbol{x}, t) = \frac{\mu_0 \tilde{N}_C I(t)}{4\pi} \int \frac{dl'}{|\boldsymbol{x} - \boldsymbol{x}_0|} \tag{6.6}$$

with $\tilde{N}_C$ being the number of windings of the coil, $I(t)$ being the current in the coil at time point t, $\mu_0 = 10^{-7}\pi 4\,\mathrm{Vs(Am)}^{-1}$ being a constant, $\boldsymbol{x}$ being the field point, $\boldsymbol{x}_0$ being the source point and dl' being a vector pointing from the source point to the field point.

Definition 6.1. The elliptic partial differential equation for TMS modeling is given as

$$\nabla \cdot \sigma\nabla\Phi = -\nabla \cdot \sigma\frac{\partial \mathbf{A}}{\partial t} \qquad in\ \Omega \tag{6.7}$$

$$\langle \sigma\nabla\Phi, \boldsymbol{n}\rangle = -\langle \sigma\frac{\partial \mathbf{A}}{\partial t}, \boldsymbol{n}\rangle \quad on\ \Gamma \setminus \Gamma_D \tag{6.8}$$

$$\Phi = 0 \qquad on\ \Gamma_D \tag{6.9}$$

Under standard and naturally satisfied regularity assumptions, there exists a unique solution $\Phi \in H^1(\Omega)$ to the TMS forward problem, which can be shown by the Lax- Milgram Lemma

Theorem 6.1 (Existence of a unique solution for TMS simulations)**.** Let Ω be a domain with Lipschitz boundary Γ and consider the Poisson equation 6.7 with inhomogeneous Neumann

boundary conditions 6.8 and the homogeneous Dirichlet boundary condition 6.9. Let furthermore $\frac{\partial A}{\partial t} \in (L^2(\Omega))^3$. Then there exists a unique solution $\Phi \in H^1(\Omega)$ to the PDE for TMS modeling.

Furthermore, the TMS forward problem fulfills the compatibility condition as shown in the following

Theorem 6.2. Let us consider the partial differential equations 6.7 - 6.9 for the TMS forward problem. The compatibility condition

$$\int_\Omega \nabla \cdot (-\sigma \frac{\partial \mathbf{A}}{\partial t} - \sigma \nabla \Phi) \, \mathrm{d}\boldsymbol{x} - \int_\Gamma \langle -\sigma \frac{\partial \mathbf{A}}{\partial t} - \sigma \nabla \Phi, \boldsymbol{n} \rangle \, \mathrm{d}\boldsymbol{x} = 0$$

is fulfilled.

Proof. Let $f = \nabla \cdot (-\sigma \frac{\partial \mathbf{A}}{\partial t} - \sigma \nabla \Phi)$ and $g = \langle -\sigma \frac{\partial \mathbf{A}}{\partial t} - \sigma \nabla \Phi, \boldsymbol{n} \rangle$. As was discussed before, the conductivity tensor fulfills $\sigma \in (L^\infty(\Omega))^{3\times 3}$ and the potential $\Phi \in H^1(\Omega)$. Furthermore, the time dependent magnetic vector potential $\mathbf{A}$ is in $C^1(\Omega)$. Therefore, the left hand side $f \in H^1(\Omega)$ and the extended version of Gauss theorem can be applied

$$\int_\Omega f \, \mathrm{d}\boldsymbol{x} = \int_\Omega \nabla \cdot (-\sigma \frac{\partial \mathbf{A}}{\partial t} - \sigma \nabla \Phi) \, \mathrm{d}\boldsymbol{x} \overset{(A.5)}{=} \int_\Gamma \langle -\sigma \frac{\partial \mathbf{A}}{\partial t} - \sigma \nabla \Phi, \boldsymbol{n} \rangle \, \mathrm{d}\boldsymbol{x} = \int_\Gamma g \, \mathrm{d}\boldsymbol{x}$$

and thus $\int_\Omega f \, \mathrm{d}\boldsymbol{x} - \int_\Gamma g \, \mathrm{d}\boldsymbol{x} = 0$. □

Remark 6.1 (Subtraction approach for the EEG forward problem)**.** The partial differential equation for TMS modeling is very similar to the PDE for the subtraction approach for the EEG forward problem (see Section 2.1), given as $\nabla \cdot \sigma(\boldsymbol{x}) \Phi^{corr}(\boldsymbol{x}) = \nabla(\sigma(\boldsymbol{x}_0) - \sigma(\boldsymbol{x})) \nabla \Phi^\infty$. While the subtraction approach utilize the analytically known potential Φ^∞ to calculate the correction potential Φ^{corr}, the time derivative of the magnetic vector potential $\mathbf{A}(\boldsymbol{x}, t)$ is used to calculate the potential field induced by TMS. With regard to numerical implementation, the main advantage of TMS modeling is that the magnetic vector potential $\mathbf{A}(\boldsymbol{x}, t)$ is free of singularities in the volume conductor model. It is therefore not necessary to use a subtraction method for TMS modeling.
As was shown by Lew and colleagues [71] and Drechsler and colleagues [34], the combination of the full subtraction approach with detailed volume conductor models led to very good numerical accuracies in sphere models. Therefore, the here presented modeling pipeline for TMS should also lead to good numerical accuracies in sphere models.

6.1.2. A finite element approach for TMS

As was shown in Theorem 6.1, the TMS problem is well defined (existence and uniqueness of the solution was proven) and thus appropriate for a variational FE formulation . When multiplying Equation 6.7 with a FE ansatz function $\psi_i \in C^\infty(\Omega)$ and integrating over Ω one

Algorithm 3 TMS modeling pipeline

Input: $NumElem, \sigma, I(t), \tilde{N}_C, \mu_0$
for $k = 1, \cdots, NumElem$ **do**
  for $i = 1, \cdots, NumElem$ **do**
    $K_{ij} = \int_\Omega \langle \sigma \nabla \psi_k, \nabla \psi_i \rangle \, \mathrm{d}\boldsymbol{x}$
  end for
end for
for $t = 1, \cdots, t_{max}$ **do**
  $\mathbf{A}(\boldsymbol{x}, t) = \frac{\mu_0 \tilde{N}_C I(t)}{4\pi} \int_C \frac{dl'}{|\boldsymbol{x} - \boldsymbol{x}_0|}$
end for
for $i = 1, \cdots, NumElem$ **do**
  $b_i = \int_\Omega \langle \sigma \frac{\partial \mathbf{A}}{\partial t}, \nabla \psi_i \rangle \, \mathrm{d}\boldsymbol{x}$
end for
Solve $\mathbf{K}\Phi^{TMS} = \boldsymbol{b}$
$\boldsymbol{E} = -\frac{\partial A}{\partial t} - \nabla \Phi$
$\boldsymbol{J} = \sigma \boldsymbol{E}$
return $\boldsymbol{J}, \boldsymbol{E}$;

obtains

$$\int_\Omega \nabla \cdot \sigma \nabla \Phi \psi_i \, \mathrm{d}\boldsymbol{x} = -\int_\Omega \nabla \cdot \sigma \frac{\partial \mathbf{A}}{\partial t} \psi_i \, \mathrm{d}\boldsymbol{x}$$

Applying integration by parts leads to

$$-\int_\Omega \langle \sigma \nabla \Phi, \nabla \psi_i \rangle \, \mathrm{d}\boldsymbol{x} + \int_\Gamma \langle \underbrace{\sigma \nabla \Phi}_{-\sigma \frac{\partial \mathbf{A}}{\partial t}}, \boldsymbol{n} \rangle \psi_i \, \mathrm{d}\boldsymbol{x} = \int_\Omega \langle \sigma \frac{\partial \mathbf{A}}{\partial t}, \nabla \psi_i \rangle \, \mathrm{d}\boldsymbol{x} - \int_\Gamma \langle \sigma \frac{\partial \mathbf{A}}{\partial t}, \boldsymbol{n} \rangle \psi_i \, \mathrm{d}\boldsymbol{x}$$

$$\Rightarrow -\int_\Omega \langle \sigma \nabla \Phi, \nabla \psi_i \rangle \, \mathrm{d}\boldsymbol{x} = \int_\Omega \langle \sigma \frac{\partial \mathbf{A}}{\partial t}, \nabla \psi_i \rangle \, \mathrm{d}\boldsymbol{x}$$

Projecting the potential Φ into the FE space one obtains a linear system $\mathbf{K}\Phi^{TMS} = \boldsymbol{b}$ with the well-known stiffness matrix 2.28, the right-hand side vector $\boldsymbol{b}$

$$\boldsymbol{b} = (b_i)_{i=1,\cdots,N} = (\int_\Omega \langle \sigma \frac{\partial \mathbf{A}}{\partial t}, \nabla \psi_i \rangle \, \mathrm{d}\boldsymbol{x})_{i=1,\cdots,N}$$

and the solution vector $\Phi^{TMS} = [\Phi_1, \ldots, \Phi_N] \in \mathbb{R}^N$.

After setting up the right-hand side vector $\boldsymbol{b}$, an AMG-CG solver with a solver accuracy level of 10^{-7} (see also Section 3.3.2.3) is used to solve the linear equation system. Finally, the electric field $\boldsymbol{E}$ and the current flow vector field $\boldsymbol{J}$ are calculated from the solution vector Φ^{TMS} at the FE nodes

$$\boldsymbol{J} = \sigma \boldsymbol{E} = \sigma(-\frac{\partial \mathbf{A}}{\partial t} - \nabla \Phi).$$

Algorithm 3 depicts the modeling pipeline for TMS which is implemented in the freely-available SimBio toolbox [126]. When the stiffness matrix $\mathbf{K}$ is available, the magnetic vector potential

$\mathbf{A}$ is calculated. In order to calculate the time-dependent magnetic vector potential, the current in the coil element $I(t)$ is required at each time point t. This leads to a matrix $\mathbf{A} \in \mathbb{R}^{(3N \times t_{max})}$ with t_{max} being the number of time points to be evaluated. In this thesis, however, all computations are performed with a rate of change of the coil current of $p(t) = 1\,\mathrm{A}\mu\mathrm{s}^{-1}$ [92]. A current $I(t) = Ip(t)$ with a constant rate of change is thus used, leading to a matrix $\tilde{\mathbf{A}} \in \mathbb{R}^{3N}$. Therefore, only the current flow fields at a specific and fixed time point of the stimulating pulse are simulated. The most time consuming part in this modeling pipeline is the calculation of the right-hand side vector $\boldsymbol{b}$ (i.e., the computation of the integral for each element). Similar to Drechsler and colleagues [34], a Stroud quadrature formula of order two is used. With regard to the subtraction approach, a quadrature order of 2 was sufficient to receive very good numerical accuracies and to reduce the computational burden substantially [34]. After solving the linear equation system $\mathbf{K}\Phi^{TMS} = \boldsymbol{b}$, the electric field $\boldsymbol{E}$ is calculated from the solution vector Φ^{TMS} at the volume conductor nodes and the time derivative of the magnetic vector potential. Finally, the current flow field is given by the product of the conductivity tensor σ with the electric field $\boldsymbol{E}$.

Algorithm 3 is implemented for high-resolution tetrahedral as well as hexahedral FE models. Also, two commonly-used coil setups are employed, namely a round-shaped circular coil and a figure-of-eight coil, see also Figures 6.2-B1 and 6.3-B1. Moreover, a script to change the location and to flip the orientation of the coil elements was developed. This is especially important when simulating a variety of coil locations and orientations in order to optimize coil montages, see Section 6.2.

6.1.3. Computer simulation results and Discussion

6.1.3.1. Spherical shell models

In this section, TMS induced current flow fields are calculated in spherical shell models $hex3.2m$ and $tet503k$. The current density distribution is visually inspected and compared to the published simulation results [145]. Two commonly-used clinical coil setups are employed, namely a round-shaped coil and a figure-of-eight coil [92, 93, 145].

Figure 6.1 depicts the current flow fields when a circular (6.1-A) and a figure-of-eight (6.1-B) coil are used for stimulation. As can be seen in the figure, in the spehere models $hex3.2m$ and $tet503k$, the current flow field pattern are very similar (compare Figures -A1 and -A2 and -B1 and -B2) . The circular coil leads to maximal current densities of about $2\,\mathrm{Am}^{-2}$, while maximal currents of about $4\,\mathrm{Am}^{-2}$ can be seen for the figure-of-eight coil. When using the circular coil, strongest current flow field amplitudes can be seen directly underneath the rim of the stimulating coil. Hardly any current density amplitudes can be seen in the brain compartment underneath the center of the round-shaped coil (Figures 6.1-A1 and -A2). The figure-of-eight coil leads to strongest intensities located in a region directly underneath the center of the stimulating coil, in line with Wagner and colleagues [145]. They centered a figure-of-eight coil

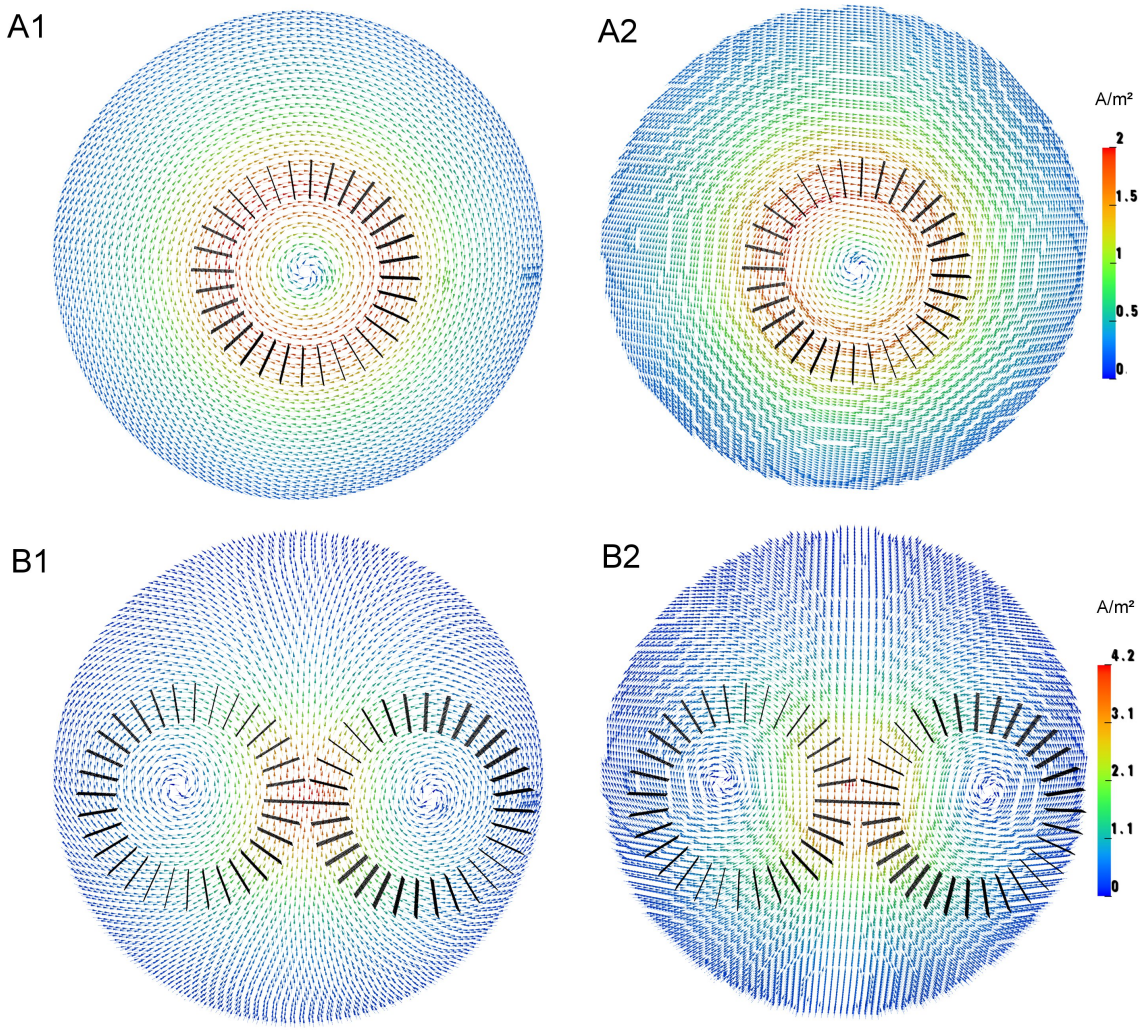

Figure 6.1.: Current density distribution $\boldsymbol{J}$ in two spherical shell models. The left column displays $\boldsymbol{J}$ on a sagittal slice through a tetrahedral sphere model, whereas the right column shows the current flow field in a hexahedral model using a circular coil (first row) and a figure-of-eight coil (second row).

10 mm above an *infinite half-plane* of conductivity $1.65\,\mathrm{Sm}^{-1}$ and investigated the current density vector field orientation on the surface of the plane. Wagner and colleagues found a very similar current flow pattern (Figures 2-C and 3-E in [145]).

Table 6.1 shows the interaction of median brain current density amplitude and distance to the nearest coil node. As can be seen, for both coil montages, the median brain current density decreases with increasing distance to the nearest coil node. This result is in line with Wagner and colleagues [145] who evaluated the normal and tangential current density magnitudes along a linear evaluation line through the center of the figure-of-eight and circular coils. They were also able to show that the tangential and normal brain current density amplitude decreases with an increasing distance to the center of the stimulating coil. Relatively low current densities can be seen in coil-remote cortical regions and in the depth of the model, see Table 6.1. As can be seen, the decrease in median current density amplitude is stronger when using a figure-of-eight coil. While the median brain current density decreases to one

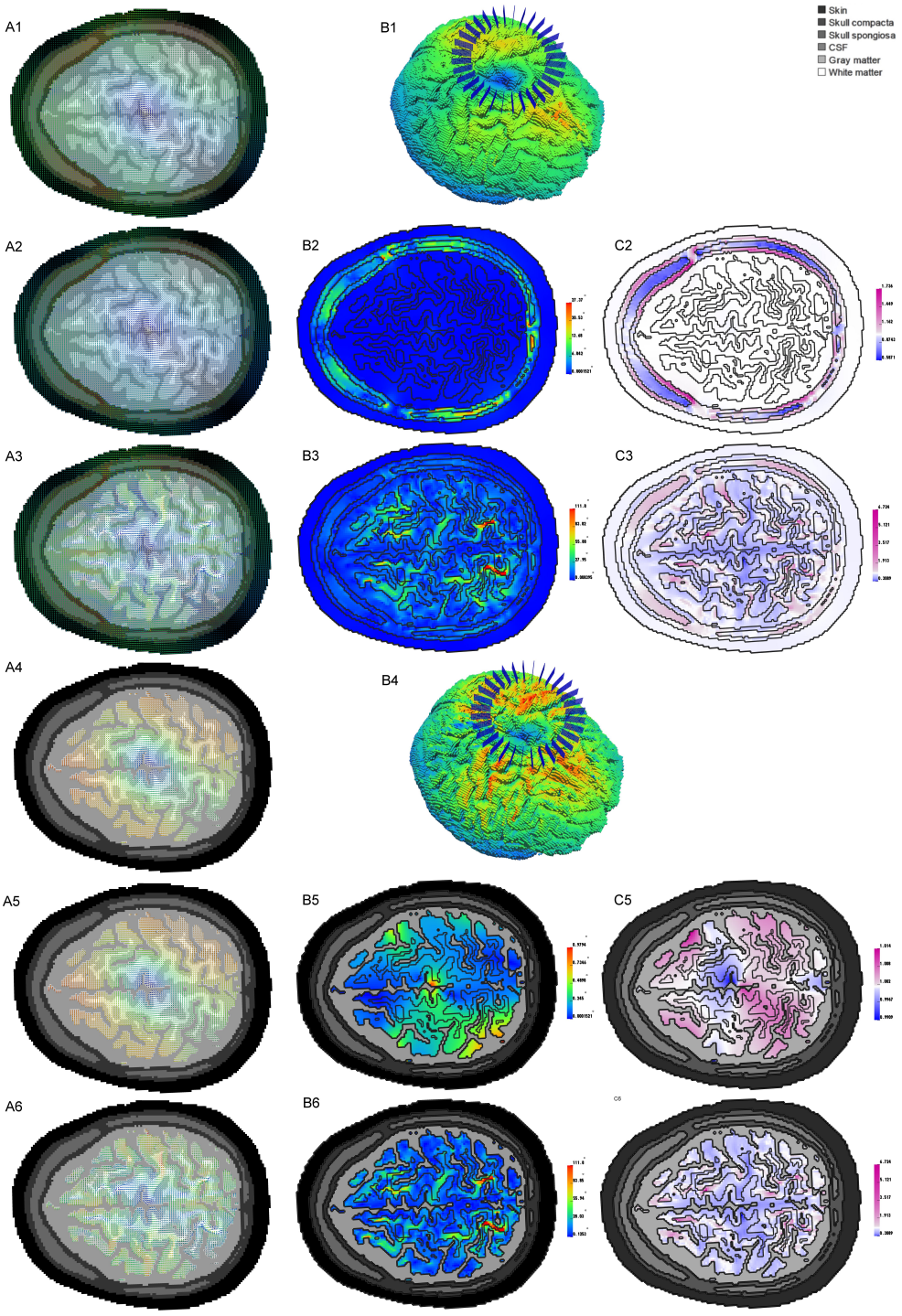

Figure 6.2.: Electric field $\boldsymbol{E}$ using a circular coil. The left column depicts the electric field for the 3CI (A1, A4), 4CI (A2, A5) and 6CI (A3, A6) head model on an axial slice through the model. The middle and right columns show change in orientation and magnitude of the electric field between the 3CI and 4CI models (B2, B5) and (C2, C5) and the 3CI and 6CI models (B3, B6) and (C3, C6). Figures A1-A3 depicts the electric field in all compartments, while Figures A4-A6 show only the brain electric fields. In Figures B1 and B4, volume renderings of the electric fields on the brain surface computed in the 3CI and 6CI models are shown, respectively.

half within 15 mm for a figure-of-eight coil, a radius of 25 mm is needed to reduce the median brain current density to one half when using a circular coil (Table 6.1). The circular coil

Table 6.1.: Percentage of the median current density in the brain compartment (Current density at 20 mm = 100 % at specific distance +,- 2.5 mm to the nearest coil node.

	Tetrahedral model [%]		**Hexahedral model** [%]	
Distance [mm]	Circular	Figure-of-eight	Circular	Figure-of-eight
20	100	100	100	100
25	82.9	73.5	76.3	69.2
30	69.5	54.7	63.1	53.0
35	58.6	43.7	53.9	40.9
40	50.4	35.6	45.2	33.2
45	43.2	29.5	39.6	27.2
50	37.7	25.9	33.3	22.7
55	32.6	20.3	29.9	19.4
60	28.8	17.6	28.6	16.7
65	25.4	15.0	23.2	13.8
70	22.7	13.0	20.0	12.9

thus induces a comparably broad current flow pattern, while the current flow pattern is very focal when using a figure-of-eight coil. As symmetric sphere models and stimulating coils are used, current density in the center of the stimulating coils is zero. This is due to the orientation of the current density to the surface of the sphere model underneath the center of the stimulating coil, in line with Tofts [132] who showed that no perpendicular currents occurred in magnetic stimulation of the nervous system. This has also been experimentally validated by Brandston and Tofts [16] who were able to show that the perpendicular currents are very small for a circular stimulating coil. For this, they measured the electric field in a tank filled with electrolyte and measured the maximal perpendicular currents to be about 8 percent of the maximal tangential currents [16].

In this section, a proof-of-concept that the SimBio-TMS pipeline is working properly was presented. Simulation results in sphere models of other groups [16, 132, 145] were replicated and the focality of the stimulation has been shown, in line with [145].

6.1.3.2. Realistic volume conductor model

As the SimBio-TMS pipeline is working properly and a constant change of current in the coil element is assumed, the electrical field $\boldsymbol{E}$ is investigated in a high-realistic six-compartment head model. The electric field was also investigated by other groups [62, 92, 93].

Skull modeling

In this section, the influence of an accurate modeling of separate skull compacta and spongiosa compartments on the electric field is investigated. In a first step the electric field is investigated

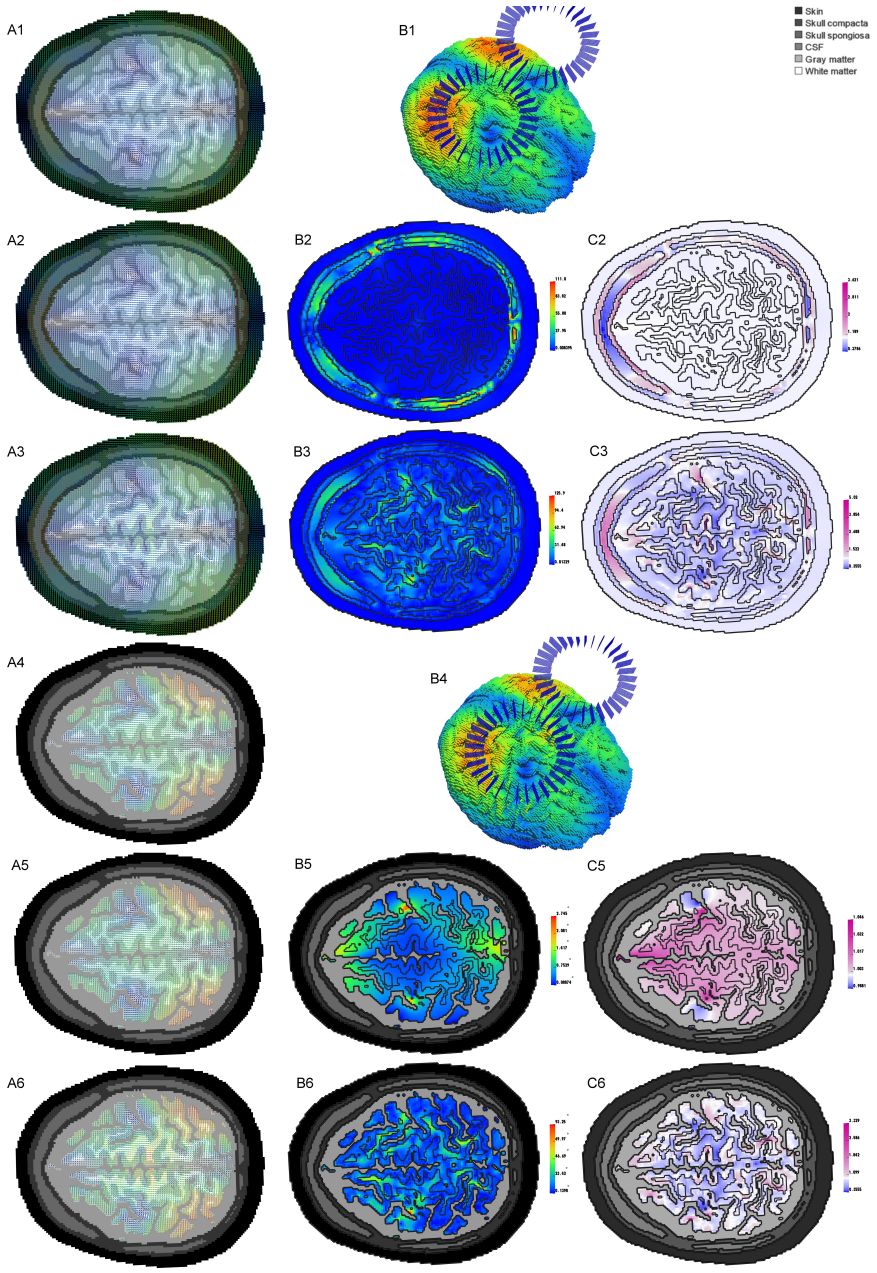

Figure 6.3.: Electric field $\boldsymbol{E}$ using a figure-of-eight coil. The left column depicts the electric field for the 3CI (A1, A4), 4CI (A2, A5) and 6CI (A3, A6) head model on an axial slice through the model. The middle and right columns show change in orientation and magnitude of the electric field between the 3CI and 4CI models (B2, B5) and (C2, C5) and the 3CI and 6CI models (B3, B6) and (C3, C6). Figures A1-A3 depicts the electric field in all compartments, while Figures A4-A6 show the brain electric fields. In Figures B1 and B4, volume renderings of the electric fields on the brain surface computed in the 3CI and 6CI models are shown, respectively..

in a low-parametric three-compartment head model (skin, skull, brain). The more realistic four-compartment head model distinguishes between skull compacta and spongiosa using conductivity values of $0.007\,\mathrm{Sm}^{-1}$ and $0.025\,\mathrm{Sm}^{-1}$ for compact and spongy bone, respectively [2]. As the results for the circular and figure-of-eight coil are very similar, mainly the effects with regard to the circular coil are presented. For the figure-of-eight coil, the main

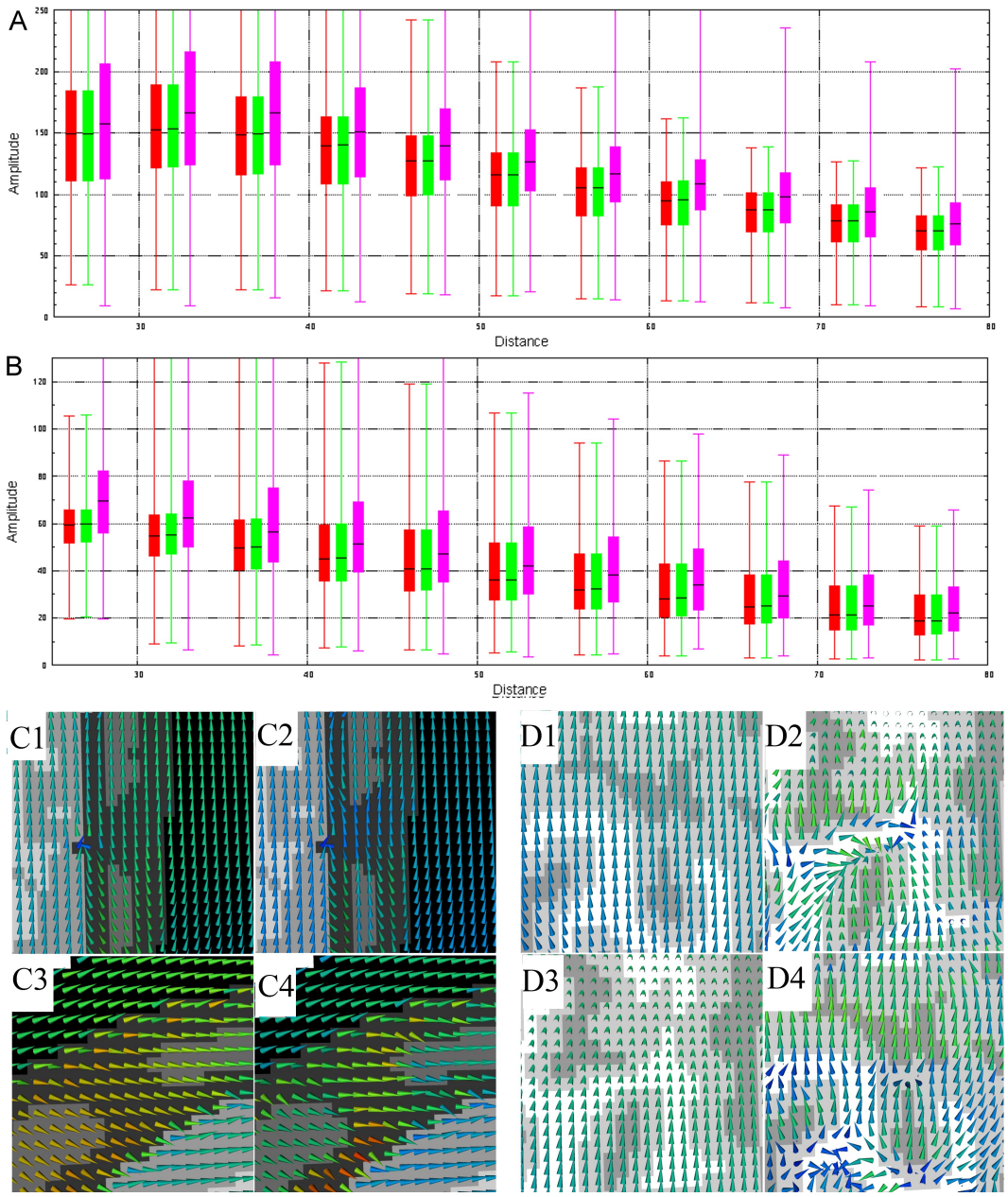

Figure 6.4.: Electric field amplitudes in elements of the brain compartment located at a specific distance (± 2.5 mm) to the nearest coil (circular coil = Figure A, figure-of-eight coil = Figure B) node are presented in a boxplot for the three models. Black dashes show the media, upper and lower quartile by means of the box and the error bars show the maximal amplitudes. Selected details of the electric field using a circular coil are shown in Figures C and D. Figures C show the effect of including a skull spongiosa compartment (C2, C4) to the low- parametric three-compartment head model (C1, C3). Figures D depict major changes in electric field between the 6CI model (D2, D4) and the 3CI model (D1, D3).

differences with respect to the circular coil are investigated; important data will be presented in parentheses following the circular coil data.

Figures 6.2-A1, -A2 (6.3-A1, -A2) depict the electrical field $\boldsymbol{E}$ on an axial slice in the 3CI and 4CI models, respectively. Moreover, changes in orientation and magnitude between the 4CI

and the 3CI model are depicted in Figures 6.2-B2, -C2 (6.3-B2, -C2). Orientation changes up to 27.3 degrees (111.8 degrees) and magnitudes changes up to a factor of 1.736 (3.621) occur in both skull compartments and are largest in the skull spongiosa compartment (Figures 6.2-B2, -C2). In the skin, CSF and brain compartments, hardly any change in orientation can be found. Similar results can be seen for the current density magnitude which increases in skull compacta and decreases in spongiosa and remains identical in the skin, CSF and brain compartments (Figures 6.2-B2, -C2). Figures 6.2-A4, -A5, -B5, -C5 (6.3-A4, -A5, -B5, -C5) show the brain electric field distribution in the 3CI and 4CI models and the change in orientation and magnitude between the 3CI and the 4CI models only in the brain compartment, respectively. As can be seen, minor changes in orientation up to 0.97 degrees (2,745 degrees) and an increase in current density up to a factor of 1.014 (1.046) can be seen in the brain compartments (Figures 6.2-B5, -C5).

The correlation between median brain vector field amplitude and distance to the nearest coil node is depicted in Figure 6.4-A (6.4-B). Almost no change in median brain vector field amplitude and maximal and minimal vector field magnitudes can be seen between the 3CI and the 4CI models.

Figures 6.4-C, -D depict magnified samples of the electric field in full resolution. Figures C show the differences in electric distribution, by comparing model 3CI(C1, C3) to model 4CI (C2, C4). When a separate spongiosa compartment is modeled, vectors in compact bone tend to be oriented towards the nearest spongiosa compartment close by. Slightly tangential electric field components occur in the spongiosa compartment in the 4CI model, while they are mainly radially oriented in the 3CI model, see Figure 6.4-C2, -C4.

For both coil montages, the electrical field in the brain is hardly affected by the presence of a spongiosa compartment. With changes in orientation and magnitude below 1 % and a maximal factor of 0.02, the model error is substantially smaller as compared to the numerical error of the modeling approach for TMS simulations. In the simulation study of Lew and colleagues [71], the full subtraction approach, which is very similar to the SimBio-TMS modeling approach, showed MAG errors below 0.1 for all source eccentricities, which is one order of magnitude higher as compared model errors that were found in this section.

In conclusion, skull compacta and spongiosa modeling was shown to not be important in realistic TMS simulations. It is therefore sufficient to use an isotropic skull representation for TMS modeling. Also, by means of reciprocity [53, 135, 142], the results clearly indicate that skull modeling did not substantially influence the results of MEG source analysis. It is therefore possible to use a calibration method to combine EEG and MEG measurements in order to individually fit the conductivity value of the skull compartment, see also Aydin and colleagues [5] for further details about skull conductivity calibration.

Volume conduction effects in the highly-realistic six-compartment head model

In this section, differences in the electrical field **E** between the 3CI and the more realistic 6CI model are investigated. Figures 6.2-A1, -A3 (6.3-A1, -A3) depict the vector fields in the 3CI

and 6CI models, respectively. Changes in orientation and magnitude between the 3CI and 6CI model are shown in Figures 6.2-B3, -C3 (6.3-B3, -C3). Changes in orientation up to 112 degrees (126 degrees) can be observed in the white matter and CSF compartments, while minor changes are visible in the skull and gray matter and hardly any changes can be seen in the skin (Figures 6.2-B3, -C3 (6.3-B3, -C3)). Magnitude increases in the skull spongiosa (up to a factor of 5.02 (6.724)), remains mainly constant in the skin and mainly decreases in the skull compacta and gray matter compartments. In the CSF and white matter regions, both, an increase and a decrease in magnitude can be observed. In the brain compartment (Figures 6.2-A4, -A5, -B5, -C5 (6.3-A4, -A5, -B5, -C5)), strongest changes in orientation of up to 93.2 degrees (111.8 degrees) can be seen in the white matter. Moreover orientation changes up to 60 degrees (55 degrees) occur in the gray matter compartment, mainly at the outermost parts of the gray matter. Figures 6.2-B1, -B4 (6.3-B1, -B4) depict a volume rendering of the electric field in the 3CI and 6CI models. While a homogeneous vector field pattern with strongest intensities located in regions directly under the rim of the stimulating coil can be seen in head model 3CI, a more widespread electric distribution can be shown in head model 6CI. A homogeneous vector field with strongest vector field amplitudes in gray matter can be observed in the 3CI model, see Figure 6.2-A4. Using the more realistic six compartment head model changed this behavior. The electric field distribution in the 6CI model is less homogeneous with strongest intensities located not only in the gray matter compartment, but also in deeper white matter structures. Moreover, vectors in lower conductive white matter regions tend to be oriented towards the more conductive gray matter compartment close by. Gray matter vectors close to the CSF are also pointing towards the CSF, because it offers a lower resistive pathway (Figure 6.2-A6).

The median brain vector field amplitude in the 6CI model decreases with an increasing distance to the stimulating coil, with an increase in median amplitude between 20 mm and 25 mm for the circular coil. This is due to the channeling effect of the CSF compartment, similar to the effect that was found in tCS (see Section 4.1). When using a figure-of-eight coil, the median current density amplitude decreases smoothly with increasing distance to the nearest coil node, see Figures 6.4-B. The median brain vector field amplitude in the 6CI models is higher as compared to the 3CI model.

Guideline for efficient yet accurate volume conductor modeling in TMS

As the effect of white matter anisotropy was investigated recently by other groups [29], the influence of white matter anisotropy modeling were not investigated. DeLucia and colleagues [29] used a three-dimensional model that included anisotropic conductivity information derived from DTI data. They found only minor effects of brain tissue anisotropy modeling on the location and intensity of the maximal electric field amplitudes. Furthermore, they reported that, with differences of the order of 10 % of the maximal electric field, anisotropy modeling has considerably more effect on the extent of the electrical field. The area affected by the stimulation was shown to be slightly larger when white matter fiber tract anisotropy was included as compared to the isotropic model [29].

Keeping this information in mind, a guideline for efficient yet accurate volume conductor modeling in TMS can be formulated: All important tissues between the stimulating coil and the target brain area should be modeled as accurately as possible. Skull compacta and spongiosa modeling and brain tissue anisotropy modeling have only small effects on the electric distribution in the target brain area. In conclusion, isotropic representation of the skin, skull, CSF, gray and white matter are needed for realistic electric field estimation in TMS. For deeper target regions, white matter anisotropy modeling might also significantly influence the electric field distribution [139].

6.2. Multi-channel stimulation system

As was shown in Table 6.1 and Figure 6.4, the electric fields induced by a figure-of-eight and round-shaped coil are comparably focal with strongest intensities located in the superficial cortical regions. When increasing the distance to the nearest coil element, the electric field decreased rapidly, see Table 6.1. Deep target regions can thus not appropriately be stimulated with the existing coil elements. In order to be able to stimulate deeper targets, an *h-coil* was introduced [109]. Roth and colleagues [109] showed in numerical simulations that the decrease in the electric field induced by an h-coil is considerably lower as compared to the figure-of-eight and circular coils. However, the stimulation of deeper target regions remains difficult. Moreover, the deeper the target vector is located, the higher the radial component of the target vector. In order to overcome the limitations of single coil TMS, sensor optimization approaches for multi-array TMS devices have been introduced recently [44, 69, 111]. Ruohonen and Ilmoniemi [111] used a planar coil set consisting of 36 small circular coil elements in a square lattice and calculated the optimized driving currents in an unbounded volume conductor model. They reported that the induced electric field was substantially more focused when 36 independent coil elements were used as compared to single coil stimulation. Moreover, the target brain region can be adapted without moving the electrode array. In 2007, Lee and colleagues [69] combined the minimum norm optimization procedure with the boundary element method in order to optimize the electric field in a more realistic volume conductor model. They used MRI data with 1 mm voxel size to extract a mesh with 500,000 triangular elements including about 250,000 vertices [69]. Recently, Gomez and colleagues [44] introduced a systematic, genetic algorithm-based techniques for multi-array TMS devices. This technique is used to minimize the volume of excited brain tissue required to generate a predefined penetration depth of the electric field [44]. For numerical validation, Gomez and colleagues [44] used a target depth $d_{stim} = 24\,\text{mm}$ and the authors were able to demonstrate that the excited volume was decreased by a factor of 3 and 2.6 when using their optimized multi-array and TMS device as compared to a figure-of-eight coil. Also, when exciting only 0.3 % of the volume, the optimized field arrays were shown to reach a depth of 27 mm into the head while the field of the figure-of-eight coil only reaches a depth of 15mm [44].

6.2.1. Novel optimization approach for multi-array TMS

In this section, a novel optimization approach for safe and well-targeted multi-array transcranial magnetic stimulation is presented. This optimization method is very similar to the optimization method for multi-array transcranial current stimulation. In order to allow focused and well-targeted stimulation, the threshold values $E_T = 150\,\mathrm{Vm}^{-1}$ and $E_M = 450\,\mathrm{Vm}^{-1}$ representing neural depolarization and painful muscle twichting are used [44]. Because there is no safety limit for the total currents applied to the stimulating coils (there is no direct contact between the coil elements and the skin surface) but a safety-threshold for painful muscle twitching, the constrained minimization problem for multi-coil TMS is defined as

$$
\begin{aligned}
(\mathbf{P}_{TMS}) \qquad & -\textstyle\int_\Omega \langle \boldsymbol{E}, \boldsymbol{e}\rangle \,\mathrm{d}\boldsymbol{x} && +\alpha \displaystyle\int_{\tilde{C}} |\boldsymbol{I}_{TMS}(t)|^2 \,\mathrm{d}\boldsymbol{x} + \beta \int_{\tilde{C}} |\boldsymbol{I}_{TMS}(t)| \,\mathrm{d}\boldsymbol{x} \to \min_{\boldsymbol{I}_{TMS}} \\
& \text{subject to} && \omega|\boldsymbol{E}| \le E_M \\
& && \nabla \cdot \sigma \nabla \Phi = -\nabla \cdot \sigma \frac{\partial \mathbf{A}(\boldsymbol{x},t)}{\partial t} && \text{in } \Omega \\
& && \langle \sigma \nabla \Phi, \boldsymbol{n}\rangle \;= -\langle \sigma \frac{\partial \mathbf{A}(\boldsymbol{x},t)}{\partial t}, \boldsymbol{n}\rangle && \text{on } \Gamma \\
& && \Phi = 0 && \text{on } \Gamma_D \\
& && \boldsymbol{E} = -\frac{\partial \boldsymbol{A}}{\partial t} - \nabla \Phi
\end{aligned}
$$

with $\mathbf{A}(\boldsymbol{x}, t)$ being the time-dependent magnetic vector potential

$$
\mathbf{A}(\boldsymbol{x},t) = \sum_{k=1}^{C} \frac{\mu_0 N_C \boldsymbol{I}_{TMS}(t)}{4\pi} \int_{\tilde{C}_k} \frac{dl'}{|\boldsymbol{x} - \boldsymbol{x}_0|}
$$

and $\boldsymbol{I}_{TMS}(t)$ being the time-dependent and optimized *driving currents* in the TMS coils $\tilde{C}$. For the sake of simplicity, it is now assumed that the driving current $\boldsymbol{I}_{TMS}$ is linear in time with regard to each coil element, i.e., $\boldsymbol{I}_{TMS}(t) = \boldsymbol{I}^k_{TMS} t$ on each coil $k = 1, \ldots, C$ with C being the number of coil elements [92]. Note that the coils are not part of the volume conductor model Ω.

Two mappings $\mathbf{A}^1_{TMS}$ and $\mathbf{A}^2_{TMS}$ are defined as

$$
\mathbf{A}^1_{TMS} : \mathbb{R}^C \to L^2(\Omega)^3, \quad \boldsymbol{I}_{TMS} \mapsto \tfrac{\partial \mathbf{A}(\boldsymbol{x},t)}{\partial t}
$$

and

$$
\mathbf{A}^2_{TMS} : L^2(\Omega)^3 \to L^2(\Omega)^3, \quad \tfrac{\partial \mathbf{A}(\boldsymbol{x},t)}{\partial t} \mapsto \boldsymbol{E}
$$

and the mapping matrix $\mathbf{A}_{TMS}$ is defined as $\mathbf{A}^2_{TMS} \circ \mathbf{A}^1_{TMS}$.

Similar to Section 5, $\boldsymbol{E} = \mathbf{A}_{TMS} \boldsymbol{I}_{TMS}$ is substituted leading to the equivalent constrained optimization problem $(\mathbf{P}^{\alpha,\beta}_{TMS,E_M})$

$$
(\mathbf{P}^{\alpha,\beta}_{TMS,E_M}) \qquad -\textstyle\int_\Omega \langle \mathbf{A}_{TMS} \boldsymbol{I}_{TMS}, \boldsymbol{e}\rangle \,\mathrm{d}\boldsymbol{x} \quad +\alpha \displaystyle\int_{\tilde{C}} |\boldsymbol{I}_{TMS}|^2 \,\mathrm{d}\boldsymbol{x} + \beta \int_{\tilde{C}} |\boldsymbol{I}_{TMS}| \,\mathrm{d}\boldsymbol{x} \to \min_{\boldsymbol{I}_{TMS}}
$$

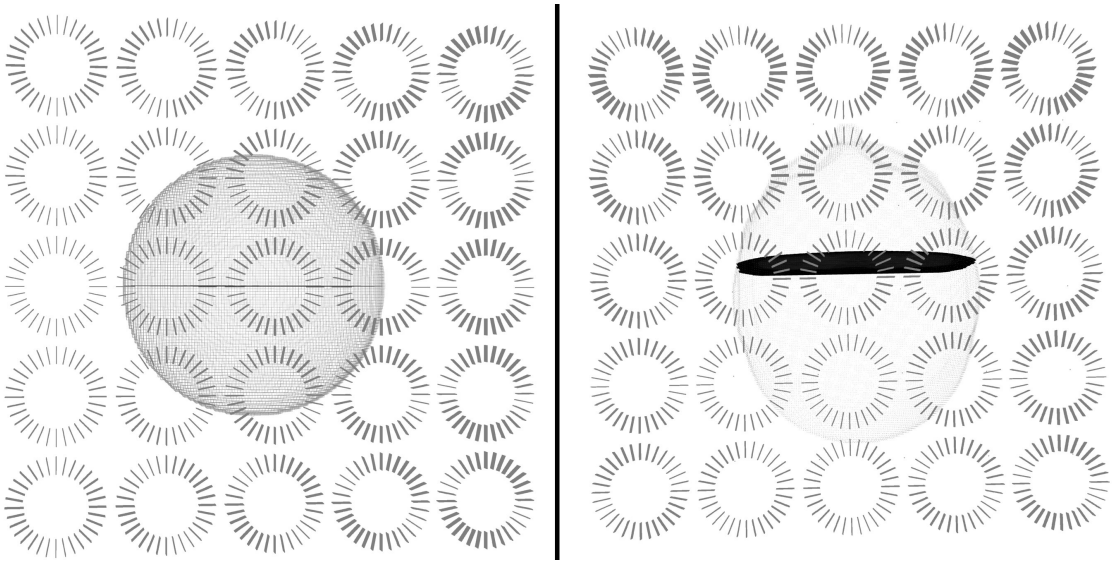

Figure 6.5.: Multi-array round-shaped coil configurations for TMS optimization. The left figure depicts the location and orientation of the 25 round-shaped coils for optimization in a spherical shell model. Right column displays the 25 round-shaped coils for optimization over a five-compartment FE head model. The black slices depict the coronal cutplanes for visualization of the optimized current densities.

$$\text{subject to} \qquad \omega|\mathbf{A}_{TMS}\boldsymbol{I}_{TMS}| \leq E_M$$

Furthermore, a mapping A^3_{TMS} incorporating the discretizations is introduced

$$A^3_{TMS} : L^2(\Omega)^3 \to \mathbb{R}^{3N}(\Omega), \quad \boldsymbol{E} \mapsto (\boldsymbol{E})_i$$

with N the number of elements and define the discretized operator $A^3_{TMS} \circ A_{TMS} = B_{TMS} \in \mathbb{R}^{3N\times C}$.

The discretized optimization problem $(\bar{\mathbf{P}}^{\alpha,\beta}_{TMS,E_M})$ for TMS optimization is introduced

$$\begin{aligned}(\bar{\mathbf{P}}^{\alpha,\beta}_{TMS,E_M}) \qquad & -\textstyle\int_\Omega \langle B_{TMS}\boldsymbol{I}_{TMS}, \boldsymbol{e}\rangle \,\mathrm{d}\boldsymbol{x} \quad +\alpha\int_{\tilde{C}} |\boldsymbol{I}_{TMS}|^2 \,\mathrm{d}\boldsymbol{x} + \beta\int_{\tilde{C}} |\boldsymbol{I}_{TMS}| \,\mathrm{d}\boldsymbol{x} \to \min_{\boldsymbol{I}_{TMS}} \\ & \text{subject to} \qquad \omega|B_{TMS}\boldsymbol{I}_{TMS}| \leq E_M\end{aligned}$$

For the sake of simplicity, the existence of at least one minimizer to the TMS optimization problem is not shown. The existence follows by similar reasoning as in Theorem 5.3. In order to find a minimizing element for the discretized optimization problem $(\bar{\mathbf{P}}^{\alpha,\beta}_{TMS,\epsilon})$, $\boldsymbol{y} = B_{TMS}\boldsymbol{I}_{TMS}$ and $\boldsymbol{z} = \boldsymbol{I}_{TMS}$ are substituted and the following augmented Lagrangian $L_{\mu_1,\mu_2}(\boldsymbol{I}_{TMS}, \boldsymbol{y}, \boldsymbol{z}, \boldsymbol{p}_1, \boldsymbol{p}_2)$ is obtained which has to be minimized

$$\begin{aligned}L_{\mu_1,\mu_2}(\boldsymbol{I}_{TMS}, \boldsymbol{y}, \boldsymbol{z}, \boldsymbol{p}_1, \boldsymbol{p}_2) \;=\; & \alpha\langle \boldsymbol{z}, \boldsymbol{z}\rangle + \beta \|\boldsymbol{z}\|_1 + \frac{\mu_1}{2}\langle \boldsymbol{z} - \boldsymbol{I}_{TMS}, \boldsymbol{z} - \boldsymbol{I}_{TMS}\rangle + \langle \boldsymbol{z} - \boldsymbol{I}_{TMS}, \boldsymbol{p}_1\rangle \\ & -\langle \boldsymbol{y}, \tilde{\boldsymbol{e}}\rangle + \frac{\mu_2}{2}\langle \boldsymbol{y} - B_{TMS}\boldsymbol{I}_{TMS}, \boldsymbol{y} - B_{TMS}\boldsymbol{I}_{TMS}\rangle \\ & +\langle \boldsymbol{y} - B_{TMS}\boldsymbol{I}_{TMS}, \boldsymbol{p}_2\rangle + v(\boldsymbol{y})\end{aligned}$$

Algorithm 4 Algorithm for the discretized minimization problem ($\bar{\mathbf{P}}^{\alpha,\beta}_{TMS,E_M}$)

Input: $B_{TMS}, \epsilon, \mu_1, \mu_2, \alpha, \beta, \omega, \tilde{\boldsymbol{e}}$, $\boldsymbol{I}^{prev}_{TMS}$, $\boldsymbol{I}^{0}_{TMS}$, $\boldsymbol{p}^0_1$, $\boldsymbol{p}^0_2$, $\boldsymbol{z}^0$, $\boldsymbol{y}^0$, N, TOL
$k = 0$
while $k < 3$ *or* $\left\|\boldsymbol{I}^k_{TMS} - \boldsymbol{I}^{prev}_{TMS}\right\| > TOL$ **do**
  $\boldsymbol{I}^{prev}_{TMS} = \boldsymbol{I}^k_{TMS}$
  $\boldsymbol{I}^{k+1}_{TMS} = (\mu_1 Id + \mu_2 B^{tr}_{TMS} B_{TMS})^{-1}(\mu_1 \boldsymbol{z}^k - Id\boldsymbol{p}^k_1 + \mu_2 B^{tr}_{TMS}\boldsymbol{y}^k - B^{tr}_{TMS}\boldsymbol{p}^k_2)$
  for $j = 1, \cdots, N$ **do**
    if $|(B_{TMS}\boldsymbol{I}^k_{TMS} + \frac{1}{\mu_2}\boldsymbol{p}^k_2 + \frac{1}{\mu_2}\tilde{\boldsymbol{e}})_j| > \frac{E_M}{\omega_j}$ **then**
      $\boldsymbol{y}^{k+1}_j = \frac{\epsilon}{\omega_j}\frac{(B_{TMS}\boldsymbol{I}^{k+1}_{TMS} + \frac{1}{\mu_2}\boldsymbol{p}^k_2 + \frac{1}{\mu_2}\tilde{\boldsymbol{e}})_j}{|(B_{TMS}\boldsymbol{I}^{k+1}_{TMS} + \frac{1}{\mu_2}\boldsymbol{p}^k_2 + \frac{1}{\mu_2}\tilde{\boldsymbol{e}})_j|}$
    else
      $\boldsymbol{y}^{k+1}_j = (B_{TMS}\boldsymbol{I}^{k+1}_{TMS} + \frac{1}{\mu_2}\boldsymbol{p}^k_2 + \frac{1}{\mu_2}\tilde{\boldsymbol{e}})_j$
    end if
  end for
  $\boldsymbol{z}^{k+1} = (\tilde{Id}^{tr}\tilde{Id} + \alpha)^{-1}\tilde{Id}^{tr}(\sqrt{\frac{\mu_1}{2}}\boldsymbol{I}^{k+1}_{TMS} + \frac{1}{\sqrt{2\mu_1}}\boldsymbol{p}^k_1 - \frac{1}{\sqrt{2\mu_1}}\beta)$
  $\boldsymbol{p}^{k+1}_1 = \mu_1(\boldsymbol{p}^k_1 + B_{TMS}\boldsymbol{I}^{k+1}_{TMS} - \boldsymbol{y}^{k+1})$
  $\boldsymbol{p}^{k+1}_2 = \mu_2(\boldsymbol{p}^k_2 + \boldsymbol{I}^{k+1}_{TMS} - \boldsymbol{z}^{k+1})$
  $k = k + 1$
end while
return $\boldsymbol{I}^{k+1}_{TMS}$, k, $\left\|\boldsymbol{I}^{k+1}_{TMS}\right\|_{\mathcal{M}(\Gamma)}$;

with μ_1, μ_2 and $\boldsymbol{p}_1, \boldsymbol{p}_2$ being the augmented Lagrangian parameters and the dual variables, respectively [15].

When substituting $B_{TMS} = B_{tCS}$ and $\boldsymbol{I}_{TMS} = \boldsymbol{I}_{tCS}$, the Lagrangian is identical to the Lagrangian for the discretized optimization problem ($\bar{\mathbf{P}}^{\alpha,\beta}_{tCS,\epsilon}$) for tCS and can thus be similarly minimized. The algorithm for solving the minimization problem for multi-array TMS is presented in Algorithm 4. Moreover, residual and objective convergence and primal and dual feasibility conditions can be proven in a similar way.

For TMS multi-array optimization, a planar coil set (also used in [111]) consisting of $C = 25$ small round-shaped coils in a square lattice is used and the coils are centered 1 cm above the outermost surface of the volume conductor models, see Figure 6.5. For optimization, a four compartment (skin, skull, CSF and brain) regular hexahedral spherical shell model with a mesh size of 2 mm is used. Moreover, according to the guideline for efficient yet accurate volume conductor modeling in TMS, a five-compartment (skin, skull, CSF, gray and white matter) geometry-adapted hexahedral FE head model is used for optimization. Similar to tCS, for all simulations, the target area Ω_t always consists of the elements corresponding to the target vectors and only the volume conductor elements in the brain are used for optimization, i.e., $\omega = 1$ only in the brain compartments and $\omega \ll 1$ in the target region and in the CSF, skin and skull compartments. Similar to Section 5, different threshold values can be used for the brain and scalp compartments, allowing to account for patient safety both at the scalp

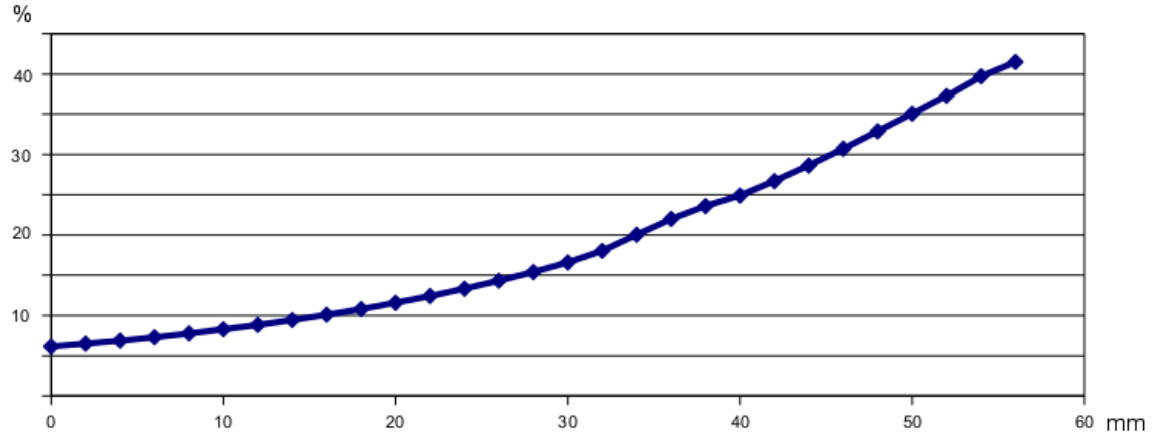

Figure 6.6.: Ratio (in percentage) between the averaged current density in non-target regions divided by current density in the target region. The stimulation depth (in mm) is depicted on the x-axis.

and brain levels.

6.2.1.1. Optimization in spherical shell models

Figure 6.7 depicts the optimized current flow fields and the corresponding stimulation protocols for four tangential target vectors at target vector depths of 2 mm (-A), 12 mm (-B), 22 mm (-C) and 32 mm (-D), respectively. As can be seen in the figure, for target depths of 2 mm and 12 mm, the optimized brain current flow fields show great focality, while for target depths of 22 mm and 32 mm, slightly less focal brain current flow fields can be seen. For all target vectors, strongest current density amplitudes in the brain compartment always occur at the CSF/brain boundary above the target region. This is due to the maximum principle for harmonic functions [42, Theorem 14.1].

The corresponding optimized stimulation protocols for multi-array transcranial magnetic stimulation are depicted in Figure 6.7 (right column). For all target vectors, hardly any driving currents can be seen at the coil directly above the target region. This is due to fact that the brain current density is zero underneath the center of a round-shaped coil (see also Section 6.1.3). Also, for all target vectors, a pattern of positive and negative driving currents at the neighboring coils can be seen, while weaker compensating currents are injected at the second neighboring coil elements. The deeper the target vector is located, the less compensating currents are injected at the second neighboring electrodes. Even some coil elements for a target vector depth of 32 mm change their polarity (from compensating to supporting currents), compare Figure 6.7-A2 and 6.7-D2. This is due to the fact that the current density must penetrate into the depth in order to maximize the current density in the target region.

In order to quantify the interaction of the focality of the optimized current flow fields and the target vector depth, a set of 30 target vectors is used for optimization. The superficial

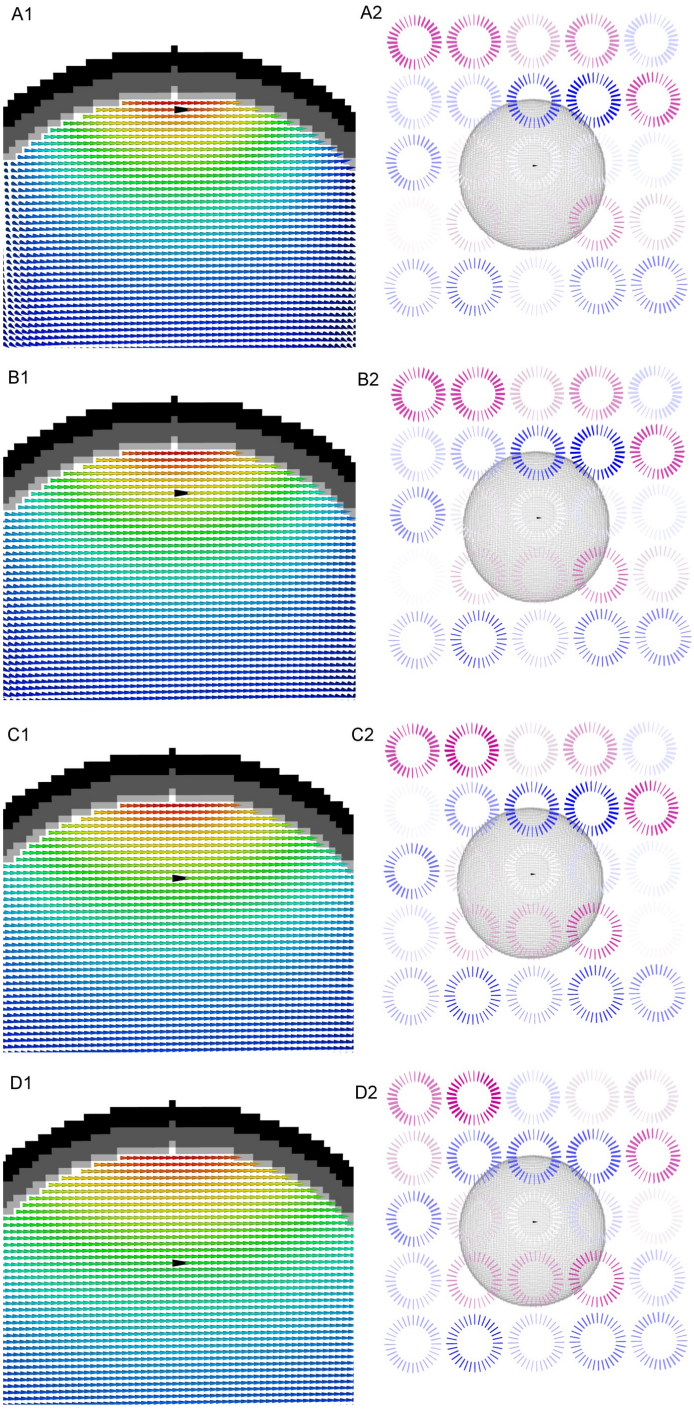

Figure 6.7.: Optimized current density distribution $\boldsymbol{J}$ in a sphere model using four tangential target vectors (black cones). The left column displays $\boldsymbol{J}$ on a saggital slice through the model and the corresponding stimulation protocols are shown on the right column. The depth of the target vector in Figures -A, -B, -C and -D is 2 mm, 12 mm, 22 mm and 32 mm, respectively.

tangential target vector at a target depth of 2 mm that was used in Figure 5.3 is selected and the target vector is consecutively moved into the depth of the model. As a regular hexahedral model with mesh size of 2 mm is used, the optimized current flow fields are thus investigated up to a target vector depth of 62 mm. Figure 6.6 depicts the interplay between current density

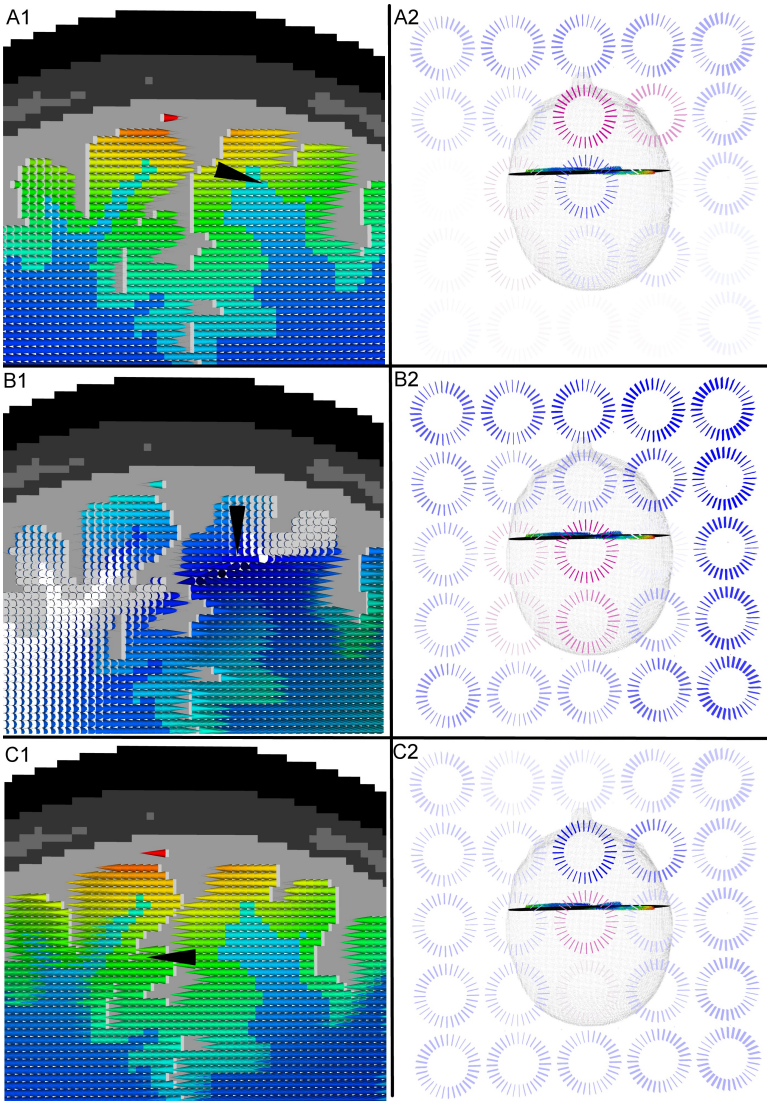

Figure 6.8.: Optimized current density distribution in a realistically shaped five compartment finite element head model using three target vectors (black cones). The optimized current density distribution in the brain compartment and the corresponding stimulation protocol are demonstrated in Figures -1 and -2, respectively.

focality and target vector depth. As can be seen, a correlation between current density focality and target vector depth can be seen, i.e., the focality of the current density decreases smoothly with increasing target vector depth.

6.2.1.2. Optimization results in realistically shaped FE head model

In this section, a realistically-shaped finite-element head model consisting of five compartments (skin, skull, CSF, gray matter and white matter) is generated following the guideline for efficient yet accurate volume conductor modeling in TMS, see Section 6.1.3.2. For optimization, three target vectors (a superficial tangential, a radial and a tangential target vector at a deeper location) are selected and the electric field is calculated using the SimBio software package.

Table 6.2.: Quantification of optimized current density in a highly-realistic four-compartment head model for different target vectors. The current density in the target region is scaled to be 100 % and the averaged current density in non-target regions is calculated for the discretized optimization problem for multi-array TMS.

Target (Figure 6.8)	**Target current density** [%]	**Non-target regions** [%]
A1	100	6.5
C1	100	10.6

Note that the coil-arrangement is sub-optimal and only used for a proof-of-concept study.

Figure 6.8 depicts the optimized electric fields and the corresponding stimulation protocols for a superficial mainly tangential target vector (-A), a radial target vector (-B) and a tangential target vector at a deeper location (-C). For the tangential target vectors (Figures 6.8-A1 and -C1), the optimized electric fields show high focality with the strongest intensities located in the target regions. While the orientation component of the deeper tangential target vector is very well approximated, the orientation component of the superficial target vector cannot be appropriately stimulated. This is due to the fact that the superficial tangential target vector has a relative high radial component, which can not be stimulated with transcranial magnetic stimulation. This can also be seen for the radial target vector in Figure 6.8-B1. The electric field in the target region is oriented orthogonally to the target vector, leading to highest current densities in non target brain regions. This is due to the fact that the L1R optimization approach tries to maximize the inner product between the target vector and the induced current density distribution. As TMS is only able to stimulate tangential components, the inner product between the target vector and the current flow field is zero for a completely radial target vector.
The corresponding stimulation protocols are depicted in Figure 6.8-2. For the superficial tangential target vectors (Figures 6.8-A2), the stimulation protocol is mainly comprised of one negative driving current at the coil above the target region and two positive driving currents at neighboring elements, respectively (Figures 6.8-A2). In order to minimize current density in non-target regions and to stimulate mainly parallel to the target vector, very weak compensating currents are injected at the second-neighboring coil elements. For the deeper target vectors, the stimulation protocol is mainly comprised of one positive driving current above the target region and two negative driving currents at the neighboring coil elements (Figures 6.8-C2). Again, compensating currents are injected at the neighboring coils, while they are very weak at the outermost coil layer. This is due to the fact that outermost coil elements only induce very weak current densities in the volume conductor model.

In order to quantify focality of the electric fields, Table 6.2 shows the electric field in the target region (scaled to 100 %) and the averaged electric field amplitudes in non-target regions for the superficial and deep tangential target vectors that were used in Figures 6.8-A1 and -C1. As can be seen, with focality values below 11%, the optimized electric fields are very focal, with the highest focality values for the superficial tangential target vector.

7 Combined tDCS and TMS optimization

The aim of this section is to shortly introduce the optimization pipeline for a combined tCS and TMS (tCMS) optimization and to provide optimization results in a spherical shell model.

7.1. Methods

In this section, the discretized optimization problems ($\bar{\mathbf{P}}^{\alpha,\beta}_{tCS,\epsilon}$) and ($\bar{\mathbf{P}}^{\alpha,\beta}_{TMS,E_M}$) for tCS and TMS are reconsidered. Furthermore, the discretized gain matrices B_{tCS} and B_{TMS} and the right-hand side vectors $\boldsymbol{I}_{tCS}$ and $\boldsymbol{I}_{TMS}$ are selected to be identical to those used in Sections 5 and 6.2.1.

For tCMS optimization, a combined gain matrix $\mathbf{B}_{tCMS} \in \mathbb{R}^{3N\times((S-1)+C)}$ is introduced such that

$$\mathbf{B}^i_{tCMS} = \begin{cases} \mathbf{B}^i_{tCS}, & \text{if } i = 1, \cdots, S-1 \\ \mathbf{B}^{i-(S-1)}_{TMS}, & \text{if } i = S, \cdots, (S-1)+C \end{cases} \tag{7.1}$$

and a combined right-hand side vector $\boldsymbol{I}_{tCMS} \in \mathbb{R}^{(S-1)+C}$ is used such that

$$\boldsymbol{I}^i_{tCMS} = \begin{cases} \boldsymbol{I}^i_{tCS}, & \text{if } i = 1, \cdots, S-1 \\ \boldsymbol{I}^{i-(S-1)}_{TMS}, & \text{if } i = S, \cdots, (S-1)+C \end{cases} \tag{7.2}$$

For optimization, a combined set of $S = 74$ scalp electrodes and $C = 25$ stimulating coil elements is used. The change of current in the TMS coils is scaled such that the norms of the gain matrices for TMS and tCS are identical. The optimization method calculates an optimal

applied pattern at the fixed electrodes and optimal driving currents at the coil elements such that the optimized current flow field is well-targeted and patient safety is ensured.

$$(\bar{\mathbf{P}}^{\alpha,\beta}_{\mathbf{tCMS},\epsilon}) \qquad -\langle B_{tCMS}\boldsymbol{I}_{tCMS}, \boldsymbol{e}\rangle \quad +\alpha\langle \boldsymbol{I}_{tCMS}, \boldsymbol{I}_{tCMS}\rangle + \beta \left\|\boldsymbol{I}_{tCMS}\right\|_1 \rightarrow \min_{\boldsymbol{I}_{tCMS}}$$
$$\text{subject to} \qquad \omega_i |(B_{tCMS}\boldsymbol{I}_{tCMS})_i| \leq \epsilon$$

When the optimization method is terminated, the scaled applied current pattern $\tilde{\boldsymbol{I}}_{tCS}$ is calculated as follows

$$\tilde{\boldsymbol{I}}_{tCS} = \frac{4\boldsymbol{I}_{tCS}}{\left\|\boldsymbol{I}_{tCS}\right\|_{\mathcal{M}(\Gamma)}}$$

and the scaled optimal driving currents $\tilde{\boldsymbol{I}}_{TMS}$ at the fixed coil elements is given as

$$\tilde{\boldsymbol{I}}_{TMS} = \frac{4\boldsymbol{I}_{TMS}}{\left\|\boldsymbol{I}_{tCS}\right\|_{\mathcal{M}(\Gamma)}}$$

In order to keep the tCS and TMS optimized current flow fields amplitudes at the same level, the scaling factor $\left\|\boldsymbol{I}_{tCS}\right\|_{\mathcal{M}(\Gamma)}$ is also used to scale the optimized driving currents $\tilde{\boldsymbol{I}}_{TMS}$. Using the scaled input values, the optimized current density distribution in the volume conductor model can be calculated as

$$\boldsymbol{J}_{tCMS} = B_{tCS}\tilde{\boldsymbol{I}}_{tCS} + B_{TMS}\tilde{\boldsymbol{I}}_{TMS} \tag{7.3}$$

7.2. Results and Discussion

In a first study, four mainly tangentially oriented (to the skull surface) target vectors are used and the discretized minimization problem for tCMS optimization is applied to calculate optimized stimulation protocols and driving currents for the presumed target vectors. After optimization, the optimized stimulation protocols are scaled such that the total current applied to all tCS electrodes is limited by 2 mA. In order to allow safe and well-targeted stimulation, the scaling vector $\left\|\boldsymbol{I}_{tCS}\right\|_{\mathcal{M}(\Gamma)}$ is then also used to calculate the scaled optimal driving currents $\tilde{\boldsymbol{I}}_{TMS}$. Finally, the scaled stimulation protocol and the scaled driving currents are used to calculate the induced current density distribution in the whole volume conductor model. Figure 7.1 depicts the optimized current flow fields for a combined tCS and TMS optimization using four mainly tangentially oriented (to the skull surface) target vectors with a target vector depth of 2 mm (Fig. 7.1-A), 12 mm (Fig. 7.1-B), 22 mm (Fig. 7.1-C) and 32 mm (Fig. 7.1-D) (see also Sections 5 and 6.2.1). As can be seen in the figure, for target vector depths of 2 mm and 12 mm, the optimized current flow fields show great focality, while for target vector depths of 22 mm and 32 mm, a slightly more widespread current flow field can be seen. In all models, strongest current density amplitudes in the brain compartment always occur at the CSF/brain boundary above the target region.

In a last study, the focality of the optimized current flow fields versus target vector depth is

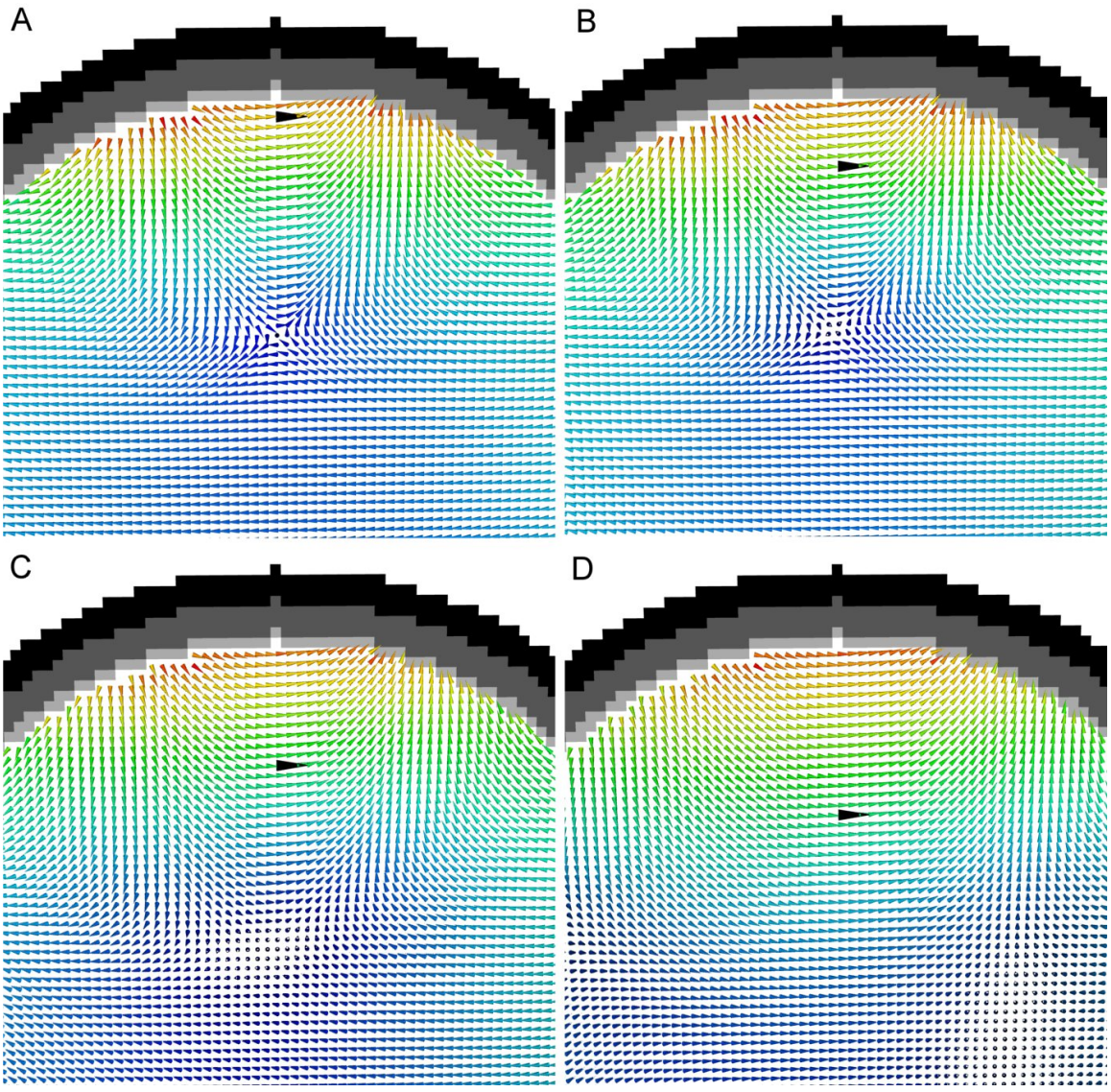

Figure 7.1.: Optimized current flow fields for a tCMS optimization. Figures -A, -B, -C and -D depict the optimized stimulation protocols for tangentially oriented target vectors with a target depth of 2 mm, 12 mm, 22 mm and 32 mm, respectively.

investigated for the tCMS optimization. Similar to Sections 5 and 6.2.1, a set of 30 tangentially oriented target vectors is used for this investigation. Figure 7.2 depicts the focality of the optimized current density vector fields versus target vector depth for tCS optimization, TMS optimization and tCMS optimization. As can be seen in the figure, for all target vector depths, tCMS optimization outperforms single tCS and TMS optimization with regard to focality of the optimized current flow fields. While the tCMS optimization is mainly driven by the tCS for target vector depth below 12 mm, the combined optimization is mainly driven by the TMS for deeper located target vectors. This indicates that a tCMS optimization might be used to achieve optimized current flow fields which exhibit greater focality as compared to single tCS or TMS optimizations. A second important result is that, for all target vectors below 10 mm, the focality of the TMS optimized current flow field is higher as compared to

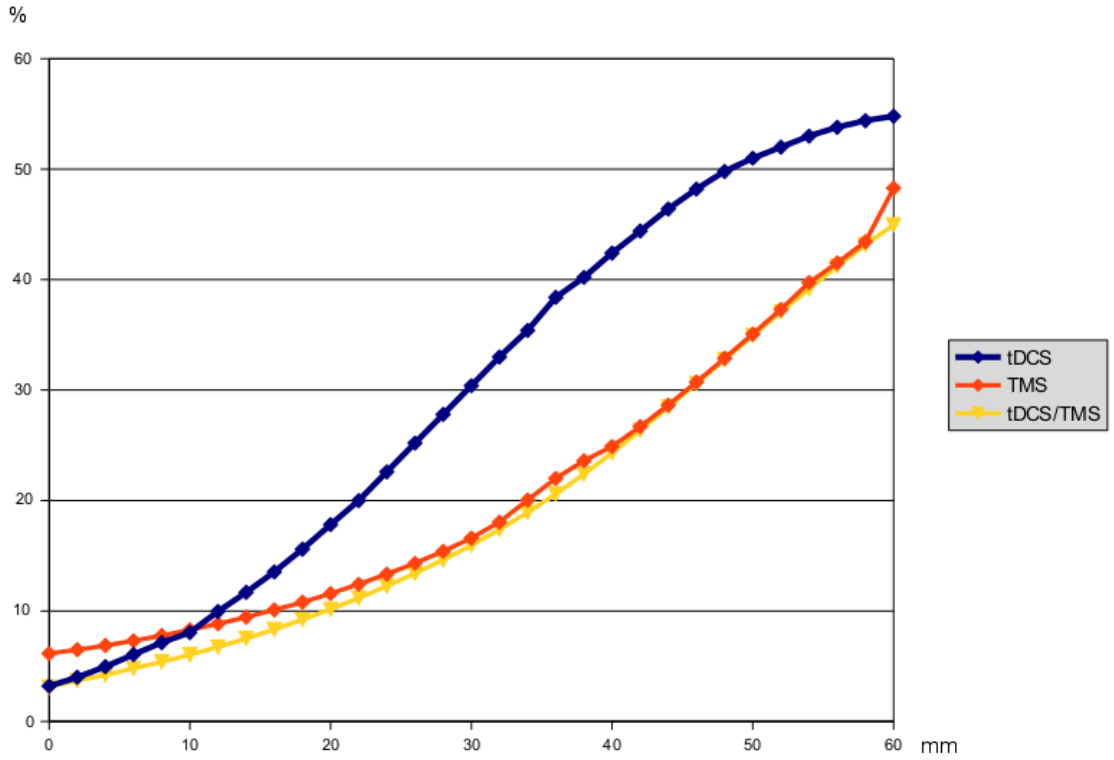

Figure 7.2.: Ratio (in percentage) between the averaged current density in non-target regions divided by the current density in the target region for tCS optimization (blue), TMS optimization (orange) and tCMS optimization (yellow). The stimulation depth (in mm) is depicted on the x-axis.

the focality of the tCS optimization, while for superficial target vectors, the focality is driven by the tCS current flow fields. The results of the last study, however, might only hold true under the assumption that the norms of the tCS and TMS influence matrices are identical. In real experiments, the TMS-induced current flow field is at least one order of magnitude higher as compared to the tCS induced current flow field.

8 Summary

The scope of this thesis was to provide and analyze a simulation pipeline for transcranial current stimulation, transcranial magnetic stimulation or a combined transcranial current and magnetic stimulation which can be used to predict inter-individually optimized stimulation protocols for patients and their specific disease. This issue was divided into four main parts

- Fast and robust generation of detailed and accurate volume conductor models for individual patients
- Implementation of accurate and fast numerical finite element approach for high-resolution volume conductor models with white matter anisotropy
- Implementation and validation of an efficient and accurate solver method
- Predicting inter-individually optimized stimulation protocols in a presumed target region while minimizing current density in non-target regions

In the following the main findings of this thesis are presented and the contributions to a simulation pipeline are discussed:

Relationship between EEG/MEG source analysis and tCS/TMS simulations

By providing analytical forward expressions for the adjoint approach (Vallaghe and colleagues [135]) and the partial integration approach (Yan and colleagues [154]), EEG forward computations and tCS simulations were linked in a clear mathematical way. It was thus shown that the electric field computed in tCS simulation studies is identical to the electrode lead vector field that serves as a sensitivity map for the considered pair of electrodes in EEG source analysis. Moreover, MEG forward computations were also shown to be related to TMS simulations. Therefore, the main findings of this thesis with regard to brain stimulation techniques are also valid for EEG/MEG source analysis too, and vice versa.

Volume conduction effects in tCS and TMS

In this thesis, important volume conduction effects for tCS and TMS were shown: Channeling effects of the skin, where the current flow was mainly oriented tangentially to the head surface from the anode to the cathode and of the CSF compartment which caused the vector field in the CSF compartment to have a higher magnitude and to be more orthogonally oriented to the cortical surface. These channeling effects resulted in orientation and magnitude changes of more than 63 degrees and 4.3 and 125 degrees and 5.1 for tCS and TMS, respectively. The TMS current flow fields were hardly affected by the presence of a more-conductive spongiosa compartment, while in tCS, channeling effects of the spongiosa compartment were found. Current vectors in lower-conductive regions tended to be oriented towards higher conductive regions close-by. Important further findings are that anisotropic white matter conductivity caused tCS current flow in directions parallel to the white matter fiber tracts and that highest cortical current magnitudes were not only found close to the stimulation sites, but for example also in deep brain areas where a lower conducting thin cortical crown is surrounded by highly conductive CSF.

Guidelines for head volume conductor modeling

A guideline for efficient yet accurate volume conductor modeling in tCS was formulated: All important tissue compartments between the electrodes and the target brain area should be modeled as accurately as possible. Isotropic representations of the compartments skin, skull, CSF and gray and white matter are essential for any simulation study. If a significant portion of spongiosa is in between the electrodes and the target brain area, the skull should be distinguished into its compact and spongy bone. For deeper target regions, white matter anisotropy is important, while it seems to be less important for superficial target regions.

Moreover a guideline for efficient yet accurately volume conductor modeling in TMS was developed: All important tissues between the stimulating coil and the target brain area should be modeled as accurately as possible. Skull compacta and spongiosa modeling and white matter anisotropy modeling have only small effects on the electric field in the target brain area. In conclusion, isotropic representation of the compartments skin, skull, CSF, gray and white matter are sufficient for realistic potential field estimation in TMS.

For a combined tCS and TMS simulation or optimization, it is recommendable to use the guideline for accurate yet efficient volume conductor modeling in tCS.

Accurate and fast numerical methods

Having linked EEG forward calculations and tCS simulations, quasi-analytical EEG forward expressions in sphere models were used to investigate numerical accuracies of commonly-used hexahedral and tetrahedral approaches for tCS. As was shown, regular and geometry-adapted hexahedral and tetrahedral FE approaches led to accurate simulation results. It was shown that while the accuracy of the most easy to realize approach based on regular hexahedral elements is already quite high, it can be substantially be improved if a geometry-adaptation

of the elements is employed in conjunction with an isoparametric FEM approach. While the latter approach does not involve any additional difficulties for the user, it reaches the high accuracies of surface-segmentation based tetrahedral FEM, which is considerably more difficult to implement and topologically less flexible in practice.

In this study, current flow orientation and magnitude changes between the CEM-based and PEM-based current flow fields were investigated. The results clearly indicated that with regard to the tCS forward computation, the PEM-based modeling pipeline is a sufficiently accurate model. However, for a simultaneous tCS stimulation and EEG measurement, the CEM-based forward problem outperformed the simple PEM-based modeling approach and should thus be used. As the hexahedral simulation pipeline for TMS led to realistic simulation results and no shunting currents between skin and coil elements have to be considered in TMS, it is recommendable to use highly-realistic geometry-adapted approach in hexahedral FE head models and to apply the PEM-based modeling procedure to calculate the current flow fields induced by tCS and/or TMS.

Accurate and fast solver methods

In order to find an optimal solver method for tCS and TMS, numerical accuracy and efficacy for the Jacobi, IC(0) and AMG preconditioner methods for the conjugate gradient method were investigated. The numerical errors RDM and MAG were calculated and an solver accuracy level of 10^{-7} was shown to be sufficient to attain an accurate numerical accuracy for the three PCG methods. However, the investigation of the solver clock time revealed that the AMG-CG solver substantially outperforms the Jacobi-CG and IC(0)-CG solvers with regard to computational efficacy and time requirements. Therefore, the use of an AMG-CG solver method with a solver accuracy level of 10^{-7} is highly recommended.

Current density optimization in tCS, TMS and combined tCS and TMS

A novel optimization approach for safe and well-targeted multi-channel transcranial current stimulation, multi-array transcranial magnetic stimulation and combined tCS and TMS stimulation has been proposed. Existence of at least one minimizer and residual and objective convergence results have been proven for the optimization methods. For discretization of the respective optimization problems the finite element method was employed and the existence of at least one minimizer to the discretized optimization problems has been shown.

With regard to tCS, the numerical results clearly revealed that the optimized current flow fields show substantially higher focality and directional agreement to the target vector in comparison to standard bipolar electrode montages. The L2R optimization procedure always led to relatively weak current densities in the brain compartment. On the other hand, the L1R optimized current density distribution along the target direction was always stronger as compared to the L2R optimized current flow field and might thus be able to induce more significant stimulation efects. Moreover, the newly invented optimization procedures guarantee patient safety and the induced current flow field was always oriented mainly parallel and inwards to the target vector. The stimulation might thus enhance cortical excitability in

the target region, while the current density is not able to enhance cortical excitability in non-target regions.

The L1R optimization method was then used to calculate optimized stimulation protocols for bi-hemispheric auditory cortex stimulation. The optimized current flow fields showed substantially greater focality and directional agreement to the auditory cortex target vectors in comparison to the standard bipolar electrode montage for auditory cortex stimulation. Furthermore, an uncertainty quantification of the optimal electrode configurations was performed for right-hemispheric auditory cortex stimulation. While the stimulation amplitudes of the main anode was influenced by a similar intensity by the uncertain conductivity of the skull as well as the white matter, the stimulation amplitudes at the two main cathodes were mainly influenced by the uncertain skull conductivity. This demonstrated that the probability density function of the stimulation protocols at the main anode and cathodes are most sensitive to the uncertainty in the skull conductivity.

With regard to TMS, the L1R discretized optimization method for multi-array TMS was applied to calculate a set of optimized driving currents in a spherical shell model. Along this line, it was shown that the novel optimization pipeline for multi-array TMS is working properly. Also, optimized driving currents were calculated in a geometry-adapted hexahedral FE head model. The optimized current flow fields showed great focality with the strongest intensities located in the target regions. Current density in non-target regions was substantially smaller as compared to the current density in the target. However, as was shown in this thesis, TMS is only able to stimulate tangential target vectors. The interplay between current density focality and target vector revealed a correlation between focality and target vector depth, i.e., current density focality decreases with increasing target vector depth.

In a last study, the optimized current flow fields were visually inspected in sphere models for a combined tCS and TMS optimization. The focality of the optimized current flow fields of combined tCS and TMS optimization was also compared with single tCS and TMS optimization for 30 tangentially oriented target vectors. While the tCMS optimization was mainly driven by the tCS for target vector depths below 12 mm, the combined optimization was mainly driven by the TMS for deeper located target vectors. This demonstrates that tCMS optimization might be used to achieve optimized current flow fields which exhibit greater focality as compared to single tCS or TMS optimization.

9 Conclusions

A novel simulation pipeline for predicting inter-individually optimized stimulation protocols for tCS, TMS and tCMS was presented, analyzed and validated.
Along this line, a pipeline for efficient yet accurate volume conductor modeling in tCS, TMS and tCMS has been proposed which allows to generate highly-realistic individually shaped head models in less than one day of working time. In a next step, the accuracy and efficacy of numerical approaches for brain stimulation techniques was investigated. The commonly-used tetrahedral and hexahedral numerical FE approaches for calculating the current flow fields were shown to be highly accurate. However, the geometry-adapted hexahedral FE approach for tCS was shown to be even more accurate as compared to a regular approach. Moreover, an AMG-CG solver method with solver accuracy level of 10^{-7} led to very accurate simulation results and was very efficient with regard to time requirements. While the numerical errors are thus clearly under control the influence of inter-individually varying conductivity profiles on optimal electrode configurations were investigated for an auditory cortex stimulation. It turned out that the probability density function of the stimulation protocols at the main electrodes were most sensitive to the uncertainty in the skull conductivity. For this reason, a skull calibration method using simultaneously measured somatosensory evoked potentials and fields [5] might be used to individually estimate the skull conductivity value of the individual subject.
With quantification of the optimized current flow fields in sphere models and realistically shaped FE head models and providing an in-depth mathematical analysis of the optimization methods, a proof of concept that the optimization method for tCS, TMS and tCMS is working properly was presented. The optimized current flow fields were visually inspected and the simulations clearly revealed that the optimized current flow fields show substantially higher focality and directional agreement with the target vectors in comparison to standard current density vector fields.

In conclusion, a proof of concept that the simulation pipeline for tCS, TMS and tCMS is working properly was presented and that a calculation of individually optimized stimulation is not only feasible for single patients but also for a larger number of patients in clinical trial studies.

10 Future perspectives

While the numerical errors of commonly-used numerical approaches for tCS and the influence of inter-individually varying conductivity profiles on optimal electrode configurations were investigated, a direct validation of computer simulations is still an open topic. For validation of the computer simulations, one could imagine two kinds of scalp measurements, direct electric field measurements that are induced by the tCS setup or indirect EEG measurements after the tCS stimulations or even acquired simultaneously to tCS stimulation. An example for such an indirect measurement was recently presented in Neuling and colleagues [82], showing the high value of the interplay between tCS computer simulation and tCS-EEG experiments. Because of the particular interest to validate modeling results and to estimate inter-individual volume conduction differences due to, e.g., inter-individual conductivity variations in especially the skull tissues (see also Section 5.4), in a future study direct as well as indirect validation studies will be performed for tCS computer simulations in animals (ferrets) and humans. The direct validation will thus be carried out using combined surface-tCS stimulation and electric field measurements through depth electrodes in ferret brains. Such combined data will allow us to directly validate simulation studies and to adjust inter-individually differing tissue conductivity parameters in a way that the simulated current flow in the ferret brains fit accordingly to the measured ones.

As the L1R optimization method for tCS/TMS and combined tCS/TMS is able to calculate stimulation protocols which fulfill a certain target direction, the effects of anodal, cathodal and perpendicular electric fields to the neuron will be investigated. Along this line, one could try to replicate the study of Bindman and colleagues [11].

As was shown in Section 5.4, the optimized stimulation protocols were most sensitive to the low-conductive skull compartment. When simultaneously measured somatosensory evoked potentials and fields are available, a skull calibration method can be used to individually

estimate the skull conductivity of the subject [5]. In a further study, the probability density functions of the main electrodes and the probability density norm are investigated in a head model with calibrated skull conductivity. In this case, the skull conductivity can be used as a deterministic model parameter, which might substantially reduce the uncertainty of the optimized stimulation protocols.

With regard to TMS electric field estimation, a constant rate of change of the coil current of $p(t) = 1\,\mathrm{A}\mu\mathrm{s}^{-1}$ was used as input values for the time-dependent magnetic vector potential $\boldsymbol{A}(\boldsymbol{x}, t)$. In a further study, realistic stimulating pulses will be used as input values for simulation. Moreover, the simulation pipeline was only implemented for tetrahedral and regular hexahedral meshes. Therefore, a simulation pipeline for geometry-adapted hexahedral FE approaches will be implemented for TMS.

In a combined tACS stimulation and EEG measurement experiment, a temporal phase shift in the stimulation artefact could be measured in the EEG electrodes. This artefact substantially increases in size when the distance to the stimulating electrodes increased (private communications with CS Herrmann, Oldenburg) and cannot be simulated when the quasistatic approximation to Maxwell's equations is used. It is therefore unclear whether the *propagation*, *capacitive* and *inductive* effects in Maxwell's equations can be neglected. A complex conductivity tensor $\sigma(1 + j\omega\epsilon_c)$ will be assumed and the differences in current flow field between a complex conductivity tensor and the quasistatic tensor σ will be investigated. In combined tACS and EEG simulations it will further be investigated whether a phase shift in the artefact can be simulated.

Higher order basis functions for the standard Lagrange FEM will be implemented and for a discontinuous Galerkin (DG) FEM approaches for tCS, TMS or tCMS simulations. With regard to EEG source analysis, a novel DG-FEM framework showed promising numerical accuracies for even highest source eccentricities (0.39 mm to the next discontinuity in conductivity [75]).

A Appendix

A.1. Convergence analysis

In this section, residual and objective convergence and primal and dual feasibility are shown for the simplified minimization problem ($\mathbf{P}_{tCS,\epsilon}$) by following the work of Boyd and colleagues [15] where further important details can be found.
An admissible set $\mathcal{D}^{ad}(\Gamma) := \{\tilde{\boldsymbol{J}} \in \mathcal{D}(\Gamma) \mid \omega|A\tilde{\boldsymbol{J}}| \leq \epsilon\} \subset \mathcal{D}(\Gamma)$ is introduced which ensures that the state constraint is always fulfilled for

$$-\int_{\Omega} \langle A\boldsymbol{J}, \tilde{\boldsymbol{e}} \rangle \, \mathrm{d}\boldsymbol{x} \quad \rightarrow \min_{\boldsymbol{J} \in \mathcal{D}^{ad}(\Gamma)}$$

This minimization problem is similar to the simplified optimization problem ($\mathbf{P}_{tCS,\epsilon}$). When splitting $\boldsymbol{z} = A\boldsymbol{J}$, the augmented Lagrangian reads

$$L_{\mu}(\boldsymbol{J}, \boldsymbol{z}, \boldsymbol{y}) = -\int_{\Omega} \langle \boldsymbol{z}, \tilde{\mathrm{e}} \rangle \, \mathrm{d}\boldsymbol{x} + \int_{\Omega} (A\boldsymbol{J} - \boldsymbol{z})\boldsymbol{y} \, \mathrm{d}\boldsymbol{x} + \frac{\mu}{2} \|A\boldsymbol{J} - \boldsymbol{z}\|_2^2$$

with μ and $\boldsymbol{p}$ being the augmented Lagrangian parameter and the dual variable, respectively [15]. We assume that the unaugmented Lagrangian L_0 has a saddle point and that the function

$$g(\boldsymbol{z}) = -\int_{\Omega} \langle \boldsymbol{z}, \tilde{\boldsymbol{e}} \rangle \, \mathrm{d}\boldsymbol{x}$$

is closed, proper and convex. Furthermore, one defines

$$\boldsymbol{q}^* = inf\{-\int_{\Omega} \langle \boldsymbol{z}, \tilde{\boldsymbol{e}} \rangle \, \mathrm{d}\boldsymbol{x} \mid A\boldsymbol{J} - \boldsymbol{z} = 0\}$$

and

$$\boldsymbol{q}^{k+1} = -\int_{\Omega^*} \langle \boldsymbol{z}^{k+1}, \tilde{\boldsymbol{e}} \rangle \, \mathrm{d}\boldsymbol{x}$$

In order to show residual convergence ($r^{k+1} = A\boldsymbol{J}^{k+1} - \boldsymbol{z}^{k+1} \to 0$ for $k \to \infty$) and objective convergence ($g(\boldsymbol{z}^{k+1}) = q^{k+1} \to q^*$ for $k \to \infty$) three inequalities are shown

- E1: $q^* - q^{k+1} \leq (\boldsymbol{y}^*)^{tr} \boldsymbol{r}^{k+1}$
- E2: $q^{k+1} - q^* \leq -(\boldsymbol{y}^{k+1})^{tr} \boldsymbol{r}^{k+1} + \mu(\boldsymbol{z}^{k+1} - \boldsymbol{z}^k)^{tr}(-\boldsymbol{r}^{k+1} - (\boldsymbol{z}^{k+1} - \boldsymbol{z}^*))$
- E3: $V^{k+1} \leq V^k - \mu \left\| \boldsymbol{r}^{k+1} \right\|_2^2 - \mu \left\| \boldsymbol{z}^{k+1} - \boldsymbol{z}^k \right\|_2^2$

with $V^k := \frac{1}{\mu} \left\| \boldsymbol{y}^k - \boldsymbol{y}^* \right\|_2^2 + \mu \left\| \boldsymbol{z}^k - \boldsymbol{z}^* \right\|_2^2$.

Inequality E1

As $(\boldsymbol{J}^*, \boldsymbol{z}^*, \boldsymbol{y}^*)$ is a saddle point for L_0 one obtains

$$L_0(\boldsymbol{J}^*, \boldsymbol{z}^*, \boldsymbol{y}^*) \leq L_0(\boldsymbol{J}^{k+1}, \boldsymbol{z}^{k+1}, \boldsymbol{y}^*) = q^{k+1} + (\boldsymbol{y}^*)^{tr} \boldsymbol{r}^{k+1}$$

and from $L_0(\boldsymbol{J}^*, \boldsymbol{z}^*, \boldsymbol{y}^*) = -\int_{\Omega^*} \langle \boldsymbol{z}^*, \tilde{\boldsymbol{e}} \rangle \, \mathrm{d}\boldsymbol{x} = q^*$ it follows that

$$q^* \leq q^{k+1} + (\boldsymbol{y}^*)^{tr} \boldsymbol{r}^{k+1}$$

Inequality E2

As $\boldsymbol{J}^{k+1}$ minimizes $L_\mu(\boldsymbol{J}, \boldsymbol{z}^k, \boldsymbol{y}^k)$ with respect to $\boldsymbol{I}$, it follows

$$\begin{aligned} 0 = \frac{\partial L_\mu}{\partial \boldsymbol{I}}(\boldsymbol{J}^{k+1}, \boldsymbol{z}^k, \boldsymbol{y}^k) &= A^{tr}\boldsymbol{y}^k + \mu A^{tr}(A\boldsymbol{J}^{k+1} - \boldsymbol{z}^k) \\ &= A^{tr}\boldsymbol{y}^{k+1} - \mu A^{tr}(A\boldsymbol{J}^{k+1} - \boldsymbol{z}^{k+1}) \\ &+ \mu A^{tr} A\boldsymbol{J}^{k+1} - \mu A^{tr}\boldsymbol{z}^k \\ &= A^{tr}(\boldsymbol{y}^{k+1} + \mu(\boldsymbol{z}^{k+1} - \boldsymbol{z}^k)) \end{aligned}$$

which implies that $\boldsymbol{J}^{k+1}$ minimizes $(\boldsymbol{y}^{k+1} + \mu(\boldsymbol{z}^{k+1} - \boldsymbol{z}^k))A\boldsymbol{J}$.
Moreover, $\boldsymbol{z}^{k+1}$ minimizes $L_\mu(\boldsymbol{J}^{k+1}, \boldsymbol{z}, \boldsymbol{y}^k)$

$$\begin{aligned} 0 = \partial L_\mu(\boldsymbol{J}^{k+1}, \boldsymbol{z}^{k+1}, \boldsymbol{y}^k) &= -\int_{\Omega^*} \langle \mathbf{1}, \tilde{\boldsymbol{e}} \rangle - (\boldsymbol{y}^k)^{tr} - \mu(A\boldsymbol{J}^{k+1} - \boldsymbol{z}^{k+1}) \, \mathrm{d}\boldsymbol{x} \\ &= -\int_{\Omega^*} \langle \mathbf{1}, \tilde{\boldsymbol{e}} \rangle - (\boldsymbol{y}^{k+1})^{tr} \, \mathrm{d}\boldsymbol{x} \end{aligned}$$

which implies that $\boldsymbol{z}^{k+1}$ minimizes $-\int_{\Omega^*} \langle \boldsymbol{z}, \tilde{\boldsymbol{e}} \rangle - (\boldsymbol{y}^{k+1})^{tr} \boldsymbol{z} \, \mathrm{d}\boldsymbol{x}$.
Therefore

$$\begin{aligned} &(\boldsymbol{y}^{k+1} + \mu(\boldsymbol{z}^{k+1} - \boldsymbol{z}^k))^{tr} A\boldsymbol{J}^{k+1} \leq (\boldsymbol{y}^{k+1} + \mu(\boldsymbol{z}^{k+1} - \boldsymbol{z}^k))^{tr} A\boldsymbol{J}^* \\ &-\int_{\Omega^*} \langle \boldsymbol{z}^{k+1}, \tilde{\boldsymbol{e}} \rangle - (\boldsymbol{y}^{k+1})^{tr} \boldsymbol{z}^{k+1} \, \mathrm{d}\boldsymbol{x} \leq -\int_{\Omega^*} \langle \boldsymbol{z}^*, \tilde{\boldsymbol{e}} \rangle - (\boldsymbol{y}^{k+1})^{tr} \boldsymbol{z}^* \, \mathrm{d}\boldsymbol{x} \end{aligned}$$

Adding the inequalities and using $(\boldsymbol{y}^{k+1})^{tr}(A\boldsymbol{J}^* - \boldsymbol{z}^*) = 0$ leads to

$$\begin{aligned}
q^{k+1} - q^* \leq \; & - \; (\boldsymbol{y}^{k+1} + \mu(\boldsymbol{z}^{k+1} - \boldsymbol{z}^k))^{tr} A\boldsymbol{J}^{k+1} \\
& + \; (\boldsymbol{y}^{k+1} + \mu(\boldsymbol{z}^{k+1} - \boldsymbol{z}^k))^{tr} A\boldsymbol{J}^* \\
& + \; (\boldsymbol{y}^{k+1})^{tr}\boldsymbol{z}^{k+1} - (\boldsymbol{y}^{k+1})^{tr}\boldsymbol{z}^* \\
& = \; -(\boldsymbol{y}^{k+1})^{tr} A\boldsymbol{J}^{k+1} \\
& - \; \mu(\boldsymbol{z}^{k+1} - \boldsymbol{z}^k)^{tr} A\boldsymbol{J}^{k+1} + (\boldsymbol{y}^{k+1})^{tr} A\boldsymbol{J}^* \\
& + \; \mu(\boldsymbol{z}^{k+1} - \boldsymbol{z}^k)^{tr} A\boldsymbol{J}^* + (\boldsymbol{y}^{k+1})^{tr}\boldsymbol{z}^{k+1} - (\boldsymbol{y}^{k+1})^{tr}\boldsymbol{z}^* \\
& = \; -(\boldsymbol{y}^{k+1})^{tr}\boldsymbol{r}^{k+1} - \mu(\boldsymbol{z}^{k+1} - \boldsymbol{z}^k)^{tr}(A\boldsymbol{J}^{k+1} - A\boldsymbol{J}^*) \\
& = \; -(\boldsymbol{y}^{k+1})^{tr}\boldsymbol{r}^{k+1} + \mu(\boldsymbol{z}^{k+1} - \boldsymbol{z}^k)^{tr}(-\boldsymbol{r}^{k+1} - (\boldsymbol{z}^{k+1} - \boldsymbol{z}^*))
\end{aligned}$$

Inequality E3

Using Inequalities (E1) and (E2) and multiplying by 2 leads to

$$\begin{aligned}
0 \; & \geq \; -(\boldsymbol{y}^*)^{tr}\boldsymbol{r}^{k+1} + (\boldsymbol{y}^{k+1})^{tr}\boldsymbol{r}^{k+1} - \mu(\boldsymbol{z}^{k+1} - \boldsymbol{z}^k)^{tr}(-\boldsymbol{r}^{k+1} - (\boldsymbol{z}^{k+1} - \boldsymbol{z}^*)) \\
& = \; 2(\boldsymbol{y}^{k+1} - \boldsymbol{y}^*)^{tr}\boldsymbol{r}^{k+1} + 2\mu(\boldsymbol{z}^{k+1} - \boldsymbol{z}^k)^{tr}\boldsymbol{r}^{k+1} + 2\mu(\boldsymbol{z}^{k+1} - \boldsymbol{z}^k)^{tr}(\boldsymbol{z}^{k+1} - \boldsymbol{z}^*)
\end{aligned}$$

Using $\boldsymbol{y}^{k+1} = \boldsymbol{y}^k + \mu\boldsymbol{r}^{k+1}$, the first term can be rewritten

$$\begin{aligned}
2(\boldsymbol{y}^{k+1} - \boldsymbol{y}^*)^{tr}\boldsymbol{r}^{k+1} & = 2(\boldsymbol{y}^k + \mu\boldsymbol{r}^{k+1} - \boldsymbol{y}^*)^{tr}\boldsymbol{r}^{k+1} \\
& = 2(\boldsymbol{y}^k - \boldsymbol{y}^*)^{tr}\boldsymbol{r}^{k+1} + \mu\left\|\boldsymbol{r}^{k+1}\right\|_2^2 + \mu\left\|\boldsymbol{r}^{k+1}\right\|_2^2 \\
& = \frac{2}{\mu}(\boldsymbol{y}^k - \boldsymbol{y}^*)^{tr}(\boldsymbol{y}^{k+1} - \boldsymbol{y}^k) + \frac{1}{\mu}\left\|\boldsymbol{y}^{k+1} - \boldsymbol{y}^k\right\|_2^2 + \mu\left\|\boldsymbol{r}^{k+1}\right\|_2^2 \\
& = \frac{1}{\mu}(\left\|\boldsymbol{y}^{k+1} - \boldsymbol{y}^*\right\|_2^2 - \left\|\boldsymbol{y}^k - \boldsymbol{y}^*\right\|_2^2) + \mu\left\|\boldsymbol{r}^{k+1}\right\|_2^2
\end{aligned}$$

where $\boldsymbol{y}^{k+1} - \boldsymbol{y}^k = (\boldsymbol{y}^{k+1} - \boldsymbol{y}^*) - (\boldsymbol{y}^k - \boldsymbol{y}^*)$ was used.
Next, the remaining terms

$$\begin{aligned}
& \mu\left\|\boldsymbol{r}^{k+1}\right\|_2^2 + 2\mu(\boldsymbol{z}^{k+1} - \boldsymbol{z}^k)^{tr}\boldsymbol{r}^{k+1} + 2\mu(\boldsymbol{z}^{k+1} - \boldsymbol{z}^k)^{tr}(\boldsymbol{z}^{k+1} - \boldsymbol{z}^*) \\
= \; & \mu\left\|\boldsymbol{r}^{k+1}\right\|_2^2 + 2\mu(\boldsymbol{z}^{k+1} - \boldsymbol{z}^k)^{tr}\boldsymbol{r}^{k+1} \\
+ \; & 2\mu(\boldsymbol{z}^{k+1} - \boldsymbol{z}^k)^{tr}((\boldsymbol{z}^{k+1} - \boldsymbol{z}^k) + (\boldsymbol{z}^k - \boldsymbol{z}^*)) \\
= \; & \mu\left\|\boldsymbol{r}^{k+1}\right\|_2^2 + 2\mu(\boldsymbol{z}^{k+1} - \boldsymbol{z}^k)^{tr}\boldsymbol{r}^{k+1} \\
+ \; & 2\mu\left\|\boldsymbol{z}^{k+1} - \boldsymbol{z}^k\right\|_2^2 + 2\mu(\boldsymbol{z}^{k+1} - \boldsymbol{z}^k)^{tr}(\boldsymbol{z}^k - \boldsymbol{z}^*) \\
= \; & \mu\left\|\boldsymbol{r}^{k+1} + (\boldsymbol{z}^{k+1} - \boldsymbol{z}^k)\right\|_2^2 + \mu\left\|\boldsymbol{z}^{k+1} - \boldsymbol{z}^k\right\|_2^2 + 2\mu(\boldsymbol{z}^{k+1} - \boldsymbol{z}^k)^{tr}(\boldsymbol{z}^k - \boldsymbol{z}^*) \\
= \; & \mu\left\|\boldsymbol{r}^{k+1} + (\boldsymbol{z}^{k+1} - \boldsymbol{z}^k)\right\|_2^2 + \mu\left\|(\boldsymbol{z}^{k+1} - \boldsymbol{z}^*) - (\boldsymbol{z}^k - \boldsymbol{z}^*)\right\|_2^2
\end{aligned}$$

$$
\begin{aligned}
&+ \quad 2\mu(\boldsymbol{z}^{k+1}-\boldsymbol{z}^{k})^{tr}(\boldsymbol{z}^{k}-\boldsymbol{z}^{*}) \\
&= \quad \mu\left\|\boldsymbol{r}^{k+1}+(\boldsymbol{z}^{k+1}-\boldsymbol{z}^{k})\right\|_2^2+\mu(\left\|\boldsymbol{z}^{k+1}-\boldsymbol{z}^{*}\right\|_2^2-\left\|\boldsymbol{z}^{k}-\boldsymbol{z}^{*}\right\|_2^2)
\end{aligned}
$$

Taking together, the following inequality is obtained

$$
\begin{aligned}
0 \quad &\geq \quad \frac{1}{\mu}(\left\|\boldsymbol{y}^{k+1}-\boldsymbol{y}^{*}\right\|_2^2-\left\|\boldsymbol{y}^{k}-\boldsymbol{y}^{*}\right\|_2^2)+\mu\left\|\boldsymbol{r}^{k+1}+(\boldsymbol{z}^{k+1}-\boldsymbol{z}^{k})\right\|_2^2 \\
&+ \quad \mu(\left\|\boldsymbol{z}^{k+1}-\boldsymbol{z}^{*}\right\|_2^2-\left\|\boldsymbol{z}^{k}-\boldsymbol{z}^{*}\right\|_2^2)
\end{aligned}
$$

which implies

$$
V^{k+1}-V^{k}\leq-\mu\left\|\boldsymbol{r}^{k+1}+(\boldsymbol{z}^{k+1}-\boldsymbol{z}^{k})\right\|_2^2
$$

and therefore

$$
\begin{aligned}
V^{k}-V^{k+1} \quad &\geq \quad \mu\left\|\boldsymbol{r}^{k+1}+(\boldsymbol{z}^{k+1}-\boldsymbol{z}^{k})\right\|_2^2 \\
&= \quad \mu\left\|\boldsymbol{r}^{k+1}\right\|_2^2+2\mu\boldsymbol{r}^{k+1}(\boldsymbol{z}^{k+1}-\boldsymbol{z}^{k})+\mu\left\|\boldsymbol{z}^{k+1}-\boldsymbol{z}^{k}\right\|_2^2
\end{aligned}
$$

and it remains to be investigated that

$$
2\mu\boldsymbol{r}^{k+1}(\boldsymbol{z}^{k+1}-\boldsymbol{z}^{k})\geq 0
$$

As was shown before, $\boldsymbol{z}^{k+1}$ and $\boldsymbol{z}^{k}$ minimize

$$
-\int_{\Omega^*}\langle\boldsymbol{z}^{k},\tilde{\boldsymbol{e}}\rangle-(\boldsymbol{y}^{k+1})^{tr}\boldsymbol{z}\,\mathrm{d}\boldsymbol{x}
$$

and

$$
\int_{\Omega^*}\langle\boldsymbol{z}^{k},\tilde{\boldsymbol{e}}\rangle-(\boldsymbol{y}^{k})^{tr}\boldsymbol{z}\,\mathrm{d}\boldsymbol{x}
$$

Adding both leads to

$$
\begin{aligned}
-\textstyle\int_{\Omega^*}\langle\boldsymbol{z}^{k+1},\tilde{\boldsymbol{e}}\rangle-(\boldsymbol{y}^{k+1})^{tr}\boldsymbol{z}^{k+1}\,\mathrm{d}\boldsymbol{x}\leq-\int_{\Omega^*}\langle\boldsymbol{z}^{k},\tilde{\boldsymbol{e}}\rangle-(\boldsymbol{y}^{k+1})^{tr}\boldsymbol{z}^{k}\mathrm{d}\boldsymbol{x} \\
-\textstyle\int_{\Omega^*}\langle\boldsymbol{z}^{k},\tilde{\boldsymbol{e}}\rangle-(\boldsymbol{y}^{k})^{tr}\boldsymbol{z}^{k+1}\,\mathrm{d}\boldsymbol{x}\leq-\int_{\Omega^*}\langle\boldsymbol{z}^{k+1},\tilde{\boldsymbol{e}}\rangle-(\boldsymbol{y}^{k+1})^{tr}\boldsymbol{z}^{k}\,\mathrm{d}\boldsymbol{x}
\end{aligned}
$$

which in turn leads to

$$
-(\boldsymbol{y}^{k+1}-\boldsymbol{y}^{k})^{tr}(\boldsymbol{z}^{k+1}-\boldsymbol{z}^{k})\leq 0
$$

Since $\mu>0$ and $\boldsymbol{y}^{k+1}-\boldsymbol{y}^{k}=\mu\boldsymbol{r}^{k+1}$, the inequality is proven.
Inequality E3 can be used to show residual convergence $\boldsymbol{r}^{k+1}\to 0$ for $k\to\infty$. As both $\left\|\boldsymbol{r}^{k+1}\right\|_2^2$ and $\left\|\boldsymbol{z}^{k+1}-\boldsymbol{z}^{k}\right\|_2^2$ are positive, it follows that $V^{k}\leq V^{0}$ and therefore that $\boldsymbol{y}^{k}$ and $\boldsymbol{z}^{k}$ are bounded. Summing up the V^{k} leads to

$$
\mu(\sum_{k=0}^{\infty}\left\|\boldsymbol{r}^{k+1}\right\|_2^2+\left\|\boldsymbol{z}^{k+1}-\boldsymbol{z}^{k}\right\|_2^2)\leq V_0
$$

which implies $\boldsymbol{r}^{k+1} \to 0$ and $\boldsymbol{z}^{k+1} - \boldsymbol{z}^k \to 0$ for $k \to \infty$. Therefore, the residuum $\boldsymbol{r}^{k+1} = A\boldsymbol{J}^{k+1} - \boldsymbol{z}^{k+1}$ converges to zero for $k \to \infty$.
As $\boldsymbol{y}^{k+1}$ is bounded and both $\boldsymbol{r}^{k+1}$ and $\boldsymbol{z}^{k+1} - \boldsymbol{z}^k$ converge to zero, the objective convergence $\lim_{k\to\infty} p^k = q^*$ directly follows from inequalities E2 and E1.
Remark A.1 (Primal and dual feasibility)**.** According to Boyd and colleagues [15], the necessary and sufficient optimality conditions for the minimization problem are primal feasibility

$$A\boldsymbol{J}^* - \boldsymbol{z}^* = 0 \tag{A.1}$$

and dual feasibility

$$0 = A^{tr}\boldsymbol{y}^* \tag{A.2}$$
$$0 = \partial g(\boldsymbol{z}^*) - \boldsymbol{y}^* \tag{A.3}$$

Boyd and colleagues [15] were able to demonstrate that Condition A.3 is always fulfilled. Condition A.2 is fulfilled when the dual residual $v^{k+1} = \mu A^{tr}(\boldsymbol{z}^{k+1} - \boldsymbol{z}^k)$ converges to zero. Since μA^{tr} is bounded and $\boldsymbol{z}^{k+1} - \boldsymbol{z}^k \to 0$ for $k \to \infty$, the dual residual $\lim_{k\to\infty} v^{k+1} = 0$. Therefore, Condition A.2 is also fulfilled.
Moreover, the convergence of the residuum $\boldsymbol{r}^{k+1}$ to zero implies that the primal feasibility condition $A\boldsymbol{J}^* - \boldsymbol{z}^* = 0$ is fulfilled.

A.2. Mathematical background

In this section, the Lebesgue spaces L^p and the Sobolev spaces W_p^k are introduced. Moreover, recall important convergence statements and well known theorems that are used in this thesis will be discussed.
Definition A.1 (Lebesgue integral, Lebesgue norm and Lebesgue spaces, [17])**.** Let f be a real-valued function on a given domain Ω. The *Lebesgue integral* of f is defined by

$$\int_\Omega f(\boldsymbol{x})\,\mathrm{d}\boldsymbol{x}$$

For $1 \le p \le \infty$ the *Lebesgue norm* is defined as

$$\|f\|_{L^p\Omega} := \Big(\int_\Omega |f(\boldsymbol{x})|^p\,\mathrm{d}\boldsymbol{x}\Big)^{1/p}$$

and for the case $p = \infty$

$$\|f\|_{L^\infty(\Omega)} := ess\ sup\ \{|f(\boldsymbol{x})| : \boldsymbol{x} \in \Omega\}$$

Finally, the *Lebesgue spaces* are defined as

$$L^p(\Omega) := \{f : \|f\|_{L^p(\Omega)} < \infty\}$$

Two functions f and g are called to be identical, when $\|f-g\|_{L^p(\Omega)}=0$, i.e., f and g differ only on a set of measure zero.

For Lebesgue spaces, important inequalities can be shown [17]

- *Hölders Inequality:*
  For $1 \leq p,q \leq \infty$ such that $1=1/p+1/q$, if $f \in L^p(\Omega)$ and $g \in L^q(\Omega)$, than $fg \in L^1(\Omega)$ and
  $$\|fg\|_{L^1(\Omega)} \leq \|f\|_{L^p(\Omega)} \|g\|_{L^q(\Omega)}$$

- *Minkowski's Inequality:*
  For $1 \leq p,q \leq \infty$ and $f,g \in L^p(\Omega)$, we have
  $$\|f+g\|_{L^p(\Omega)} \leq \|f\|_{L^p(\Omega} + \|g\|_{L^p(\Omega)}$$

- *Schwarz' Inequality:*
  Using Hölders Inequality with $p=q=2$, we have
  $$\int_\Omega |f(\boldsymbol{x})g(\boldsymbol{x})| \,\mathrm{d}\boldsymbol{x} \leq \|f\|_{L^2(\Omega)} \|g\|_{L^2(\Omega)}$$

In order to define *Banach spaces*, the norm of a vector space is defined.
Definition A.2 (Norm, normed linear space and complete, [17])**.** Let V be a vector space. A *norm* $\|.\|$ is a function on V having the following properties:

- $\|f\| \geq 0 \; \forall f \in V$ and $\|f\|=0 \Leftrightarrow f=0$
- $\|cf\| = |c| \, \|f\| \;\; \forall c \in \mathbb{R}, f \in V$
- $\|f+g\| \leq \|f\| + \|g\| \;\; \forall f,g \in V$

A vector space with the metric $d(f,g)=\|f-g\|$ is called *normed linear space*. A normed linear space is called *complete* if every *Cauchy sequence* of elements $f \in V$ has a limit $\tilde{f} \in V$.

Further details about linear spaces can be found in [17].
Definition A.3 (Banach space, [17])**.** A normed linear space $(V, ||.||)$ is called a *Banach space* if it is complete with respect to the metric induced by the norm, $||.||$.

A very fundamental result is presented in the following
Theorem A.1 ([17])**.** For $1 \leq p \leq \infty$, $L^p(\Omega)$ is a Banach space.

In order to describe Sobolev spaces, a multi-index notation is needed:
Definition A.4 (Multi-index, [17])**.** A *multi-index* α is an n-tupel of $\alpha_i \geq 0$. The length of α is given as
$$|\alpha| := \sum_{i=1}^{n} \alpha_i$$

For $\phi \in C^\infty$, we define the partial derivatives $D^\alpha \phi$ as

$$D^\alpha \phi = (\frac{\partial}{\partial x_1})^{\alpha_1}, \cdots, (\frac{\partial}{\partial x_n})^{\alpha_n} \phi$$

Given a vector $\boldsymbol{x} = (x_1, \cdots, x_n)$, we define $\boldsymbol{x}^\alpha = x_1^{\alpha_1} \cdots x_n^{\alpha_n}$

The set of locally integrable functions is defined in the following
Definition A.5 (Locally integrable functions, [17])**.** Let Ω be a domain. The set of *locally integrable* functions is denoted by

$$L^1_{loc}(\Omega) := \{f : f \in L^1(K) \ \ \forall compact\ K \subset \ interior\ \Omega\}$$

This definition allows to define the weak derivative of a locally integrable function
Definition A.6 (Weak derivative, [17])**.** A locally integrable function $f \in L^1_{loc}(\Omega)$ has a *weak derivative* D^α_ω if there exists a function $g \in L^1_{loc}(\Omega)$ such that

$$\int_\Omega g(\boldsymbol{x})\phi(\boldsymbol{x})\,\mathrm{d}\boldsymbol{x} = (-1)^{|\alpha|} \int_\Omega f(\boldsymbol{x})\phi^{(\alpha)}(\boldsymbol{x})\,\mathrm{d}\boldsymbol{x} \quad \forall \phi \in C^\infty_0(\Omega).$$

If such g exists, we define $D^\alpha_\omega f = g$

This allows to define Sobolev spaces
Definition A.7 (Sobolev norm and Sobolev space, [17])**.** Let $k \geq 0$ be a integer and let $f \in L^1_{loc}(\Omega)$. Suppose that the weak derivatives $D^\alpha_\omega f$ exists for all $|\alpha| \leq k$. The *Sobolev norm* is defined as

$$\|f\|_{W^k_p(\Omega)} := (\sum_{|\alpha| \leq k} \|D^\alpha_\omega f\|^p_{L^p(\Omega)})^{1/p}$$

for $1 \leq p < \infty$. For $p = \infty$, we define

$$\|f\|_{W^k_\infty(\Omega)} := \max_{|\alpha| \leq k} \|D^\alpha_\omega f\|_{L^\infty(\Omega)}\,.$$

In both cases, we define the *Sobolev spaces* via

$$W^k_p(\Omega) := \{f \in L^1_{loc}(\Omega) : \|f\|_{W^k_p(\Omega)} < \infty\}.$$

In the following, we denote $H^k(\Omega) = W^{k,2}(\Omega) = \{u \in L^2(\Omega) : D^\alpha \in L^2(\Omega)\ \forall 0 < |\alpha| < k\}$.
Definition A.8 (Graph of Lipschitz function, Lipschitz boundary [17])**.** A domain Ω_i is called to be a *Graph of a Lipschitz function* ψ_i if

$$\Omega_i = \{(\boldsymbol{x}, \boldsymbol{y}) \in \mathbb{R}^n | \boldsymbol{x} \in \mathbb{R}^{n-1}, \boldsymbol{y} \leq \psi_i(\boldsymbol{x})\}$$

Ω has a *Lipschitz boundary* $\partial\Omega$ if there exists a collection of open sets O_i, an $\epsilon > 0$, an integer N and a finite number M such that for all $\boldsymbol{x} \in \partial\Omega$ the ball of radius ϵ centered at $\boldsymbol{x}$ is contained in some O_i. Furthermore, no more than N of the sets O_i intersect nontrivially

and each domain $O_i \cap \Omega = O_i \cap \Omega_i$ with Ω_i being a domain whose boundary is a graph of a Lipschitz function ψ_i satisfying $\|\psi_i\|_{Lip(\mathbb{R}^{n-1})} \leq M$.

In this thesis, each volume conductor model Ω has a Lipschitz boundary $\partial\Omega$. Using this definition, the Sobolev spaces can now be related to the $\mathbb{R}^n$:

Theorem A.2. Suppose that Ω has a Lipschitz boundary. Then there exists an *extension* mapping $E : W_p^k(\Omega) \to W_p^k(\mathbb{R}^n)$ defined for all $\epsilon > 0$ and real numbers p in the range $1 \leq p \leq \infty$ satisfying $Ev|_\Omega = v$ for all $v \in W_p^k(\Omega)$ and

$$\|Ev\|_{W_p^k(\mathbb{R}^n)} \leq C \|v\|_{W_p^k(\Omega)}$$

where C is independent of v.

Proof. See [17] page 33, Theorem 1.4.5 □

In a next step, the trace theorem is introduced, which is especially important for the sensor optimization approaches, see Section 5:

Theorem A.3 (Trace theorem, [17])**.** Suppose that Ω has a Lipschitz boundary and that p is a real number that fulfills $1 \leq p \leq \infty$. Then there exists a constant C such that

$$\|v\|_{L^p(\partial\Omega)} \leq C \|v\|_{L^p(\Omega)}^{1-\frac{1}{p}} \|v\|_{W_p^1(\Omega)}^{\frac{1}{p}} \quad \forall v \in W_p^1(\Omega)$$

The divergence theorem can be applied for functions $u, v \in \mathcal{C}^1(\overline{\Omega})$ as will be discussed in the following

Theorem A.4 (Divergence theorem, see Evans [35], page 628, Theorem2)**.** Let $\boldsymbol{u}, \boldsymbol{v} \in \mathcal{C}^1(\overline{\Omega})$. Then

$$\int_\Omega \nabla \boldsymbol{u}\boldsymbol{v} \, \mathrm{d}\boldsymbol{x} = -\int_\Omega \boldsymbol{u} \nabla \boldsymbol{v} \, \mathrm{d}\boldsymbol{x} + \int_{\partial\Omega} \langle \boldsymbol{u}\boldsymbol{v}, \boldsymbol{n} \rangle \, \mathrm{d}\boldsymbol{s} \tag{A.4}$$

Proof. see Evans [35], page 628. □

Under certain conditions, the divergence theorem (Gauss theorem) still holds true for functions $\boldsymbol{u}, \boldsymbol{v} \notin C^1(\Omega)$

Theorem A.5 (Extended version of divergence theorem)**.** Suppose that the domain Ω has a Lipschitz boundary $\partial\Omega$ and let $\boldsymbol{v} \in W^1(\Omega)$. Then the following equation holds

$$\int_\Omega \nabla \cdot F \, \mathrm{d}\boldsymbol{x} = \int_{\partial\Omega} \langle F, \boldsymbol{n} \rangle \, \mathrm{d}\boldsymbol{s}$$

Proof. See [6], Theorem 5.12 □

A.3. Additional figures

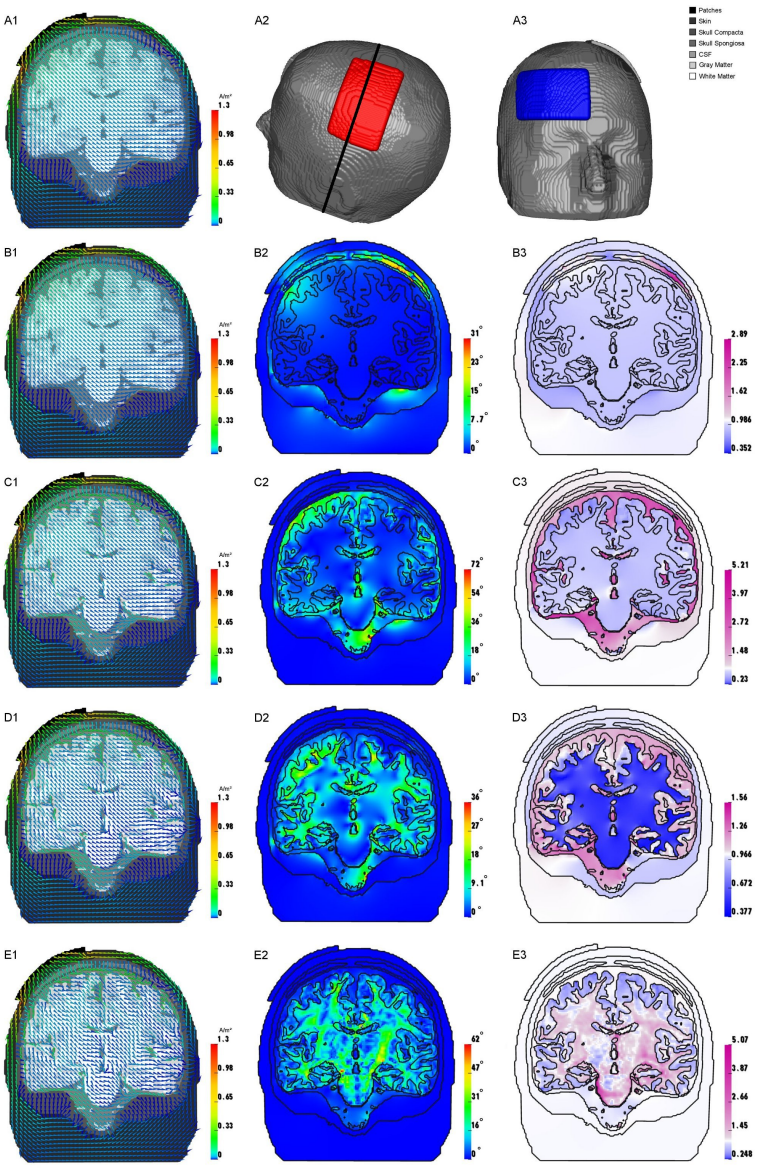

Figure A.1.: Current density for motor cortex stimulation. The structure of the figure is identical to Figure 4.1

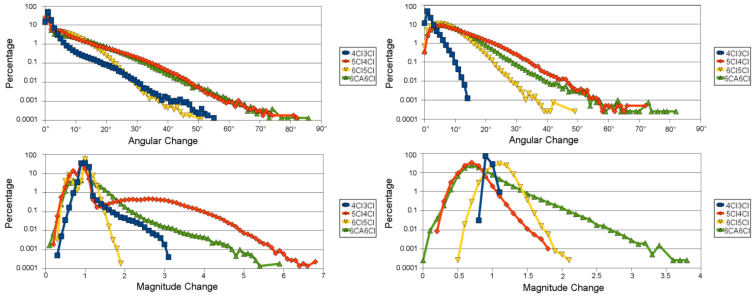

Figure A.2.: Statistical evaluation of the current density orientation (Ang) and magnitude (Mag) changes for motor cortex stimulation. The structure of the figure is identical to Figure 4.4

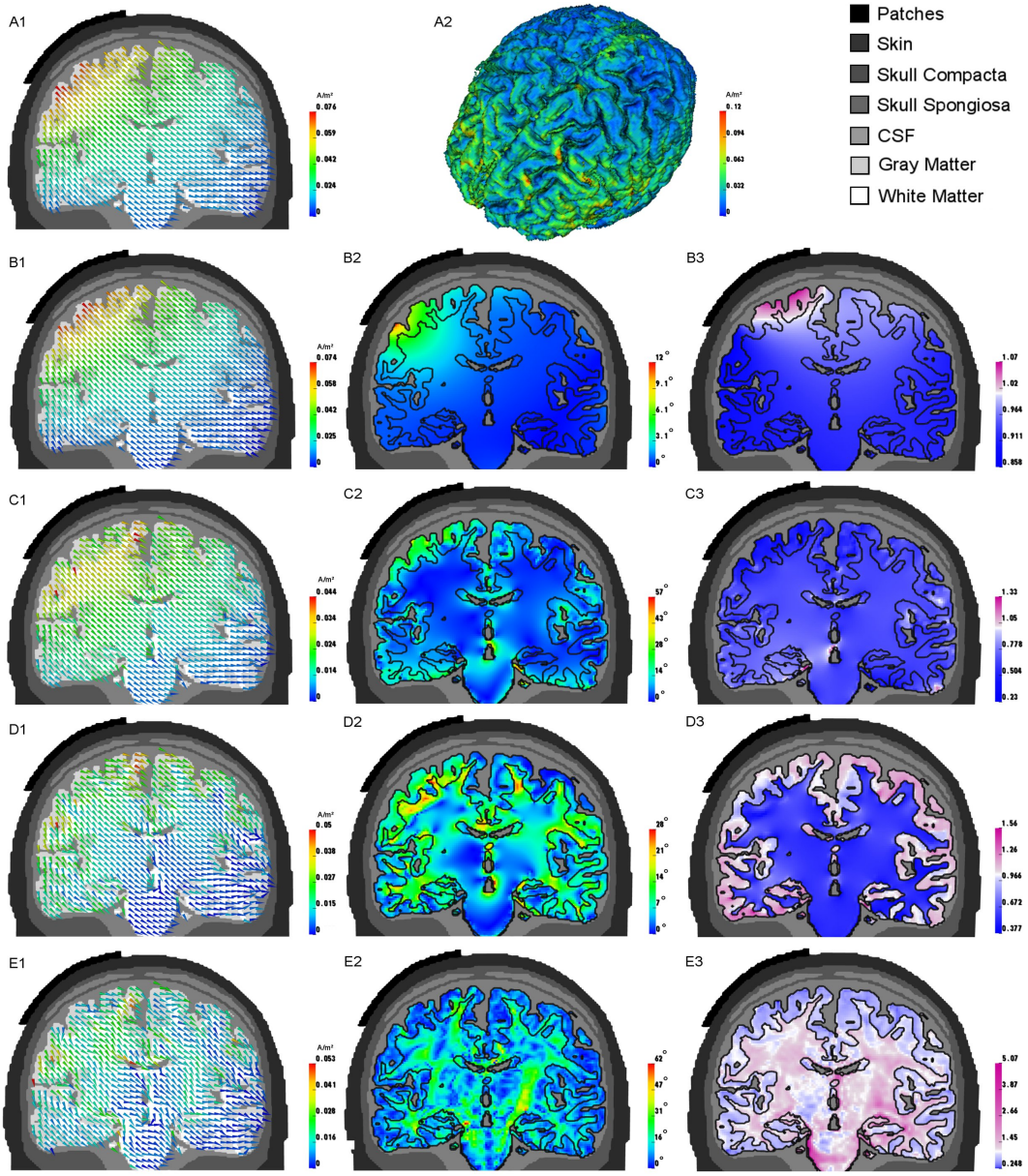

Figure A.3.: Current density distribution only in the brain compartment for motor cortex stimulation. This structure of the figure is identical to Figure 4.2

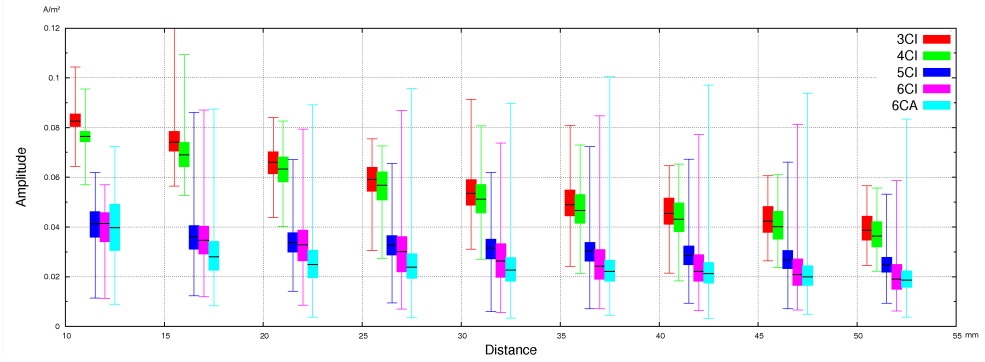

Figure A.4.: Boxplot for each of the five models with motor cortex stimulation. The structure of the figure is identical to Figure 4.3

B

Publications and Awards

Peer-reviewed publications and journal impact factor (IF)

1. **Wagner, S.**, Rampersad, S.M., Aydin, Ü., Vorwerk, J., Oostendorp, T.F., Neuling, T., Herrmann, C.S., Stegeman, D.F. and Wolters, C.H., Investigation of tDCS volume conduction effects in a highly realistic head model, *J. Neural Eng.*, 11:016002(14pp), (2014).
   First and corresponding Author: IF: 3.4 (2013), DOI, PubMed, Eprint, pdf

2. Neuling, T., Rach, S., **Wagner, S.**, Wolters, C.H. and Herrmann, C.S., Good vibrations: oscillatory phase shapes perception, *NeuroImage*, 63(2), pp.771–778, (2012).
   Coauthor: IF: 6.3, PubMed, DOI, EPRINT, pdf Faculty of 1000, 20.Nov.2012; F1000 Prime Recommendation: DOI Web

3. Neuling, T., **Wagner, S.**, Wolters, C.H., Zaehle, T. and Herrmann, C.S., Finite element model predicts current density distribution for clinical applications of tDCS and tACS, *Front. Psychiatry*, 3(83), pp.1-10, (2012).
   Shared First Author: No IF, PubMed, pdf, DOI

4. Schmidt, C., **Wagner, S.**, Burger, M., van Rienen, U. and Wolters, C.H. Impact of uncertain head tissue conductivity in the optimization of transcranial direct current stimulatoin for an auditory target *J. Neural Eng.*, accepted for publication, (2015)
   Shared First Author: IF: 3.415

5. **Wagner, S.**, Burger, M. and Wolters, C.H. An optimization approach for well-targeted transcranial direct current stimulation *SIAM Journal on Applied Mathematics (SIAP)*, submitted
   First and corresponding Author: IF: 1.414

6. **Wagner, S.**, Lucka, F., Vorwerk, J., Herrmann, C.S., Nolte, G., Burger, M. and Wolters, C.H. Using reciprocity for relating the modeling of transcranial current stimulation and the EEG forward problem *NeuroImage*, Invited submission to special issue *Combining Transcranial Electrical Stimulation (tES) And Neuroimaging*, submitted
First and corresponding Author: IF: 6.132

Proceedings and journal impact factor (IF)

1. **Wagner S.**, Aydin Ü., Vorwerk J., Herrmann, C., Burger M., Wolters C.H., Volume Conduction and Optimized Stimulation Protocols in Transcranial Current Stimulation, First Int.Conf on Basic and Clinical multimodal Imaging (BaCI), Geneva, Switzerland (2013). Clin EEG Neurosci, 44(4):E1-E121, (Oct.2013).
First author: IF: 3.2, DOI, Web, pdf of abstract

2. Wolters CH, Aydin Ü, Lanfer B, Lew S, Lucka F, Ruthotto L, Vorwerk J, **Wagner S.**, Influence of Volume Conduction on EEG and MEG Source Analysis and Brain Stimulation, First Int.Conf on Basic and Clinical multimodal Imaging (BaCI), Geneva, Switzerland, Clin EEG Neurosci, 44(4):E1-E121, (Oct.2013).
Coauthor: IF: 3.2, DOI, Web, pdf of abstract

3. **Wagner, S.**, Lucka, F., Burger, M., Grasedyck, L., Haueisen, J. and Wolters, C.H., Comparison of direct and reciprocal forward modeling approaches in EEG source analysis, Biomedical Engineering, 57(Suppl.1), p.310, doi: 10.1515/bmt-2012-4069, (2012).
First author: IF: 1.2, PubMed, Eprint, Web of Knowledge, pdf

4. **Wagner, S.**, Rampersad, S., Aydin, Ü., Vorwerk, J., Neuling, T., Hermann, C.S., Stegeman, D. and Wolters, C.H., Volume conduction effects in tDCS using a 1mm geometry-adapted hexahedral finite element head model, Biomedical Engineering, 57(Suppl.1), p.329, doi: 10.1515/bmt-2012-4072, (2012).
First author: IF: 1.2, PubMed, Eprint, Web of Knowledge, pdf

5. **Wagner, S.**, Vorwerk, J., Ruthotto, L., Kugel, H., Burger, M., Knösche, T.R., Maess, B. and Wolters, C.H., Sensitivity of EEG leads to volume conductor properties, Biomedical Engineering, 57 (Suppl.1), p.793, doi: 10.1515/bmt-2012-4065,(2012).
First author: IF: 1.2, PubMed, Eprint, Web of Knowledge, pdf

Selection of other Proceedings (some peer-reviewed)

1. **Wagner, S.**, Aydin, Ü., Vorwerk, J., Herrmann, C., Burger, M., Wolters, C.H., New numerical methods for electrode optimization and current density modeling in tCS, In (org. Brooks, MacLeod, Tucker): Morning workshop "Computational and imaging tools

for targeting non-invasive brain stimulation", *20th Annual Meeting of the Organization for Human Brain Mapping*, Hamburg, Germany, June 8-12, Web, (2014).

2. **Wagner, S.**, Aydin, Ü., Vorwerk, J., Burger, M., Wolters, C.H., Volume conduction and optimized stimulation protocols in transcranial current stimulation Innovative Verarbeitung bioelektrischer und biomagnetischer Signale (BBS2014), PTB Berlin, April 10.-11, 2014, Program

Poster presentations

1. Engwer, C., Ludewig, J., Vorwerk, J., **Wagner, S.** and Wolters, C.H., A Discontinuous Galerkin Finite Element approach for the EEG forward problem, Biomag2014, 19th Int.Conf. on Biomagnetism, Aug.24-28, Halifax, Canada, (2014). Web pdf of poster

2. **Wagner S.**, Aydin Ü., Vorwerk J., Herrmann, C., Burger M., Wolters C.H., Volume conduction and optimized stimulation protocols in transcranial current stimulation, Neurovisionen 9, Cologne, Germany, Nov.29 (2013). pdf of poster

3. **Wagner S.**, Aydin Ü., Vorwerk J., Herrmann, C., Burger M., Wolters C.H., Volume conduction and optimized stimulation protocols in transcranial current stimulation, First Int.Conf on Basic and Clinical multimodal Imaging (BaCI), Geneva, Switzerland (2013). DOI, Web, pdf of abstract

4. **Wagner, S.**, Vorwerk, J., Ruthotto, L., Kugel, H., Burger, M., Knösche, T.R., Maess, B. and Wolters, C.H., Sensitivity of EEG leads to volume conductor properties, Biomag2012, 18th Int.Conf. on Biomagnetism, Aug.26-30, Paris, France, (2012). Web

5. **Wagner, S.**, Lucka, F., Burger, M., Grasedyck, L., Haueisen, J. and Wolters, C.H. Comparison of direct and reciprocal forward modeling approaches in EEG source analysis, Biomag2012, 18th Int.Conf. on Biomagnetism, Aug.26-30, Paris, France, (2012). Web

6. **Wagner, S.**, Rampersad, S., Vorwerk, J., Aydin, Ü., Neuling, T., Herrmann, C.S., Stegemann, D. and Wolters, C.H., Volume conduction effects in tDCS using a 1mm geometry-adapted hexahedral finite element head model, Biomag2012, 18th Int.Conf. on Biomagnetism, Aug.26-30, Paris, France, (2012). Web

Awards

1. Journal of Neural Engineering: Selected as one of the 16 highlights of 2014: **Wagner S**, Rampersad SM, Aydin U, Vorwerk J, Oostendorp TF, Neuling T, Herrmann CS, Stegeman DF, Wolters CH, Investigation of tDCS volume conduction effects in a highly realistic head model, J. Neural Eng. 11:016002(14pp), (2014).

2. Award for best poster presentation
   Wagner S., Aydin Ü., Vorwerk J., Herrmann, C., Burger M., Wolters C.H., Volume conduction and optimized stimulation protocols in transcranial current stimulation, Neurovisionen 9, Cologne, Germany, Nov.29 (2013).

3. Faculty of 1000, 20.Nov.2012; F1000 Prime Recommendation of: Neuling T., Rach S., **Wagner S.**, Wolters C.H. and Herrmann C.S., NeuroImage, 63(2):771-778, (2012).

Supervisor for master theses

1. S. Homölle, Master Thesis in Mathematics, Fachbereich Mathematik und Informatik, University of Münster. *Implementation and comparison of different approaches to the tDCS optimization problem*, (2015).

2. B. Agsten, Master Thesis in Mathematics, Fachbereich Mathematik und Informatik, University of Münster. *Comparing the complete and point electrode model for combining tCS and EEG*, (2015).

3. F.Meyer, Master Thesis in Mathematics, Fachbereich Mathematik und Informatik, University of Münster. *Convergent adaptive Finite Element Methods for the solution of the EEG forward problem with the help of the subtraction method*, (2013).

Bibliography

[1] B. Agsten. Comparing the complete and point electrode model for combining tCS and EEG. *Master Thesis in Mathematics, Fachbereich Mathematik und Informatik, University of Münster*, 2015. 60

[2] M. Akhtari, HC. Bryant, AN. Mamelak, ER. Flynn, L. Heller, JJ. Shih, M. Mandelkern, A. Matlachov, DM. Ranken, ED. Best, MA. DiMauro, RR. Lee, and WW. Sutherling. Conductivities of three-layer live human skull. *Brain Topography*, 14:151–167, 2002. 7, 31, 62, 63, 68, 133

[3] A. Antal, TZ. Kincses, MA. Nitsche, and W. Paulus. Manipulation of phosphene thresholds by transcranial direct current stimulation in man. *Experimental Brain Research*, 150:375–378, 2003. 4, 76

[4] A. Antal and W. Paulus. Transcranial direct current stimulation and visual perception. *Perception*, 37:367–374, 2008. 82

[5] U. Aydin, J. Vorwerk, P. Küpper, M. Heers, H. Kugel, A. Galka, L. Hamid, J. Wellmer, C. Kellinghaus, S. Rampp, and CH. Wolters. Combining EEG and MEG for the reconstruction of epileptic activity using a calibrated realistic volume conductor model. *Plos One*, 9(3):e93154, 2014. 8, 43, 122, 124, 135, 153, 156

[6] L. Banjai. Boundary element method. *Lecture notes, Institut fuer Mathematik, Universitaet Zuerich*, 2007. 164

[7] PJ. Basser, J. Mattiello, and D. LeBihan. MR diffusion tensor spectroscopy and imaging. *Biophysical Journal*, 66(1):259–267, 1994. 7

[8] SB. Baumann, DR. Wozny, SK. Kelly, and FM. Meno. The electrical conductivity of human cerebrospinal fluid at body temperature. *IEEE Transactions on Biomedical Engineering*, 44:220–223, 1997. 7, 63

[9] U. Baysal and J. Haueisen. Use of a priori information in estimating tissue resistivities-application to human data in vivo. *Physiological Measurement*, 25:737–748, 2004. 7

[10] TEJ. Behrens, MW. Woolrich, M. Jenkinson, H. Johansen-Berg, RG. Nunes, S. Clare,

PM. Matthews, JM. Brady, and SM. Smith. Characterization and propagation of uncertainty in diffusion-weighted MR imaging. *Magnetic Resonance in Medicine*, 50:1077–1088, 2003. 31

[11] LJ. Bindman, OC. Lippold, and JW. Redfearn. Long-lasting changes in the level of the electrical activity of the cerebral cortex produced bypolarizing currents. *Nature*, 196:584–585, 1962. 88, 93, 155

[12] PS. Boggio, R. Ferrucci, SP. Rigonatti, P. Covre, M. Nitsche, A. Pascual-Leone, and F. Fregni. Effects of transcranial direct current stimulation on working memory in patients with Parkinson's disease. *Journal of the Neurological Sciences*, 249:31–38, 2006. 4

[13] PS. Boggio, SP. Rigonatti, RB. Ribeiro, ML. Myczkowski, MA. Nitsche, A. Pascual-Leone, and F. Fregni. A randomized, double-blind clinical trial on the efficacy of cortical direct current stimulation for the treatment of major depression. *International Journal of Neuropsychopharmacology*, 11:249–254, 2008. 80, 81

[14] CA. Bosetti, MJ. Birdno, and WM. Grill. Analysis of the quasi-static approximation for calculating potentials generated by neural stimulation. *Journal of Neural Engineering*, 5:44–53, 2008. 77

[15] S. Boyd, N. Parikh, E. Chu, B. Peleato, and J. Eckstein. Distributed optimization and statistical learning via the alternating direction method of multipliers. *Foundations and Trends in Machine Learning*, 3(1):1–122, 2011. 101, 102, 140, 157, 161

[16] NM. Branston and PS. Tofts. Magnetic stimulation of a volume conductor produces a negligible component of current perpendicular to the surface. *Clinical Neurophysiology*, 423:67pp, 1990. 132

[17] SC. Brenner and LR. Scott. The mathematical theory of finite element methods. *Springer*, SBN: 978-0-387-75933-3. 34, 161, 162, 163, 164

[18] DL. Camacho, RH. Hopper, GM. Lin, and BS. Myers. An improved method for finite element mesh generation of geometrically complex structures with application to the skullbase. *Journal of Biomechanics*, 30:1067–1070, 1997. 29, 31

[19] A. Charturvedi, CR. Butson, SF. Lempka, SE. Cooper, and CC. McIntyre. Patient-specific models of deep brain stimulation: influence of field model complexity on neural activation predictions. *Brain Stimulation*, 3:65–67, 2010. 76

[20] M. Chen and DJ. Mogul. Using increased structural detail of the cortex to improve the accuracy of modeling the effects of transcranial magnetic stimulation on neocortical activation. *IEE Transactions on Biomedical Engineering*, 57(5):1216–1226, 2009. 126

[21] R. Chen, J. Classen, C. Gerloff, P. Celnik, EM. Wassermann, M. Hallet, and LG. Cohen. Depression of motor cortex excitability by low-frequency transcranial magnetic stimulation. *Neurology*, 48(5):1398–1403, 1997. 4

[22] MJ. Cook and ZJ. Koles. A high-resolution anisotropic finite-volume head model for EEG source analysis. *Conf Proc IEEE Eng Med Biol Soc 2006*, 1:4536–4539, 2006. 22

[23] OD. Creutzfeldt, GH. Gromm, and H. Kapp. Influence of transcranial d-c currents on cortical neuronal activity. *Experimental Neurology*, 5:436–452, 1962. 88, 93

[24] AM. Dale and MI. Sereno. Improved localizadon of cortical activity by combining EEG and MEG with MRI cortical surface reconstruction: a linear approach. *Journal of Cognitive Neuroscience*, 5(2):162–176, 1993. 16

[25] M. Dannhauer, B. Lanfer, CH. Wolters, and T. Knösche. Modeling the human skull in EEG source analysis. *Human Brain Mapping*, 32:1383–1399, 2011. 7, 62

[26] A. Datta, JM. Baker, M. Bikson, and J. Fridriksson. Individualized model predicts brain current flow during transcranial direct-current stimulation treatment in responsive stroke patient. *Brain Stimulation*, 4:169–174, 2011. 5, 29, 36, 43, 45, 64, 74, 76, 77, 91

[27] A. Datta, V. Bansal, J. Diaz, J. Patel, D. Reato, and M. Bikson. Gyri-precise head model of transcranial direct current stimulation: improved spatial focality using a ring electrode versus concentional rectangular pad. *Brain Stimulation*, 2:201–207, 2009. 62, 73, 74

[28] A. Datta, M. Bikson, and F. Fregni. Transcranial direct current stimulation in patients with skull defects and skull plates: high-resolution computational FEM study of factors altering cortical current flow. *NeuroImage*, 52:1268–1278, 2010. 29, 43, 45, 73, 75, 77

[29] M. De Lucia, GJ. Parker, K. Embleton, JM. Newton, and V. Walsh. Diffusion tensor MRI-based estimation of the influence of brain tissue anisotropy on the effects of transcranial magnetic stimulation. *NeuroImage*, 36(4):1159–1170, 2007. 6, 125, 136

[30] J. de Munck and MJ. Peters. A fast method to compute the potential in the multisphere model. *IEEE Transactions on Biomedical Engineering*, 48(11):1166–1174, 1993. 8, 11, 26, 27, 42, 43

[31] J. de Munck, B. van Dijk, and H. Spekreijse. Mathematical dipoles are adequate to describe realistic generators of human brain activity. *IEEE Transactions on Biomedical Engineering*, 35(11):960–966, 1988. 3, 13, 14

[32] L. Ding and B. He. Sparse source imaging in EEG with accurate field modeling. *Human Brain Mapping*, 29(9):1053–1067, 2008. 16

[33] JP. Dmochowski, A. Datta, M. Bikson, Y. Su, and LC. Parra. Optimized multi-electrode stimulation increases focality and intensity at target. *Journal of Neural Engineering*, 8:046011, 2011. 4, 5, 9, 36, 45, 62, 89, 91, 92, 93, 113, 115, 116

[34] F. Drechsler, CH. Wolters, T. Dierkes, H. Si, and L. Grasedyck. A full subtraction approach for finite element method based source analysis using constrained Delaunay tetrahedralisation. *NeuroImage*, 46:1055–1069, 2009. 8, 11, 20, 22, 127, 129

[35] LC. Evans. Partial differential equations. *American mathematical society, graduate studies in mathematics*, 19, 1998. 34, 164

[36] P. Faria, M. Hallet, and PC. Miranda. A finite element analysis of the effect of electrode area and inter-electrode distance on the spatial distribution of the current density in tDCS. *Journal of Neural Engineering*, 8:066017, 2011. 5, 73

[37] R. Ferrucci, F. Mameli, I. Guidi, S. Mrakic-Sposta, M. Vergari, S. Marceglia, F. Cogiamanian, S. Barbieri, E. Scarpini, and A. Priori. Transcranial direct current stimulation improves recognition memory in Alzheimer disease. *Neurology*, 71:493–498, 2008. 4

[38] F. Fregni, S. Thome-Sousa, MA. Nitsche, SD. Freedman, KD. Valente, and A. Pascual-Leone. A controlled clinical trial of cathodal DC polarization in patients with refractory epilepsy. *Epilepsia*, 47:335–342, 2006. 4, 5, 80, 81, 91

[39] JH. Frijns, A. de Snoo, and R. Schoonhoven. Improving the accuracy of the boundary element method by the use of second-order interpolation functions. *IEEE Transactions on Biomedical Engineering*, 47:1336–1346, 2000. 21

[40] M. Fuchs, M. Wagner, and J. Kastner. Boundary element method volume conductor models for EEG source reconstruction. *Clinical Neurophysiology*, 112(8):1400–1407, 2001. 21

[41] DB. Geselowitz. On bioelectric potentials in an inhomogeneous volume conductor. *Biophysical Journal*, 7:1–17, 1967. 21

[42] D. Gilbarg and NS. Trudinger. Elliptic partial differential equations of second order. *Springer*, 2001. 107, 115, 141

[43] D. Güllmar, J. Haueisen, and JR. Reichenbach. Influence of anisotropic electrical conductivity in white matter tissue on the EEG/MEG forward and inverse solution. A high-resolution whole head simulation study. *NeuroImage*, 51:145–163, 2010. 7

[44] L. Gomez, F. Cajko, L. Hernandez-Garcia, A. Grbic, and E. Michielsson. Numerical analysis and design of single-source multicoil TMS for deep and focused brain stimulation. *IEEE Transactions on Biomedical Engineering*, 60(10):2771–2782, 2013. 6, 137, 138

[45] MH. Gutknecht. A brief introduction to krylov space methods for solving linear systems. *Proc of the International Symposium on Frontiers of Computational Science*, 2005. 48

[46] W. Hackbusch. Iterative solution of large sparse systems of equations. *Springer Verlag. Applied Mathematical Sciences*, 1994. 49

[47] H. Hallez, B. Vanrumste, P. Van Hese, Y. D'Asseler, I. Lemahieu, and R. Van de Walle. A finite difference method with reciprocity used to incorporate anisotropy in electroencephalogram dipole source localization. *Physics in Medicine and Biology*, 50(16):3787–3806, 2005. 22, 42

[48] RF. Hartl, SP. Sethi, and RG. Vickson. A survey of the maximum principles for optimal control problems with state constraints. *Siam Review*, 37(2):181–218, 1995. 95

[49] J. Haueisen. Methods of numerical field calculation for neuromagnetic source localization. *Dissertation, Shaker Verlag*, 1996. 122

[50] J. Haueisen, DS. Tuch, C. Ramon, PH. Schimpf, VJ. Weedeen, JS. George, and JW. Belliveau. The influence of brain tissue anisotropy on human EEG and MEG. *NeuroImage*, 15:159–166, 2002. 7

[51] V. Hédou-Rouillier. A finite difference method to solve the forward problem in electroencephalography (EEG). *Journal of Computational and Applied Mathematics*, 167(1):35–58, 2004. 22

[52] B. He and Z. Liu. Multimodal functional neuroimaging: integrating functional MRI and EEG/MEG. *IEEE Reviews in Biomedical Engineering*, 1:23–40, 2008. 3

[53] H. Helmholtz. Ueber einige gesetze der vertheilung elektrischer stroeme in koerperlichen leitern mit anwendung auf die thierisch - elektrischen versuche. *Annual Review of Physical Chemistry*, 89:211–233, 1853. 8, 11, 18, 135

[54] CS. Herrmann, S. Rach, T. Neuling, and D. Stüber. Transcranial alternating current stimulation: a review of the underlying mechanisms and modulation of cognitive processes. *Annual Review of Physical Chemistry*, 7:279, 2013. 4, 78, 82

[55] R. Herzog, G. Stadler, and G. Wachsmuth. Directional sparsity in optimal control of partial differential equations. *SIAM Journal on Control and Optimization*, 50(2):943–963, 2012. 96

[56] MS. Hämäläinen, R. Hari, R. Ilmoniemi, J. Knuutila, and O. Lounasmaa. Magnetoencephalography: theory, instrumentation, and applications to noninvasive studies of the working human brain. *Reviews of Modern Physics*, 65:413–497, 1993. 3, 7, 12

[57] RN. Holdefer, R. Sadleir, and MJ. Russell. Predicted current densities in the brain during transcranial electrical stimulation. *Clinical Neurophysiology*, 117:1388–1397, 2006. 5, 74, 75, 76

[58] S. Homölle. Implementation and comparison of different approaches to the tDCS optimization problem. *Master Thesis in Mathematics, Fachbereich Mathematik und Informatik, University of Münster*, 2015. 120

[59] F. Hummel, P. Celnik, P. Giraux, A. Floel, WH. Wu, C. Gerloff, and LG. Cohen. Effects of non-invasive cortical stimulation on skilled motor function in chronic stroke. *Brain*, 128:490–499, 2005. 4

[60] C. Im, H. Jung, J. Choi, SY. Lee, and K. Jung. Determination of optimal electrode positions for transcranial direct currnt stimulation (tDCS). *Physics in Medicine and Biology*, 53:N219–N225, 2008. 5, 91

[61] MB. Iyer, U. Mattu, J. Grafman, M. Lomarev, S. Sato, and EM. Wassermann. Safety and cognitive effect of frontal DC brain polarization in healthy subjects. *Neurology*, 64:872–875, 2005. 4

[62] A. Janssen, SM. Rampersad, F. Lucka, B. Lanfer, S. Lew, U. Aydin, CH. Wolters, DF. Stegeman, and TF. Oostendorp. The influence of sulcus width on simulated electric fields induced by transcranial magnetic stimulation. *Physics in Medicine and Biology*, 58(14):4881–4896, 2013. 6, 125, 132

[63] M. Jenkinson, M. Pechaud, and S. Smith. BET2: MR-based estimation of brain, skull and sclap surfaces. *11th Annual Meeting of the Organization for Human Brain Mapping*, 2005. 30

[64] L. Jing, S. Zhu, and B. He. A finite difference method for solving the three-dimensional EEG forward problem. *Conf Proc IEEE Eng Med Biol Soc 2005*, 2:1540–1543, 2005. 22

[65] DK. Jones. The effect of gradient sampling schemes on measures derived from diffusion tensor MRI: a Monte Carlo study. *Magnetic Resonance in Medicine*, 51:807–815, 2004. 30

[66] K. Joos, D. De Ridder, P. Van de Heyning, and S. Vanneste. Polarity specific suppression effects of transcranial direct current stimulation for Tinnitus. *Neural Plasticity*, 930860:8pp, 2014. 4

[67] EM. Khedr, MA. Ahmed, N. Fathy, and JC. Rothwell. Therapeutic trial of repetitive transcranial magnetic stimulation after acute ischemic stroke. *Neurology*, 65(3):466–468, 2005. 4

[68] B. Lanfer, M. Scherg, M. Dannhauer, TR. Knösche, M. Burger, and CH. Wolters. Influence of skull segmentation inaccuracies on EEG source analysis. *NeuroImage*, 62:418–431, 2012. 7

[69] C. Lee, C. Im, and H. Jung. Analysis and design of whole-head magnetic brain stimulators: a simulation study. *International Journal of Control, Automation and Systems*, 5(3):337–342, 2007. 6, 137

[70] A. Leemann and DK. Jones. The B-matrix must be rotated when correcting for subject motion in DTI data. *Magnetic Resonance in Medicine*, 61:1336–1349, 2009. 31

[71] S. Lew, CH. Wolters, T. Dierkes, C. Röer, and RS. MacLeod. Accuracy and run-time comparison for different potential approaches and iterative solvers in finite element method based EEG source analysis. *Applied Numerical Mathematics*, 59(8):1970–1988, 2009. 8, 22, 43, 49, 50, 127, 135

[72] JL. Lions. Optimal control of systems governed by partial differential equations. *Dunod and Gauthier-Villars, Paris*, 1968. 95

[73] NK. Logothetis, C. Kayser, and A. Oeltermann. In vivo measurement of cortical

impedance spectrum in monkeys: implications for signal propagation. *Neuron*, 55(5):809–823, 2007. 77

[74] MD. Lucia, GJM. Parker, K. Embleton, JM. Newton, and V. Walsh. Diffusion tensor MRI-based estimation of the influence of brain tissue anistropy on the effects of transcranial magnetic stimulation. *NeuroImage*, 36(4):1159–1170, 2007. 6, 125

[75] J. Ludewig. Discontinous galerkin methods for the EEG forward problem. *Master Thesis in Mathematics, Fachbereich Mathematik und Informatik, Univ. Münster*, 2013. 156

[76] J. Malmivuo and R. Plonsey. Bioelectromagnetism: Principles and Applications of Bioelectric and Biomagnetic Fields. *Oxford University Press, New York*, 1995. 42

[77] PC. Maranda, M. Lomarev, and M. Hallet. Modeling the current distribution during transcranial direct current stimulation. *Clinical Neurophysiology*, 117:1623–1629, 2006. 5, 43, 73, 77, 91

[78] JC. Maxwell. Dynamical theory of the electromagnetic field. *Philosophical Transactions of the Royal Society of London*, 155:459–512, 1864. 11

[79] JWH. Meijs, OW. Weier, MJ. Peters, and A. von Oosterom. On the numerical accuracy of the boundary element method. *IEEE Transaction on Biomedical Engineering*, 36:1038–1049, 1989. 21

[80] M. Mohr. Simulation of bioelectric fields: the forward and inverse problem of electroencephalographic source analysis. *Dissertation Universität Erlangen-Nürnberg, Institut Informatik*, 2004. 18

[81] T. Neuling, S. Rach, S. Wagner, CH. Wolters, and CS. Herrmann. Good vibrations: oscillatory phase shapes perception. *NeuroImage*, 63(2):771–778, 2012. 83, 90, 91

[82] T. Neuling, S. Wagner, CH. Wolters, T. Zaehle, and CS. Herrmann. Finite-element model predicts current density distribution for clinical applications of tDCS and tACS. *Frontiers Psychiatry*, Sep 24:3:83, 2012. 4, 5, 6, 79, 80, 81, 82, 83, 125, 155

[83] MA. Nitsche, S. Doemkes, T. Kakaköse, A. Antal, D. Liebetanz, N. Lang, F. Tergau, and W. Paulus. Shaping the effects of transcranial direct current stimulation of the human motor cortex. *Journal Neurophysiology*, 97:3109–3117, 2007. 76, 77

[84] MA. Nitsche and W. Paulus. Excitability changes induced in the human motor cortex by weak transcranial direct current stimulation. *Journal Physiology*, 527:633–639, 2000. 4, 5, 64, 77, 91

[85] MA. Nitsche and W. Paulus. Sustained excitability elevations induced by transcranial DC motor cortex stimulation in humans. *Neurology*, 57(10):1899–1901, 2001. 4, 62

[86] J. Nocedal and SJ. Wright. Numerical optimization. *Springer-Verlag*, 1999. 46

[87] G. Nolte. The magnetic lead field theorem in the quasi-static approximation and its use

for magnetoencephalography forward calculation in realistic volume conductors. *Physics in Medicine and Biology*, 48(22):3637–3652, 2003. 17, 42

[88] SH. Oh, SY. Lee, MH. Cho, TS. Kim, and IH. Kim. Electrical conductivity estimation from diffusion tensor and T2: a silk yarn phantom study. *The International Society for Magnetic Resonance in Medicine*, 14:30–34, 2006. 7

[89] TF. Oostendorp, J. Delbeke, and DF. Stegeman. The conductivity of human skull: results of in vivo and in vitro measurements. *IEEE Transaction on Biomedical Engineering*, 47:1487–1492, 2000. 7

[90] TF. Oostendorp, YA. Hengeveld, CH. Wolters, J. Stinstra, G. van Elswijk, and DF. Stegeman. Modeling transcranial DC stimulation. *IEEE EMBS Conference, Vancouver, British Columbia, Canada*, pages 4226–4229, 2008. 5, 75

[91] R. Oostenveld and TF. Oostendorp. Validating the boundary element method for forward and inverse EEG computations in the presence of a hole in the skull. *Human Brain Mapping*, 17:179–192, 2002. 7, 62

[92] A. Opitz, M. Windhoff, RM. Heidemann, R. Turner, and A. Thielscher. How the brain tissue shapes the electric field induced by transcranial magnetic stimulation. *NeuroImage*, 58:849–859, 2011. 6, 125, 129, 132, 138

[93] A. Opitz, M. Windhoff, A. Reichenbach, and A. Thielscher. Calculation of the electric field induced by TMS: influence of white matter anisotropy. *Poster presented at Magstim/University of Oxford TMS Summer School, Oxford, UK.*, 2010. 6, 125, 129, 132

[94] AB. Owen. Variance components and generalized Sobol' indices. *Cornell University Library*, page arXiv:1205.1774, 2012. 124

[95] M. Parazzini, S. Fiocchi, E. Rossi, A. Paglialonga, and P. Ravazzani. Transcranial direct current stimulation: estimation of the electric field and of the current density in an anatomical human head model. *IEEE Transactions on Biomedical Engineering*, 58(6):1773–1780, 2011. 5, 43, 45, 75, 76

[96] JH. Park, SB. Hong, DW. Kim, M. Suh, and CH. IM. A novel array-type transcranial direct current stimulation (tDCS) system for accurate focusing on target brain areas. *IEEE Transactions on Magnetics*, 47:882–885, 2011. 5, 91, 92

[97] R. Plonsey and D. Heppner. Considerations on quasi-stationarity in electro-physiological systems. *Bulletin of Mathematical Biology*, 29:657–664, 1967. 12, 33

[98] R. Pohlmeier, H. Buchner, G. Knoll, A. Rienäcker, R. Beckmann, and J. Pesch. The influence of skull-conductivity misspecification on inverse source localization in realistically shaped finite element head models. *Brain Topography*, 9:157–162, 1997. 7

[99] BK. Puri, NJ. Davey, PH. Ellaway, and SW. Lewis. An investigation of motor function in

schizophrenia using transcranial magnetic stimulation of the motor cortex. *The British Journal of Psychiatry*, 169(6):690–695, 1996. 4

[100] S. Pursiainen, F. Lucka, and CH. Wolters. Complete electrode model in EEG: relationship and differences to the point electrode model. *Physics in Medicine and Biology*, 57(4):999–1017, 2012. 9, 18, 55

[101] T. Radman, RL. Ramos, JC. Brumberg, and M. Bikson. Role of cortical cell type and morphology in sub-and suprathreshold uniform electric field stimulation. *Brain Stimulation*, 2:215–228, 2009. 76

[102] C. Ramon, P. Schimpf, J. Haueisen, M. Holmes, and A. Ishimaru. Role of soft bone, CSF and gray matter in EEG simulations. *Brain Topography*, 16:245–248, 2004. 7, 63

[103] SM. Rampersad, DF. Stegeman, and TF. Oostendorp. Single-layer skull approximations perform well in transcranial direct current stimulation modeling. *Transactions on Neural Systems and Rehabilitation Engineering*, 2012. 5, 74, 77

[104] JP. Reilly. Applied bioelectricity: From electrical stimulation to electropathology. *New York: Springer*, 1998. 45, 77

[105] S. Reitzinger, U. Schreiber, and U. van Rienen. Algebraic multigrid for complex symmetric matrices and applications. *Journal of Computational and Applied Mathematics*, 155:405–421, 2003. 50

[106] JR. Romero, D. Anschel, R. Sparing, M. Gangitano, and A. Pascual-Leone. Subthreshold low frequency repetitive transcranial magnetic stimulation selectively decreases facilitation in the motor cortex. *Clinical Neurophysiology*, 113:101–107, 2002. 4

[107] BJ. Roth, LG. Cohen, M. Hallet, W. Friauf, and PJ. Basser. A theoretical calculation of the electric field induced by magnetic stimulation of a peripheral nerve. *Muscle and Nerve*, 13:734–741, 1990. 126

[108] BJ. Roth, D. Ko, IR. von Albertini-Carletti, D. Scaffidi, and S. Sato. Dipole localization in patients with epilepsy using the realistically shaped head model. *Electroencephalography and Clinical Neurophysiology*, 102:159–166, 1997. 7, 62

[109] Y. Roth, A. Zangen, and M. Hallett. A coil design for transcranial magnetic stimulation of deep brain regions. *Journal of Clinical Neurophysiology*, 19(4):361–370, 2003. 137

[110] M. Rullmann, A. Anwander, M. Dannhauer, SK. Warfield, FH. Duffy, and CH. Wolters. EEG source analysis of epileptiform activity using a 1mm anisotropic hexahedra finite element head model. *NeuroImage*, 44:399–410, 2009. 7, 31, 63

[111] J. Ruohnen and RJ. Ilmoniemi. Focusing and targeting of magnetic brain stimulation using multiple coils. *Medical and Biological Engineering and Computing*, 36:297–301, 1998. 6, 17, 18, 137, 140

[112] L. Ruthotto, H. Kugel, J. Olesch, B. Fischer, J. Modersitzki, M. Burger, and C Wolters. Diffeomorphic Susceptibility Artefact Correction of Diffusion-Weighted Magnetic Resonance Images. *Physics in Medicine and Biology*, 57:5715–5731, 2012. 7, 31

[113] RJ. Sadleir and A. Argibay. Modeling skull electrical properties. *Annals of Biomedical Engineering*, 35:1699–1712, 2007. 7

[114] RJ. Sadleir, TD. Vannorsdall, DJ. Schretlen, and B. Gordon. Transcranial direct current stimulation (tDCS) in a realistic head model. *NeuroImage*, 54(4):1310–1318, 2010. 5, 64, 75

[115] RJ. Sadleir, TD. Vannorsdall, DJ. Schretlen, and B. Gordon. Target optimization in transcranial direct current stimulation. *Frontiers Psychiatry*, 3:90, 2012. 4, 5, 6, 36, 91, 92

[116] R. Salvador, A. Mekonnen, G. Ruffini, and PC. Miranda. Modeling the electric field induced in a high resolution realistic head model during transcranial current stimulation. *IEEE EMBS Conference, Buenos Aires, Argentina*, pages 2073–2076, 2010. 5, 63, 73, 74, 75

[117] R. Salvador, S. Silva, PJ. Basser, and PC. Miranda. Determining which mechanisms lead to activation in the motor cortex: A modeling study of transcranial magnetic stimulation using realistic stimulus waveforms and sulcal geometry. *Clinical Neurophysiology*, 122:748–758, 2011. 4, 6

[118] A. Schiela and W. Wollner. Barrier methods for optimal control problems with convex nonlinear gradient state constraints. *SIAM Journal on Optimization*, 21(1):269–286, 2011. 96

[119] PH. Schimpf. Application of quasi-static magnetic reciprocity to finite element models of the MEG lead-field. *IEEE Transactions on Biomedical Engineering*, 54(11):2082–2088, 2007. 18, 42

[120] PH. Schimpf, C. Ramon, and J. Haueisen. Dipole models for the EEG and MEG. *IEEE Transactions on Biomedical Engineering*, 49:409–418, 2002. i, 8, 11, 42, 43

[121] C. Schmidt, S. Wagner, M. Burger, U. von Rienen, and CH. Wolters. Impact of uncertain head tissue conductivity in the optimization of transcranial direct current stimulation. *Journal of Neural Engineering*, page submitted, 2015. 122, 123, 124

[122] J. Shewchuk. An introduction to the conjugate gradient method without the agonizing pain. *Technical reportm CMU-CS-TR-94-125, Carnegie Mellon University*, 1994. 46, 47

[123] H. Si. TetGen, a quality tetrahedral mesh generator and three-dimensional delaunay triangulator. *Weierstrass Institute forApplied Analysis and Stochastics*, 2004. 29

[124] H. Si. Adaptive tetrahedral mesh generation by constrained Delaunay refinement. *International Journal of Numeral Methods in Engineering*, 75(7):856–880, 2008. 29

[125] HR. Siebner, C. Mentschel, C. Auer, and B. Conrad. Repetitive transcranial magnetic stimulation has a beneficial effect on bradykinesia in Parkinson's disease. *Neuroreport*, 10(3):589–594, 1999. 4

[126] SimBio. SimBio: A generic environment for bio-numerical simulationsSimBio: A generic environment for bio-numerical simulations. 2015. 128

[127] SM. Smith. Fast robust automated brain extraction. *Human Brain Mapping*, 17:143–155, 2002. 30

[128] E. Somersalo, M. Cheney, and D. Isaacson. Existence and uniqueness for electrode models for electric current computed tomography. *SIAM: SIAM Journal on Applied Mathematics*, 52(4):1023–1040, 1992. 56

[129] M. Stenroos, A. Hunold, and J. Haueisen. Comparison of three-shell and simplified volume conductor models in magnetoencephalography. *NeuroImage*, 94:337–348, 2014. 22

[130] HS Suh, SH. Kim, WH. Lee, and TS. Kim. Realistic simulation of transcranial direct current stimulation via 3-D high-resolution finite element analysis: effect of tissue anisotropy. *IEEE EMBS Conference, Minneapolis, Minnesota, USA*, pages 638–641, 2009. 5, 75, 76

[131] WH. Theodore, K. Hunter, R. Chen, F. Vega-Bermudez, B. Boroojerdi, P. Reeves-Tyer, K. Werhahn, KR. Kelly, and L. Cohen. Transcranial magnetic stimulation for the treatment of seizures - A controlled study. *Neurology*, 59(4):560–562, 2002. 4

[132] PS. Tofts. The distribution of induced currents in magnetic stimulation of the nervous system. *Physics in Medicine and Biology*, 35(8):1119–1128, 1990. 132

[133] C. Tsai. A framework for computing dense optical flow fields with flexible and robust regularization. *Dissertation, University of California, Santa Barbara*, 2008. 50

[134] DS. Tuch, VJ. Wedeen, AM. Dale, JS. George, and JW. Belliveau. Conductivity tensor mapping of the human brain using diffusion tensor MRI. *Proceedings of the National Academy of Sciences*, 98:11697–11701, 2001. 7, 31, 63

[135] S. Vallaghe, T. Papadopoulo, and M. Clerc. The adjoint method for general EEG and MEG sensor-based lead field equations. *Physics in Medicine and Biology*, 54:135–147, 2009. i, 8, 11, 18, 22, 25, 26, 42, 135, 149

[136] B. Vanrumste, G. Van Hoey, R. Van de Walle, MR. D'Havé, IA. Lemahieu, and PA. Boon. The validation of the finite difference method and reciprocity for solving the inverse problem in EEG dipole source analysis. *Brain Topography*, 14(2):83–92, 2001. 22

[137] F. Vatta, F. Meneghini, F. Esposito, S. Mininel, and F. Di Salle. Realistic and spherical head modeling for EEG forward problem solution: a comparative cortex-based analysis. *Computational Intelligence and Neuroscience*, page 972060, 2010. 16

[138] J. Vorwerk. Comparison of numerical approaches to the EEG forward problem. *Diploma thesis in Mathematics, Fachbereich Mathematik und Informatik, University of Muenster*, 2011. 31

[139] J. Vorwerk, JH. Cho, S. Rampp, H. Hamer, TR. Knösche, and CH. Wolters. A guideline for head volume conductor modeling in EEG and MEG. *NeuroImage*, 100:590–607, 2014. 8, 29, 44, 78, 137

[140] J Vorwerk, M Clerc, M Burger, and CH Wolters. Comparison of boundary element and finite element approaches to the EEG forward problem. *Biomedical Engineering/Biomedizinische Technik*, 57(SI-1 Track-O):795–798, 2012. 43, 44

[141] S. Wagner. An adjoint FEM approach for the EEG forward problem. *Diploma thesis in Mathematics, Fachbereich Mathematik und Informatik, University of Muenster*, 2011. 22, 24, 26, 39

[142] S. Wagner, SM. Rampersad, Ü. Aydin, J. Vorwerk, T. Neuling, CS. Herrmann, DF. Stegeman, and CH. Wolters. Investigation of tDCS volume conduction effects in a highly realistic head model. *Journal of Neural Engineering*, 11:016002 (14pp), 2014. 4, 5, 6, 8, 20, 29, 43, 45, 61, 62, 66, 67, 68, 71, 72, 91, 125, 135

[143] T. Wagner, F. Fregni, U. Eden, C. Ramos-Estebanez, A. Grodzinsky, M. Zahn, and A. Pascual-Leone. Transcranial magnetic stimulation and stroke: A computer-based human model study. *NeuroImage*, 30:857–870, 2006. 6, 125

[144] T. Wagner, F. Fregni, S. Fecteau, A. Grodzinsky, M. Zahn, and A. Pacsual-Leone. Transcranial direct current stimulation: a computer-based human model study. *NeuroImage*, 35:1113–1124, 2007. 4, 5, 36, 62, 73, 74, 75, 76, 91, 93

[145] T. Wagner, M. Zahn, AJ. Grodzinsky, and A. Pacual-Leone. Three-dimensional head model simulation of transcranial magnetic stimulation. *IEEE Transactions on Biomedical Engineering*, 51(9):1586–1598, 2004. 6, 125, 129, 130, 132

[146] EM. Wassermann and J. Grafman. Recharging cognition with DC brain polarization. *Trends in Cognitive Sciences*, 9:503–505, 2005. 77

[147] D. Weinstein, L. Zhukov, and C. Johnson. Lead-field bases for electroencephalography source imaging. *Annals of Biomedical Engineering*, 28(9):1059–1065, 2000. 20, 21, 42

[148] M. Windhoff, A. Opitz, and A. Thielscher. Electric field calculations in brain stimulation based on finite elements: an optimized processing pipeline for the generation and usage of accurate individual head models. *Human brain mapping*, 34(4):923–935, 2013. 43

[149] CH. Wolters, A. Anwander, G. Berti, and U. Hartmann. Geometry adapted hexahedral meshes improve accuracy of finite element method based EEG source analysis. *IEEE Transactions on Biomedical Engineering*, 54:1446–1453, 2007. 22, 31

[150] CH. Wolters, L. Grasedyck, and W. Hackbusch. Efficient computation of lead field

bases and influence matrix for the FEM-based EEG and MEG inverse problem. Part I: complexity considerations. *Inverse Problems*, 20:1099–1116, 2004. 20, 21, 42

[151] CH. Wolters, H. Köstler, C. Möller, J. Härdtlein, L. Grasedyck, and W. Hackbusch. Numerical mathematics of the subtraction method for the modeling of a current dipole in EEG source reconstruction using finite element head models. *SIAM Journal on Scientific Computing*, 30(1):24–45, 2007. 3, 22, 23, 35, 43

[152] CH. Wolters, M. Kuhn, A. Anwander, and S. Reitzinger. A parallel algebraic multigrid solver for finite element method based source localization in the human brain. *Computing and Visualization in Science*, 5:165–177, 2002. 8

[153] Y. Xie, J. Yuan, X. Ma, and X. Guan. Calculation of EEG problems with anisotropic conducting media by the Finite Volume Method. *IEEE Transactions on Magnetics*, 37(5):3749–3752, 2001. 22

[154] Y. Yan, Pl. Nunez, and RT. Hart. Finite-element model of the human head: scalp potentials due to dipole sources. *Medical and Biological Engineering and Computing*, 29(5):475–481, 1991. 24, 42, 149

[155] T. Zaehle, S. Rach, and CS. Herrmann. Transcranial alternating current stimulation enhances individual alpha activity in human EEG. *PLoS One*, 5:e13766, 2010. 62

[156] Y. Zhang, M. Brady, and S. Smith. Segmentation of brain MR images through a hidden Markov random field model and the expectation-maximization algorithm. *IEEE Transactions on Medical Imaging*, 20:45–57, 2001. 31